Mohamed Boudiaf University - M’sila

FACULTY OF SCIENCES

PHYSICS DEPARTEMENT

Order N°:

Thesis

To obtain the degree of

DOCTORATE 3rd cycle

Field: Physics

Option: Physics of materials

Presented by:

Mekki Houria

Theme

Study of the physical properties of new materials for application in the field of energy

At……. with the board of examiners:

Latelli H’mida	Professor	M’sila university	President
Baaziz Hakim	Professor	M’sila university	Supervisor
Charifi Zoulikha	Professor	M’sila university	Co-supervisor
Djaballah Yassine	Professor	Batna university	Examiner
Righi Haroun	Professor	Batna university	Examiner
Bensehil Ilhem	MCA	M’sila university	Examiner
Ghellab Torkia	MCA	M’sila university	Invited

Academic year: **2023/2024**

Dedication

This humble work is dedicated to

My adoring husband, my queen Balkis

The apple of my eye, my father

And to my esteemed mother, noblewoman, my darling

I express my gratitude to you more than anybody else, and I pray that God will protect you for me.

Thank you so much

Acknowledgments

The present thesis was conducted at the level of physics and chemistry of materials laboratory, faculty of science, M'sila University Mohammed Boudiaf under the supervision of Pr. Baaziz Hakim.

First and foremost, I would like to extend my appreciation to "Allah" for providing me with guidance, mental fortitude, protection, and the ability to successfully complete this research.

I would like to express my greatest appreciation to my supervisor Pr. Baaziz Hakim for his guidance, support, and invaluable expertise throughout this journey. his mentorship has been instrumental in shaping the direction of my research and pushing me to explore new horizons.

I would also like to extend my gratitude to the esteemed members of my dissertation committee, whose insightful feedback and constructive criticism will help to refine and strengthen my work. Their commitment to academic excellence has been a constant source of inspiration.

Without neglecting to express the gratitude to the physics and chemistry of materials laboratory members for their encouragement and feedback on several occasions especially the president of the laboratory Pr. Charifi Zoulikha, MCA. Ghellab Torkia and Dr. Ilyas Mili.

I am extremely grateful to Professor Latelli H'mida from university of M'sila for consenting to preside the jury for my thesis defense. I would like also to express my sincere gratitude to the esteemed board of examiners Professor Yassine Djaballah and Dr. Righi Haroun from university of Batna and MCA Ilham Bensehil from university of M'sila whose insightful feedback and constructive criticism will help to refine and strengthen my work.

Many thanks to my teachers in the Department of physics primarily Professor Ouali Ameur.

Abstract

Our thesis explores double half-Heusler alloys class of multifunctional materials. The main objective of our research is to investigate the structural, electronic, optical, elastic and thermoelectric properties of double half Heusler alloys $ScX´Y_2Sn_2$ (X´=Nb, Ta; Y=Ni, Pd, Pt). The current computations are conducted utilizing the full potential linearized augmented plane wave approach (FP-LAPW) that is based in density functional theory (DFT) that was carried out using WIEN2K code. the total energy is calculated by considering the exchange-correlation potential using the Local Density Approximation (LDA) and Generalized Gradient Approximation (GGA). Moreover, the Engel-Vosko (EV-GGA) and mBJ approaches are utilized to calculate the electronic and optical properties. The band structure of our double Heusler alloys exhibits semiconductors behavior, as evidenced by indirect band gaps ranging from 0.47 to 0.851 eV. Density of state diagrams reveal that d states predominate in the valence and conduction bands for atoms of Ni, Pd, Pt, Ta, and Sc. Furthermore, the optical properties, including the dielectric function, refractive index, reflectivity spectra, optical conductivity, and the energy loss function, are also considered. In addition, the elastic constants, the bulk modulus B and the shear modulus G were determined, identified the mechanical stability of our alloys. The BoltzTrap code, which is based on the semi-classical Boltzmann transport theory, was utilized to compute the transport coefficients, including electrical conductivity, electronic thermal conductivity, and Seebeck coefficient. The lattice thermal conductivity regarded as independent thermoelectric parameter following the Slacks equation, with the help of Gibbs program to obtain the Debye temperature, Grüneisen parameter...

The thermoelectric analysis suggests that these double half Heusler alloys are p-type materials. Furthermore, these alloys are considered as a potential candidate for thermoelectric devices.

Keywords: Double half Heusler alloys, DFT, EV-GGA approximation, electronic structure, optical, elastic, anisotropy, thermoelectric.

Résumé

Notre thèse explore la classe des alliages doubles demi-Heusler, des matériaux multifonctionnels. L'objectif principal de notre recherche est d'étudier les propriétés structurelles, électroniques, optiques, élastiques et thermoélectriques des doubles demi-alliages de Heusler $ScX'Y_2Sn_2$ (X'=Nb, Ta ; Y=Ni, Pd, Pt). Les calculs actuels sont effectués en utilisant l'approche d'onde plane augmentée linéarisée à plein potentiel (FP-LAPW) qui est basée sur la théorie de la fonctionnelle de la densité (DFT) qui a été effectuée en utilisant le code WIEN2K. L'énergie totale est calculée en considérant le potentiel d'échange-corrélation en utilisant l'approximation de densité locale (LDA) et l'approximation de gradient généralisée (GGA). En outre, les approches Engel-Vosko (EV-GGA) et mBJ sont utilisées pour calculer les propriétés électroniques et optiques. La structure de bande de nos alliages de Heusler double présente un comportement semi-conducteur, comme le montrent les bandes interdites indirectes allant de 0,47 à 0,851 eV. Les diagrammes de densité d'état révèlent que les états d prédominent dans les bandes de valence et de conduction pour les atomes de Ni, Pd, Pt, Ta et Sc. En outre, les propriétés optiques, y compris la fonction diélectrique, la réflectance optique, l'indice de réfraction, le spectre de réflectivité, la conductivité optique et la fonction de perte d'énergie, sont également prises en compte. En outre, les constantes élastiques, le module de compressibilité B et le module de cisaillement G ont été déterminés, identifiant la stabilité mécanique de nos alliages. Le code BoltzTrap, qui est basé sur la théorie semi-classique du transport de Boltzmann, a été utilisé pour calculer les coefficients de transport, y compris la conductivité électrique, la conductivité thermique électronique et le coefficient Seebeck. La conductivité thermique du réseau est considérée comme un paramètre thermoélectrique indépendant selon l'équation de Slack, avec l'aide du programme de Gibbs pour obtenir la température de Debye, le paramètre de Grüneisen...

Le résultat thermoélectrique suggère que ces alliages double semi Heusler sont des matériaux de type p. En outre, ils sont considérés comme des candidats potentiel pour les dispositifs thermoélectriques.

Mots-clés : les alliages double half Heusler, DFT, L'approximation EV-GGA, structure électronique, optique, élastique, anisotropie, thermoélectrique.

ملخص

تستكشف أطروحتنا فئة سبائك نصف هسلر المزدوجة من المواد متعددة الوظائف. الهدف الرئيسي من بحثنا هو دراسة الخصائص الهيكلية، الإلكترونية، البصرية، المرونية والكهر وحرارية لسبائك Heusler النصف المزدوجة ($ScX´Y_2Sn_2$ (X´=Nb, Ta; Y=Ni, Pd, Pt) . يتم إجراء الحسابات الحالية باستخدام طريقة الموجة المستوية المتزايدة خطيا (FP-LAPW)التي تعتمد على نظرية الكثافة الوظيفية (DFT) التي تم تنفيذها باستخدام كود WIEN2K .يتم حساب إجمالي الطاقة من خلال كمون تبادل ارتباط و ذللك باستخدام تقريب الكثافة المحلية (LDA) وتقريب التدرج المعمم .(GGA) علاوة على ذلك، يتم استخدام نهج Engel-Vosko (EV-GGA)و mBJلحساب الخصائص الإلكترونية والبصرية. يُظهر هيكل النطاق الخاص بسبائك Heuslerالمزدوجة سلوك أشباه الموصلات، كما يتضح من فجوات النطاق غير المباشرة التي تتراوح من 0.47 إلى 0.851 eV. تكشف مخططات كثافة الحالة أن الحالات d تهيمن على نطاقات التكافؤ والتوصيل للذراتNi, Pd، Pt ، Ta وScعلاوة على ذلك، تم أيضًا أخذ الخصائص البصرية، بما في ذلك دالة العزل الكهربائي، معامل الانكسار، طيف الانعكاس، الناقلية البصرية، ودالة ضياع الطاقة، ايضا في الاعتبار. بالإضافة إلى ذلك، تم تحديد الثوابت المرنة ومعامل الحجم B ومعامل القص G، مما أدى إلى تحديد الاستقرار الميكانيكي لسبائكنا. تم استخدام كودBoltzTrap ، الذي يعتمد على نظرية النقل بولتزمان شبه الكلاسيكية، لحساب معاملات النقل، بما في ذلك التوصيل الكهربائي، والتوصيل الحراري الإلكتروني، ومعامل سيبيك. تعتبر الناقلية الحرارية للشبكة معامل كهروحراري مستقل تتبع معادلة Slack بمساعدة برنامج Gibbs للحصول على درجة حرارة Debyeومعامل Grüneisen...

تشير النتائج الكهرو حرارية إلى أن سبائك هسلر النصف المزدوجة هي مواد من النوع p,علاوة على ذلك تعتبر أيضا مرشحًا محتملاً للأجهزة الكهرو حرارية.

الكلمات المفتاحية: الانصاف المضاعفة لخلائط هسلر، كثافة الدالة، تقريب EV-GGA,البنية الالكترونية، الضوئية، المرونية، تباين الخواص، الكهرو حرارية.

List of Contents

Heusler alloys

Chapter II: Calculations Methods

Density Functional Theory (DFT)

Full Potential Linearized Augmented Plane wave (FP-LAPW)

and

Boltzmann Transport Theory

Density Functional Theory (DFT)

Full Potential Linearized Augmented Plane wave (FP-LAPW)

Boltzmann Transport Theory

Chapter III: Results and Discussions

List of figures

List of tables

List of Abbreviations

DFT	Density Functional Theory
FP-LAPW	Full Potential Linearized Plane Wave
SCF	Self-Consistent Field
E_F	Fermi Energy Level
DOS	Density of States
GGA	Generalized Gradient Approximation
LDA	Local density approximation
EV-GGA	Engel-Vosko-GGA
PBE	Perdew-Burke-Ernzerhof
mBJ	modified-Beck and Jonson
BTE	Boltzmann Transport Equation
RTA	Relaxation Time Approximation
ZT	Thermoelectric Figure of merit
DHH	Double Half-Heusler
TMs	Transition metals
HM	Half metallic
N_V	Number of valence electrons
M_t	Total magnetic moment
TMR	Tunneling magnetoresistance
GMR	Giant magnetoresistance
SP	Slater Pauling
SGSs	Spin gapless Semiconductors
LTC	Lattice Thermal conductivity
ELF	Energy Loss Function

General Introduction

General Introduction

The need for energy resources is experiencing a significant surge as a result of rapid advancements in technology. Consequently, scientists have been compelled to actively explore alternative sources of energy. In addition, the majority of the energy is wasted in the form of waste heat, with only a quarter being utilized as mechanical power [1,2]. Finding renewable and sustainable alternatives to fossil fuels was essential for resolving the energy crisis. A thermoelectric generator (TEG) has the potential to transform directly this thermal energy into electrical energy [3,4]. Thermoelectric devices are comprised of two distinct semiconductor materials, namely n-type and p-type, which are thermally coupled in parallel and electrically connected in series. As a result of a temperature gradient, charged carriers are displaced within the material and eventually diffuse from the heated to the cooled surface. The term for this occurrence is the Seebeck effect. Indeed, thermoelectric (TE) devices are currently being intensively researched as a viable clean energy solution for the recovery of waste heat in automotive applications, this is due to its advantageous characteristics, such as silent operation, absence of moving components, and lack of environmentally detrimental fluids. This, in turn, has the potential to decrease carbon dioxide (CO_2) emissions.

Ioffe pioneered semiconductors for TE [5, 6]. His findings created a period of growth in TE research in the 1950s and early 1960s, resulting in the discovery and study of numerous novel materials. Goldsmid [7] demonstrated Bi_2Te_3 potential as a TE material, which continues to be the foundation of the industry today. Using semiconductor alloys instead of binary compounds to reduce thermal conductivity led to the development of various material classes, including skutterudites, clathrates, Half-Heusler compounds, and complex chalcogenides, as promising candidates for TE applications.

The performance of thermoelectric material is measured by its dimensionless figure of merit $ZT = S^2\sigma T/\kappa$ .Material transport properties can be optimized for high ZT, Seebeck coefficient and electrical conductivity should be high, whereas thermal conductivity should be low. Good thermoelectric materials can be obtained by minimizing the thermal conductivity of selected

semiconductors without impairing electrical transport. adding phonon scattering sources to the material reduces phonon lifespan.

Heusler alloys, which were first identified in 1903, have been widely applied in electronic spin devices, Including magnetoresistance (GMR) [8], magneto resistive random-access memory (MRAM) [9], and magnetic sensors [10]. Heusler alloys (HA) have been increasingly recognized for their wide range of functional properties in several fields such as electronics, spintronics, magnetism, and thermoelectric. These alloys exhibit various intriguing characteristics, including semiconducting behavior [11], half-metallicity, ferromagnetism [12], spin gapless semiconducting features [13], shape memory effect [14], and superconductivity [15].

Anand et al. recently introduced the concept of double half-Heusler (DHH) alloys, which are distinguished by their increased structural complexity and consequently diminished k_L values. A variety of chemical formulations are observed in this novel class of half Heusler alloys, including triple ($X'_2X''Y_3Z_3$), double quaternary ($X'X''Y_2Z_2$, $X_2Y'Y''Z_2$, $X_2Y_2Z'Z''$), and quadruple ($X'_3X''Y_4Z_4$) [16]. In this work, the primary focus is on the quaternary double half Heusler alloys, which have the following features: semiconductors with an indirect and narrow band gap, a significant contribution to the density of states from the d-orbital, mechanical stability, and a Debye temperature of around 400 K [17-24].

The focus of this research is to investigate the physical properties of the new form of Heusler alloys which are double half Heusler alloys $ScX'Y_2Sn_2$ (X'=Nb, Ta; Y=Ni, Pd, Pt), with the intention of applying it in the field of energy, in particular thermoelectric application. Nevertheless, no prior research has been conducted on the physical properties of these alloys. In order to predict new materials with potential applications in the energy sector and comprehend their diverse properties. in this thesis, a theoretical examination is presented based on density functional theory (DFT). The structural and electronic properties are computed using the Wien2k code [25] in the present study, whereas the transport coefficients are computed with the assistance of additional programs. calculating the lattice thermal conductivity using the Gibbs code [26]. however, the BoltzTrap code is employed in order to compute the electron Boltzmann transport equation [27].

The structure of this thesis is as follows: After a brief general introduction, the first chapter provides a comprehensive overview about Heusler alloys and thermoelectricity. These

multifunctional materials demonstrated a wide range of electrical properties, which allowed them to be utilized for a variety of applications, in particular, thermoelectric application. the second chapter consists of computational methods which include three sections, the first one is the density functional theory (DFT), this section of chapter describes how the Schrödinger equation for many body systems was developed through numerous approximations before being formulated in its ultimate form, as well as the method used for obtaining a self-consistent solution. afterwards, we present the full potential augmented plane wave method (FP-LAPW), and the last section is devoted to the Boltzmann transport theory. In third chapter the results and discussions of the structural, electronic, optical, elastic and thermoelectric properties of double half Heusler alloys are presented.

References

[1] J. Yang, F.R. Stabler, J. Electron. Mater. **38**, 1245 (2009).

[2] K. Schierle-Arndt, W. Hermes, Chemie in unserer Zeit **47**, 92 (2013).

[3] T.M. Tritt, Annu. Rev. Mater. Res. **41**, 433 (2011).

[4] G.J. Snyder, E.S. Toberer, Nat. Mater. **7**, 105 (2008).

[5] A. Ioffe, *Semiconductor Thermoelements and Thermoelectric Cooling* (Infosearch, London, 1957).

[6] A. Ioffe, Sci. Am. **199**, 31 (1958).

[7] H. Goldsmid, *Applications of Thermoelectricity*, Methuen's Monographs on Physical Subjects (Methuen, London, 1960).

[8] J. S. Moodera, L. R. Kinder, T. M. Wong and R. Meservey, Large Magnetoresistance at Room Temperature in Ferromagnetic Thin Film Tunnel Junctions, Phys. Rev. Lett., 74(16), 3273. Merit (1995).

[9] G. Binasch, P. Grünberg, F. Saurenbach and W. Zinn, Enhanced magnetoresistance in layered magnetic structures with antiferromagnetic interlayer exchange, Phys. Rev. B: Condens. Matter Mater. Phys., 39, 4828 (1989).

[10] S. A. Wolf, D. D. Awschalom, D. M. Treger, et al., Spintronics: A Spin-Based Electronics Vision for the Future, Science, 294, 1488 (2001).

[11] Felser C, Fecher G H and Balke B Spintronics: A Challenge for Materials Science and Solid-State Chemistry Angew. Chem. Int. Ed. 46 668–99 (2007).

[12] Jung D, Koo H-J and Whangbo M-H Study of the 18-electron band gap and ferromagnetism in semi-Heusler compounds by non-spin-polarized electronic band structure calculations J. Mol. Struct. THEOCHEM 527 113–9 (2000).

[13] Özdoğan K, Şaşıoğlu E and Galanakis I Slater-Pauling behavior in LiMgPdSn-type multifunctional quaternary Heusler materials: Half-metallicity, spin-gapless and magnetic semiconductors J. Appl. Phys. 113 193903 (2013).

[14] Sutou Y, Imano Y, Koeda N, Omori T, Kainuma R, Ishida K and Oikawa K Magnetic and martensitic transformations of NiMnX(X=In,Sn,Sb) ferromagnetic shape memory alloys Appl. Phys. Lett. 85 4358–4360 (2004).

[15] Klimczuk T, Wang C H, Gofryk K, Ronning F, Winterlik J, Fecher G H, Griveau J-C, Colineau E, Felser C, Thompson J D, Safarik D J and Cava R J Superconductivity in the Heusler family of intermetallics Phys. Rev. B 85 174505 (2012).

[16] S. Anand, M. Wood, Y. Xia, C. Wolverton and G. J. Snyder, Joule, 3(5) 1226-1238 (2019).

[17] Mekki H, Baaziz H, Charifi Z, Ghellab T, Genç A, Uğur, Uğur G Uğur *G, Solid State Communications 363(2023)* .

[18] G. Ugur, A.K. Kushwaha, M. Güler, Z. Charifi, S¸. Ugur, E. Güler, H. Baaziz, *Materials Science in Semiconductor* (2022).

[19] Z Charifi, H Baaziz, S¸ Ug˘ur, and G Ugur, *Indian J Phys* (2022).

[20] Slamani A, Khelfaoui F, Sadouki O,Bentayeb A,BoudiaK, Belkharroubi F, *Emergent Materials 6(2) 681-690 (2023).*

[21] Rached Y, Caid M,Merabet M,Benalia S,Rached H,Djoidi L,Mokhtari M, Rached D, *International Journal of Quantum Chemistry 122(9) (2022)* .

[22] Sahni B, Alam A*(2023).*

[23] Sâad Essaoud S, Bouhemadou A, Ketrfi M,Allali D, Bin-Omran S, *Physica B: Condensed Matter 657(2023).*

[24] Berarma K, Essaoud S,Mousa A,Azrar S,Al-Reyahi A, *Semiconductor Science and Technology 37(5) (2022).*

[25] P. Blaha, K. Schwarz, G. Madsen, D. Kvasnicka, J. Luitz, Wien2k, Techn. Universitat,

Vienna, Austria, (2001).

[26] MA Blanco, E Francisco, and V Luana, Computer Physics Communications **158** (1), 57 (2004).

[27] Georg KH Madsen and David J Singh, Computer Physics Communications **175** (1), 67(2006).

Chapter I

Thermoelectricity

And

Heusler Alloys

1 Thermoelectricity

I. 1. Introduction

The global community is confronted with a formidable obstacle in the form of escalating greenhouse gas emissions and the exponential depletion of fossil fuel reserves, which exacerbate the already substantial energy demand [1]. approximately 68% of the energy generated in the United States is wasted or not utilized [2]. Thermoelectric energy conversion is a sort of renewable energy technology that has garnered significant attention and is anticipated to have a crucial part in satisfying the world's future energy needs. Thermoelectric modules are essentially solid-state heat engines that may directly convert thermal energy into electrical energy by producing a voltage when put in a thermal gradient. This technology may have a wide range of applications due to the fact that the transition to a more sustainable energy system involves efforts to reduce waste and improve energy efficiency. In addition to waste heat recovery, thermoelectric (TE) devices have been studied for their application in TE-solar hybrid systems [3], TE-refrigeration [4], and as radioisotope thermoelectric generators (TEGs) for deep-space missions such as NASA's Voyager and Cassini probes [5]. Thermoelectric devices are composed of solid-state components, meaning they do not have any moving elements that can cause vibrations. Additionally, they do not release any environmentally damaging gasses or fluids.

Heusler compounds, particularly double half Heusler, are regarded as highly promising candidates for optimal thermoelectric materials due to their exceptional electrical transport properties. Our research focuses on investigating this novel category of materials, and the obtained findings represent a significant and original scientific contribution to the current body of literature.

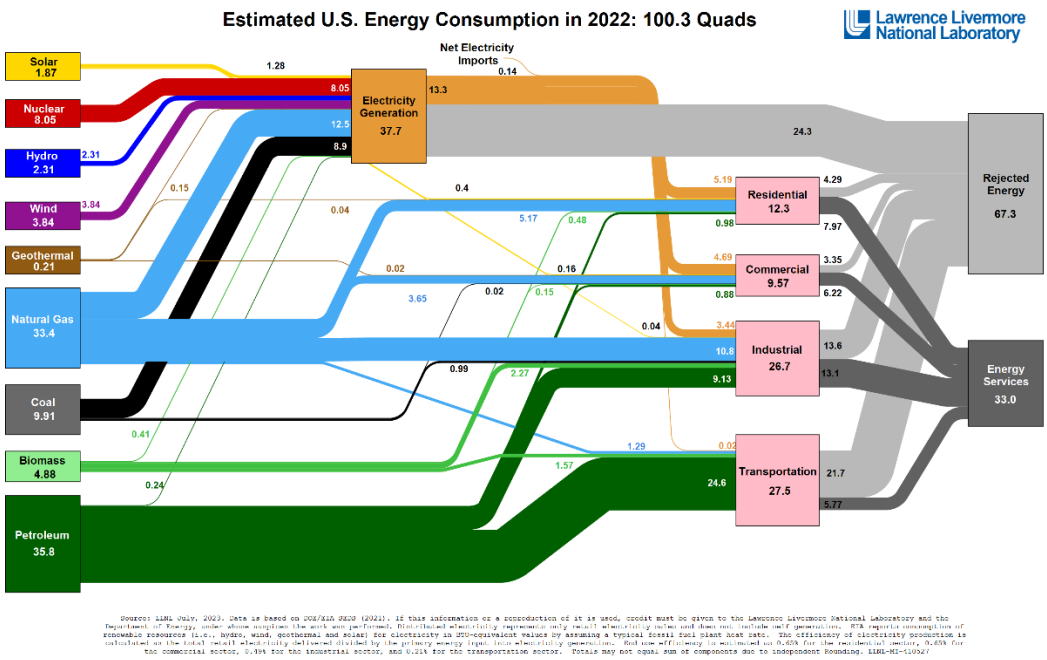

Figure.I.1: The 2022 energy flow chart from Lawrence Livermore National Laboratory outlines energy production sources, energy consumption patterns in the United States, and the amount of trash generated [2].

I. 2. Thermoelectric effects

I. 2. 1. Seebeck effect

Thomas Seebeck discovered the thermoelectric effect in 1821[6]. He pointed out that connecting two different wires at different temperatures created an electric field that threw off a nearby compass. The identical phenomenon depicted in Figure.I.2 is observed when a temperature gradient is created within a bulk material.

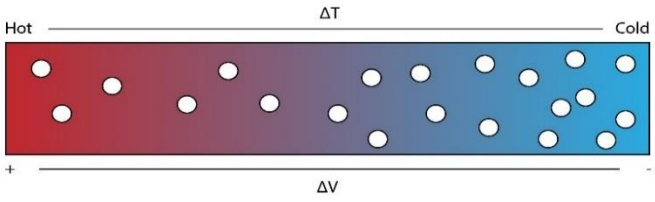

Figure.I.2: Illustration of the Seebeck effect [7].

When a material is exposed to a temperature gradient *(*ΔT*)*, the electrical charge carriers on the heated side exhibit a greater velocity compared to the carriers on the cold side. This leads to a

comparatively higher density of charge carriers on the colder side of the material. The voltage differential that occurs is determined by both the Seebeck coefficient and the temperature gradient.

$$\Delta V = -S\Delta T \tag{I-1}$$

The direction of current is defined by the nature of the charge carriers, which can be either electrons (n-type) or holes (p-type). The carrier type is determined by the sign of the Seebeck coefficient which is negative for electron-dominant carriers and positive for hole-dominant carriers.

I. 2. 2. Peltier effect

In 1834, a French watchmaker and scientist named Jean Charles Peltier, discovered that when an electric current flow through the junction of two metals, heat is absorbed at one junction and released at the other. This phenomenon is referred to as the Peltier effect, which is the opposite of the Seebeck effect [8]. The coefficient of proportionality between the quantity of heat released or absorbed and the current carried through is currently known as the Peltier coefficient, and it is defined as

$$Q = \Pi\, I \tag{I-2}$$

Q represents the heat released at the contact point and I is the electric current.

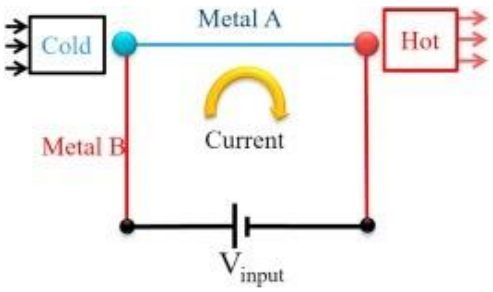

Figure.I.3: Explanation of thermoelectric cooling using the Peltier effect [9].

I. 2. 3. Thomson effect

In 1851, William Thomson, later known as Lord Kelvin who made significant contributions to the field of thermodynamics, established a correlation between the two effects (Seebeck and Peltier) and added a third effect called the Thomson effect. The Thomson effect states that when

an electric current flow through a material with a temperature differential, it will result in a heat exchange, either cooling or heating the material depending on its properties [10].

For a given point x and current I, the heat flux gradient $\frac{dQ}{dx}$ (Q is the heat) is connected to the temperature gradient $\frac{dT}{dx}$ using the equation (I-3). Where τ denotes the Thomson effect.

$$\frac{dQ}{dx} = \tau I \frac{dT}{dx} \tag{I-3}$$

Subsequently, Thomson proposes the two following relations, referred to as the Kelvin relation, which connect the three previously introduced thermoelectric coefficients. Where T is the absolute temperature.

$$\pi = ST \tag{I-4}$$

$$\tau = T \frac{dS}{dT} \tag{I-5}$$

I. 3. Thermoelectric devices

Thermoelectric devices, whether for refrigerators or generators, are electrically coupled pairs of semiconductors. A pair is created by a p-type material with holes as charge carriers, a positive Seebeck coefficient, an n-type material with electrons, and a negative Seebeck coefficient. As seen in Figure.I.4, n-type semiconductors exhibit a Fermi level that is higher compared to intrinsic semiconductors and is in closer proximity to the conduction band. p-type semiconductors have a higher energy level closer to the valence band.

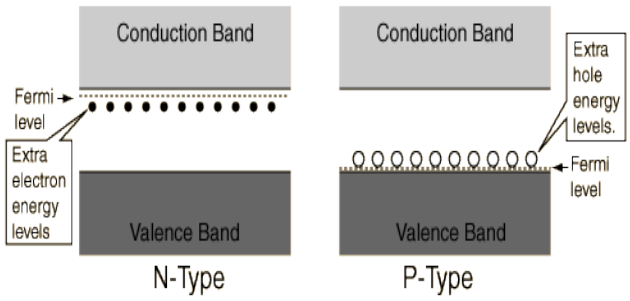

Figure.I.4: n-type vs p-type semiconductor.

As illustrated in the Figure.I.5 (a) and (b), when both n and p types are connected to a conductor material, the distinct couples are electrically arranged in series and thermally aligned to create a thermoelectric couple. When a temperature difference is applied across a thermoelectric device, free charge carriers (electrons for n-type materials and holes for p-type materials) diffuse from hot to cold, generating a voltage difference (Seebeck voltage) that drives an electrical current Figure I.5.(a). Conversely, in cooling mode Figure I.5.(b), an electrical current across the thermoelectric couple generates a temperature difference at the interface. This case uses the Peltier effect, causing one end of the thermoelectric material to increase and the other to decrease in temperature.

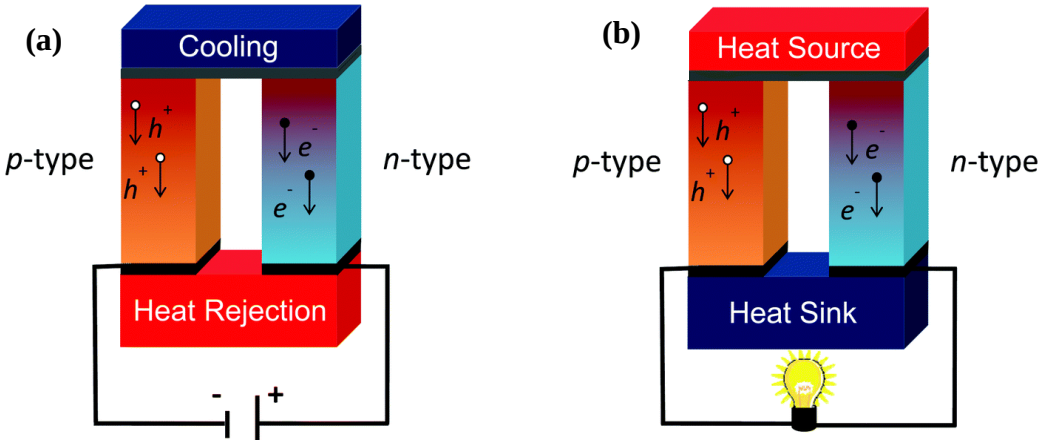

Figure.I.5: An illustration of the thermoelectric (TE) effect in both a Peltier cooler (a) and a TE generator (b) [11].

I. 4. Thermoelectric efficiency: Figure of merit

The thermoelectric Figure of merit (ZT), first proposed by Altenkirch in 1911 [12], is utilized to quantify the thermoelectric performance of a device and assess its efficiency (TE). Equation (I-6) defines the Figure of merit for a thermoelectric material.

$$ZT = \frac{S^2 \sigma T}{\kappa} = \frac{S^2 T}{\rho \kappa} \tag{I-6}$$

$$\kappa = \kappa_e + \kappa_{lat} \tag{I-7}$$

T represents the absolute temperature, S is the Seebeck coefficient, σ the electrical conductivity is the inverse of electric resistivity, and κ is the thermal conductivity which is

calculated as the sum of two parts: the electronic part (κ_e), which signifies the heat transferred by charge carriers (e.g., electrons or holes), and the lattice part (κ_{lat}), which signifies the heat transferred by phonons (lattice vibrations), as formally represented in equation (I-7). Additionally, The Seebeck coefficient and electrical conductivity are collectively known to as the power factor in which $PF = S^2\sigma$. The thermoelectric efficiency for power generation can be defined according to the equation (I-7):

$$\eta_{max} = \eta_C \frac{\sqrt{1+ZT}-1}{\sqrt{1+ZT}+\frac{T_C}{T_H}} \tag{I-8}$$

The temperature on the hot side is represented by T_H, the temperature on the cold side is represented by T_C and the Carnot efficiency is donated by the term η_C in which the efficiency of a thermoelectric device is directly proportional to the Carnot efficiency η_C :

$$\eta_C = \frac{T_H - T_C}{T_H} \tag{I-9}$$

The challenging undertaking is to achieve maximum efficiency in the material's transport properties. Indeed, let's look at the expression of the Figure of merit $ZT = \frac{S^2\sigma T}{\kappa}$. We can see that to have a high ZT value, The Seebeck coefficient and the electrical conductivity must be as high as possible. In contrast, the thermal conductivity has to be as low as possible.

Nevertheless, there is a connection between the three parameters, and the carrier concentration directly impacts all three of these characteristics, as shown in Figure.I.6. As the concentration of carriers increases, the electrical conductivity also increases. However, simultaneously, the Seebeck coefficient decreases as the thermal conductivity increases. Based on the diagram. The ZT parameter reaches its maximum value within a specific carrier concentration range (10^{19} to 10^{21} Cm^{-3}), specifically in strongly doped semiconductors [13].

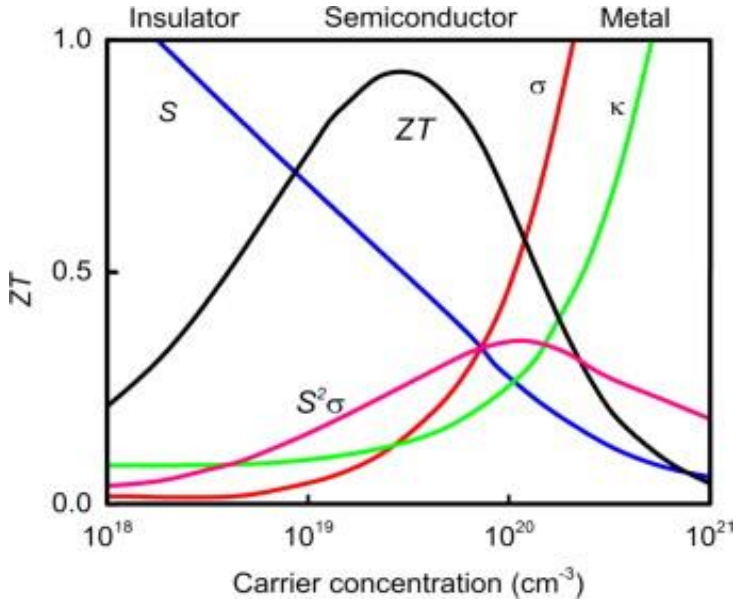

Figure.I.6: The Seebeck coefficient (S), electric conductivity (σ), power factor (*PF*), thermal conductivity (κ), and Figure of merit (*ZT*) as a function of carrier concentration [14].

I. 5. Transport properties

Equation (I-6) demonstrates a significant correlation between the ZT parameters, mainly the electrical conductivity, Seebeck coefficient, and thermal conductivity. To achieve an optimal solution and maximize the performance indicator, it is necessary to thoroughly comprehend the impact of these parameters.

I. 5. 1. Electrical conductivity

The parameter σ is directly correlated to both the carrier concentration n, and the mobility of the charge carrier μ, as stated in the equation (I-9) [14].

$$\sigma = \frac{1}{\rho} = ne\mu \qquad \text{(I-9)}$$

Where ρ represents electrical resistivity and e represents carrier charge.

Equation (I-9) clearly indicates that in order to get a high σ, a high charge carrier concentration is necessary, which in turn has a conversely influence on S. The mobility of charge carriers can be characterized in terms of their effective mass m^*,see equation (I-10).

$$\mu = \frac{e\tau}{m^*} \tag{I-10}$$

The symbol m* represents the effective mass, whereas τ denotes the relaxation time which is the mean time between charge carrier collisions.

I. 5. 2. Seebeck coefficient

The Seebeck coefficient can be derived from the Mott equation using the Boltzmann transport theory [15].

$$S = \frac{\pi^2}{3}\frac{k_B^2 T}{e}\left\{\frac{d\ln(\sigma(E))}{dE}\right\}_{E=E_F} \tag{I-11}$$

In which $e, \sigma(E)$ are the elementary charge and electrical conductivity that is a function of energy E at the Fermi level E_F ,on the other hand $\frac{d\ln(\sigma(E))}{dE}$ is the slope of the DOS. By substituting equation (I-9) into the Mott equation, we obtain:

$$S = \frac{\pi^2 k_B^2}{3e}T\left\{\frac{1}{n}\frac{dn(E)}{dE} + \frac{1}{\mu}\frac{d\mu(E)}{dE}\right\}_{E=E_F} \tag{I-12}$$

This illustrates the conflict concerning the optimization of ZT, as the Seebeck coefficient and electrical conductivity exhibit opposing dependencies on the number of charge carriers see equation (I-12), further, when the carrier concentration is high the electrical conductivity is also high but the Seebeck coefficient has a low value, therefore it's necessary to find a compromise. This may typically be achieved for carrier concentrations ranging from 10^{19} to 10^{21} carriers per Cm^{-3} [14].

The Seebeck coefficient for metals or degenerate semiconductors can be expressed as [14]:

$$S = \frac{8\pi^2 k_B^{\,2}}{3eh^2} m^* T\left(\frac{\pi}{3n}\right)^{3/2} \tag{I-13}$$

The symbols h, k_B and m^* represent the Planck constant, the Boltzmann constant, and the effective mass of the density-of-states (DOS), respectively.

Furthermore, The Seebeck coefficient is affected by the effective mass, which is inversely related to the band curvature of the electronic band structure at the Fermi energy, as well as the carrier concentration.

I. 5. 3. Thermal conductivity

As was mentioned in the preceding section (I.4) ,the thermal conductivity κ of a given material is determined by adding the contributions of two components: the lattice component κ_{lat} , which represents the heat conducted by phonons, and the electronic component κ_e , which represents the heat carried by charge carriers ,see equation (I-7).

According to the Wiedemann-Franz law the electronic thermal conductivity κ_e is related to the electrical conductivity σ [14], as defined in equation (I-13).

$$\kappa_e = L\sigma T \tag{I-14}$$

Where L is the Lorentz number, the Lorentz number does not remain constant and is affected by temperature and carrier concentration. A commonly employed value for metals and degenerate semiconductors is 2.4 x 10^{-8} W Ω K^{-2}. A value of 1.6 x 10^{-8} W Ω K^{-2} is determined for half Heusler compounds [16], which are the primary subject of study in this thesis.

Lattice thermal conductivity can be written as:

$$\kappa_{latt} = \frac{1}{3} C_V \upsilon_S L = \frac{1}{3} C_V \upsilon_s^2 \tau \tag{I-15}$$

Where C_V , υ_S , L denote the specific heat at constant volume, the average velocity and the mean free-path of phonons which is linked to phonon relaxation time τ via phonon velocity $\upsilon = L/\tau$.

I. 6. Thermoelectric materials

In 1952, Ioffe emerged as a pioneer in proposing semiconductors as highly promising materials for thermoelectric (TE) applications [17,18]. Goldsmid discovered the significant potential of Bi2Te3 as a thermoelectric (TE) material [19]. Ioffe's suggestion to utilize semiconductor alloys instead of basic binary compounds to reduce thermal conductivity has resulted in the wide range of material classes available today, including skutterudites, clathrates,

Half-Heusler compounds, and complex chalcogenides. These materials show great potential as candidates for thermoelectric applications. There are certain criteria for the selection of high-quality thermoelectric materials. As previously mentioned, excellent thermoelectric materials are typically doped semiconductors with carrier concentrations ranging from 10^{19} to 10^{20} per cm^3 with heavy elements and complex unit cells. Also, the most significant aspect is that the material should have a narrow band gap. Based on these characteristics several promising thermoelectric materials emerge with different temperature range. these materials can be categorized into two groups are mostly inorganic: conventional and new materials [20].

I. 6. 1. Conventional thermoelectric materials

Conventional thermoelectric materials are bulk doped semiconductor alloys or chalcogenide compounds. It can be classified into three categories according to the ideal temperature range: Bi_2Te_3-based materials for temperature applications below 150 ˚C, PbTe-based materials for temperature between (150–500 ˚C), and SiGe for use at temperatures over 500 ˚C [21-23].

Bismuth Telluride (Bi_2Te_3) based alloy, these materials are widely recognized and have a thermoelectric figure of merit (ZT) that can approach unity at ambient temperature. The peak ZT values for the commonly researched p-type compositions $Bi_xSb_{2-x}Te_3$ can reach up to 1.4-1.5, while the greatest ZT for the n-type $Bi_2Te_{3-x}Se_x$ is approximately 1 [24,25]. The researchers have determined that the figure of merit (ZT) increases from 0.58 to 1.16 when materials are fabricated in a nanostructure morphology.

Lead Telluride (PbTe) and its alloys is a remarkable thermoelectric performance, it has attracted a lot of research attention in the mid-temperature region (500 K-900 K). The figure of merit is close to 0.8. Recent studies have found that single phase PbTe-based materials have achieved maximum ZT values of approximately 1.4, whereas homogeneous PbTe-PbSe materials have reached values as high as 1.8 [26].

Silicon–Germanium alloys ($Si_{1-x}Ge_x$) Silicon is the second most prevalent element on Earth, which classifies these materials as some of the best thermoelectric materials documented in scientific literature for use in high-temperature applications (with a hot side temperature above 500 ˚C). Furthermore, they are not only cost-effective but also very non-toxic, making them an

excellent choice for thermoelectric applications [21]. 30% germanium. Silicon-germanium alloys are utilized in deep-space probe radioisotope thermoelectric generators [11].

I. 6. 2. New thermoelectric materials

Slack proposed **Phonon-glass electron-crystal (PGEC)** materials in 1995 [27] where the material has a complex intermetallic cage structure, providing good electrical properties like crystals and poor thermal conductivity like glass [28]. There are two main groups of recently developed materials that are commonly referred to as PGEC materials: clathrates and Skutterudites [29]. Both types of structures have a cage structure that allows for the insertion of a big metal atom, which contributes to scatter phonons and reducing the thermal conductivity.

Skutterudites, possess MX_3 generic formula where M is a metal such as Co, Ir and Rh, X is a Sb, P or As, as for example $CoSb_3$ or $CoAs_3$. these materials have been fine-tuned resulting a new formula which is LM_4X_{12}, L represents a rare earth element. The materials exhibit high figures of merit within the temperature range of 700–900 K, which places them as potential options for power generation in the intermediate to high temperature range [11]. For instance, a ZT peak value 1.7 in quadruple filled n-type skutterudites $Ba_{0.08}La_{0.05}Yb_{0.04}Co_4Sb_{12}$ at 580 C° was found [30].

Clathrates have a $X_8Y_{16}Z_{30}$ chemical formula, the element X represent Sr, Ba, or Ca; Y is Al or Ga and Z is Ge, Si or Sn. The maximum figures of merit are achieved around 800–900 K, making them suitable for moderate to high-temperature energy recovery [11].as an example, $Ba_8Ga_{16}Ge_{30}$ clathrates n-type has ZT value 1.35 at 630 C° [31].

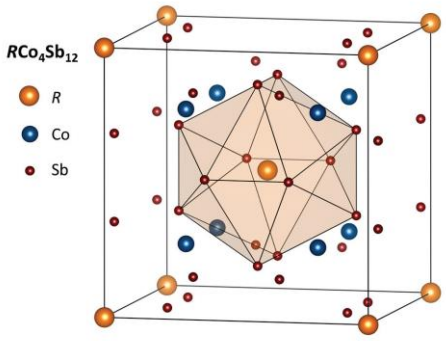

Figure.I.7: Crystal structure of the filled skutterudite RCo_4Sb_{12} [32].

Gascoin et al [33] proposed Zintl phases as a promising thermoelectric materials candidate in 2005. The usual characteristics of these semiconductors include a complex structure and a narrow band gap. Numerous researches have been conducted on these materials, with best ZT values ranging from 1 to 1.5 [34]. TE oxides are good TE performers [36], because they are ecological and generally stable at high temperatures. One example of this is $Ca_3Co_4O_9$ ($ZT \approx 1$).

Research is also being conducted on the use of organic materials including polymers, Carbon nanotubes (CNTs) and graphene as thermoelectric materials [37]. These materials possess the characteristics of being recyclable, economical, mechanically flexible, and having low thermal conductivity. Table.I.1 presents a summary of the ZT values for a selection of the most advanced thermoelectric materials.

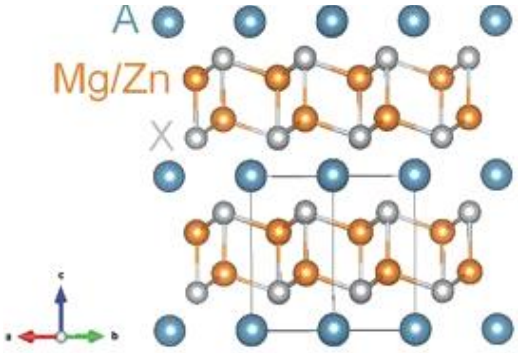

Figure.I.8: Crystal structure of Zintl AZn_2X_2 compounds such as $CaZn_2Sb_2$ [35].

Half-Heusler alloys, in particular, have complex crystal structure and their chemical composition include a wide range of atoms that limit the mean free path of phonons. these materials garnered a lot of interest among TE materials for temperature going up to 600 C° which is about the same temperature as most sources of waste heat in industry. half-Heusler alloys have excellent transport properties, relatively high Seebeck coefficients, and diverse combinations of elements [38]. As an example, for n-type half Heusler the Seebeck coefficient range from -100 to -300 μV, and electrical conductivity in the range 10^5-10^7 $(\Omega.m.s)^{-1}$ [39,40]. Moreover, they have high thermal and mechanical stability and from an economic standpoint these materials are low toxicity and low cost, more detailed description of these materials will be provided.

Table.I. 1: Thermoelectric figures of merit for typical examples of various thermoelectric material families [11].

TE family	*Representative examples*	*n/p*	*Peak ZT*	*Temperature of maximum ZT/K*
Chalcogenides [41]	$Bi_2Te_{3-x}Se_x$	n	1.15	370
	$AgPb_{18}SbTe_{20}$	n	2.2	800
	Cu_5FeS_4	p	0.55	543
Oxides [42]	$LaCrO_3$	p	0.14	1600
	$La_{0.15}Sr_{0.775}TiO_{3-\delta}$	n	0.41	973
Oxy-chalcogenides [41]	$Bi_{0.875}Ba_{0.125}CuSeO$	p	1.4	923
	$Bi_{0.975}Cu_{0.975}SeO$	p	0.84	750
Skutterudites [43]	$Ba_{0.08}La_{0.05}Yb_{0.04}Co_4Sb_{12}$	n	1.7	850
	$Yb_{0.25}La_{0.60}Fe_{2.7}Co_{1.3}Sb_{12}$	p	0.99	700
Intermetallics [44]	$Yb_{14}MnSb_{11}$	p	1.04	1228
	Zn_4Sb_3	p	1.3	673
Clathrates [45]	$Ba_8Ge_{16}Ge_{30}$	n	1.35	900
	$Ba_8Ge_{16}Al_3Ge_{27}$	p	0.61	760
Half-Heuslers [46]	TiNiSn	n	0.4	775
	$Zr_{0.3}Hf_{0.65}Ta_{0.05}NiSn$	n	0.85	870
Silicon–germanium alloys [47]	$Si_{0.8}Ge_{0.2}$ doped with P	n	1.3	1173
Metal silicides [47]	$Mg_{1.86}Li_{0.14}Si_{0.3}Sn_{0.7}$	p	0.5	750

2

Heusler Alloys

I.7. Heusler Alloys

I.7. 1. Introduction

Heusler Compounds history dates back to 1903, where the German mining engineer "Friedrich Heusler" discovered a new class of intermetallic compound Cu_2MnX (X=Al, In, Sn, Sb, Bi) known as Heusler alloys, which exhibits ferromagnetic properties, despite the fact that none of its individual components had magnetic properties on their own [48,49]. Subsequently, the phenomenon of ferromagnetism was discovered in more compounds made from Manganese (Mn) and Copper (Cu) along with elements as Antimony (Sb), Tin (Sn). Since their discovery, over a two thousand compounds have been identified. Bradley and Rodgers [50], also Otto Heusler (Heusler's son) [51], determined that Cu_2MnAl crystallizers in FCC structure (space group F-m3m,225) in 1934.

Additionally, Heusler's son found that there is a possibility of another sort of crystalline arrangement, which is today known as an inverter or inverted Heusler compound and has the space group T_2^d with 216 classifications [51]. Not long after (1951-1952) Heusler's discovery, Nowotny and Juza presented results on a separate set of materials namely LiMgAs (Nowotny) and CuMgAs (Juza), These materials have since been commonly referred to as the Nowotny-Juza-Phases. The Nowotny-Juza phases and Heusler compounds were linked by L. Castelliz who synthesized NiMnSb [52,53], which is currently recognized as a half Heusler compound.

A half metallic ferromagnetic behavior in NiMnSb compound was reported for the first time by Groot et al in 1983 [54], derived from first principles calculations. In the late eighties, A. Fert and colleagues proposed the concept of incorporating half-metallic behavior into spintronic applications [55]. Heusler compounds have intriguing properties as magnetic, topological,

multiferroic, and thermoelectric properties have generated significant interest and play a crucial role in the advancement of intelligent materials for a wide range of potential uses (see Figure.I.9).

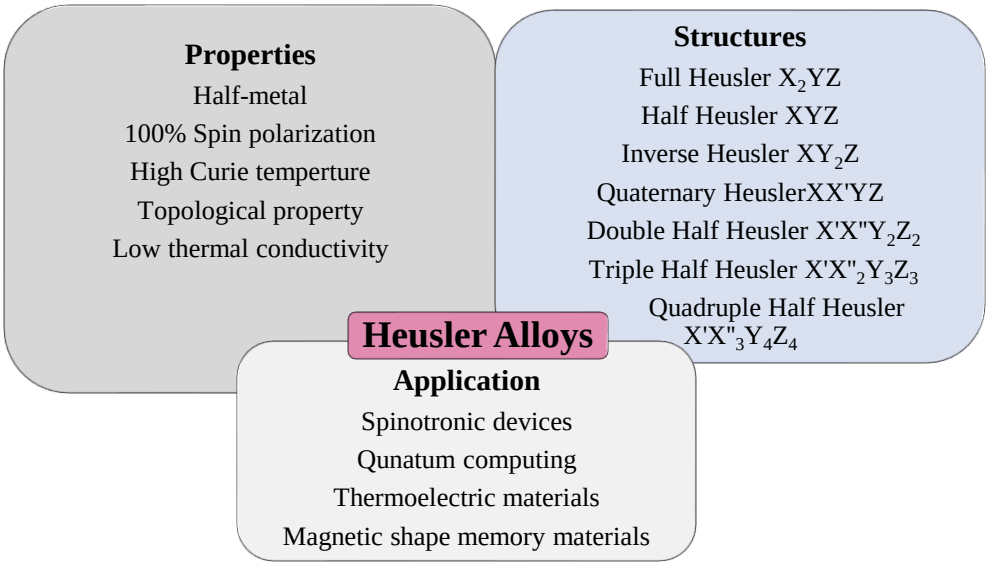

Figure.I.9: An overview of Heusler alloys.

HH compounds consist of elements with high melting points as an example we take elements of our double half Heusler compounds, are as follow: Scandium (1539º C), Niobium (2468º C), Nickel (1453º C), Tantalum (2996º C), Platinum (1772º C), and Palladium (1552º C). Additionally, these compounds also contain an element with a relatively low melting point, such as Tin (232º C). Thus, a high temperature is required for their preparation techniques. Additional methods of preparation for HH compounds are typically induction heating [56], Arc melting, solid state reaction, [57] new preparation technique as melt spinning [58] and spark plasma sintering (SPS) [59].

Heusler alloys can be made from a range of elements from different region periodic table These alloys are typically composed of one main group element (Z) with low melting point and two transition metals (X, Y) with high melting point comparing to X atom (see Figure.I.10). They can be categorized into two most common groups. Compounds with the chemical formula X_2YZ consist of four face-centered cubic (FCC) sublattices are known as full Heusler alloys while compounds with the formula XYZ consist of three FCC sublattices are defined as half Heusler.

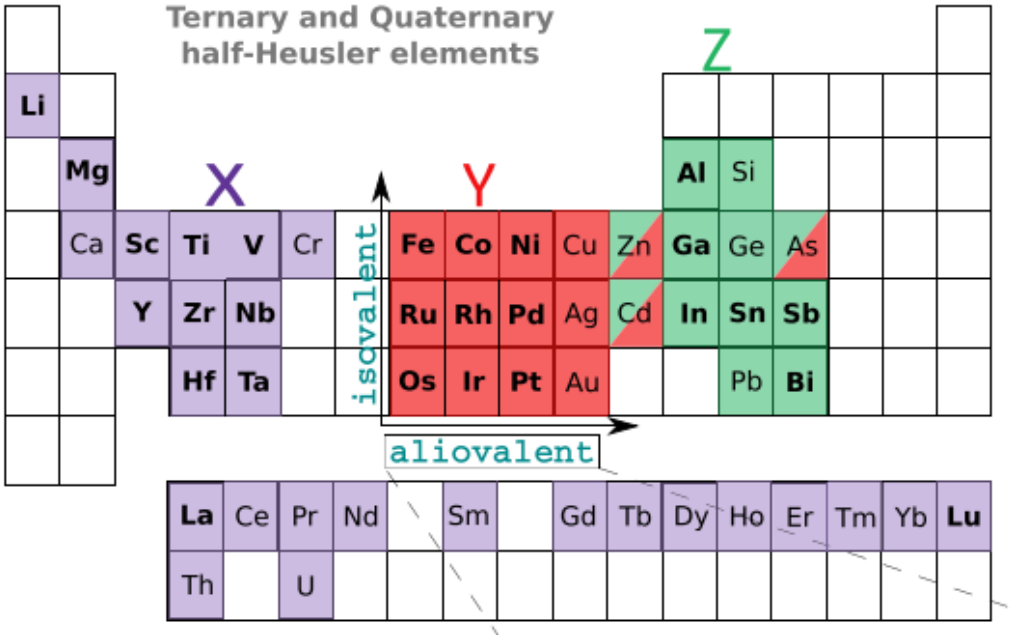

Figure.I.10: Elements of the half Heusler structure are shown in the periodic table using a color scheme in which X denotes violets, Y denotes red, and Z is green [1].

I.8. Types of Heusler alloys

I.8. 1. Full Heusler

Full Heusler alloys is identified by the general formula X_2YZ with a 2:1:1 stoichiometry where X and Y are transition metals and Z is an element belonging to groups III to V on the periodic table. These alloys crystallize in the face centered cubic (FCC) structure with space group Fm-3m (space group N°225, Cu_2MnAl prototype, $L2_1$ structure type), and they have four interpenetrating FCC lattices where the X atoms are located at the tetrahedral sites with coordinates $\left(\frac{1}{4},\frac{1}{4},\frac{1}{4}\right)$ and $\left(\frac{3}{4},\frac{3}{4},\frac{3}{4}\right)$, the Y atoms are placed at the octahedral sites with coordinates $\left(\frac{1}{2},\frac{1}{2},\frac{1}{2}\right)$, and the Z atoms are positioned at the top $(0,0,0)$ and in the centers of the faces [60]. The sequence of the full Heusler alloy is X-Y-X-Z where X possess large valence than Y [61]. Figure.I.11 shows a face-centered cubic lattice of the full-Heusler alloy Cu_2MnAl. Full Heusler alloys are typically ferromagnetic metals and have gained attention as half-metallic materials, these materials have emerged as promising candidates for spin injection in spintronic

devices [62]. The first half-metallic Full Heusler is Co_2MnSn [63,64].

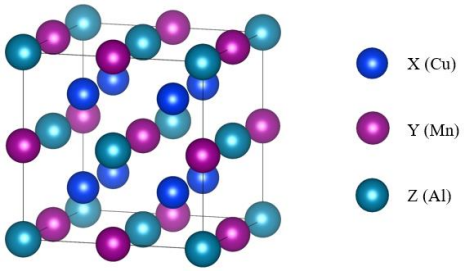

Figure.I.11: The face-centered cubic lattice of the full-Heusler Cu_2MnAl alloy [65].

Heusler alloys exhibit many crystallographic phases depending on the arrangement of atoms inside the crystal lattice These phases can be categorized as follows [66].

- The $L2_1$ phase, type of the Cu_2MnAl prototype which was explained previously, where all the atoms are perfectly ordered.
- The B2 phase, type of CsCl exhibits random occupation of the Y and Z atom positions.
- The C1 phase, type of CaF2 where the X and Z atom positions are randomly occupied by these two atoms.
- The B32a phase, type of NaTl where the X atoms which occupy the FCC lattice are

mixed with the Y atoms, while the X atoms on the tetrahedral sites are mixed with Z atoms.

- The DO3 phase type of BF_3, the X and Y atoms or the X and Z atoms are randomly distributed.
- The A2 phase type of W (tungsten) is characterized by the random occupation of all atomic positions by three different types of atoms.

The previously mentioned phases are illustrated in the subsequent figure.

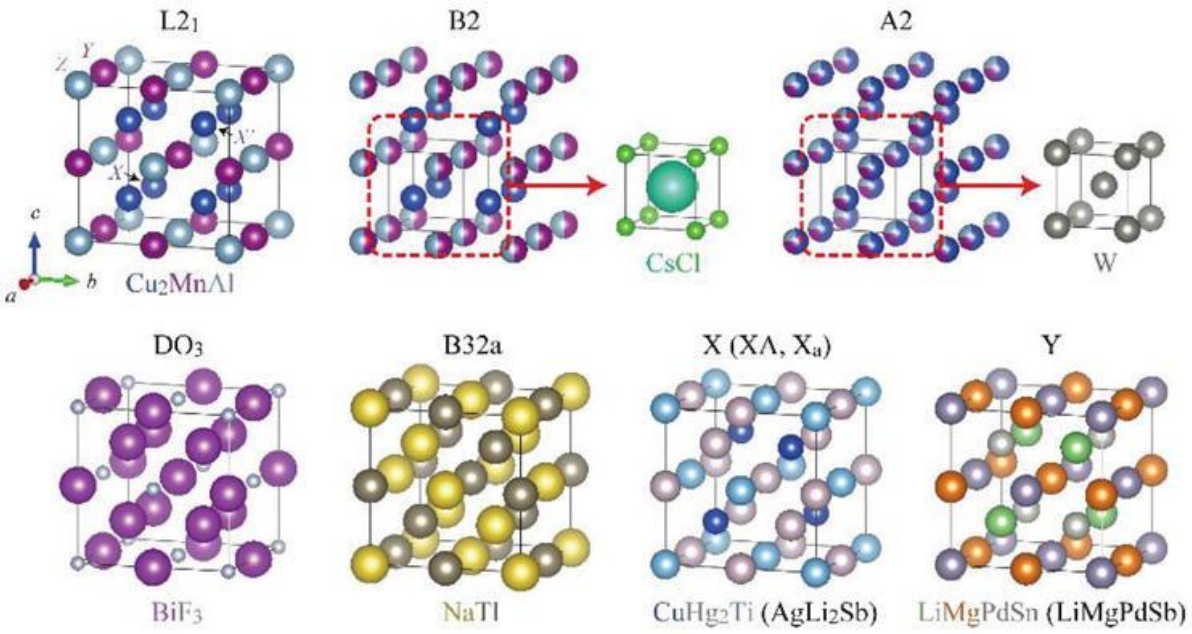

Figure.I.12: Crystal structures of full Heusler alloys. A structural symbol is put above each crystal structure, while a prototype structure is presented below [66].

I.8. 2. Half Heusler

Half Heusler alloys are intermetallic compounds that have the general formula XYZ which crystallize in a non-centrosymmetric cubic structure $C1_b$ (MgAgAs structure type, space group 216, $F\bar{4}3m$) with stoichiometry 1:1:1. X and Y in Heusler alloys are transition metals or rare earth elements, while Z is a main group element. exhibits a higher electronegativity such as Ge, Sn and Pb. The X atoms occupy the 4b Wyckoff position at coordinates $\left(1/2, 1/2, 1/2\right)$, the Y atoms occupy the 4a Wyckoff position at coordinates $\left(1/4, 1/4, 1/4\right)$, and the Z atoms occupy the origin 4a Wyckoff position at coordinates $\left(0,0,0\right)$.Meanwhile, the 4d Wyckoff position at coordinates $\left(3/4, 3/4, 3/4\right)$remains unoccupied [67].half Heusler alloy can be classified as a hybrid compound consisting of XZ with a rocksalt crystal structure, as well as XY and YZ with a zinc-blende crystal structure.

The characteristics of these half Heusler alloys are significantly influenced by the valence electron concentration (VEC) or the number of valence electrons (Nv) in the primitive cell. That identifies the band structure and subsequently affect the physical properties of the compounds [68,69].

For instance, alloys with N_V=21,22 have been proposed as materials that exhibit half-metallic ferromagnetic properties such as NiMnSb [70], a superconducting behavior is induced when N_V=27. Specifically, compounds with Nv = 18 display characteristics of a closed shell structure, making them either semimetals or semiconductors [68]. According to empirical investigations and band structure computations, a considerable number of 18 VEC-Heusler systems, which are composed of light transition metals such as CoTiSb or NiTiSn, demonstrate semiconducting properties exhibiting narrow band gaps in the density of states (DOS) at the Fermi energy (EF) [68]. This class of alloys has been shown to have good thermoelectric properties [71]. Prior research on the electronic structure [72] of Heusler compounds with narrow band gaps has demonstrated that the gap states observed near E_F have a significant impact on the transport properties of these alloys.

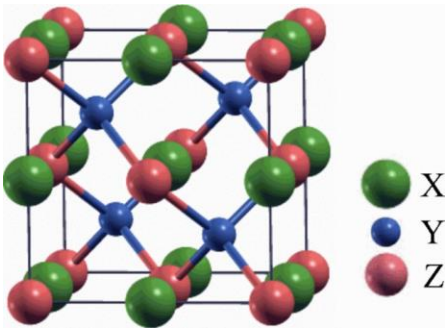

Figure.I.13: Crystal structure of half-Heusler compound XYZ [73].

Three distinct atomic arrangement are seen in this particular structure, as illustrated in the table below:

Table.I.2: Different occupations of non-equivalent sites of the $C1_b$ type.

Arrangement	**4a**	**4b**	**4c**
Type I	X	Y	Z

Type II	Z	X	Y
Type III	Y	Z	X

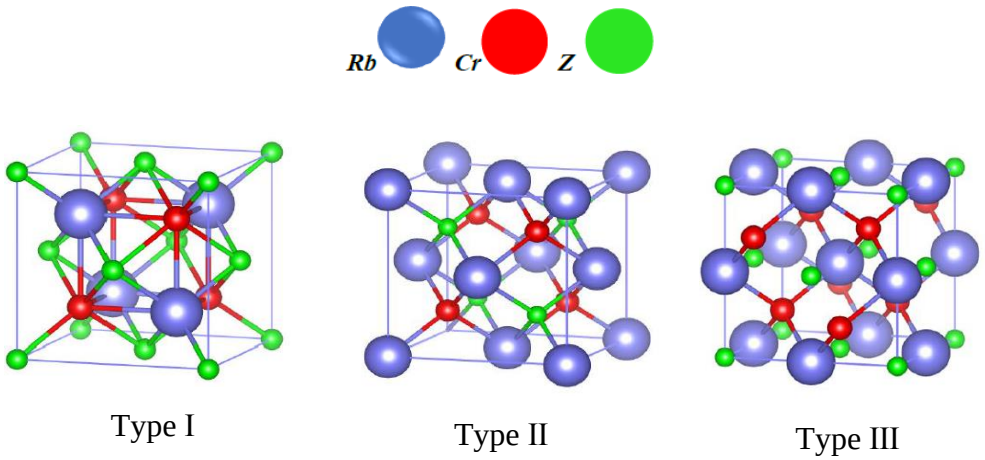

Figure.I.14: Crystal structure of the three arrangements of RbCrZ (Z=S, Se, Te) half Heusler alloys [74].

I.8. 2. 1. Half Heusler and Zintel model

Half Heusler alloys can be defined as compounds comprising of two components, namely a covalent component and an ionic component. Atoms X and Y exhibit unique cationic properties, whereas atom Z might be regarded as the anionic counterpart. The crystal structure of half-Heusler (HH) alloys XYZ can be derived by combining a rocksalt-type and a zincblende-type lattice (see Figure.I.15). As previously stated, HH crystal structures are composed of three interpenetrating FCC lattices. The atoms of the NaCl (Rock salt) structure are located in the octahedral sites, while the covalent dominating ZnS structure (Zinc blende) occupies the remaining tetrahedral holes. The sublattice of the rock salt type is composed of the elements with the lowest and highest electro positivity (X and Z). This sublattice exhibits the strongest ionic interaction.

On the other hand, the sublattice of the zinc blende type consists of the elements Y and Z, which have the lowest difference in electronegativity.

To simplify and understand these complicated materials, The Zintl-Anion Framework, based on the Zintl model, is applied to the ZnS lattice (YZ) of the HH structure, known as the YZ framework. This approach was first proposed by Köhler and colleagues [75].

Zintl compounds are solids made of electropositive cations that submit their valence electrons to form an anionic framework and closed valence shell by charge transfer and covalent bonding [76]. According to the Zintl-Klemm idea, HH compounds can be represented as an ionic interaction of $X^{n+}(YZ)^{n-}$, which refers to the valence electron interaction between the most electropositive element X and the YZ framework. Element X transfers all of its valence electrons to the more electronegative elements Y and Z.

Consequently, each of the elements achieved a closed-shell form, resulting in an 18-electron configuration for XYZ, where Y is a d^{10} transition metal. For example, the compound TiCoSb, Titanium (Ti) donates its valence electrons to cobalt (Co) and antimony (Sb), resulting Ti^{4+} (d^0) and Co (d^{10}) and Sb (s^2p^6) closed shell ions. So, HH compounds are stable due to their closed-shell 18-electron structure. The valence balanced rule, which extends the concept of the 18-electron rule for half-Heusler stipulates those compounds with a net valence (NV) of zero for all three components are stable [77].

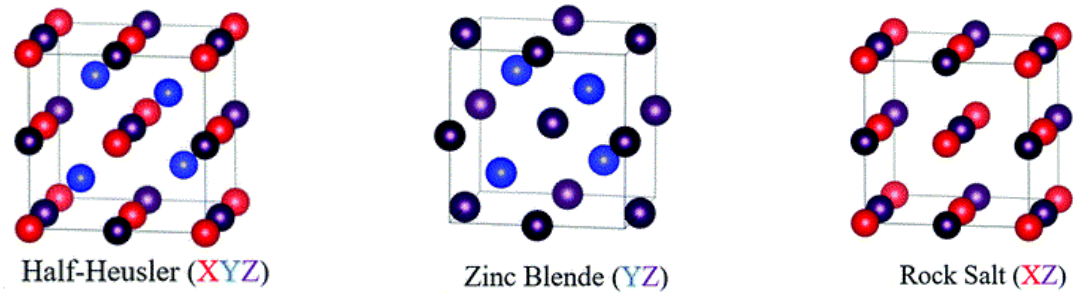

Figure.I.15: Crystal structure of half-Heusler (HH) alloys XYZ can be derived by combining a rock salt-type and a zincblende-type lattice [78].

I.8. 3. Inverse Heusler

Heusler alloys are classified into several subfamilies, one of the most notable of which is the inverse Heusler which is the new form of full Heusler alloys. In which element Y possesses a greater atomic number than element X (Z(Y)>Z(X)). X and Y represent transition metal atoms, while Z refers to a main block or P block element having sp valence electrons [79]. Atoms in full

Heusler alloys are arranged in the sequence X-Y-X-Z, whereas in inverse Heusler alloys, the order is X-X-Y-Z, this implies that the positions of Y and X are swapped., these alloys crystalize in X type structure with prototype $CuHg_2Ti$ and $AgLi_2Sb$. and exhibit a face-centered cubic lattice structure, but their space group $F\bar{4}3m$ (216) is distinct from that of full-Heusler compounds. Inverse Heusler alloys are a type of Heusler alloys that show potential for use in low magnetic moment systems. They are specifically employed in spintronics applications [80]. The Figure.I.16 displays the Inverse-Heusler structure of Ti_2MnAl.

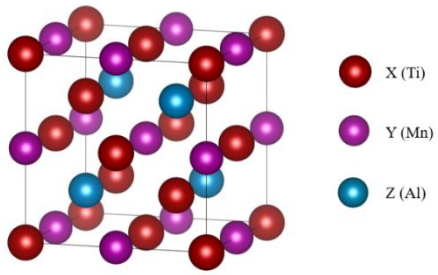

Figure.I.16: Face-centered cubic lattice of inverse-Heusler Ti_2MnAl [65].

I.8. 4. Quaternary Heusler

An additional sort of Heusler alloys is known as quaternary Heusler alloys, consisting of four atoms with different chemical properties. The general formula for these compounds is XX'YZ, where X and X' occupy positions 4a and 4d, respectively. Element Y is located at position 4b, while element Z is positioned at 4c. This alloy has the LiMgPdSn prototype, which is commonly referred to as the Y phase and belongs to space group $F\bar{4}3m$ (216). In which, x and z represent transition metals, while Z represents a main block or P block element with sp valence electrons [81]. Typically, the structure remains stable when the number of valence electrons in atom X is greater than that of atoms X' and Y. while the number of electrons in the valence of the Y atom is less than that of the X' atom [82]. quaternary Heusler alloys exhibit similar characteristics to half Heusler, therefore, they can be crystallized into one of three distinct crystal forms.

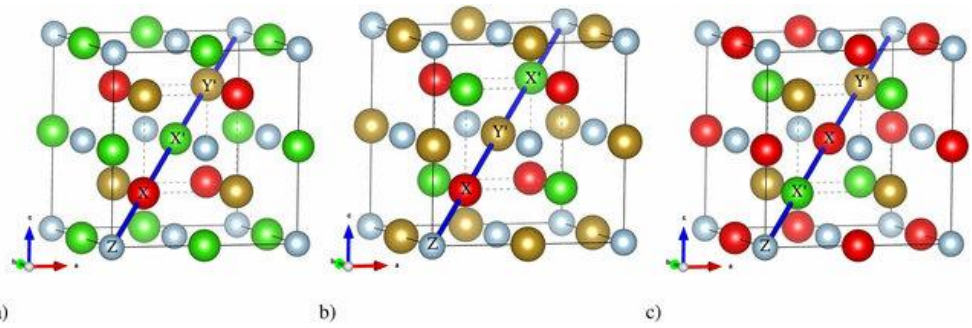

Figure.I.17: Crystal structures of quaternary Heusler alloys XX'YZ in the three possible arrangements [83].

Table.I.3: Comparison of various categories of Heusler alloys [84].

Structures	***General Formula***	***Type***	***Space Group***	***Ratio***	***Sublattices***	***Example***
Full Heusler	X_2YZ	$L2_1$	Fm3m	2:1:1	Four	Co_2MnAl
Half Heusler	XYZ	$C1_b$	$F\bar{4}3m$	1:1:1	Three	NiMnSb
Inverse Heusler	XY_2Z	X	Fm3m	2:1:1	Four	$CrCo_2Ga$
Quaternary Heusler	XX'YZ	Y	$F\bar{4}3m$	1:1:1:1	Four	YFeCrSb

I.8. 5. Double half Heusler (DHH)

A novel category of Heusler alloys was explored firstly by Anand et al, known as quaternary double half Heusler (DHH) alloys with the generic formula X'X"Y_2Z_2, X_2Y'Y"Z_2, and X_2Y_2Z'Z" [85]. These alloys are a type of intermetallic compounds which is named after the Heusler alloys and are considered as stable quaternary alloys (see Figure.I.17 a), which based on aliovalent substitution of two different atoms (X' and X"), (Y' and Y") or (Z' and Z") between two ternary half Heusler alloys (X'YZ and X"YZ), (XY'Z and XY"Z) or (XYZ 'and XYZ") in other words, X_2Y'Y"Z_2 vs XYZ, where Y' and Y" are aliovalent. Furthermore, aliovalent substitution can result in a distinct composition that maintains valence balance. For instance, in $Ti_2FeNiSb_2$, the atoms

Fe and Ni substitute on the atomic Y-site (see Figure.I.18 b), which is a distinguishing feature of the combination, generating an 18-electron ternary half Heusler [86]. The DHH alloys are inspired by double perovskites, where the term "double" refers to the doubling of the perovskite formula unit from ABO_3 to A_2BBO_6. As stated previously Anand et al. conducted extensive research on these materials when they investigated the thermodynamic stability of 315 DHH compositions using convex-hull analysis within OQMD i.e., the Open Quantum Materials Database. It was determined that the DHH, in general, would have lower lattice conductivity than ternary half Heusler due to their larger number of atoms in the primitive unit cell and complexity of crystal structure [85].

DHH possess several distinctive characteristics such as high thermoelectric efficiency, a half-metallic nature, and magnetic properties and exceptional mechanical properties. Their potential applications in thermoelectric devices, spintronic devices, magnetic devices, and other fields are presently under investigation.

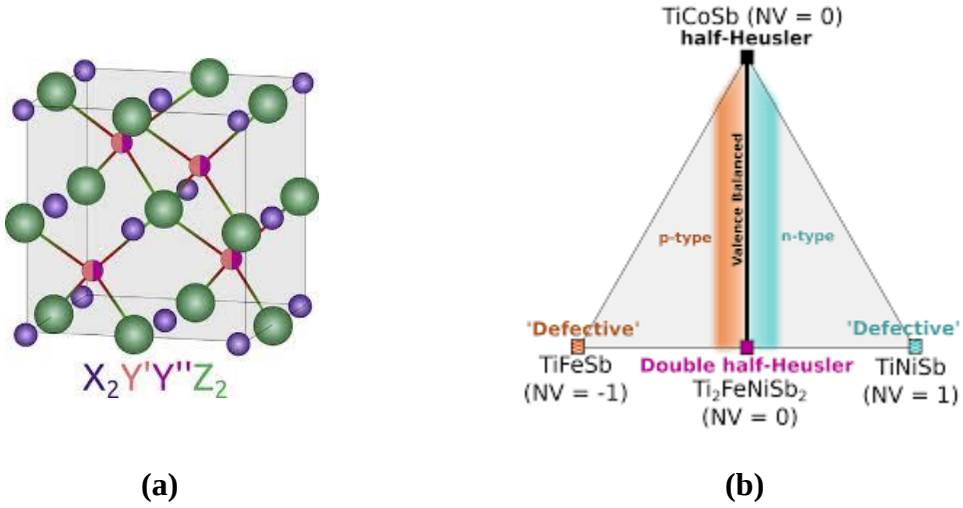

(a) **(b)**

Figure.I.18: (a) The double half Heusler structure with the general formula $X_2Y'Y''Z_2$, (b) pseudoternary diagram $TiFe_xCo_yNi_{1-x}Sb$ based on aliovalent substitution on the atomic Y-site [85].

I.9. Heusler alloys and magnetism

The scientific world became interested in Heusler compounds in 1903 when F. Heusler discovered that the compound Cu_2MnAl exhibits ferromagnetic properties, despite none of its individual constituents being ferromagnetic [87,88].

The half Heusler alloys possess a single magnetic sublattice due to the fact that only the atoms located on the octahedral sites are capable of carrying a magnetic moment. Magnetic half-Heusler alloys are mostly obtained by experiment and are limited to X=Mn and rare earth metals. However, experimental findings have revealed a small magnetic moment for nickel, in addition to the late transition metals. However, most Heusler alloys composed of rare earth elements, as found in existing literature, exhibit either semiconducting or semi-metallic structures, or are anti-ferromagnetic with a lower Neel temperature range [89].

In the full Heusler alloys, the presence of two X atoms in the tetrahedral sites leads to a distinct situation. This arrangement enables a magnetic interaction between the X atoms and the creation of a second magnetic sublattice that is more spread out. These alloys exhibit various magnetic phenomena due to the presence of two distinct magnetic sublattices. Currently, these compounds are known to demonstrate ferromagnetism, ferrimagnetism, and half-metallic ferromagnetism.

I.10. Half metallicity

Half-metallic magnets have been a focus of interest for spintronics and magnetoelectronic applications for the last twenty years [90]. There are various materials that are considered to be half metallic, including binary magnetic oxides such as CrO_2 and Fe_3O_4, diluted magnetic semiconductors like $Ga_{1-x}Mn_xAs$, zinc-blende compounds including MnAs and CrAs, and colossal magnetoresistance materials like Sr_2FeMoO_6 and $La_{0.7}Sr_{0.3}MnO_3$. In addition to these materials, Heusler alloys (NiMnSb) have garnered significant attention due to their half-metallic nature, which initially proposed by de Groot et al based-on band structure studies [91]. Ishida et al. have suggested that the full-Heusler alloys, specifically Co_2MnZ (where Z represents either Si or Ge), are likewise considered to be half-metals.

The density of states of a half-metallic magnet is schematically shown in Figure.I.19. The majority-spin (spin up) exhibits metallic behavior, while the minority-spin (spin down) exhibits

non-metallic behavior (semiconductor with energy band gap). This results 100% spin polarization P of the conduction spin channel expressed by the subsequent expression.

$$P_F = \frac{N_\uparrow(E_F) - N_\downarrow(E_F)}{N_\uparrow(E_F) + N_\downarrow(E_F)} \quad \text{(I-16)}$$

This feature enhances the efficacy of magnetoelectronic devices.

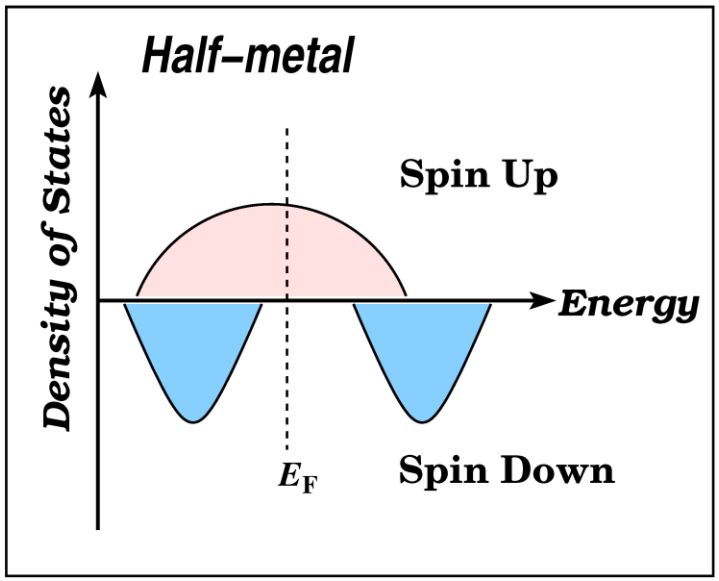

Figure.I.19: (a) Half metallic Ferromagnet with high band gap and same-direction spins. (b) Normal Ferromagnet with spins in opposite directions and no band gap [92].

I.11. Slater Pauling behavior

Half-metallic Heusler alloys display metallic properties for the spin-up electronic band structure and semiconducting properties for the spin-down electronic band structure. This characteristic makes them suitable for various spintronic applications. The growth of this study field has been significantly influenced by the use of Slater-Pauling principles. These rules have been established by ab initio electronic structure calculations, which provide a direct connection between the electronic properties (specifically, the presence of a spin-down energy gap) and the magnetic properties (namely, the total spin magnetic moment).

The magnetic moment, expressed in terms of multiples of the Bohr magnetons (μ_B), is determined by:

$$M_t = Z_t - 2n_\downarrow \tag{I-19}$$

The term $2n_\downarrow$ represents the total number of electrons in the minority states. By disregarding the s and p electrons, it is possible to compute the magnetic moment in a specific region of the Slater-Pauling curve using the following formula:

$$M_t = N_V - 6 \tag{I-20}$$

This implies that the magnetic moment per atom is equal to the mean number of valence electrons minus six. At the Fermi level, half-metallic ferromagnets have a band gap in the minority density of states. The band gap necessitates an integer number of occupied minority states, which the case $M_t = N_V - 6$ meets [93,94]. In cases where the average valence electron concentration is not integer, it is more convenient to utilize the valence electron number per formula unit N_V.

The Slater Pauling rule for Half-Heusler alloys (XYZ) with three atoms per formula unit is expressed as:

$$M_t = Z_t - 18 \tag{I-21}$$

The full Heusler alloys (X_2YZ) consists of four atoms per unit cell, resulting in the formula.

$$M_t = Z_t - 24 \tag{I-22}$$

The symbol M_t represents the total magnetic moment of spin, while Z_t represents the total number of valence electrons. The value of Z_t is determined by adding the number of electrons with spin-up and spin-down, while M_t is determined by subtracting them.

$$Z_t = N_\uparrow + N_\downarrow \tag{I-17}$$

$$M_t = N_\uparrow - N_\downarrow \tag{I-18}$$

Figure.I.20 displays the total spin magnetic moments obtained from ab initio calculations. These moments are shown against the total number of valence electrons for a few chosen semi-Heusler compounds investigated in Reference [95]. The total spin magnetic moments of the majority of the compounds tested align precisely with the line indicating the SP rule. CoTiSb is a widely recognized semiconductor with precisely 18 valence electrons. The compounds depicted by the red spheres and highlighted with a yellow backdrop exhibit characteristic of half-metals. Compounds such as RhMhSb and NiMnSe exhibit modest deviations from ideal SP behavior due to the presence of a spin-down energy gap.

However, the Fermi level intersects either the valence or conduction spin-down band. CoFeSb, which possesses 22 valence electrons, is a half-metallic compound that exhibits the highest achievable total spin magnetic moment. Adding an extra valence electron to Z_t does not make the half-metallic state more energetically advantageous, as five electrons would need to be accommodated in the antibonding spin-up bands.

A special case of half Heusler alloys which contain alkali metals. In a recent study, Xiaotian Wang afterward Thuy Hoang and colleagues conducted a detailed analysis of compounds with the chemical formula XCrZ (X = Li, K, Rb, Cs; Z= S, Se, Te) [96] and ACrZ, where A represents an alkali metal (Li, Na, or K) and Z represents P, As, or Sb [97]. It was demonstrated that they also exhibit half-metallic properties, follow the modified S-P rule recently presented by Damewood et al.

$$M_t = \left(Z_t - 8\right)\mu_B \tag{I-18}$$

Subsequently, analogous formulas have been established for various other groups of Heusler compounds, including the inverse Heuslers [98] and the ordered quaternary Heuslers [99,100]. For inverse Heusler, there are three main variations of the SP rule, each dependent on the type of hybridization. For X elements such as Sc or Ti, the total spin magnetic moment per formula unit (or unit cell) in μ_B can be determined using the SP rule $M_t = Z_t - 18$. The equation $M_t = Z_t - 24$ is true whether X represents either Cr or Mn in the SP form. The specific shape of the SP was determined to be dependent on the material for the case where X is equal to V. There

are a total of 14 spin-down bands that are occupied in these compounds. These alloys, which exhibit half-metallic behavior, adhere to the $M_t = Z_t - 28$ SP criterion.

In similar manner, for quaternary half Heusler it was found that the majority of these compounds likewise exhibited half-metallic properties, adhering to the Slater-Pauling rule for full-Heusler compounds, where $M_t = Z_t - 24$ However, there were a few exceptions that followed the variant $M_t = Z_t - 18$.

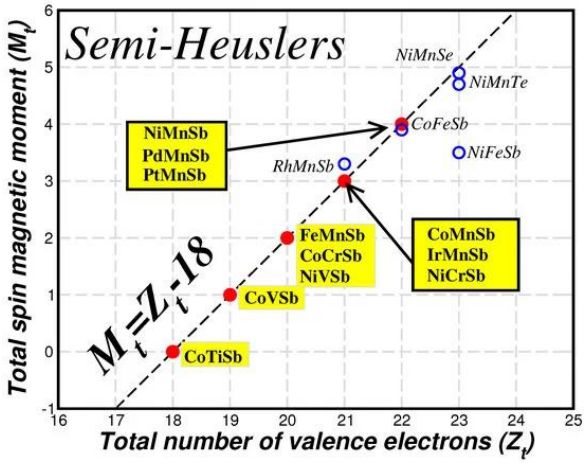

(a)

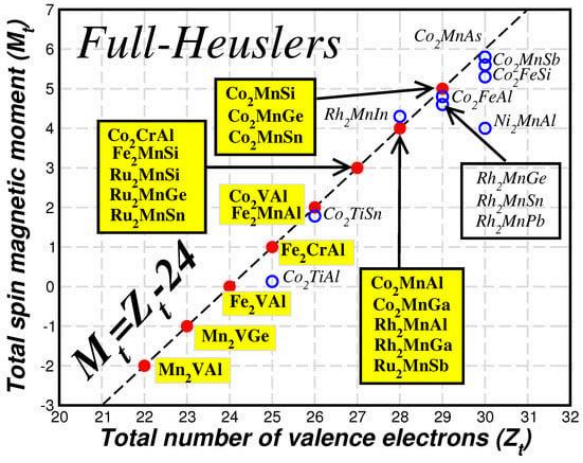

(b)

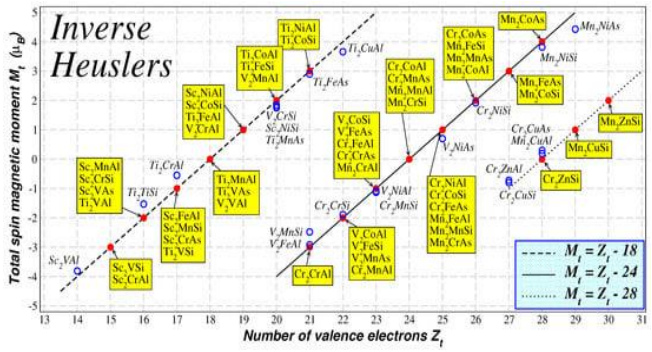

(c)

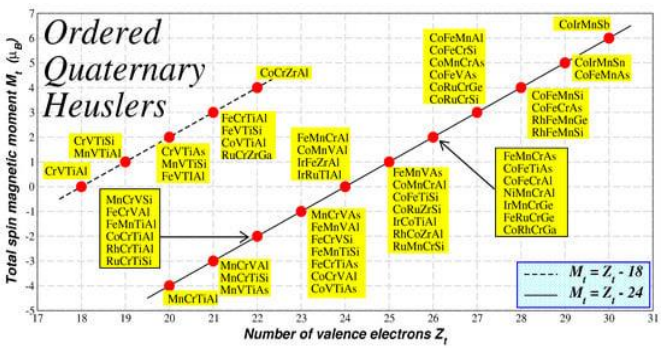

(d)

Figure.I.20: The total spin magnetic moments (M_t) in μ_B as a function of the number of valence electrons (Z_t) in the unit cell for selected Heusler. (a) alloys half Heusler alloys, (b) full Heusler alloys, (c) inverse Heusler alloys and (d) quaternary Heusler alloys [92].

I.12. Spin-Gapless Semiconducting Behavior in Heusler Alloys

Spin-gapless semiconductors (SGSs), initially introduced by Wang in 2008 [101]. This class has garnered significant research attention during the past decade due to its potential applications in spintronics. As illustrated in Figure.I.21 in type-I SGSs, the minority-spin bands exhibit similar behavior to that of HMMs, but the majority-spin bands exhibit distinct behavior. The conduction and valence band edges are in contact at the Fermi level, creating a zero-width gap. On the other hand, type-II SGSs possess a distinct electronic band structure. The materials exhibit an energy band gap below and above the Fermi level for various spin-channels.

Additionally, the valence- and conduction-band borders of different spin-channels come into contact at the Fermi level. Ab-initio calculations indicate that multiple Heusler compounds show either type-I or type-II spin gapless semiconductor (SGS) characteristics. Mn_2CoAl was the first Heusler alloy investigated for type-I SGS characteristics [102]. Furthermore, this Heusler compound exhibits elevated electron and hole mobility, together with a Curie temperature of 720 K [102], rendering it well-suited for spintronic applications at room temperature.

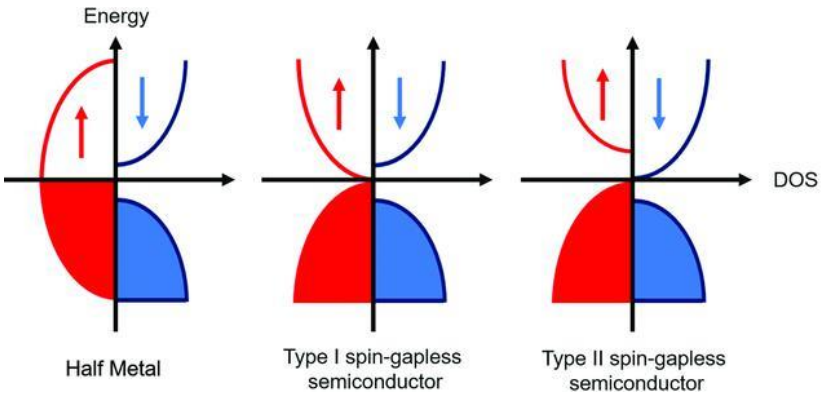

Figure.I.21: Density of states diagrams for a half metal and the two types of spin-gapless semiconductor f in the MCoVZ Heuslers [103].

I.13. Application of Heusler alloys

In the literature, a huge variety of Heusler alloys were described to investigate their potential applications. Figure.I.22 provides a comprehensive overview of the key characteristics of these extraordinary materials, which include semiconductors, metals, magnets, and topological insulators. These materials have various technological applications in fields such as spintronics, thermoelectric, opto-electronics and a lot more.

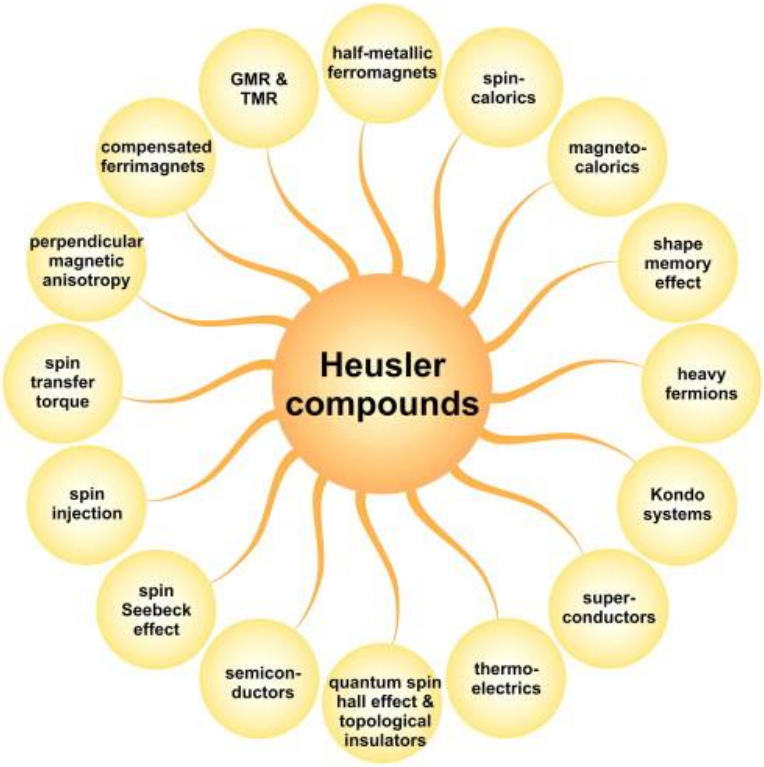

Figure.I.22: Overview on the different aspects of Heusler alloys [104].

The bar diagram of experimental and DFT investigations into different varieties of Heusler alloys is depicted in Figure.I.23. It can be seen from this diagram that experimental and theoretical investigations devote more attention to quaternary, inverse, and half Heusler alloys, while full Heusler alloys are given little attention. Hence, Full Heusler alloys possess significant potential

for utilization in ferromagnetic shape memory alloys. However, additional Heusler alloys have garnered significant experimental and theoretical interest due to their potential uses in spintronics, solar cells, and thermoelectric generators. This is mostly due to the fact that they exhibit half-metallic behavior, which makes them a potential material for spintronic devices.

Heusler alloys have been extensively researched due to their prospective applications in Spintronics, Magnetocaloric effect, and Magnetic shape memory alloys [105]. spintronics also known as spin electronics, which is based on electron charges and spins. Modern information technology necessitates enhanced data processing speeds and larger storage capacities. In spintronics-based magnetic semiconductors, ferromagnetism is the dominant behavior, surpassing other magnetic behaviors such as iron ability to form a permanent magnet [106]. Heusler alloys involve superconducting compounds in addition to metallic and semiconducting materials. The initial superconducting Heusler materials, Pd_2ReSn and Pd_2RePb, were documented by Ishikawa et al [104].

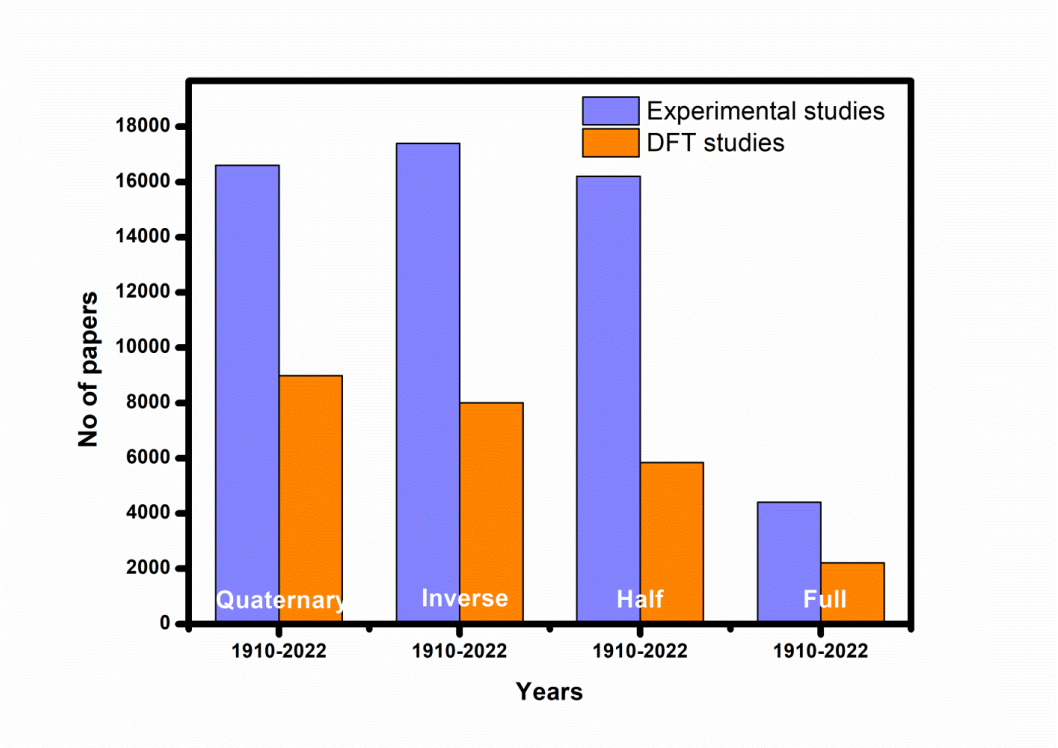

Figure.I.23: Experimental and DFT studies of Heusler alloys were published between 1910 and 2022 [84].

The primary benefit of Spintronic devices is in their utilization of electron spin rather than charge. Spintronics offers advantages such as lower power consumption, faster operation, higher storage density, lower cost, immunity to data loss during power outages, and the ability to store data in a single chip. Everyday life involves interaction with spintronics, which includes devices such as Giant magneto resistance (GMR) that was discovered in 1986 by P. Grünberg [107], magnetic tunnel junction (MTJ), and magnetic spin valve (MSV) [108]. Presently, MTJ and GMR are viable options for digital information storage, including hard disk devices and magnetic random-access memory [109]. In addition to spintronics, Heusler alloys can be utilized in the field of thermoelectric due to their easy production and non-toxic elements [110].

Recently, a novel category of states known as topological states has arisen. Topological Insulators are materials that have been the subject of recent experimental investigation following their theoretical prediction [111]. A direct band gap is required at the midpoint of the Brillouin zone Γ point for these materials. They are semiconductors characterized by a large spin-orbit coupling and a tunable band gap in bulk and well structures [112]. Many half-Heusler compounds are thought to be topological insulators based on band-structure estimates such as ScPtBi.

Furthermore, Heusler alloys have been used in other fields such as solar cells and thin films. Shape memory alloys are a distinct category of alloys that have the ability to maintain their initial shape even after being deformed or twisted, and can return to their original shape when exposed to a specified temperature. The Ni_2MnGa system is currently a highly studied material due to its shape memory properties and its potential use in actuator devices.

Heusler compounds exhibit fascinating characteristics and applications, including exceptional super elasticity and catalytic properties. One of the research directions in the future will be the study of maximum entropy alloys of Heusler.

The current trend in materials design is moving towards the utilization of machine learning techniques. We anticipate that our research will provide valuable insights for future experimental and theoretical investigations on Heusler alloys.

Chapter II

Calculation Methods

« It, therefore, becomes desirable that approximate practical methods of applying quantum mechanics should be developed which can lead to an explanation of the main features of complex atomic systems without too much computation »

Paul Dirac

Density Functional Theory (DFT)

Full Potential Augmented Plane Wave method (FP-LAPW)

and

Boltzmann Transport Theory

Paul Dirac: (1902-1984) was an English theorical physicist who is regarded as one of the most significant physicists of the 20th century.

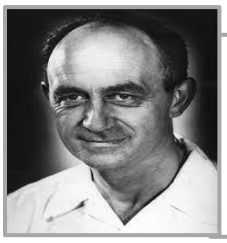

Enrico Fermi: (1901-1954) is a physicist and the creator of the world's first reactor, he works with Thomson on Thomas-Fermi model such is Viewed as a precursor to modern functional theory.

Erwin Schrödinger: (1887-1961) physicist who developed number of fundamental results in quantum theory, he was the author of many works on various aspects of physics.

Lu Jeu Sham: (1938) is a Chinese physicist. He is best known for his work with Walter Kohn on Kohn-Sham equations.

John Clarke Slater: (1900-1976) was a physicist who made major contributions to the theory of the electronic structure of atoms molecules and solids.

Vladimir Fock: (1898-1974) was a physicist. Who did foundational work on quantum mechanics and quantum electrodynamics and developed the Hartree-Fock method in 1930.

Walter Kohn: (1923-2016) was a theorical physicist and theorical chemist who played the leading role in the development of density functional theory.

Douglas Hartree: (1897- 1958) was an English mathematician and physicist most famous for the development of numerical analysis and its application to the Hartree–Fock equations of atomic physics.

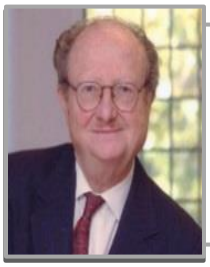

Pierre Hohenberg: (1934-2017) a theorical physicist who worked primarily on mechanic. He formulated in 1964 with Walter Kohn the Hohenberg-Kohn theorem in the course of his work on density functional theory.

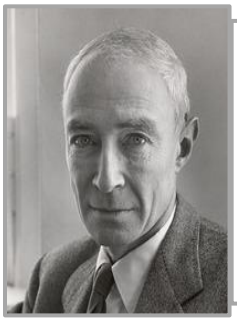

***J Robert Oppenheimer*: (**1904-1967) was a theorical physicist. Oppenheimer's achievements in physics included the Born-Oppen approximation for molecular wave function and works on the theory of electrons and positrons.

1

Density Functional Theory

II.1. Introduction

In various disciplines of the physical sciences and engineering, the progress of science and technology relies on comprehending and manipulating the characteristics of matter at the atomic and molecular scale. Density functional theory is a highly effective method for solving the Schrödinger equation, which describes the quantum behavior of atoms and molecules. Previously practiced by a few physicists and chemists at the forefront of quantum mechanical theory, this approach is now widely used by researchers in various fields such as chemistry, physics, materials science, chemical engineering, and geology [113].

Condensed matter physics and materials science focus on this topic, which is how electrons and nuclei interact and what effects this has on their properties. The vast number of highly interacting electrons and nuclei in the studied material makes a direct solution of the Schrodinger equation extremely challenging. Indeed, the purported many-body system is exceedingly complex to solve with complete accuracy. Hence, it is widely acknowledged that advancements rely on creating an approximate and manageable solution to the complex many-body issue.

This chapter is structured into three distinct sections. The first part focuses on introducing the fundamentals of density functional theory (DFT), which involves the solution of many-body Schrödinger equations. The second part includes the full potential linearized augmented plane wave approach which is a specific method within the broader framework of DFT. the Boltzmann transport theory is discussed in the final section.

II.2. Schrödinger equation

Solids consists of electrons, which are lighter and negatively charged particle, as well as massive nuclei, which are positively charged. When N nuclei are present, the issue of N+ZN electromagnetically interacting particles arises. Time independent Schrödinger equation is given by [114]:

$$\hat{H}\Psi = E\Psi \tag{II-1}$$

In which, Ψ is the wave function of the crystal, E is the total energy of the system. $\hat{H}$ is the Hamiltonian operator which includes all kinetic energy terms and particles potential (electrons and nuclei). The Hamiltonian is defined as:

$$\hat{H}_{tot} = T_e + T_n + V_{e-e} + V_{e-n} + V_{n-n} \tag{II-2}$$

where the kinetic energy of electrons and nuclei is denoted by T_e, T_n, and V_{e-e}, V_{e-n} and V_{n-n} represent the potential energy of electron-electron Coulomb interaction, electron-nucleus Coulomb interaction and nucleus-nucleus Coulomb interactions. These terms can be represented as follows:

$$T_n = -\frac{\hbar^2}{2}\sum_i \frac{\nabla^2_{\vec{R}_i}}{M_i} \tag{II-3}$$

$$T_e = -\frac{\hbar^2}{2}\sum_i \frac{\nabla^2_{\vec{r}_i}}{m_e} \tag{II-4}$$

$$V_{n-e} = -\frac{1}{4\pi\varepsilon_0}\sum_{i,j}\frac{e^2 Z_i}{\left|\vec{r}_i - \vec{R}_j\right|} \tag{II-5}$$

$$V_{ee} = \frac{1}{8\pi\varepsilon_0}\sum_{i\neq j}\frac{e^2}{\left|\vec{r}_i - \vec{r}_j\right|} \tag{II-6}$$

$$V_{n-n} = \frac{1}{8\pi\varepsilon_0}\sum_{i\neq j}\frac{e^2 Z_i Z_j}{\left|\vec{R}_i - \vec{R}_j\right|} \tag{II-7}$$

Consider M_n represent the mass of the nucleus at $\vec{R}_i$, and m_e represent the mass of the electron situated at $\vec{r}_i$, e represents the charge of an electron, while Z represents the charge of the nucleus.

The Hamiltonian can be written as:

$$\hat{H} = -\frac{\hbar^2}{2}\sum_i \frac{\nabla^2_{\vec{R}_i}}{M_n} + -\frac{\hbar^2}{2}\sum_i \frac{\nabla^2_{\vec{r}_i}}{m_e} + \frac{1}{8\pi\varepsilon_0}\sum_{i\neq j}\frac{e^2}{\left|\vec{r}_i - \vec{r}_j\right|} + \frac{1}{8\pi\varepsilon_0}\sum_{i\neq j}\frac{e^2 Z_i Z_j}{\left|\vec{R}_i - \vec{R}_j\right|} + -\frac{1}{4\pi\varepsilon_0}\sum_{i,j}\frac{e^2 Z_i}{\left|\vec{r}_i - \vec{R}_j\right|} \qquad (\text{II}-8)$$

It is impossible to solve the Schrödinger equation due to complicating effects of the interactions between the particles (the vast number of electrons and nuclei, on the order of 10^{23}), we must employ some approximations in different levels.

II.3. Level 1: The Born-Oppenheimer approximation

The Born-Oppenheimer approximation [115], also known as the adiabatic approximation, is the initial assumption made in the theory of electronic structure. This approximation results in the decoupling of electronic and nuclear motions. Due to the significantly greater mass of nuclei over 2000 times that of individual electrons $\left(m_{nuclei} \rangle\rangle m_e\right)$.Consequently, the electrons start perceiving the external potential linked to stationary nuclei, leading to the expression of the wave function.

$$\Psi\left(\vec{r},\vec{R}\right) = \Psi_n\left(\vec{R}\right)\Psi_e\left(\vec{r},\vec{R}\right) \qquad \text{(II-9)}$$

Resulting in the so-called electronic Hamiltonian which consisting of T_e, $V_{e\text{-}e}$ and V_{ex} reflects the kinetic energy of electrons, the electron-electron interaction and potential of the nuclei acting on electrons.

$$\hat{H}_{tot} = T_e + V_{e-e} + V_{ex} \qquad \text{(II-10)}$$

The equation of Schrödinger can be given by:

$$\hat{H}_e \Psi_e = E_e \Psi_e \qquad \text{(II-11)}$$

$$\left[-\frac{\hbar^2}{2}\sum_i \frac{\nabla^2_{\vec{r}_i}}{m_e} + \frac{1}{8\pi\xi_0}\sum_{i\neq j}\frac{e^2}{\left|\vec{r}_i-\vec{r}_j\right|} - \underbrace{\frac{1}{4\pi\xi_0}\sum_{i,j}\frac{e^2 Z_i}{\left|\vec{r}_i-\vec{R}_j\right|}}_{V_{ex}} \right]\Psi_e = E\Psi_e \qquad \text{(II-12)}$$

The equation (II-10) is still hard to solve for a system involving many particles due to a large number of electrons. In order to address this issue, two approximation strategies are implemented. The Hartree-Fock method [116,117] comes first which based on the assumption of free electrons, followed by the density functional theory.

II.4. The Hartree approximation

One of the first and most simple approximations approach to solve the problem of many electrons (because of the interaction electron-electron) can be considered as that proposed by Douglas Hartree (1928) [118]. This approximation assumes for that the electrons have no effect on each other.so, if we suppose two electrons 1 and 2 the probability of finding the electron of coordinate r_1 in orbital 1 is independent of the electron of the coordinate r_2.

the Hamiltonian for the electrons can be expressed as:

$$H_e = \sum_i^N h_i \qquad \text{(II-13)}$$

The monoelectronic Hamiltonian is denoted by h_i.

The basic of this approximation is that the many-electron wave function can be written as a simple product of N monoelectronic wave functions which so called Hartree product (HP):

$$\Psi\left(\vec{r}_1,\vec{r}_2,....,\vec{r}_N\right) = \Psi_1\left(\vec{r}_1\right)\Psi_2\left(\vec{r}_2\right).....\Psi_N\left(\vec{r}_N\right) \qquad \text{(II-14)}$$

The equation of Schrödinger of one electron in Hartree approximation [119]:

$$\left(-\frac{\hbar^2}{2m}\nabla^2 + V_H\left(\vec{r}\right) + V_{ex}\left(\vec{r}\right)\right)\Psi_i\left(\vec{r}\right) = E\Psi_i\left(\vec{r}\right) \qquad \text{(II-15)}$$

While: $V_{eff} = V_H(\vec{r}) + V_{ext}(\vec{r})$

The term $V_{ext}(\vec{r})$ refers to the attraction force between the electron and the nucleus. $V_H(\vec{r})$ indicates the effect of the other electrons, where we assume that they create a negative charge distribution. In other words, the electron is influenced by the average electrostatic potential $V_H(\vec{r})$ generated by its neighboring electrons [120].

Single electron average potential it is given as follows:

$$V_H = \sum_{i \neq j} \int \frac{\left|\Psi_j\left(\vec{r}_j\right)\right|^2}{\left|\vec{r} - \vec{r}'\right|} d\vec{r}' \qquad \text{(II-16)}$$

$\Psi_j\left(\vec{r}_j\right)$ represents the wave function of a single electron.

This method is founded on the assumption of free electrons, neglecting the influence of electron interactions and spin states. An outstanding advantage of this technique is the proposal of a self-consistent solution to the electronic system issue. It carries significant implications:

- The overall Coulombic repulsion, denoted as V_{ee}, is overstated in the electronic system.
- Easy to resolve, however yields unsatisfactory outcomes.
- The Pauli exclusion principle is disregarded.

An appropriate wave function should exhibit antisymmetry upon the exchange of two electrons. The "Hartree-Fock" [116,117] approximation considers the spin while solving the Schrödinger equation.

II.4.1. Hartree-Fock approximation

The Hartree approximation considers electrons as distinguishable entities. However, electrons are half-integral intrinsic spin $1/2$ particles known as fermions. According to Pauli principle [120], two fermions cannot occupy the same quantum state due to the requirement of an antisymmetric multiple-fermion wave function. However, the Hartree wavefunction is anti-symmetric as it does not describe electron-electron interactions. If there is an exchange of two electrons, the wave function must undergo a change in sign. The Hartree-Fock method employed

a single Slater determinant [122] to express the total wavefunction of multi-particle systems in the following manner:

$$\psi\left(\vec{r}_1,\vec{r}_2,....,\vec{r}_N\right)=\frac{1}{\sqrt{N!}}\begin{bmatrix}\psi_1\left(\vec{r}_1\right) & \cdots & \psi_N\left(\vec{r}_1\right)\\ \vdots & \ddots & \vdots\\ \psi_1\left(\vec{r}_N\right) & \cdots & \psi_N\left(\vec{r}_N\right)\end{bmatrix} \tag{II-17}$$

$\frac{1}{\sqrt{N!}}$ is a normalization factor or orthonormal spin-orbitals.

In equation (II-17), the Pauli exclusion principle is maintained, meaning that when two electrons are swapped, the wavefunction sign is altered. Furthermore, when two electrons possess identical quantum states, the wavefunction is reduced to zero. It is evident that the Hartree-Fock wavefunction incorporates an exchange element that is not included in the Hartree solution. This additional term allows for the minimization of the ground state energy, resulting in the best feasible approximation to the accurate energy. In contrast to single-electron wave functions, this function can be computed by minimizing the total energy using the variational principle. Thus, we return to the Hartree equation generalized as the monoelectronic wave equation:

$$\left(-\frac{\hbar^2}{2m}\nabla^2+V_H\left(\vec{r}\right)+V_{ex}\left(\vec{r}\right)+V_X\left(\vec{r}\right)\right)\Psi_i\left(\vec{r}\right)=E\Psi_i\left(\vec{r}\right) \tag{II-18}$$

$V_X\left(\vec{r}\right)$ is a Fock term [123] that acts on a wave function $\Psi_i\left(\vec{r}\right)$.

$$V_X\left(\vec{r}\right)\psi_i\left(\vec{r}\right)=\sum\delta_{\sigma_i\sigma_j}\psi_j\left(\vec{r}\right)\int\frac{\psi^*{}_j\left(\vec{r}\right)\psi_i\left(\vec{r}\right)}{\left|\vec{r}-\vec{r}'\right|}d^3\vec{r}' \tag{II-19}$$

As already stated, the Fock exchange term arises due to the fermion nature of electrons and their adherence to the Pauli exclusion principle. This term is responsible for the energy separation between electrons. It displays as a spatial separation between electrons with the same spin, either $\downarrow-\downarrow$ or $\uparrow-\uparrow$. It represents an effective magnetic interaction that emerges from an initially electrostatic interaction. The primary limitation of the Hartree-Fock approach is its full disregard for electron correlations [123], excluding those related to exchange interactions. Consequently, the electrons behave as if their motions were independent of each other. The energy associated with

the absence of electronic correlation E_{corr} is considered as the discrepancy between the exact total energy E_{exact} of the electronic system and that of the Hartree-Fock E_{HF} .

$$E_{corr} = E_{exact} - E_{HF} \quad \text{(II-19)}$$

E_{corr} is a negative value, indicating that E_{HF} is consistently higher than the precise energy $E_{HF} \rangle E_{exact}$.

The Hartree-Fock approximation is a valuable tool in the study of atoms and molecules. Nevertheless, this method is computationally demanding and less precise when applied to materials with a substantial number of electrons. However, a more advanced and Effective approach is the density functional theory.

II.5. Level 2: Density Functional Theory

The density functional theory (DFT) originated from the research conducted by Thomas and Fermi in the 1920s [124, 125]. The suggested model included the innovative concept of substituting the intricate N-body wave-function and its corresponding Schrödinger equation with the simpler electron density and its associated computational method. The initial model was subsequently enhanced by a number of additional contributors including Dirac [126] and von Weizsacker, by incorporating an exchange energy functional that depends on the electron density,

Before 1964, DFT was just a model because it was built on ideas that had not been proven in an official way. However, in that particular year, Hohenberg and Kohn [127] presented evidence demonstrating that every measurable quantity may be expressed as a functional of the electronic density of the lowest energy state, thereby establishing this model as a theory. The following year, Kohn and Sham [128] introduced a scheme that enabled the execution of calculations utilizing DFT.

There are three formulae that can be used to sum up this scheme, by solving these three equations in a self-consistent manner, we may determine both the ground state density and the ground state energy of the electronic system under investigation. Even so, there is a crucial piece of knowledge that is lacking preventing DFT from becoming a completely precise theory. Within

the effective potential, there exists an undefined term known as the exchange and correlation potential. This term includes all interactions between electrons, in addition to the exchange interaction that arises from the Pauli exclusion principle. Two prominent types of functionals, known as local density approximation (LDA) and generalized gradient approximation (GGA). Kohn and Sham first suggested the local density approximation for this functional in 1965 [128].

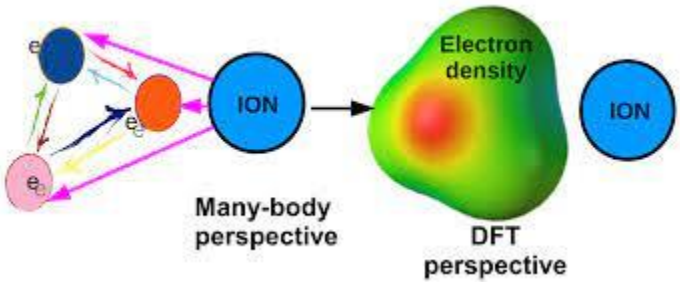

Figure.II.3: Example of the basic concept of a density functional theory is to characterize the interactions between electrons and ions as an electron ensemble represented by its density [129].

II.5.1. Thomas-Fermi -Dirac theory

The Thomas-Fermi (TF) model, first presented in 1927 by Thomas [125] and Fermi [130], was the forerunner to DFT. The electron density $\rho(\vec{r})$ was employed as the fundamental variable instead of the wavefunction in this approach. A system's total energy in an external potential $V_{ext}(\vec{r})$ is represented as an electron density functional $\rho(\vec{r})$ as:

$$E_{TF}\left[\rho(\vec{r})\right] = C_F \int \rho(\vec{r})^{\frac{5}{3}} d^3\vec{r} + \int \rho(\vec{r}) V_{ext}(\vec{r}) dr + \frac{1}{2}\iint \frac{\rho(\vec{r})\rho(\vec{r}')}{|\vec{r}-\vec{r}'|} dr dr' \qquad \text{(II-20)}$$

$$T_{TF}\left[\rho(\vec{r})\right] = C_F \int \rho(\vec{r})^{\frac{5}{3}} d^3\vec{r} \qquad \text{(II-21)}$$

The term $T_{TF}\left[\rho(r)\right]$ refers to the kinetic energy of electrons that do not interact with one other in a uniform electron gas (HEG). In which, in atomic unit.

$$C_F = \frac{3\left(3\pi^2\right)^{\frac{2}{3}}}{10} = 2871\ u.a \qquad \text{(II-22)}$$

The Thomas-Fermi-Dirac (TFD) model, an enhanced version of the original TF model, is derived based on the proposal of Dirac [126]. The distinction between these two models resides in the electron-electron interaction term. In the Thomas-Fermi (TF) model, this term simply accounts for the classical electrostatic repulsion between the electrons. However, in the Thomas-Fermi-Dirac (TFD) model, it includes both the electronic repulsion energy and the exchange energy of the uniform electron gas. Therefore, the Thomas-Fermi model has important implications since it served as the foundation for a more precise theory (DFT) and provided valuable insights into constructing a density functional.

II.5.2. The Hohenberg-Kohn theorems

As previously stated, the fundamental concept underlying all density functional theories is that each property of a system of particles that interact with each other can be mathematically described as a functional of the density of the system's lowest energy state. Here we provide the two theorems first out by Hohenberg and Kohn [127] in 1964.

First theorem the initial theorem proposed by Hohenberg and Kohn indicates that the electron density provides a unique determination of the Hamiltonian operator, and hence, all the properties of the system.

«This theorem says that the external potential $V_{ext}(r)$ *is a unique functional of the ground state density* $\rho(r)$ *within a constant. Since* $V_{ext}(r)$ *fixes* $\hat{H}$ *, the full many particles ground state is also a unique functional. No two* $V_{ext}(r)$ *may have the same ground state* $\rho(r)$*. Thus,* $\rho(r)$ *determines N,* $V_{ext}(r)$*, and all ground state parameters». We can define total energy as:*

$$E\left[\rho(\vec{r})\right] = F_{HK}\left[\rho(\vec{r})\right] + \int \rho(\vec{r})\, V_{ext}(\vec{r})\, d^3\vec{r} \qquad \text{(II-23)}$$

$$F_{HK} = T_e\left[\rho(\vec{r})\right] + V_{e-e}\left[\rho(\vec{r})\right] \qquad \text{(II-24)}$$

$F_{HK}\left[\rho(\vec{r})\right]$ represents Hohenberg and Kohen's universal functional, $V_{ext}(\vec{r})$ is the external potential that is affecting these particles and V_{e-e} refers to the electron-electron interaction.

The first Hohenberg-Kohn theorem states that the ground-state density contains all the necessary information to determine all relevant physical properties, including every observable quantity. However, we are now faced with the inquiry: How can we ascertain the ground state density of a certain electronic system? The second Hohenberg-Kohn theorem provides the solution to this question.

Second theorem:

«For a given external potential and a fixed number of electrons, the ground state of the system is the overall minimum of the functional $E\left[\rho(\vec{r})\right]$*, The density that minimizes this functional corresponds to the density of the fundamental* $\rho_0(\vec{r})$ » [125]. $E\left[\rho(\vec{r})\right]$ reaches its minimum value when the density $\rho(\vec{r})$ corresponds to the exact density of the ground state $\rho_0(\vec{r})$.

$$E(\rho_0) = Min\left[E(\rho)\right] \tag{II-25}$$

Hohenberg and Kohn established that the ground state's density is the one that minimizes the energy $E\left[\rho(\vec{r})\right]$.Additionally, every other property is a functional of this density. the energy of the fundamental state of an electronic system in an external potential is determined, using the variational method.

$$\left.\frac{\partial E\left[\rho(\vec{r})\right]}{\partial \rho(\vec{r})}\right|_{\rho_0(\vec{r})} = 0 \tag{II-26}$$

By imposing the conservation constraint that ensures the total number of particles remains constant:

$$\int \rho(\vec{r})\, d^3\vec{r} = N \tag{II-27}$$

The solution to this problem can be obtained by employing the method of Lagrange multipliers.

$$G\left[\rho(\vec{r})\right] = \int \rho(\vec{r})\, d^3\vec{r} - N \tag{II-28}$$

In this case, the constraint becomes:

$$G\left[\rho(\vec{r})\right]=0 \tag{II-29}$$

Furthermore, if we incorporate an auxiliary function $A\left[\rho(\vec{r})\right]$ such that:

$$A\left[\rho(\vec{r})\right]=E\left[\rho(\vec{r})\right]-\mu G\left[\rho(\vec{r})\right] \tag{II-30}$$

Considering that μ is a Lagrange multiplier, the issue that has to be resolved is as follows:

$$\partial A\left[\rho(\vec{r})\right]=\int\frac{\partial A\left[\rho(\vec{r})\right]}{\partial\rho(\vec{r})}\rho(\vec{r})d^3\vec{r}=0 \tag{II-31}$$

Let it be:

$$G\left[\rho(\vec{r})\right]=\partial\left\{E\left[\rho(\vec{r})\right]-\mu\left(\int\rho(\vec{r})\,d^3\vec{r}-N\right)\right\}=0 \tag{II-32}$$

It is necessary to compute the functional derivative of $A\left[\rho(\vec{r})\right]$:

$$\frac{\partial A\left[\rho(\vec{r})\right]}{\partial\rho(\vec{r})}=\frac{\partial}{\partial\rho(\vec{r})}\left\{E\left[\rho(\vec{r})\right]-\mu\left(\int\rho(\vec{r})\,d^3\vec{r}-N\right)\right\}=\frac{\partial E\left[\rho(\vec{r})\right]}{\partial\rho(\vec{r})}-\mu\frac{\partial}{\partial\rho(\vec{r})}\left[\int\rho(\vec{r})\,d^3\vec{r}\right]=$$

$$\frac{\partial E\left[\rho(\vec{r})\right]}{\partial\rho(\vec{r})}-\mu \tag{II-33}$$

If we substitute this last expression into the expression for $\partial A\left[\rho(\vec{r})\right]$, it results in:

$$\partial A\left[\rho(\vec{r})\right]=\int\left[\frac{\partial E\left[\rho(\vec{r})\right]}{\partial\rho(\vec{r})}-\mu\right]\rho(\vec{r})d^3\vec{r}=0 \tag{II-34}$$

$$G\left[\rho(\vec{r})\right]=0\Rightarrow\int\left[\frac{\partial E\left[\rho(\vec{r})\right]}{\partial\rho(\vec{r})}-\mu\right]=\int\rho(\vec{r})d^3\vec{r} \tag{II-35}$$

$$\Leftrightarrow\left[\frac{\partial E\left[\rho(\vec{r})\right]}{\partial\rho(\vec{r})}=\mu\right] \tag{II-36}$$

Following this, we need to compute the functional derivative of $E\left[\rho(\vec{r})\right]$. According to equation (II-23), this functional derivative is written as:

$$\frac{\partial E\left[\rho(\vec{r})\right]}{\partial \rho(\vec{r})} = V_{ext}(\vec{r}) + \frac{\partial F_{HK}\left[\rho(\vec{r})\right]}{\partial \rho(\vec{r})} \tag{II-37}$$

By substituting equation (II-36) into expression (II-37), we derive the following equation:

$$\mu = \frac{\partial E\left[\rho(\vec{r})\right]}{\partial \rho(\vec{r})} = V_{ext}(\vec{r}) + \frac{\partial F_{HK}\left[\rho(\vec{r})\right]}{\partial \rho(\vec{r})} \tag{II-38}$$

In which the quantity μ denotes the chemical potential of the system. This equation of Euler-Lagrange type, constitutes the fundamental equation of the DFT formalism.

Unfortunately, Hohenberg and Kohn's theorem fails to provide any insight regarding the form of EF. There is no precise formula available to express kinetic energy as a functional of the electron density. The Kohn and Sham [128] equations are the exclusive solution to this issue, designed to provide the essential groundwork for efficiently utilizing the theorems of Hohenberg and Kohn [127].

II.5.3. Kohn-Sham equations

Based on the Hohenberg-Kohn theories [127], Kohn-Sham [128] suggested a new formulation to solve many-electron systems. The KS formulation requires replacing the original many-body system with an auxiliary independent particle system, while assuming that both systems possess same ground state density. Whereby the original interacting system with a real potential onto a fictitious non-interacting system, in which the electrons move within an effective Kohn-Sham single particle potential. The auxiliary Hamiltonian for the independent-particle system is:

$$\hat{H}_{KS} = -\frac{\hbar^2}{2m_e}\nabla^2 + V_{KS}(\vec{r}) \tag{II-39}$$

The ground state of a system with N independent electrons is determined by solving one-electron Schrödinger equations.

$$\left[-\frac{\hbar^2}{2m_e}\nabla^2 + V_{KS}(\vec{r})\right]\phi_i(\vec{r}) = \varepsilon_i \phi_i(\vec{r}) \tag{II-40}$$

where one electron is in each of the N orbitals $\Psi_i(\vec{r})$ with the lowest eigenvalues ε_i, the formula for auxiliary system density is given by:

$$\rho(\vec{r}) = \sum_{i=1}^{N} \left| \varphi_i(\vec{r})^2 \right| \tag{II-41}$$

This is governed by the conservation condition (II-27). For non-interacting independent particles, the formula for the kinetic energy $T_{KS}(\rho(\vec{r}))$ is:

$$T_{KS}(\rho(\vec{r})) = \sum_{i=1}^{N} \left\langle \varphi_i(\vec{r}) \right| -\frac{\hbar}{2m_e} \nabla^2{}_i \left| \varphi_i(\vec{r}) \right\rangle \tag{II-42}$$

Subsequently, the universal functional $F_{KS}(\rho(\vec{r}))$ was reformulated as:

$$F_{KS}(\rho) = T_{KS}(\rho(\vec{r})) + E_H(\rho(\vec{r})) + E_{xc}(\rho(\vec{r})) \tag{II-43}$$

The classic electrostatic (Hartree) energy of electrons $E_H(\rho(\vec{r}))$ is given by:

$$E_H[\rho(\vec{r})] = \frac{1}{2} \iint \frac{\rho(\vec{r})\rho(\vec{r}')d^3r d^3r'}{|\vec{r} - \vec{r}'|} \tag{II-44}$$

By applying the variational principle of Hohenberg and Kohn [127], based on the given equation:

$$\mu = \frac{\partial E[\rho(\vec{r})]}{\partial \rho(\vec{r})} = V_{ext}(\vec{r}) + \frac{\partial E_H[\rho(\vec{r})]}{\partial \rho(\vec{r})} + \frac{\partial T_S[\rho(\vec{r})]}{\partial \rho(\vec{r})} + \frac{\partial E_{XC}[\rho(\vec{r})]}{\partial \rho(\vec{r})} \tag{II-45}$$

When comparing equation (II-45) to a similar equation for a non-interacting electron system, moving in an effective potential $V_{eff}(\vec{r})$.

$$\mu = V_{eff}(\vec{r}) + \frac{\partial T_S[\rho(\vec{r})]}{\partial \rho(\vec{r})} \tag{II-46}$$

It is seen that the two equations are similar.

$$V_{eff}\left(\vec{r}\right)=V_{eff}\left[\rho\left(\vec{r}\right)\right]=V_{ext}\left(\vec{r}\right)+\frac{\partial E_H\left[\rho\left(\vec{r}\right)\right]}{\partial\rho\left(\vec{r}\right)}+\frac{\partial E_{XC}\left[\rho\left(\vec{r}\right)\right]}{\partial\rho\left(\vec{r}\right)} \quad \text{(II-47)}$$

$$V_{eff}\left(\vec{r}\right)=V_{ext}\left(\vec{r}\right)+\frac{1}{4\pi\varepsilon_0}\int\frac{\rho\left(\vec{r}'\right)}{\left|\vec{r}-\vec{r}'\right|}d^3\vec{r}+\frac{\partial E_{XC}\rho\left(\vec{r}\right)}{\partial\rho\left(\vec{r}\right)} \quad \text{(II-48)}$$

The exchange and correlation potential are determined by the derived functional:

$$\frac{\partial E_{XC}\left[\rho\left(\vec{r}\right)\right]}{\partial\rho\left(\vec{r}\right)}=V_{XC}\left[\rho\left(\vec{r}\right)\right] \quad \text{(II-49)}$$

The Schrödinger equation that has to be solved using the Kohn-Sham approach has the following form:

$$H_{KS}\phi_i\left(\vec{r}\right)=\left[-\frac{\hbar^2}{2m_e}\nabla^2+V_{eff}\left(\vec{r}\right)\right]\phi_i\left(\vec{r}\right)=\varepsilon_i\phi_i\left(\vec{r}\right) \quad \text{(II-50)}$$

The equations (II-48) and (II-50) are corresponding to the Kohn-Sham equations. In order to be resolved, they must be self-consistently. Starting from an initial density a potential $V_{eff}\left(\vec{r}\right)$ is acquired, for which the equation is solved and a new density electronic is then determined. Using this new density, it is possible to compute a new potential that is considered to be improved. This method is iterated in a self-consistent way until convergence is attained, until the new electron density reaches a level that is equivalent or nearly identical to the prior one.

II.5.3.1. Solving the Kohn-Sham equations

The resolution of the Schrödinger equation, with the Kohn-Sham approximation, is simplified to solving an equation of the following form:

$$\left[-\frac{\hbar^2}{2m_e}\nabla^2+\frac{1}{4\pi\varepsilon_0}\int\frac{\rho\left(\vec{r}'\right)}{\left|\vec{r}-\vec{r}'\right|}d^3\vec{r}+V_{ext}\left(\vec{r}\right)+V_{XC}\left(\vec{r}\right)\right]\phi_m\left(\vec{r}\right)=\varepsilon_i\phi_m\left(\vec{r}\right) \quad \text{(II-51)}$$

To achieve a solution for the Kohn-Sham equations, it is essential to choose a basis for the wave functions that can be mathematically represented as a linear combination of Kohn-Sham orbitals (KS orbitals).

$$\varphi_m\left(\vec{r}\right)=\sum_{p=1}^{p} C_p^m \varphi_p^b\left(\vec{r}\right) \qquad \text{(II-52)}$$

Where $\varphi_p^b\left(\vec{r}\right)$ are the basis functions, C_p^m the expansion coefficients, and where P is the dimensionality of the basis set.

Following this, the process of solving the Kohn-Sham equation involves identifying the coefficients C_p^m.

By selecting a base and, consequently, a finite value of P, it is possible to convert the Schrodinger equation (II-50) into its secular form.

$$\begin{bmatrix} \cdots & \cdots & \cdots \\ \vdots & \left\langle \varphi_i^b \middle| H \middle| \varphi_j^b \right\rangle - \varepsilon_m \left\langle \varphi_i^b \middle| \varphi_j^b \right\rangle & \vdots \\ \cdots & \cdots & \cdots \end{bmatrix} \begin{bmatrix} C_1^m \\ \vdots \\ C_p^m \end{bmatrix} = \begin{bmatrix} 0 \\ \vdots \\ 0 \end{bmatrix} \qquad \text{(II-53)}$$

The matrix elements of the single-particle Hamiltonian and the elements of the covering matrix can be distinguished as follows:

$$\left(H_{ij}-\xi_m S_{ij}\right)C_p^m=0 \qquad \text{(II-54)}$$

$$H_{ij}=\left\langle \varphi_i^b \middle| H \middle| \varphi_j^b \right\rangle \qquad \text{(II-55)}$$

$$S_{ij}=\left\langle \varphi_i^b \middle| \varphi_j^b \right\rangle \qquad \text{(II-56)}$$

The Kohn Sham equations offer a method to derive the exact density and energy of the ground energy state of a condensed matter system. As previously stated, it is necessary to solve the KS equations consistently due to the close connection between the effective Kohn-Sham potential V_{KS} and the electron density $\rho(r)$. Typically, this is achieved numerically via self-consistent iterations, as illustrated in Figure.II.7. The process starts by utilizing an initial electron density, often a superposition of atomic electron densities.

$$\rho_{in}=\rho_{cristal}=\sum \rho_{at} \qquad \text{(II-57)}$$

Following that, the orbitals are filled and the new density is calculated in the following form:

$$\rho_{out}\left(\vec{r}\right)=\sum_{i=1}^{N}\left|\phi_i\left(\vec{r}\right)\right|^2 \tag{II-58}$$

This closes the first cycle. In this stage, convergence acceleration is utilized to create a new density by combining the output density $\rho_{out}\left(\vec{r}\right)$ and the input density of the cycle $\rho_{in}\left(\vec{r}\right)$.

One of the most straightforward procedures pertaining to this mixture can be expressed as follows:

$$\rho_{in}{}^{i+1}=\left(1-\alpha\right)\rho_{in}{}^{i}+\alpha\rho_{out}{}^{i} \tag{II-59}$$

Where α define the mixture parameter and i corresponds to the i^{th} iteration.

Following this, the newly defined density input is incorporated into a second cycle self-consistent. This process is repeated iteratively until the criterion of convergence initially set is achieved. The accuracy of a computation becomes increasingly crucial when the convergence criteria $\rho_{out}\left(\vec{r}\right)-\rho_{in}\left(\vec{r}\right)$ is weak. When convergence is reached, the energy of the ground state of the system considered is known.

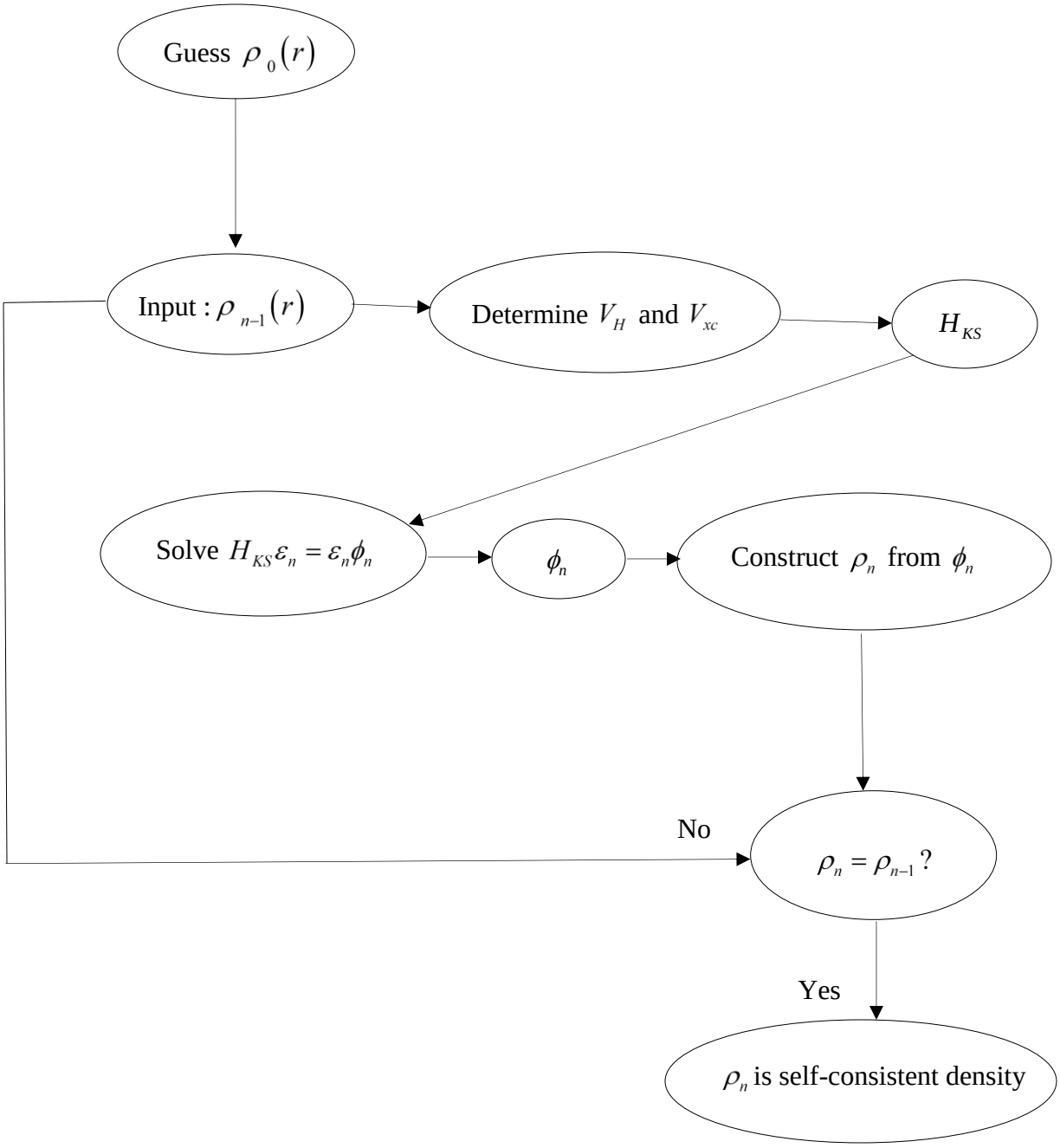

Figure.II.4: Flowchart of self-consistency loop for solving KS equations.

II.6. Exchange and correlation approximations

The accuracy of the ground state energy computed by density functional theory relies on the accurate definition of the exchange-correlation functional. There are numerous methods for estimating the exchange-correlation energy, but the most common is the local density approximation (LDA) [131] and generalized gradient approximation (GGA) [132]. Additionally, there exist advanced exchange correlation functionals, including hybrid functionals that incorporate a part of the Hartree-Fock exchange potential.

II.6. 1. Local Density Approximation (LDA)

Local density approximation (LDA) [131] is the most straightforward method for determining correlation exchange energy. This approximation is based on the assumption that the electron density may be considered locally as a uniform electron gas. The expression for the total exchange-correlation functional $E_{xc}\left[\rho(\vec{r})\right]$ can be formulated as follows:

$$E_{xc}^{LDA}\left[\rho(\vec{r})\right]=\int \rho(\vec{r})\xi_{xc}^{LDA}\left[\rho(\vec{r})\right]d^3\vec{r} \tag{II-60}$$

Where $\xi_{xc}^{LDA}\left[\rho(\vec{r})\right]$ is the exchange-correlation energy for a homogeneous electron gas with uniform density $\rho(\vec{r})$ .The corresponding exchange-correlation potential is:

$$V_{xc}^{LDA}(\vec{r})=\frac{\partial E_{xc}^{LDA}\left[\rho(\vec{r})\right]}{\partial\rho(\vec{r})}=\xi_{xc}^{LDA}\left[\rho(\vec{r})\right]+\rho(\vec{r})\frac{\partial\xi_{xc}^{LDA}\left[\rho(\vec{r})\right]}{\partial\rho(\vec{r})} \tag{II-61}$$

The term $\xi_{xc}^{LDA}\left[\rho(\vec{r})\right]$ can be estimated by the addition of two components, one representing the exchange term and the other representing the correlation term:

$$\xi_{xc}^{LDA}\left[\rho(\vec{r})\right]=\xi_{x}^{LDA}\left[\rho(\vec{r})\right]+\xi_{c}^{LDA}\left[\rho(\vec{r})\right] \tag{II-62}$$

Where the exchange term is known as «Dirac exchange» and is given by:

$$\xi_{xc}^{LDA}\left[\rho(\vec{r})\right]=-C_x\rho(\vec{r})^{\frac{1}{3}}=-\frac{3}{4}\left(\frac{3}{\pi}\rho(\vec{r})\right)^{\frac{1}{3}}\Rightarrow C_x=\frac{3}{4}\left(\frac{3}{\pi}\right)^{\frac{1}{3}} \tag{II-63}$$

$$E_{xc}^{LDA}\left[\rho(\vec{r})\right]=-C_x\int\rho(\vec{r})^{\frac{4}{3}}d\vec{r} \tag{II-64}$$

Analytical solutions can be used to solve the exchange term and the correlation component cannot be precisely defined. Regarding this, Wigner [135], Vosko-Wilk-Nussair [136], Perdew-Zunger [137] developed parameterizations for exchange-correlation functionals through the utilization of quantum Monte Carlo simulations [136]. The electron density in a real system is not uniform, which is something that should be taken into consideration.

The Local Density Approximation (LDA) often yields excellent accords with empirical observations regarding structural and vibrational properties, dipole moments, elastic moduli, and phase stability. The use of this approximation for the calculation of exchange-correlation energy is particularly suitable for homogeneous systems or systems with slowly varying density. Consequently, this approach is effective when applied to metals with a uniform density, but it is inadequate for systems with significant variations in electron density and materials that include d or f electrons, such as transition metals. The LDA often underestimates the real bandgap by 50%

II. 6. 2. The generality of the LDA (LSDA) approximation

For systems with spin polarization [137], the Local Spin Density Approximation (LSDA) provides a much better approximation, particularly for atoms, radical molecules, or magnetic solids. In this approximation, the correlation exchange energy is defined as:

$$E_{xc}^{LDA}\left[\rho\uparrow(\vec{r}),\rho\downarrow(\vec{r})\right]=\int\rho(\vec{r})\xi_{xc}^{LDA}\left[\rho\uparrow(\vec{r}),\rho\downarrow(\vec{r})\right]d^3\vec{r} \qquad \text{(II-65)}$$

where $\xi_{xc}^{LDA}\left[\rho\uparrow(\vec{r}),\rho\downarrow(\vec{r})\right]$ denotes the exchange-correlation energy per particle of homogeneous electron gas.

LSDA underestimates the magnitude of the total exchange-correlation energy of an atom or molecule by approximately 10% for small atomic numbers; its relative error diminishes as the atomic number increases. By approximately 2%, LSDA overestimates the bond energies between atoms and underestimates the bond lengths and lattice constants. Therefore, LSDA remains valuable in and of itself, particularly with regard to solids where its uniform-gas appropriate criteria are more important. Moreover, LSDA establishes a solid foundation for subsequent developments in functional approximation.

II. 6. 3. Generalized Gradient Approximation (GGA)

Most of the corrections that have been introduced to the (LDA) [131] are based on the idea of taking into account local variations in density. As a result, the electron density gradient was added, which led to the development of the Generalized Gradient Approximation (GGA) [132], this approximation is highly precise. The most commonly utilized Generalized Gradient Approximations (GGA) are the formulations introduced by Becke [138], Perdew et al [139], and Perdew, Burke, and Enzerhof (PBE) [132].

The exchange and correlation energy are dependent on the electron density and its gradient, it can be written in the form:

$$E_{XC}{}^{GGA}\left[\rho(\vec{r})\right]=\int \rho(\vec{r})\,\xi_{xc}\left[\rho(\vec{r}),\left|\nabla\rho(\vec{r})\right|\right]d^{3}\vec{r} \qquad \text{(II-66)}$$

$\left[\rho(\vec{r}),\left|\nabla\rho(\vec{r})\right|\right]$ the given expression denotes the energy associated with the exchange and correlation effects per electron in a system of interacting electrons with non-uniform density.

In general, GGA outperforms LDA when it comes to predicting bond length and binding energy of molecules, crystal lattice constants, and other parameters, particularly in systems characterized by rapid variations in charge density. In ionic crystals, where the lattice constants derived from LDA calculations correspond well with experimental data but GGA overestimates it, LDA results are occasionally overcorrected by GGA. However, it should be noted that both LDA and GGA exhibit poor performance in correlated materials, including those with localized electrons, strongly transition metal oxides, rare-earth elements, and compounds. This limitation results in estimations that go beyond LDA and GGA.

II.6. 4. modified Beck and Johnson approximation (mBJ-GGA)

A new modified version of the exchange potential, initially suggested by Becke and Johnson [140], Tran and Blaha [141] have recently proposed modifying the Becke-Johnson potential to enhance energy gap calculations. The modified Becke and Johnson potential proposed by Tran and Blaha which has the following form [140]:

$$v^{mbj}{}_{x;\sigma}(r)=cv^{BR}{}_{x;\sigma}(r)+(3c-2)\frac{1}{\pi}\sqrt{\frac{5}{12}}\sqrt{\frac{2t_{\sigma}(r)}{\rho_{\sigma}(r)}} \qquad \text{(II-67)}$$

In which $\rho_\sigma(r)=\sum_{i=1}^{N_\sigma}\left|\psi_{i,\sigma}\right|^2$ is the electron density, $t_\sigma=\frac{1}{2}\sum_{i=1}^{N_\sigma}\left|\psi_{i,\sigma}{}^{*}\nabla\psi_{i,\sigma}\right|^2$ is the kinetic energy density and $v_{x,\sigma}^{BR}(r)$ is the Becke-Russell (BR) exchange potential [142].

$$v_{x,\sigma}^{BR}(r)=-\frac{1}{b_\sigma(r)}\left[1-e^{x_\sigma(r)}-\frac{1}{2}x_\sigma(r)e^{-x_\sigma(r)}\right] \quad \text{(II-68)}$$

The Becke-Roussel potential is introduced to minimize the Coulomb potential $x_\sigma(r)$ and is determined by a non-linear equation involving $\rho_\sigma(r),\nabla_{\rho_\sigma}(r),\nabla^2\rho_\sigma(r)$ and $t_\sigma(r)$, The function $b_\sigma(r)$ is given by:

$$b_\sigma=\left[\frac{x^3{}_\sigma(r)e^{-x_\sigma(r)}}{8\pi\rho_\sigma(r)}\right]^{\frac{1}{3}} \quad \text{(II-69)}$$

The potential of Becke-Roussel suggested in this context is about equivalent to the potential of Slater employed in Beck and Johnson [140], The most significant alteration occurs when the parameter c is introduced into the functional formula. It is crucial to note that when c is equal to 1, the outcome reverts back to the functional suggested by Becke and Johnson. The selection of this parameter is based on a linear dependence on the square root of the average value $\frac{\left|\vec{\nabla}\rho(r)\right|}{\rho(r)}$,The suggested format for c is given by:

$$c=\alpha+\beta\left(\left(\frac{1}{V_{cell}}\int\frac{\left|\vec{\nabla}\rho(r')\right|}{\rho(r')}d^3r'\right)\right)^{\frac{1}{2}} \quad \text{(II-70)}$$

α and β are two free parameters that represent the volume of the unit cell in the system. $\alpha=-0.012\quad\beta=1.023\ bohr^{\frac{1}{2}}$.

Thus, the mBJ approximation increases the energy gap, leading to results that align with empirical findings. In contrast, LDA approximations and GGA provide narrower gaps. The gaps obtained by the mBJ involve a range of distinct systems, from insulators with extensive gaps to semiconductors with small gaps. It is important to note that the modified potential of Becke and

Johnson (BJ) is an exchange potential that incorporates the exchange of holes. The self- consistent implementation of the BJ exchange potential has been incorporated into the WIEN2K code [143].

II.6. 5. Engel Vosko approximation (EV-GGA)

The conventional semi-local approximations of the exchange-correlation (XC) functionals, including the local density approximation (LDA) and the generalized gradient approximation (GGA), have proven to be highly accurate in predicting numerous properties of solids, as we have previously discussed. Unfortunately, both of these approximations are not accurate enough to adjust the energy band gap. Engel and Vosko developed a new functional version of the Generalized Gradient Approximation (GGA) to address this deficiency. Their aim was to provide an improved potential for both exchange and correlation. This approach, which is known as EV-GGA [144], which provides an improved bandgap and additional properties that are primarily determined by the accuracy of the correlation and potential.

2

Full Potential Augmented Plane Wave (FP-LAPW)

II.7. Linearized augmented plane wave method (FP-LAPW)

II.7. 1. Introduction

Density functional theory is an effective method for many-body problem treatment. Nevertheless, it is crucial to select the suitable wave function basis for effectively solving the Khon-Sham equations. Several methods exist for solving the Schrödinger equation. These methods vary in terms of the type of potential employed and the wave functions selected as a basis. One of these methods is a linear combination of atomic orbitals (LCAO) [145,146] that allow the treatment of transition metals. Orthogonalized plane wave (OPW) methods and their derivatives [145,147] can be employed to analyze the conduction bands of simple metals with a "s-p" characteristic. Cellular methods, such as augmented plane waves (APW) [148],The linearized methods developed by Andersen [149]:linearized augmented plane waves (LAPW) and linearized "muffin-tin" orbitals (LMTO) can reduce calculation times by several orders of magnitude.

In light of this, the linear augmented plane wave (LAPW) [150,151] approach is a key modification of the augmented plane wave (APW) method developed by Slater (1937,1964) [152,153].Therefore, before we begin this new approach we shall begin by providing a brief recapitulation of the method (APW), which is widely used for solving the electronic structure through the utilization of the Kohn-Sham (KS) equations.

II.7. 2. Augmented plane wave method (APW)

The APW method was developed by Slater in 1937 [148]. In which, he introduces the Muffin-tin (MT) potential approximationto describe the crystal potential.based on this

approximation the unit cell is divided into two types of regions, non-overlapping atomic spheres, often known as the Muffin-tin (MT) region, and an interstitial region (Figure.II.8).

Region one: The muffin tin region.

In this region, the electrons are in close proximity to the nuclei and exhibit behavior similar to that of free atoms. They can be more effectively characterized using atomic-like functions. The region in which the spheres occupy space is referred to as the muffin tin region with radius R_α .

Region two: The interstitial region

The space remaining beyond the spheres is referred to as the interstitial region.Since the electrons are essentially free (electrons are far from nuclei), they are described by plane waves.

In these two regions, two different basic sets are employed: Radial solutions of the Schrodinger equation within the sphere (MT), and plane waves in the interstitial region.

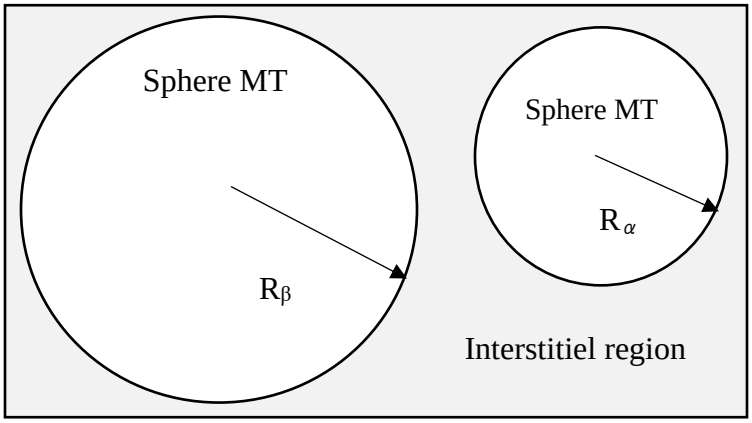

Figure.II.3: Unit cell division in non-overlapping muffin tin spheres and interstitial region with two atoms.

We can now define a basis function APW, with two regions determined by the wave function $\phi(\vec{r})$ can be expressed in the following manner:

$$\phi(\vec{r}) = \begin{cases} \dfrac{1}{\Omega^{\frac{1}{2}}} \sum_G C_G e^{i(\vec{G}+\vec{K})\vec{r}} & \vec{r} \in I \\ \sum_{lm} A_{lm} U_l(r) Y_{lm}(r) & \vec{r} \in S \end{cases} \qquad \text{(II-71)}$$

The Bloch vector is denoted as $\vec{K}$, the reciprocal lattice vector is denoted as $\vec{G}$, Ω is the unit cell volume and C_G , A_{lm} are the expansion coefficients in spherical harmonics $Y_{lm}(r)$.

$U_l(r)$ is the numerical solution to the radial Schrödinger equation is as follows:

$$\left\{ -\frac{d^2}{dr^2} + \frac{l(l+1)}{r^2} + V(r) - E_l \right\} rU_l(r) = 0 \qquad \text{(II-72)}$$

E_l is a parameter and $V(r)$ the spherical component of the potential in the sphere. Equation (II-72) defines radial functions that are automatically orthogonal to every eigenstate of the Hamiltonian which disappears at the sphere's limit [148]. This can be seen via the Schrodinger equation given below:

$$(E_2 - E_1) r\, U_1 U_2 = U_2 \frac{d^2 r U_1}{dr^2} - U_1 \frac{d^2 r U_2}{dr^2} \qquad \text{(II-73)}$$

U_1 and U_2 are the radial solutions that correspond to the energies E_1 and E_2 , respectively.

Slater made certain choice for wave functions and showed that plane waves satisfy the Schrödinger equation when the potential is constant, whereas radial functions satisfy the equation when the potential is spherical. This establishes that E_l is really the eigenvalue. This approximation (MT) produces extremely good results, particularly for compact structures such as face-centered cubic (fcc) and hexagonal close-packed (hcp). However, this estimate gives acceptable results for bcc structures, Thus, this approach isn't recommended when material symmetry decreases [148]. In order to maintain the continuity of the function $\phi(\vec{r})$ on the sphere MT surface, it is necessary to develop the coefficients A_{lm} as a function of the coefficient C_G of the plane waves that occur in the interstitial regions. As a result of the calculations [154], we obtain the following expression:

$$A_{lm} = \frac{4\pi i^{l}}{\sqrt{\Omega}\ \mathrm{U}_1 \left|R_{MT}\right|} \sum_{G} C_G\, j_l \left(\left|\vec{K}+\vec{G}\right| R_{MT}\right) Y^{*}{}_{lm}\left(\vec{K}+\vec{G}\right) \qquad \text{(II-74)}$$

j_l represents the Bessel function.

Where the origin is the sphere center and r_l its radius. The A_{lm} are defined by the coefficients of the plane waves and the energy parameters E_l .These terms are variational coefficients in the APW approach. In the interstitial region, the wave functions act like plane waves, whereas in the core region, they grow and behave as radial functions.

The APW functions are the solutions of the Schrödinger equation for an energy E_l , which is equivalent to the energy band identified by the index G. Consequently, the energy bands (for a certain point k) cannot be determined using a straightforward diagonalization process. Instead, it is imperative to consider the secular determinant as a function of the energy.

Equation (II-71) contains a function $U_l(r)$ that is dependent on E_l and can become zero on the surface of the sphere MT, this results in a separation between the radial functions and the plane waves. To address this issue, numerous modifications have been implemented to the (APW) method, particularly those suggested by Koelling [155] and Andersen [149]. The modification consists of representing the wave function $\phi(\vec{r})$ inside the spheres by a linear combination of the radial functions $U_l(r)$ and their derivatives $\dot{U}_l(r)$ with respect to the energy, thus giving rise to the FP-L APW method.

II.7. 3. LAPW concept

The LAPW method [149] is a method used to solve the Kohn and Sham equations in order to determine the ground state density, total energy, and eigenvalues of a many-electron system, using specialized bases.

The bases inside the sphere in the LAPW approach are linear combinations of radial functions $U_l(r)Y_{lm}(r)$ and their derivatives with respect to energy $\dot{U}_l(r)Y_{lm}(r)$ .The U functions are defined with a fixed E_l exactly as in the (APW) method (equation. II-73). The derivative of U_l with respect to energy obeys the following equation [152]:

$$\left[-\frac{d^2}{dr^2}+\frac{l(l+1)}{r^2}+V(r)-E_l\right] r\dot{U}_l(r)=rU_l(r) \tag{II-75}$$

The wave function is expressed in the following form:

$$\phi(\vec{r})=\begin{cases}\dfrac{1}{\Omega^{\frac{1}{2}}}\sum_G C_G e^{i(\vec{K}+\vec{G})\vec{r}} & \vec{r}\in I\\ \sum_{lm}\left[A_{lm}U_l(r)+B_{lm}\dot{U}_l(r)\right]Y_{lm}(r) & \vec{r}\in S\end{cases} \tag{II-76}$$

B_{lm} and A_{lm} are coefficients that are corresponding to the function $\dot{U}_l, U_l$ respectively. It is found that the method (LAPW) consistently employs plane waves in the interstitial region, similar to the APW method. However, within the sphere, linearly augmented plane waves (LAPW) are utilized. The radial functions can be expanded in proximity of E_l as follows [156]:

$$U_l(E,r)=U_l(E_l,r)+(E-E_l)\dot{U}(E_l,r)+O\left((E-E_l)^2\right) \tag{II-77}$$

$O\left((E-E_l)^2\right)$ represents the quadratic error committed.

The error incurred in the computation of the function and energy in the FP-LAPW method is of the same magnitude as $(E-E_l)^2$ and $(E-E_l)^4$ [154], respectively. Linearly augmented plane waves (LAPW) method provides a good basis within an energy interval that is relatively broad. In addition, all valence bands may normally be addressed using a single value of E_l. If this can't be performed, the energy region needs to be divided into two or more windows, which is an excellent simplification with regards to the (APW) method.

II.7. 4. Energies linearization E_l

The Augmented wave functions $\dot{U}_l$ and U_l are orthogonal to each state of the core, and they are absolutely confined to the MT sphere. Unfortunately, this condition is not satisfied, except in the case where the states of the core do not have the same number l, consequently, to avoid the risk of encountering of the semi-core states with the valence states. The (APW) method does not address this issue, but the non-orthogonality of some core states in the (FP-LAPW) method

requires a sensitive choice of the parameter E_l.We are unable to conduct the calculation in this case without modifying E_l.

Local orbital development is the optimal resolution in such cases. Nevertheless, this option may not be accessible in all programs, in such cases, the maximum sphere radius possible must be selected. It is important to mention that the different E_l should be defined independently from one another. The energy bands consist of distinct orbitals. To get a precise computation of the electronic structure, it is necessary to select E_l as closely as possible to the energy of the band, provided that the band possesses the same l value.

II.7. 4. 1. Development of local orbitals

The objective of the LAPW approach is to get accurate band energies in proximity to the linearization energies E_l [149]. In most materials, choosing energies in the center of the bands is sufficient. Unfortunately, it is not always possible to determine a single value of E_l that can be used to compute all energy bands for certain materials. This applies to materials that possess $4f$ orbitals [157,158] and transition metals [159,160]. This is the main issue with the semi-core state, which lies in between the core and valence states. To address this problem, we may either employ multiple energy windows or utilize developments in local orbitals.

II.7. 4. 2. LAPW with Local Orbitals (LAPW+LO)

The development of the method (LAPW) in local orbitals involves altering its base orbitals to avoid multiple windows.by adding a third type of basic function. The concept is to process all the bands within a single energy window. Singh [157] introduced the notation «LO» to represent these orbitals, which are expressed as a linear combination of two radial functions associated with two distinct energies and the derivative with respect to the energy of one of these functions.

$$\phi_{lm}\left(\vec{r}\right)=\begin{cases}0 & \vec{r}\notin S\\ \left[A_{lm}^{LO}U_l\left(r,E_{1,l}\right)+B_{lm}^{LO}\dot{U}_l\left(e,E_{1,l}\right)+C_{lm}^{LO}U_l\left(r,E_{2,l}\right)\right]Y_{lm}\left(r\right) & \vec{r}\in S\end{cases} \quad \text{(II-78)}$$

In this case, the C_{lm} coefficients are identical to the A_{lm} and B_{lm} coefficients that were previously defined. In addition, the error introduced during the calculation of conduction and valence bands is diminished by this modification.

II.7. 4. 3. The APW+LO method

The main problem associated with the APW method is the energy dependency of all base functions This issue has been mitigated by the Linearized Augmented Plane Wave with local orbitals (LAPW+LO) method. Although this method has the advantage of eliminating the energy dependence on the basis set, it suffers from larger basis sets. This sets limitations on the APW and LAPW+LO methods. Sjösted, Nordström, and Singh [161] enhanced the present method by creating a base that incorporates the advantages of the (APW) method with the (LAPW+LO) method. The description by which an appropriate basis set is described is known as the Augmented Plane Wave with local orbitals (APW+lo) method.

This approach aligns with an energy-independent basis, similar to the LAPW+LO method, and only requires a slightly larger plane wave cutoff energy compared to the APW method. It requires using a typical APW base. However, considering $U_l(r)$ for a given energy E_l in order to maintain the advantage offered by the linearization of the issue to the eigenvalues. Nonetheless, a fixed energy basis does not offer a good description of the eigenfunction, we additionally include local orbitals to provide variational flexibility at the level of radial basis functions.

«APW+lo», it is based on two types of functions.

- The first one is the APW basis function with a set of fixed energies E_l .

$$\phi(\vec{r}) = \begin{cases} \frac{1}{\Omega^{\frac{1}{2}}} \sum_G C_G e^{i(\vec{K}+\vec{G})\vec{r}} & \vec{r} \in I \\ \sum_{lm} \left[A_{lm} U_l(r) \right] \; Y_{lm}(r) & \vec{r} \in S \end{cases} \qquad \text{(II-79)}$$

- The second one represents a different type of local orbitals.

$$\phi_{lm}(\vec{r}) = \begin{cases} 0 & \vec{r} \notin S \\ \left[A_{lm}^{lo} U_l(r, E_{1,l}) + B_{lm}^{lo} \dot{U}_l(e, E_{1,l}) \right] Y_{lm}(r) & \vec{r} \in S \end{cases} \qquad \text{(II-80)}$$

The energies employed in the APW and local orbitals parts of the basis are often the same. The coefficients A_{lm}^{lo} and B_{lm}^{lo} can be determined by the process of normalization and by ensuring that the local orbitals at the muffin-tin border are equal to zero. This base produces comparable results to the LAPW+LO approach while allowing the product $R_{\min} * K_{\max}$ to be lowered by a value of one

II.7. 5. FP-LAPW concept

The Full Potential Linearized Augmented Plane Waves (FP-LAPW) method does not include any approximations about the form of the potential or the charge density. They are rather developed in the Fourier series in the interstitial region and harmonics of the lattice within each atomic sphere. This is where the term «Full-Potential» got its original meaning. Therefore, this method assures the continuity of the potential on the MT sphere surface and displays as follows:

$$V(\vec{r}) = \begin{cases} \sum_k V_k e^{i\vec{k}\vec{r}} & r \in I \\ \sum_{lm} V_{lm}(r) Y_{lm}(\vec{r}) & r \in S \end{cases} \qquad \text{(II-81)}$$

Similarly, the charge density is generated in the following manner:

$$\rho(\vec{r}) = \begin{cases} \sum_k \rho_k e^{i\vec{k}\vec{r}} & r \in I \\ \sum_{lm} \rho_{lm}(r) Y_{lm}(\vec{r}) & r \in S \end{cases} \qquad \text{(II-82)}$$

II.7. 6. The Wien2k Code

II.7. 6. 1. General description of the Wien2k code

When it comes to calculating the following properties of solids, WIEN2k is a DFT code that is extensively employed in computational materials science, electronic band structure with high precision, Density of states, Optical properties, Magnetic properties, Transport properties, Phonons, Surface and interface properties and Defects and impurities. The development of this software package was undertaken by Peter Blaha and Karl Heinz Schwarz, who are affiliated with the Vienna University of Technology's Institute of Materials Chemistry [162]. The code was first publicly released in 1990. After that, the subsequent versions were named WIEN93, WIEN97, and WIEN2k (we used the version WIEN2k (year 2000)), respectively, based on the year they were published. The language FORTRAN90 was used in the creation of the WIEN2k package it consists of numerous programs interconnected using C-shell scripts. The computations for this package might be run on any form of Unix or Linux using a computer, workstations, servers, or supercomputers for a variety of crystal systems with up to 100 atoms in per formula unit cell. The diagram below depicts the flow and utilization of several programs (Figure.II.9).

Case generation in WIEN2k: In order to start a new formal proceeding, it is essential to contain the following information

- The angles and lattice parameters (in Bohr or Angstroms).
- The type of lattice or spacegroup (primitive, face-centered, hexagonal, etc).
- The coordinates of all equivalent atoms expressed as fractions of the unit cell.
- Alternatively, only the inequivalent positions can be specified using the new StructGen.
- The corresponding ones will be automatically generated

II.7. 6. 2. Initialization of the calculation

Once the basic input files have been generated, the calculation is initialized by Execution of initialize calc this will provide you with the essential steps to initiate the computation. The calculating initialization process involves the automatic execution of multiple steps, with x being the script used to initiate WIEN2k programs.

x nn: This expression is used to compute the closest neighboring points within a given distance. This calculation is essential for determining the radii of atomic spheres. To do this calculation, you need to specify a distance factor, denoted as f, such as 2.

x sgroup: The x sgroup function determines the point and space groups associated with the provided structure.

x symmetry: generates from a raw **case.struct** file the space group symmetry operations, determines the point group of the individual atomic sites, generates the LM expansion for the lattice harmonics and local rotation matrices.

x lstart: the x lstart function calculates atomic densities and defines the treatment of orbitals in band structure computations, such as whether they are considered core or band states, and whether local orbitals are included or not.

We are required to indicate the preferred exchange-correlation potential namely PBE-GGA (Perdew-Burke-Ernzerhof 96), LSDA, WC-GGA (Wu-Cohen 06), PBE sol-GGA (Perdew et al 08) along with an energy value that typically divides valence from core states, commonly set at -6.0 Ry.

x kgen: the x kgen function generates a k-mesh within the Brillouin zone (BZ). It is necessary to indicate the total number of k-points in the Brillouin Zone (BZ).

x dstart: The x dstart function provides an initial density for the self-consistent field (SCF) cycle by combining atomic densities obtained in lstart.

II.7. 6. 3. The SCF calculation

The SCF cycle consists of the following steps:

LAPW0: LAPW0 is a computational method that calculates the total potential, V_{tot}, by combining the Coulomb potential V_C, with the exchange-correlation potential, V_{xc}. It uses the total electron density as the input. The numerical computation of the exchange-correlation potential is performed on a grid.

LAPW1: (BANDS) computes the electronic energy levels and corresponding wavefunctions of the valence bands. Lapw1 initializes the Hamiltonian and the overlap matrix.

LAPW2: is a computational tool that calculates the states and densities of a core.

MIXER: (adding and mixing of charge densities) mixes input and output densities. The sum of the electron densities of the valence, semi-valence, and core states produces the new total density. Taking only the new densities would, however, lead to instabilities in the iterative SCF process. To have a stable SCF cycle new and old densities need to be mixed, to obtain a new density.

To initiate the execution of a system in the wien2k code, the first step is to provide the struct file «case-Struct» as an input file. This file comprises fundamental characters that define the geometric properties of the system that was investigated. These characters include the lattice parameters and angles, the type of lattice, and the number of equivalent atoms. Figure.II.8 presents an example of a struct file that describes the numerous parameters of a material under investigation.

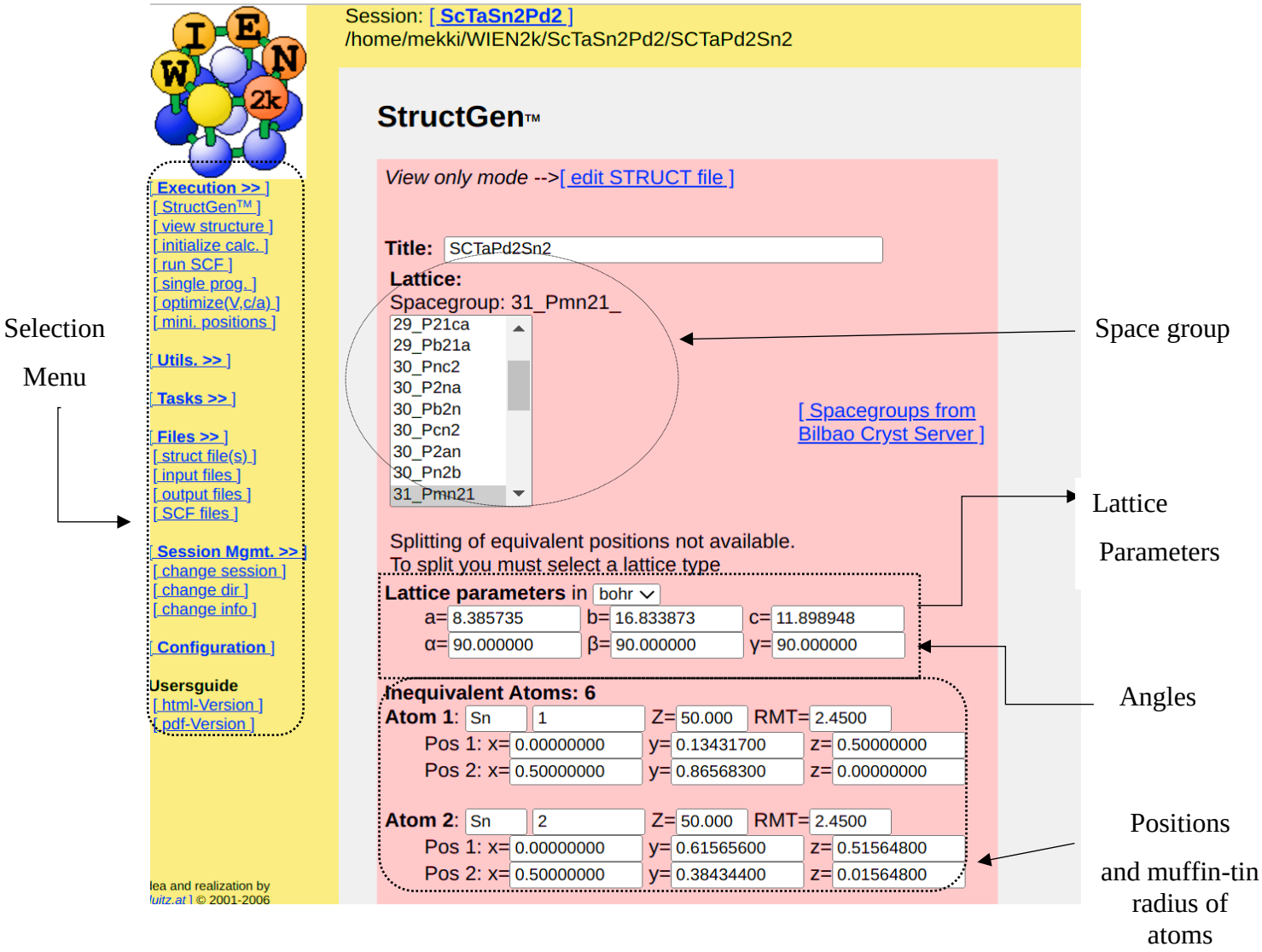

Figure.II.4: Example of StructGen of w2web.

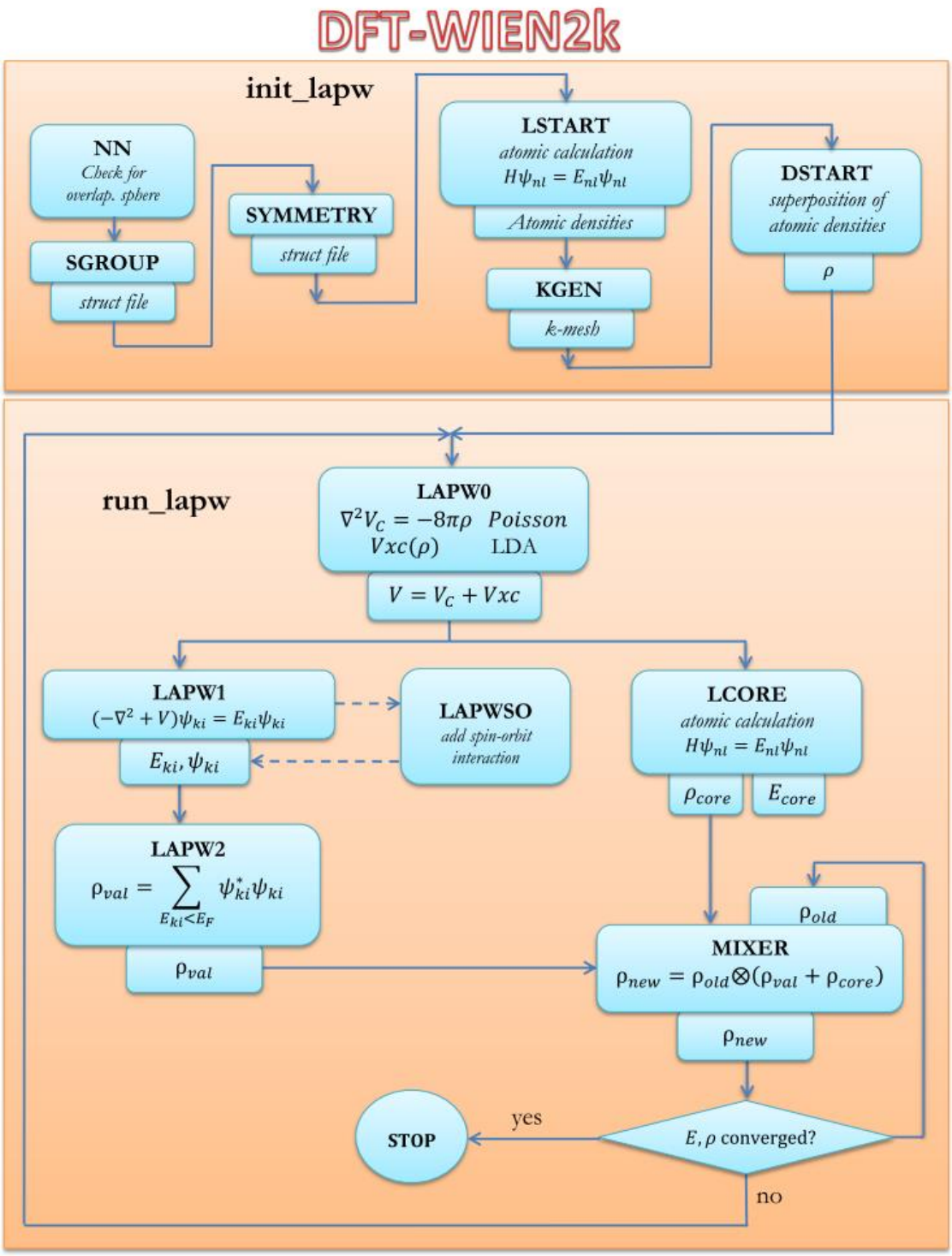

Figure.II.5: Flow chart of WIEN2k code [163].

3

Boltzmann Transport Theory

II.8. Boltzmann Transport Theory

II.8. 1. Boltzmann transport equation

The fundamental mechanism behind transport in materials is the response of carriers, which can be electrons or phonons, to an external field such as an electric or magnetic field and/or a temperature gradient, whom make the system deviate from equilibrium. At equilibrium, the distribution function of a gas of electron energy $\varepsilon\left(\vec{K}\right)$ is given by the Fermi-Dirac function, which describes the probability occupation of a state by an electron located at the position $\vec{r}$ with a wave vector $\vec{K}$ [164].

$$f_0\left(\vec{r},\vec{K}\right)=\frac{1}{e^{\left(\varepsilon\left(\vec{K}\right)-\mu\left(\vec{r}\right)\right)/k_BT\left(\vec{r}\right)}+1} \tag{II-83}$$

In a non-equilibrium system, the distribution function undergoes a transition from f_0 to $f\left(\vec{r},\vec{K},t\right)$ which depend on the spatial coordinates $\vec{r}$, the wave vector $\vec{K}$, and the time t.

Liouville's theorem states that [165], in the absence of impurity collisions, the function distribution remains constant over time. For this particular situation, the written form can be expressed as:

$$f\left(\vec{r},\vec{K},t\right)=f\left(\vec{r}+\Delta\vec{r},\vec{K}+\Delta\vec{K},t+\Delta t\right) \tag{II-84}$$

The transfer equation can be expressed as follows:

$$\frac{df}{dt}=0 \tag{II-85}$$

Electrons interact and scatter as a result of the presence of forces (The process of particle diffusion can occur because of temperature gradients, impurities, phonons, or defects….), we obtain:

$$\frac{df}{dt} = \vec{v}.\nabla_{\vec{r}} f + \frac{1}{\hbar}\vec{F}.\nabla_{\vec{K}} f + \frac{\partial f}{\partial t} = \left(\frac{\partial f}{\partial t}\right)_{collision} \tag{II-86}$$

Where $\vec{v}$ is the velocity of the particle. The variation over time of the distribution function can be expressed as the sum of two terms related to the applied forces, external field (drift) and internal forces (collisions).

$$\frac{\partial f}{\partial t} = \underbrace{-\vec{v}.\nabla_{\vec{r}} f - \frac{1}{\hbar}\vec{F}.\nabla_{\vec{K}} f}_{drift} - \left(\frac{\partial f}{\partial t}\right)_{collision} \tag{II-87}$$

under stable conditions $\partial f / \partial t = 0$:

$$\frac{\partial f}{\partial t} = \left(\frac{\partial f}{\partial t}\right)_{drift} + \left(\frac{\partial f}{\partial t}\right)_{collision} = 0 \tag{II-88}$$

In light of the fact that the concept of collision is difficult to describe in general. In 1954, Bhatnagar, Gross, and Kross (BGK) [166] proposed a hypothesis regarding relaxation time. This hypothesis aimed to simplify the study of the collision part in the Boltzmann equation.

$$\frac{\partial f}{\partial t} = \left(\frac{\partial f}{\partial t}\right)_{collision} = -\frac{f(\vec{r},\vec{K},t) - f_0(\vec{r},\vec{K})}{\tau_{\vec{K}}} \tag{II-89}$$

This formula indicates that when the external fields are altered, the system decay exponentially to its equilibrium state as a result of collisions. The term of (drift) then becomes null.

II.8. 2. Boltzmann equation linearization

From the equation (II-88) and (II-89), Under the effect of an external force (electromagnetic field $\vec{F}$), we are able to obtain the Boltzmann equation when stationary states are being considered.

$$v_{\vec{K}}\nabla_{\vec{r}} f + \frac{1}{\hbar}\vec{F}.\nabla_{\vec{K}} f = -\frac{f\left(\vec{r},\vec{K},t\right) - f_0\left(\vec{r},\vec{K}\right)}{\tau_{\vec{K}}} \quad \text{(II-90)}$$

$$\vec{F} = e\left[\vec{E} + \vec{v}\times\vec{B}\right] \quad \text{(II-91)}$$

Where e is the electron charge. We express $\nabla_{\vec{r}} f$ regarding temperature gradient and determine $\vec{v}$ as a function of $\vec{K}$:

$$v_{\vec{K}} = \frac{1}{\hbar}\frac{\partial \varepsilon_{\vec{K}}}{\partial K} \quad \text{(II-92)}$$

Where $\varepsilon_{\vec{K}}$ is the energy band.

$$v_{\vec{K}}.\nabla_{\vec{r}} T\frac{\partial f}{\partial T} + \frac{1}{\hbar}e\left[\vec{E} + \vec{v}\times B\right].\nabla_{\vec{K}} f = -\frac{f\left(\vec{r},\vec{K},t\right) - f_0\left(\vec{r},\vec{K}\right)}{\tau_{\vec{K}}} \quad \text{(II-93)}$$

In absence of magnetic fields ($\vec{B} = \vec{0}$), Assuming the homogeneity of space $\nabla_{\vec{r}} T = 0$, the Boltzmann equation (BTE) can be expressed as:

$$\frac{e}{\hbar}\vec{E}\nabla_{\vec{K}} f = -\frac{f\left(\vec{r},\vec{K},t\right) - f_0\left(\vec{r},\vec{K}\right)}{\tau_{\vec{K}}} \quad \text{(II-94)}$$

By substituting $\nabla_{\vec{K}} f$ with $\nabla_{\vec{K}} f_0$ as an approximation solution, we get [164]:

$$f_{\vec{K}} \approx f_0 - \frac{e}{\hbar}\tau_{\vec{K}}.\nabla_{\vec{K}} f_0.\vec{E} \quad \text{(II-95)}$$

With: $$\nabla_{\vec{K}} f_0 = \frac{\partial f_0}{\partial \varepsilon_{\vec{K}}}.\frac{\partial \varepsilon_{\vec{K}}}{\partial \vec{K}} = \frac{\partial f_0}{\partial \varepsilon_{\vec{K}}}.\hbar\vec{v}_{\vec{K}} \quad \text{(II-99)}$$

The linearized Boltzmann transport equation as a function of energy band $\varepsilon_{\vec{K}}$ and group velocity $\vec{v}_{\vec{K}}$:

$$= f_{\vec{K}} \approx f_0\left(\varepsilon_{\vec{K}}\right) + e\left(-\frac{\partial f_0}{\partial \varepsilon}\right)\tau_{\vec{K}} v_{\vec{K}}.\vec{E} \quad \text{(II-100)}$$

When $\left|f - f_0\right| \langle\langle f_0$, The approximation performs effectively in weak electric fields.

II.8. 3. Transport coefficients

It is critical to be able to compute the transport parameters of a system in order to understand thermoelectricity. When considering the macroscopic level, the relations between the temperature gradient ∇T and the electric field $\vec{E}$ with their electrical current $\vec{J}$ in an isotropic solid are [167]:

$$\vec{J} = \sigma\vec{E} + S\sigma.\left(-\nabla T\right) \tag{II-101}$$

Where σ is the electrical conductivity, S is the Seebeck coefficient is the voltage difference generated by a temperature gradient in the absence of any electrical current. At this point, for the microscopic model of transport, the electrical current of carriers is generally defined as:

$$\vec{J} = e\sum_{\vec{K}} f_{\vec{K}}\vec{v}_{\vec{K}} \tag{II-102}$$

by substituting equation (II-100) into Equation (II-102) we obtain:

$$\vec{J} = e\sum_{\vec{K}} f_{\vec{K}}\vec{v}_{\vec{K}} = ef_0\left(\varepsilon_{\vec{K}}\right)\sum_{\vec{K}}\vec{v}_{\vec{K}} + e^2\left(-\frac{\partial f_0}{\partial\varepsilon}\right)\tau_{\vec{K}}\vec{v}_{\vec{K}}\vec{v}_{\vec{K}}.\vec{E} \tag{II-103}$$

From the equation (II-101) it is evident that in the absence of a temperature gradient, the macroscopic electrical current is denoted by $\vec{J} = \sigma\vec{E}$, thus [168]:

$$\sigma = e^2\sum_{\vec{K}}\left(-\frac{\partial f_0}{\partial\varepsilon}\right)\tau_{\vec{K}}\vec{v}_{\vec{K}}\vec{v}_{\vec{K}} = \sum_{\vec{K}}\left(-\frac{\partial f_0}{\partial\varepsilon}\right)\sigma\left(\vec{K}\right) \tag{II-104}$$

Where $\sigma\left(\vec{K}\right) = \tau_{\vec{K}}\vec{v}_{\vec{K}}\vec{v}_{\vec{K}}$

The Seebeck coefficient is expressed in the following manner:

$$S = \frac{\sum_{\vec{K}} \left(-\frac{\partial f_0}{\partial E} \right) \tau_{\vec{K}} \vec{v}_{\vec{K}} \vec{v}_{\vec{K}} \left(\varepsilon_{\vec{K}} - \mu \right)}{eT \sum_{\vec{K}} \left(-\frac{\partial f_0}{\partial \varepsilon} \right) \tau_{\vec{K}} \vec{v}_{\vec{K}} \vec{v}_{\vec{K}}} \tag{II-105}$$

The electronic contribution to thermal conductivity can be defined as follows:

$$\kappa_e = \kappa_0 - T\sigma S^2 \tag{II-106}$$

$$\kappa_e = K_B^2 T \sum_{\vec{K}} \left(-\frac{\partial f_0}{\partial E} \right) \tau_{\vec{K}} \vec{v}_{\vec{K}} \vec{v}_{\vec{K}} \left(\frac{\varepsilon_K - \mu}{K_B T} \right)^2 - T\sigma S^2 \tag{II-107}$$

In order to simplify the calculation of the transport coefficients, it is possible to treat the relaxation time as a constant (not depending on K anymore) in BoltzTrap code [169]. This is referred to as the constant relaxation time approximation (CRTA). By substituting the relaxation time $\tau_{\vec{K}}$ (which depends on the direction of the wave vector $\vec{K}$) with τ (which is independent of the direction) in equation (II-104) the electrical conductivity is expressed as:

$$\frac{\sigma}{\tau} = e^2 \sum_{\vec{K}} \left(-\frac{\partial f_0}{\partial \varepsilon} \right) \vec{v}_{\vec{K}} \vec{v}_{\vec{K}} \tag{II-108}$$

S becomes independent of τ and its values agree with many experimental results as long as the relaxation of the carrier (E) does not change significantly over a few KT energy scale [170].

$$S = \frac{\sum_{\vec{K}} \left(-\frac{\partial f_0}{\partial E} \right) \vec{v}_{\vec{K}} \vec{v}_{\vec{K}} \left(\varepsilon_{\vec{K}} - \mu \right)}{eT \sum_{\vec{K}} \left(-\frac{\partial f_0}{\partial \varepsilon} \right) \vec{v}_{\vec{K}} \vec{v}_{\vec{K}}} \tag{II-109}$$

II.8. 4. BoltzTraP code

Boltzmann **Tra**nsport **P**roperties (BoltzTraP**)** [169], is a program designed to calculate the semi-classical transport coefficients of materials based on First Principles electronic band structures. The code utilizes a mesh of energy bands and is interfaced to the WIEN2k, ABINIT, SIESTA, VASP, and QuantumEspresso programs.

In BoltzTraP, transport coefficients such as the Seebeck coefficient, electronic thermal conductivity, and electrical conductivity can be computed by solving the Boltzmann transport equation with assuming that the relaxation time remains constant.

Chapter III

Results and Discussions

III.1. Introduction

Heusler alloys have made a substantial impact on industrial technology since their first discovery in 1903 [171]. This is mainly due to their exceptional performance in the fields of optoelectronics, thermoelectrics, and spintronics.

These alloys are derived from a broader class of compounds known as half-Heusler alloys. These newly developed alloys are ternary intermetallic compounds with a crystal structure that is similar to that of the standard Heusler alloys. The distinguishing feature of double half-Heuslers is their distinct quaternary composition, which is characterized by aliovalent substitution. This is different from the more typical isovalent substitution found in other quaternary configurations. Aliovalent substitution in double half-Heuslers refers to the substitution of specific elements in the crystal lattice with others that have a distinct valence state [85]. The deviation from the typical isovalent substitution is essential for generating unique combinations with balanced valence, resulting in the stabilization of organized ground states. Double half-Heusler compounds are expected to be more stable compared to quaternary structures with isovalent alloying.

The nomenclature for double half-Heuslers is derived from the notion of double perovskites, in which the "double" denotes a doubling of the perovskite formula unit. This nomenclature emphasizes the unique compositional and structural attributes of these materials. The alloys are characterized by the existence of two distinct elements, represented as Y' and Y", in the Y-site of the crystal lattice ($X_2Y'Y''Z_2$). These elements are not isovalent. This configuration creates additional opportunities for enhancing these materials' properties, which makes them interesting options for a various of applications.

Anand et al. introduced the double half-Heusler (DHH), which are distinguished by their structural complexity, resulting in significantly lower κ_L values comparing to ternary half-Heusler. The recently introduced Heusler alloys encompass several chemical formulas, including those of the double quaternary class. ($X'X''Y_2Z_2$, $X_2Y'Y''Z_2$, $X_2Y_2Z'Z''$) [85]. In general, the study of double half-Heusler alloys is a potential field of research for discovering new materials with specific characteristics for various technological uses such as thermoelectric, transparent conducting thin-film and topological band structures [85].

The main objective of this chapter is to analyze the structural properties of the recently developed quaternary double-half Heusler alloys. $ScX'Y_2Sn_2$ (X'=Nb, Ta; Y=Ni, Pd, Pt), including lattice parameter, compressibility modulus, and its derivative. In addition, we investigate the electronic properties of the DHHs, which are band structure and density of states, as well as the optical properties, including the behavior of the material in response to an electric field knows as the dielectric function, optical conductivity, and absorption coefficient. Furthermore, we have conducted a study on the elastic (elastic constant, elastic modulus….) and thermoelectric properties (Seebeck coefficient, ZT….). there have been no reports of any experimental or theoretical studies conducted on our double half Heusler alloys $ScX'Y_2Sn_2$ (X´=Nb, Ta; Y=Ni, Pd, Pt).

Table III.1: The electronic configuration of element atoms in ascending order of orbital energies.

Element	*Symbol*	*Atomic Number*	*Electronic Configuration*	*Reduced electronic configuration*
Scandium	*Sc*	*21*	$1s^2\ 2s^2\ 2p^6 3s^2 3p^6 3d^1 4s^2$	$[Ar]_{18}\ 3d^1 4s^2$
Niobium	*Nb*	*41*	$1s^2\ 2s^2\ 2p^6 3s^2 3p^6 3d^{10} 4s^2 4p^6 4d^4 5s^1$	$[Kr]_{36}\ 4d^4 5s^1$
Nickel	*Ni*	*28*	$1s^2\ 2s^2\ 2p^6 3s^2 3p^6 3d^8 4s^2$	$[Ar]_{18}\ 3d^8 4s^2$
Tantalum	*Ta*	*73*	$1s^2\ 2s^2\ 2p^6 3s^2 3p^6 4s^2 3d^{10} 4p^6 5s^2 4d^{10} 5p^6 6s^2 4f^{14} 5d^3$	$[Xe]\ 4f^{14} 5d^3 6s^2$
Tin	*Sn*	*50*	$1s^2 2s^2 2p^6 3s^2 3p^6 4s^2 3d^{10} 4p^6 5s^2 4d^{10} 5p^2$	$[Kr]_{18}\ 4d^{10} 5s^2 5p^2$
Palladium	*Pd*	*46*	$1s^2 2s^2 2p^6 3s^2 3p^6 4s^2 4p^6 3d^{10} 5s^2 5p^6 4d^2$	$[Kr]_{36}\ 4d^2 5s^2 5p^6$
Platinum	*Pt*	*78*	$1s^2 2s^2 2p^6 3s^2 3p^6 4s^2 3d^{10} 4p^6 5s^2 4d^{10} 5p^6 6s^1 4f^{14} 5d^9$	$[Xe]\ 4f^{14} 5d^9 6s^1$

III.2. Computational details

The current calculations are conducted utilizing the full-potential linearized augmented plane wave (FP-LAPW) approach, which has been incorporated in the WIEN2K code [143]. Within essentially the frame work of the DFT. Two different approaches were approximated in order to perform the computation of exchange and correlation potential.

The Generalized Gradient Approximation (GGA), parameterized by Perdew, Burke, and Ernzerhof [132] and the local density approximation (LDA), parameterized by Perdew and Wang [131]. In order to enhance the energy band gaps and further investigate the electronic properties of our findings:

- L'approximation mBJ (modified Becke-Johnson) [140].
- L'approximation d'Engel-Vosko (EV-GGA) [144].

The FP-LAPW method pertains to dividing of each unit cell into distinct muffin-tin (MT) spheres with non-overlapping boundaries, characterized by radii denoted as R_{MT} and an interstitial zone situated between the spheres. The Kohn and Sham wave functions are formulated using spherical harmonics within the muffin-tin spheres, with a maximum value of $\ell_{\max} = 10$. In the interstitial area, these wave functions are expressed as Fourier series and expanded into plane waves, with a cutoff RMT=9.Therefore, the value of R_{MT} is determined by the shortest radius of muffin-tin spheres and K_{max} represents the maximum wave vector employed in the construction of plane wave eigenfunctions. self-consistent calculations are considered to have converged when the total energy remains constant. The IRelast package tool, which was made by Jamal et al, was used to study the elastic properties [172]. The Boltz-Trap code was used to compute the transport coefficients, based on Boltzmann's semi-classical transport theory [169]. Considering that the relaxing time remains relatively constant over the energy scale of a few $K_B T$, $\tau \sim 3.1\times10^{-14} s$ this value was determined using the mathematical formula derived by Mili et al [173].

Table III.2: Values of R_{MT}, $R_{MT}.K_{max}$ and K-Points of double half Heusler alloys $ScX'Y_2Sn_2$ (X´=Nb, Ta; Y=Ni, Pd, Pt).

Alloys	*Atom*	R_{MT} *(a.u.)*	$R_{MT}.K_{max}$	*K-Points*
$ScNbNi_2Sn_2$	**Sc**	2.42	9	1000
	Nb	2.28		
	Ni1	2.39		
	Ni2	2.39		
	Sn1	2.41		
	Sn2	2.41		
$ScTaPd_2Sn_2$	**Sc**	2.37	9	1000
	Ta	2.31		
	Pd1	2.31		
	Pd2	2.31		
	Sn1	2.36		
	Sn2	2.36		
$ScTaPt_2Sn_2$	**Sc**	2.34	9	800
	Ta	2.26		
	Pt1	2.37		
	Pt2	2.37		
	Sn1	2.34		
	Sn2	2.34		

III.2.1. Convergence tests of $R_{MT}.K_{max}$ and K-Points

In the context of electronic structure computations, namely within the framework of density functional theory (DFT) or other quantum mechanical approaches, it is necessary to conduct convergence tests to optimize the input parameters in terms of both time and accuracy. The parameters that require testing mostly include: K-points and $R_{MT}.K_{max}$. therefore, achieving convergence in findings is of utmost importance when considering the selection of K-points and $R_{MT}.K_{max}$.

The convergence of DHH alloys was investigated in this study using the GGA approximation. The determination of the optimal value for the cutoff parameter $R_{MT}.K_{max}$ was achieved by implementing the subsequent steps. Initially, the total energy of the crystal cell was computed for various values of $R_{MT}.K_{max}$, ranging from 7 to 9. Subsequently, the resulting data was utilized to generate a graphical representation displaying the relationship between the total energy and the

$R_{MT}.K_{max}$ values, as illustrated in Figure.III.1 Based on the presented data, it is evident that the overall energy of the $ScNbNi_2Sn_2$, $ScTaPd_2Sn_2$ and $ScTaPt_2Sn_2$ alloys exhibits a significant drop as the $R_{MT}.K_{max}$ value increases. This decrease in energy is observed when the total energy converges towards its minimum value from the value of $R_{MT}.Kmax=9$ for all DHHs alloys. Similarly, we conducted an analysis to determine the convergence of the optimal number of K-points within a range of 500 to 1000, with an increment of 100. Figure.III.2 illustrates the relationship between the total energy and the number of K-points. Based on the analysis of these curves, it can be observed that the total energy begins to converge when the number of K-points reaches 1000 for $ScNbNi_2Sn_2$ and $ScTaPd_2Sn_2$ while the value 800 is for $ScTaPt_2Sn_2$.

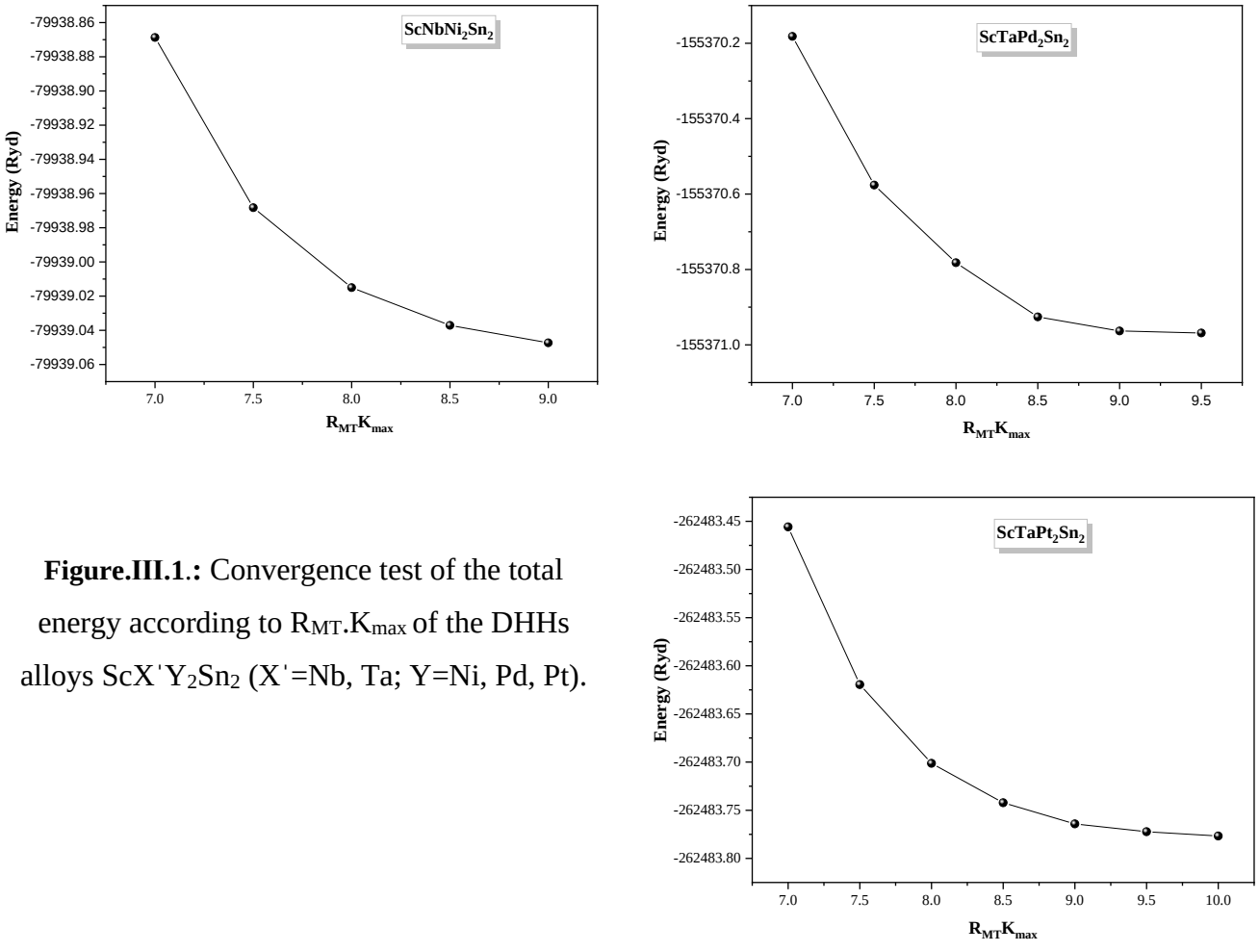

Figure.III.1.: Convergence test of the total energy according to $R_{MT}.K_{max}$ of the DHHs alloys $ScX'Y_2Sn_2$ (X'=Nb, Ta; Y=Ni, Pd, Pt).

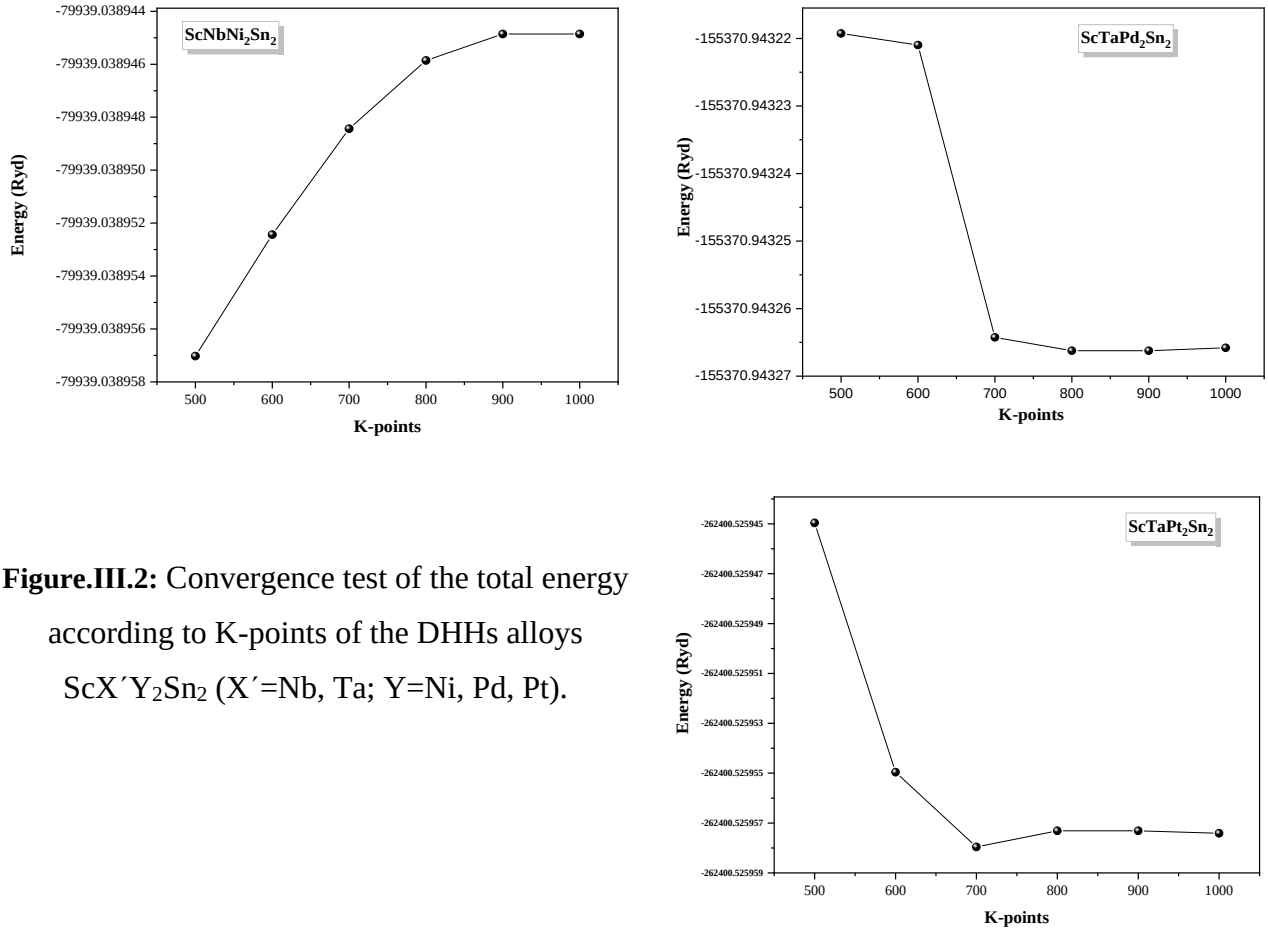

Figure.III.2: Convergence test of the total energy according to K-points of the DHHs alloys $ScX'Y_2Sn_2$ (X′=Nb, Ta; Y=Ni, Pd, Pt).

III.3. Structural properties

III.3. 1. Crystal structure stability

The initial crucial step in an ab-initio calculation involves determining the structural parameters of the material under investigation such as the lattice constants, interatomic distance and bulk modulus. Having these informations allows us to obtain access to additional physical properties such as electronic, optical, and other properties.

The alloys $ScNbNi_2Sn_2$, $ScTaPd_2Sn_2$ and $ScTaPt_2Sn_2$ are half-Heusler-derived structured and crystallize in the simple orthorhombic with the space group *Pmn2₁* (N°31), which can be considered as a combine of 17-electron ScNiSn and 19-electron NbNiSn for $ScNbNi_2Sn_2$, 17-electron ScPdSn and TaPdSn 19-electron for $ScTaPd_2Sn_2$ and ScPtSn and TaPtSn 19-electron for $ScTaPt_2Sn_2$. the crystal structures of the double half Heusler are depicted in Figure.III.4, These sort of double half-Heusler structures is defined by the addition of two half-Heusler-structured

alloys with a unique crystal arrangement based on aliovalent substitution. The general formula $XX'Y_2Z_2$ represents the double half Heusler alloys $ScNbNi_2Sn_2$, $ScTaPd_2Sn_2$, and $ScTaPt_2Sn_2$ where X and Y are transition metals and Z the main group element (see figure.III.3). These alloys typically have a valence electron count of 18. The occupation sites X are identical, resulting in a net valence (NV) of zero. The explicit NV electrons for the $ScNbNi_2Sn_2$, $ScTaPd_2Sn_2$ and $ScTaPt_2Sn_2$ unit cells are:

$$NV = 3\left(0.5Sc^{+3}s^0d^0\right)+5\left(0.5Nb^{+5}s^0d^0\right)-0\left(Ni^0d^{10}\right)-4\left(Sn^{-4}s^2p^6\right)=0$$

$$NV = 3\left(0.5Sc^{+3}s^0d^0\right)+5\left(0.5Ta^{+5}s^0d^0\right)-0\left(Pd^0d^{10}\right)-4\left(Sn^{-4}s^2p^6\right)=0$$

$$NV = 3\left(0.5Sc^{+3}s^0d^0\right)+5\left(0.5Ta^{+5}s^0d^0\right)-0\left(Pt^0d^{10}\right)-4\left(Sn^{-4}s^2p^6\right)=0$$

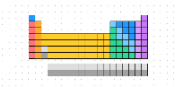

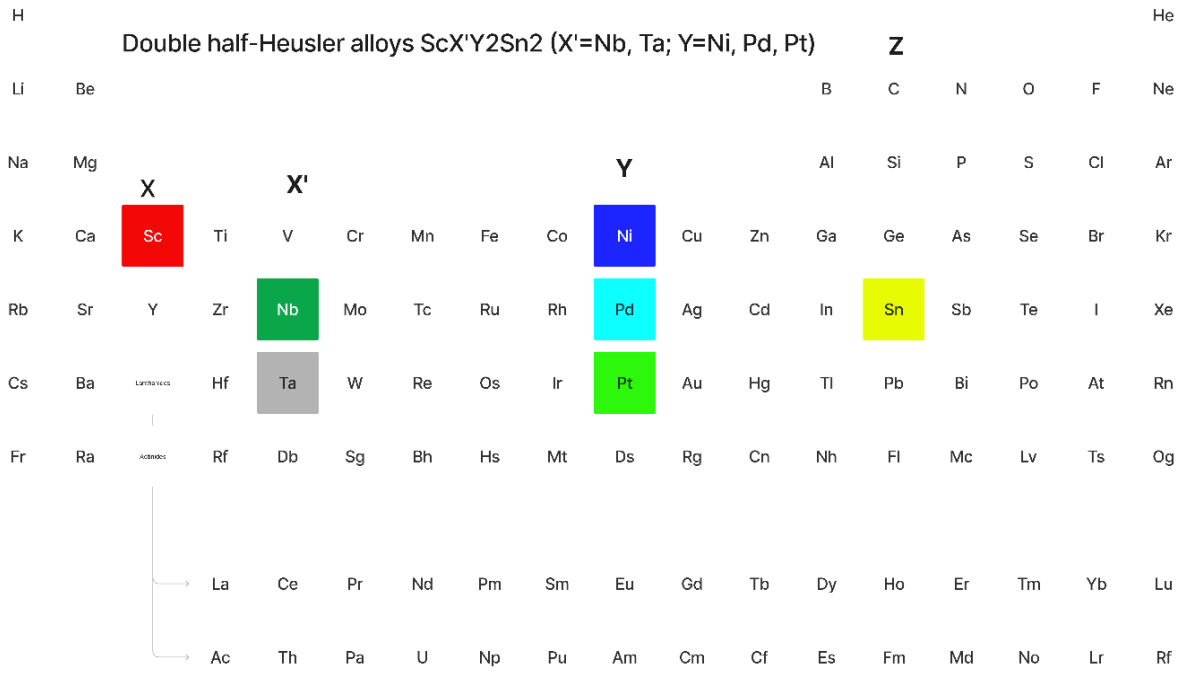

Figure.III.3: Selected elements from the periodic table for the studied DHH alloys $XX'Y_2Z_2$ materials in this dissertation based on the color plan.

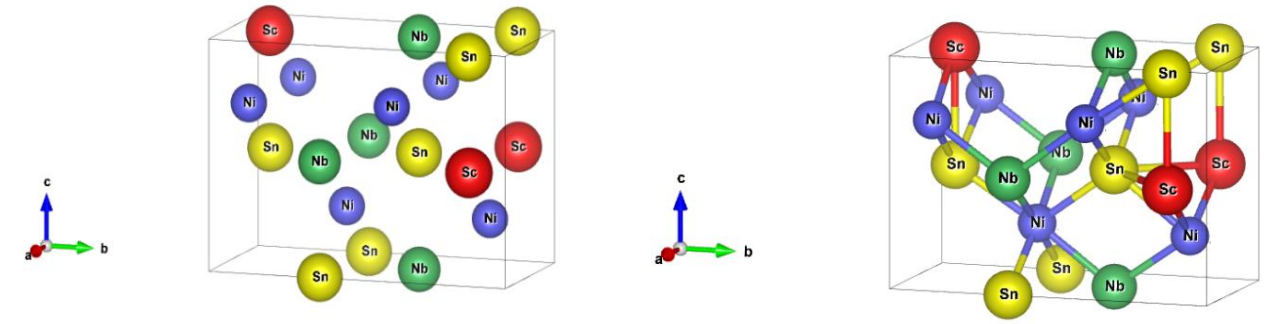

(a)

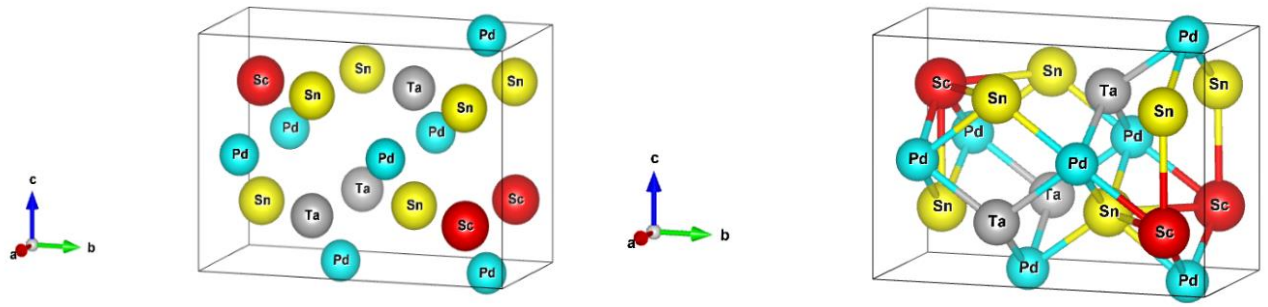

(b)

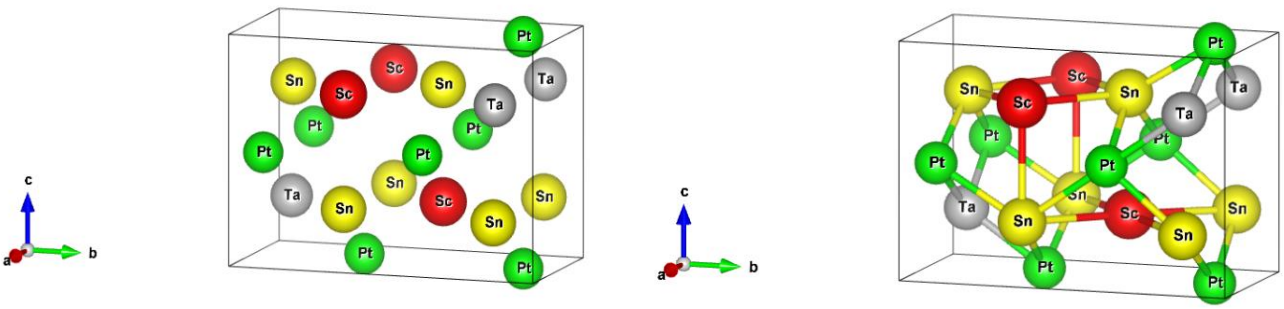

(c)

Figure.4: Crystal structure of double half-Heusler compounds (a) $ScNbNi_2Sn_2$ (b) $ScTaPd_2Sn_2$ (c) $ScTaPt_2Sn_2$ according to (111) direction.

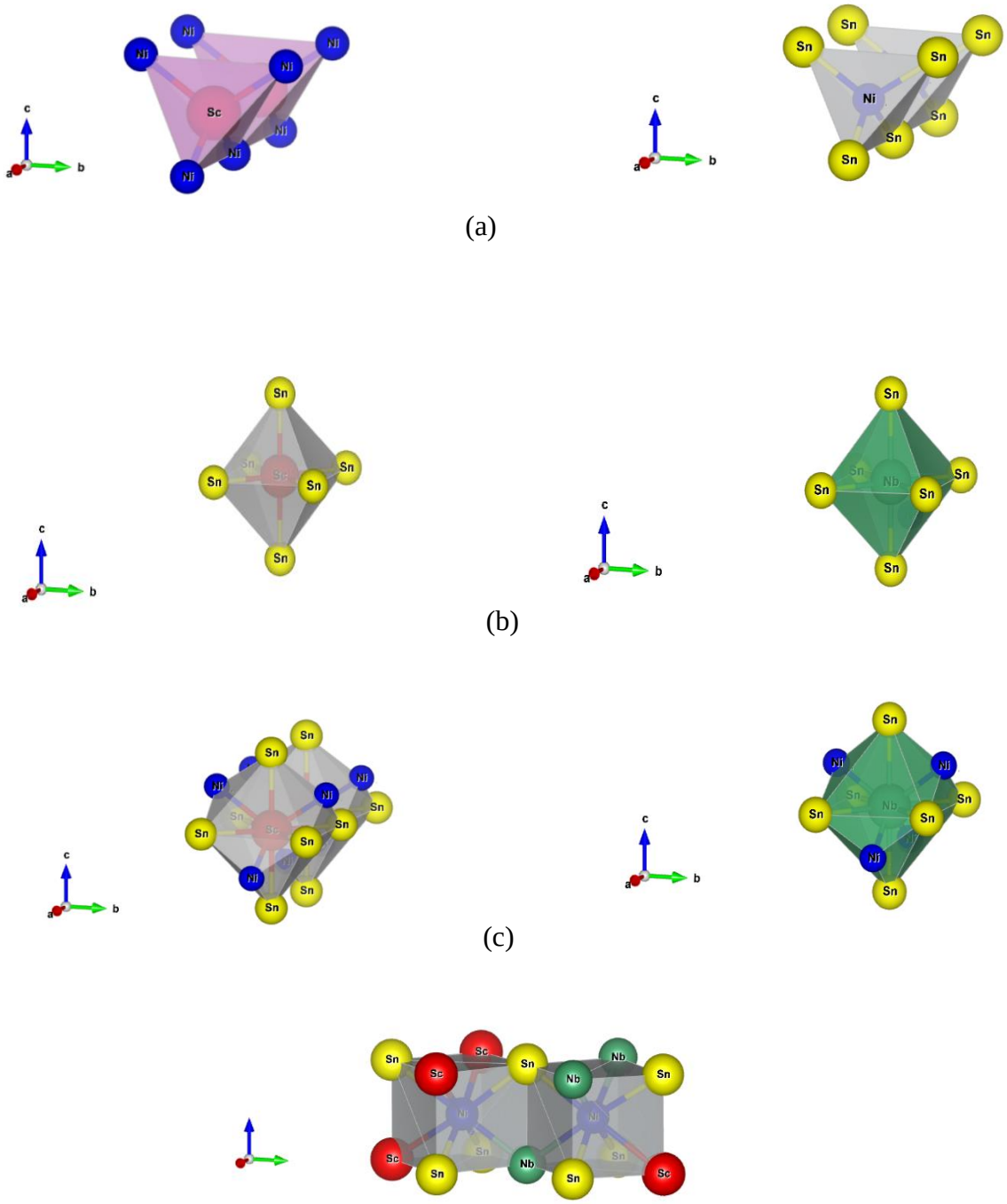

Figure.III.5: (a) Tetrahedral configuration YZ_4, XY_4, (b) Octahedral $X'Z_6$, XZ_6, (c) Bicapped square prism XY_4Z_6, $X'Y_4Z_6$, (d) Cube YXX'_3Z_3, $YX_3X'Z_3$ according to the direction (111) of DHH $ScNbNi_2Sn_2$.

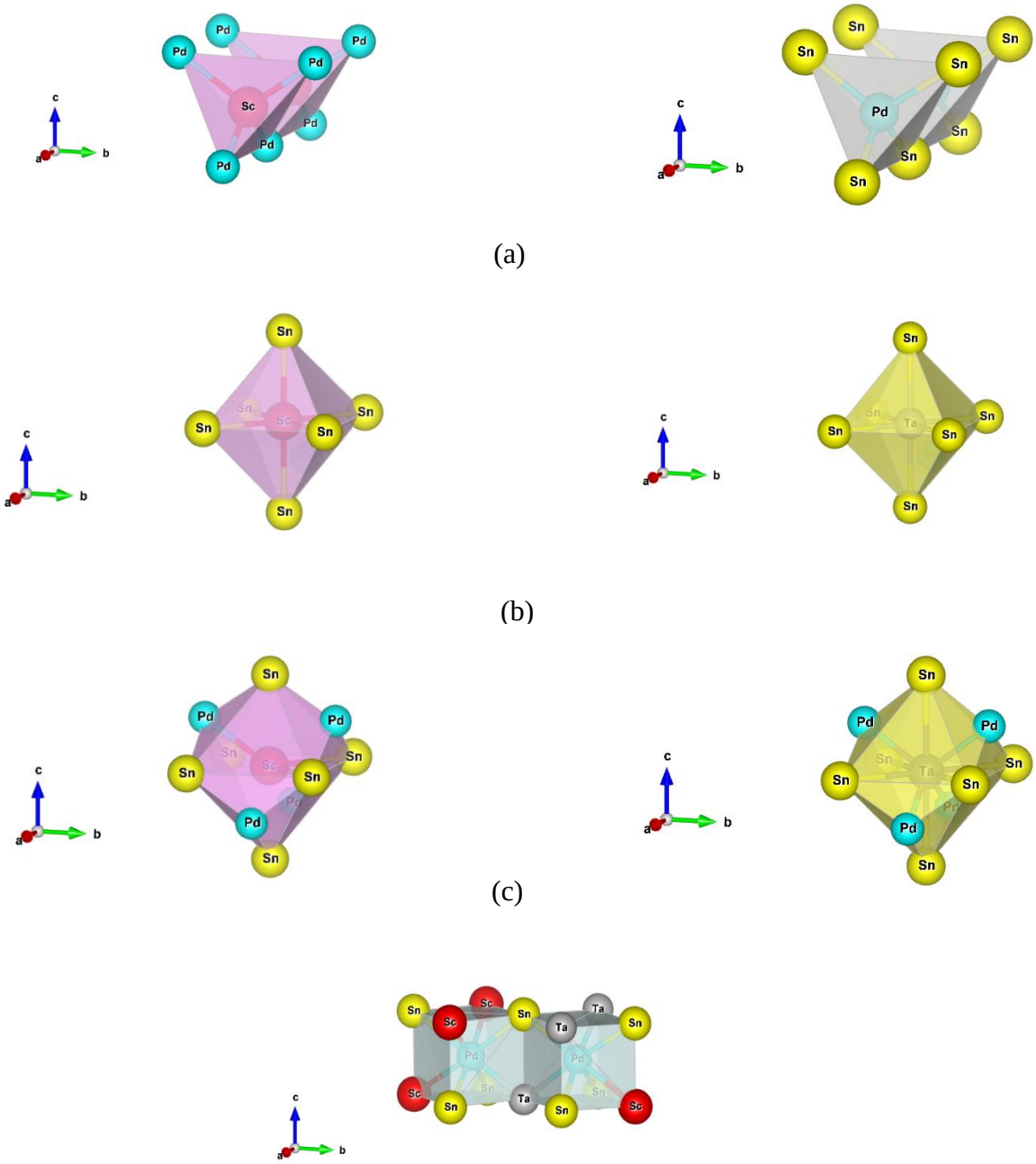

Figure.III.6: (a) Tetrahedral configuration YZ_4, XY_4, (b) Octahedral $X'Z_6$, XZ_6, (c) Bicapped square prism XY_4Z_6, $X'Y_4Z_6$, (d) Cube YXX'_3Z_3, $YX_3X'Z_3$ according to the direction (111) of DHH $ScTaPd_2Sn_2$.

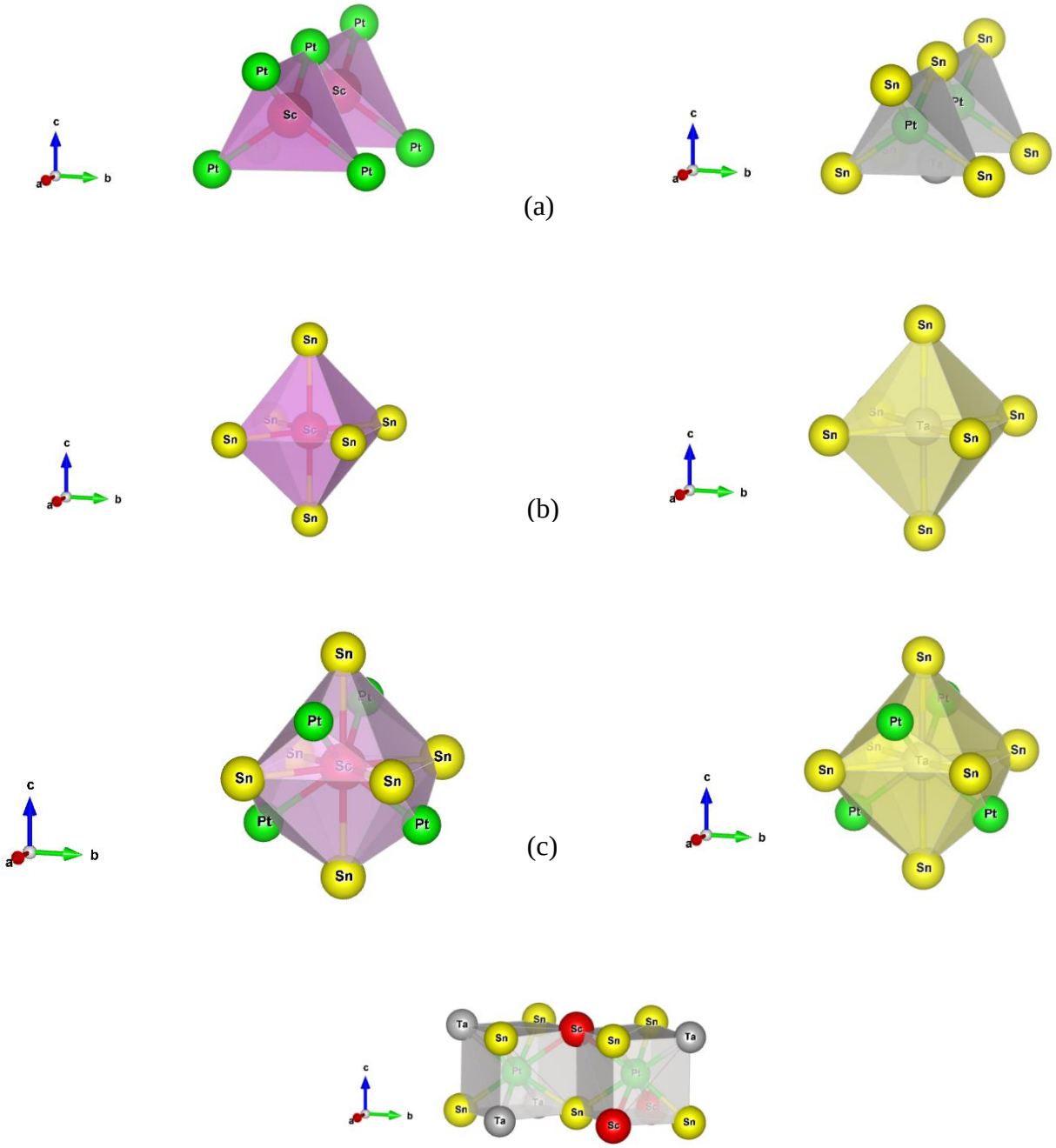

Figure.III.7: (a) Tetrahedral configuration YZ_4, XY_4, (b) Octahedral $X'Z_6$, XZ_6, (c) Bicapped square prism XY_4Z_6, $X'Y_4Z_6$, (d) Cube YXX'_3Z_3, $YX_3X'Z_3$ according to the direction (111) of DHH $ScTaPt_2Sn_2$.

Table III.3: Atomic positions of the DHH alloys $ScX'Y_2Sn_2$ (X'=Nb, Ta; Y=Ni, Pd, Pt) with GGA and LDA approximations.

Alloys		***Atomic Positions***					
		GGA			***LDA***		
		x	***Y***	***z***	***x***	***y***	***z***
$ScNbNi_2Sn_2$ (31_Pmn21)	***Sc***	0.50000000	0.12255800	0.98976200	0.50000000	0.12255800	0.98976200
		0.00000000	0.87744200	0.48976200	0.00000000	0.87744200	0.48976200
	Nb	0.00000000	0.37347500	0.50000000	0.00000000	0.37347500	0.50000000
		0.50000000	0.62652500	0.00000000	0.50000000	0.62652500	0.00000000
	Ni1	0.00000000	0.13507300	0.73516800	0.00000000	0.13507300	0.73516800
		0.50000000	0.86492700	0.23516800	0.50000000	0.86492700	0.23516800
	Ni2	0.00000000	0.61712200	0.75465800	0.00000000	0.61712200	0.75465800
		0.50000000	0.38287800	0.25465800	0.50000000	0.38287800	0.25465800
	Sn1	0.50000000	0.62574100	0.50200300	0.50000000	0.62574100	0.50200300
		0.00000000	0.37425900	0.00200300	0.00000000	0.37425900	0.00200300
	Sn2	0.00000000	0.87545300	0.98729500	0.00000000	0.87545300	0.98729500
		0.50000000	0.12454700	0.48729500	0.50000000	0.12454700	0.48729500
$ScTaPd_2Sn_2$ (31_Pmn21)	***Sc***	0.50000000	0.12166132	0.75504239	0.50000000	0.12129255	0.75527526
		0.00000000	0.87833868	0.25594239	0.00000000	0.87870745	0.25527526
	Ta	0.00000000	0.37356296	0.26112829	0.00000000	0.37445311	0.26257249
		0.50000000	0.62643704	0.76112829	0.50000000	0.62554689	0.76257249
	Sn1	0.50000000	0.62678591	0.26624628	0.50000000	0.62686446	0.26909440
		0.00000000	0.37321409	0.76624628	0.00000000	0.37313554	0.76909440
	Sn2	0.00000000	0.87488038	0.75024701	0.00000000	0.87420593	0.75042107
		0.50000000	0.12511962	0.25024701	0.50000000	0.12579407	0.25042107
	Pd1	0.00000000	0.13462731	0.50000000	0.00000000	0.13596442	0.50000000
		0.50000000	0.86537269	0.00000000	0.50000000	0.86403558	0.00000000
	Pd2	0.00000000	0.61538705	0.51745290	0.00000000	0.61449293	0.51972493
		0.50000000	0.38461295	0.01745290	0.50000000	0.38550707	0.01972493

$ScTaPt_2Sn_2$ (31_Pmn21)	Sc	0.50000000	0.62243198	0.26900163	0.50000000	0.62236016	0.26911455
		0.00000000	0.37756802	0.76900163	0.00000000	0.37763984	0.76911455
	Ta	0.00000000	0.87556905	0.75938957	0.00000000	0.87562822	0.75976681
		0.50000000	0.12443095	0.25938957	0.50000000	0.12437178	0.25976681
	Sn1	0.00000000	0.37796990	0.27383598	0.00000000	0.37790028	0.27382003
		0.50000000	0.62203010	0.77383598	0.50000000	0.62209972	0.77382003
	Sn2	0.50000000	0.13007003	0.75178726	0.50000000	0.12995092	0.75227878
		0.00000000	0.86992997	0.25178726	0.00000000	0.87004908	0.25227878
	Pt1	0.00000000	0.11402053	0.50000000	0.00000000	0.11383886	0.50000000
		0.50000000	0.88597947	0.00000000	0.50000000	0.88616114	0.00000000
	Pt2	0.00000000	0.63662292	0.52598238	0.00000000	0.63694832	0.52667802
		0.50000000	0.36337708	0.02508238	0.50000000	0.36305168	0.02667802

In order to determine the equilibrium parameters, specifically the lattice parameter a_0, compressibility modulus B, and its derivative B', the total energy was computed as a function of volume. Subsequently, the resulting curve was interpolated using the Murnaghan equation of state [174]:

$$E(V) = E_0 + \frac{B}{B'(B'+1)}\left[V\left(\frac{V_0}{V}\right)^{B'} - V_0\right] + \frac{B}{B'}(V - V_0) \quad \text{(III-1)}$$

Where E_0, V_0, B_0 and B' are respectively: total energy, equilibrium volume, modulus of compressibility and its derivative. The modulus of compressibility is given by:

$$B_0 = -V\left(\frac{\partial P}{\partial V}\right)_T \quad \text{(III-2)}$$

$$P = -\left(\frac{\partial E}{\partial V}\right)_S \quad \text{(III-3)}$$

$$B_0 = V\frac{\partial^2 E}{\partial V^2} \quad \text{(III-4)}$$

The equilibrium volume is determined by the minimum of the curve $E(V)$.

In the present investigation, we conducted force optimization to fully relax the atomic structures of the DHH alloys at various volumes. This allowed us to achieve the totally stable geometric structures of the alloys. The atomic positions of the double half Heusler $ScX'Y_2Sn_2$ (X'=Nb, Ta; Y=Ni, Pd, Pt) using LDA and GGA approximations are given in Table.III.3.

In order to study the magnetic stability of these alloys, we computed the total energy for ferromagnetic (FM) and non-magnetic (PM) magnetic states for double Heusler alloys $ScX'Y_2Sn_2$ (X'=Nb, Ta; Y=Ni, Pd, Pt) using the LDA and GGA approximations. The following Figure.III.8 depicts the variation in total energy as a function of volume for the DHH alloys, clearly show that the non-magnetic (PM) state is the most stable state for the three DHH alloys.

To precisely explain the structural properties of our DHH alloys $ScX'Y_2Sn_2$ (X'=Nb, Ta; Y=Ni, Pd, Pt) we optimized a computation using two different approximations GGA and LDA indicates that the GGA approximation with the non-magnetic state yields the lowest energy, as shown in Figure.III.9. Therefore, it can be inferred that the GGA approximation is the most suitable for describing the structural properties. Consequently, the GGA and EV-GGA approximations results will be prevailing in the subsequent subsections.

Table III.4 shows the optimized results for the lattice parameter a, b and c bulk modulus B (GPa), and its first derivative B'. To precisely explain the structural properties of our DHH alloys, we optimized a computation using two different approximations GGA and LDA. Unfortunately, there are no other theoretical or empirical data to compare.

Based on the current findings shown in Table III.5, the calculated optimized b/a and c/a ratios were 2.0074,1.4188 for $ScTaPd_2Sn_2$ 2.002, 1.4161 for $ScTaPt_2Sn_2$ and 2.0074/2.0073,1.4167/1.4169 for $ScNbNi_2Sn_2$ within the LDA and GGA, respectively. These values indicate a slight distortion of all alloys. With regard to the modulus of compressibility from Table III.6, for both approximations GGA and LDA, it can be noted that $ScNbNi_2Sn_2$ and $ScTaPd_2Sn_2$ are more compressible than $ScTaPt_2Sn_2$ as the value of B is greater for $ScTaPt_2Sn_2$ alloy, as well as the compressibility derivative for $ScTaPt_2Sn_2$ is higher than those $ScNbNi_2Sn_2$ and $ScTaPd_2Sn_2$ alloys.

The interatomic distances were analyzed using both GGA and LDA approximations, and the results are presented in Table III.7.

Figure.III.16, Figure.III.6 and Figure.III.7 show the tetrahedral configuration YZ_4, XY_4, Octahedral $X'Z_6$, XZ_6, Bicapped square prism XY_4Z_6, $X'Y_4Z_6$, Cube YXX'_3Z_3, $YX_3X'Z_3$ according to the direction (111) of DHH $ScX'Y_2Sn_2$ (X'=Nb, Ta; Y=Ni, Pd, Pt).

For the $ScNbNi_2Sn_2$ alloy, as shown in Figure.III.17, Sc is bonded in a 10-coordinate geometry to four Ni and six Sn atoms. There are three shorter (2.646 Å) and one longer (2.758 Å) Sc–Ni bond length. There are three shorter (3.0231 Å) and three longer (3.049 Å) Sc–Sn bond lengths. Nb is bonded to four Ni and six Sn atoms to form distorted face-sharing $NbNi_4Sn_6$ tetrahedra. There is one shorter (2.5005 Å) and three longer (2.6125 Å) Nb–Ni bond lengths (see Table 1). There are three shorter (3.0259 Å) and three longer (3.05024 Å) Nb–Sn bond lengths. There are two inequivalent Ni sites. In the first Ni site, Ni is bonded in a body-centered cubic geometry to one Sc, three equivalent Nb, and four Sn atoms. There is one shorter (2.55 Å) and three longer (2.65 Å) Ni–Sn bond lengths. In the second Ni site, Ni is bonded in a body-centered cubic geometry to three equivalent Sc, one Nb, and four Sn atoms. There are three shorter (2.60 Å) and one longer (2.72 Å) Ni–Sn bond length. There are two inequivalent Sn sites. In the first Sn site, Sn is bonded in a 10-coordinate geometry to three equivalent Sc, three equivalent Nb, and four Ni atoms. In the second Sn site, Sn is bonded in a 10-coordinate geometry to three equivalent Sc, three equivalent Nb, and four Ni atoms.

For the $ScTaPd_2Sn_2$ alloy, according to Figure.III.6, Sc is bonded in a 10-coordinate geometry. Sc is attached to four Pd and six Sn atoms to form distorted face -sharing $ScPd_4Sn_6$ tetrahedra Sc-Pd lengths chemical bonds are divided into tree shorter (2.72001Å) and one longer (2.84417Å). Three shorter (3.09396Å) and three longer (3.12966Å) bond lengths of Sc–Sn, furthermore we delete the Sc-Pd bond we get octahedral site $ScSn_6$ .to form the distorted face sharing $TaPd_4Sn_6$ tetrahedra Ta is bonded to four Pd and six Sn atoms, four Ta-Pd lengths chemical bonds one is shorter (2.58594Å) and three longer (2.67836Å) (see Table 1). Four Ta-Sn bond lengths three are shorter (3.11014Å) and three longer (3.13954Å) Nb–Sn. Two incompatible Pd sites which shape a body centered cubic geometry to each Sc, Ta, Sn. In the first Pd site, Pd is bonded to one Sc, three equivalent Ta, and four Sn atoms. Four Pd-Sn bonds one is shorter (2.64530 Å) and three longer (2.70 Å). In terms of the second Pd site, we note that Pd is bonded to three Sc, one Ta, and four

Sn atoms. Four Pd-Sn bonds, three are shorter (2.69Å) and one longer (2.77 Å). for the Tin atom has two distinct sites. In the first Sn site, Sn is connected in 10 coordinates to three equivalent Sc, three equivalent Ta, and four Pd atoms. For the second Sn atom, Sn has 10-coordinate 3 Sc, 3 Ta, and 4 Pd atoms.

As an example, considering the interatomic distance Sc-Sn1 3.12Å (3.1Å) in $ScTaPd_2Sn_2$ which indicates quite similarities to $ScNbNi_2Sn_2$ and $ScTaPt_2Sn_2$ using GGA and LDA, respectively (see Table III.8.). the interatomic distance Sn-Pd1/ Sn-Pd2 bonds 2.69/2.7 Å in $ScTaPd_2Sn_2$ is slightly same bond lengths in $ScTaPt_2Sn_2$ 2.72/2.70 Å in the GGA approximation.

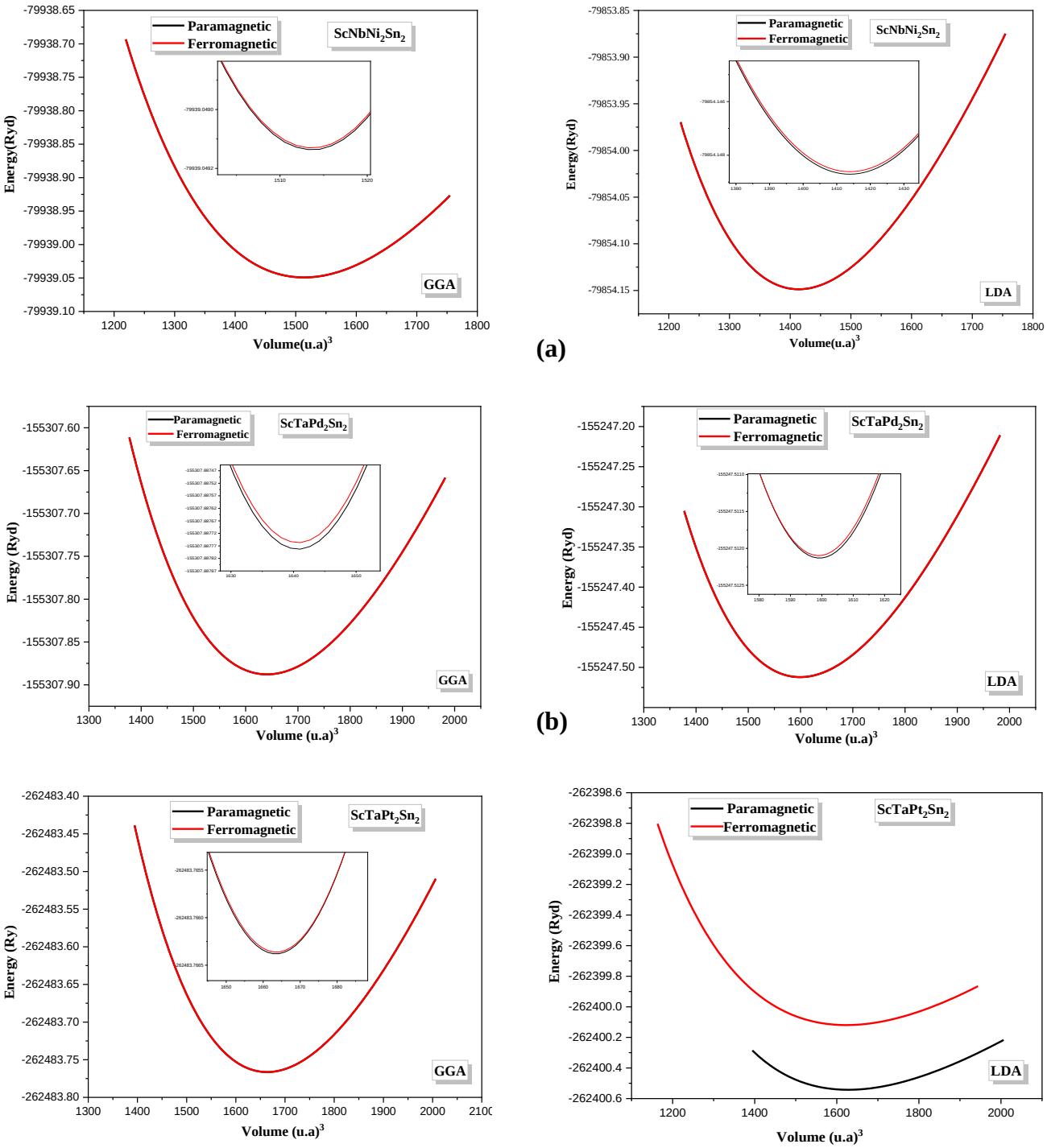

Figure.III.8: Variation of energy as a function of volume for the paramagnetic and ferromagnetic states of the double half-Heusler alloys (a) $ScNbNi_2Sn_2$, (b) $ScTaPd_2Sn_2$ and (c) $ScTaPt_2Sn_2$ using two approximations GGA and LDA.

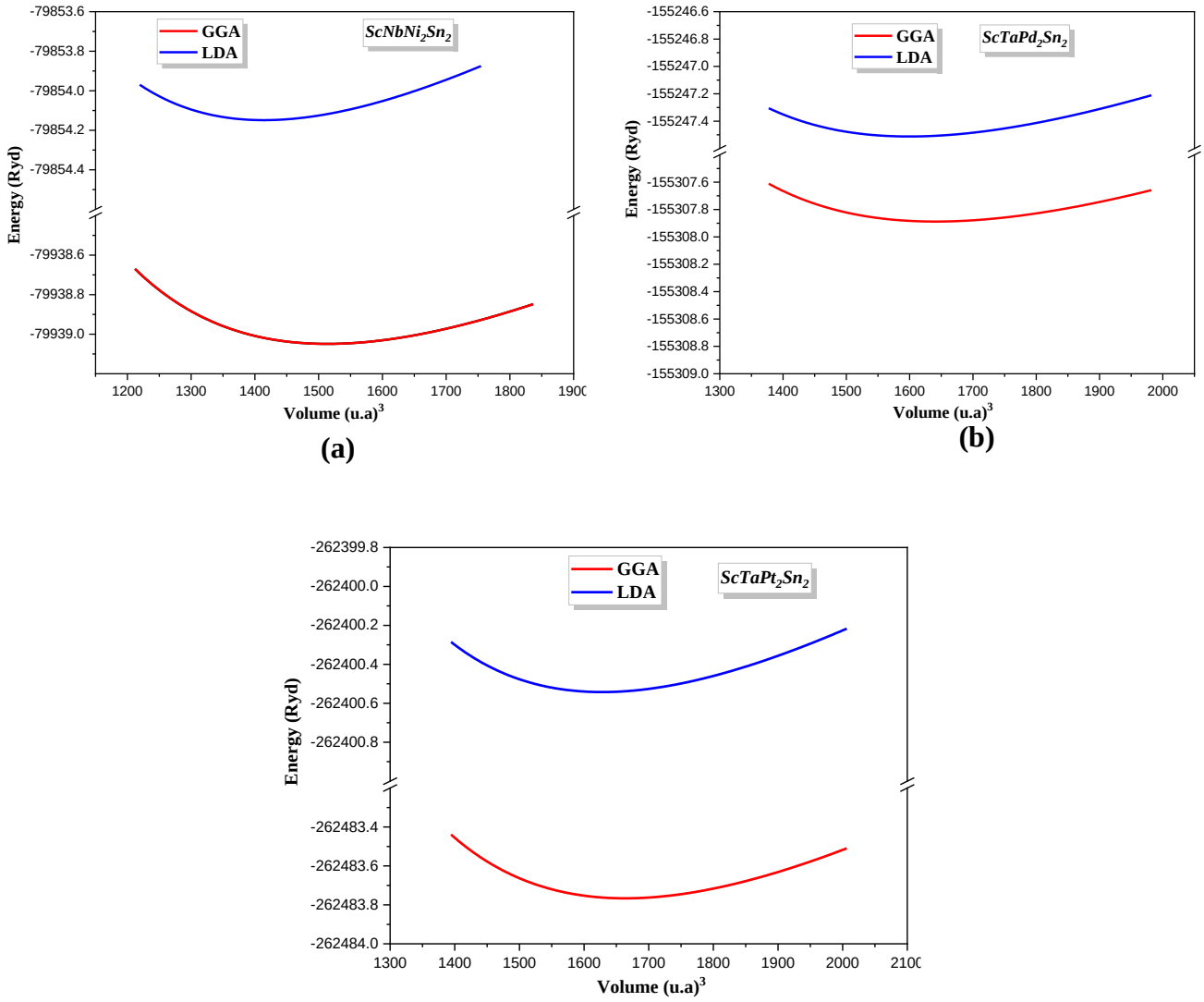

Figure.III.9: Variation of energy as a function of volume using two approximations GGA and LDA for the double half-Heusler compounds (a) $ScNbNi_2Sn_2$, (b) $ScTaPd_2Sn_2$ and (c) $ScTaPt_2Sn_2$.

Table III.4: Calculated structural parameters lattice (Å), bulk modulus B (GPa) and its first derivative B′, energy (Ryd), magnetic moment (μ_B) for DHH compounds (a) $ScNbNi_2Sn_2$, (b) $ScTaPd_2Sn_2$ and (c) $ScTaPt_2Sn_2$ using GGA and LDA approximations.

(a) $ScNbNi_2Sn_2$

Alloy	***approximation***	***Physical parameters***	***Paramagnetic***	***Ferromagnetic***
$ScNbNi_2Sn_2$	***GGA***	*a (Å)*	4.2873	4.2789
		b	8.6064	8.5895
		c	6.0740	6.0632
		b/a	2.0074	2.0074
		c/a	1.4167	1.4169
		B (GPa)	120.81	121.10
		B`	4.53	4.45
		E_{min} *(Ryd)*	− 79939.0489	-79938.9406
		M_{Tot} (μ_B)	-	-0.00034
	LDA	*a (Å)*	4.1912	4.1912
		b	8.4133	8.4135
		c	5.9389	5.9389
		b/a	2.0073	2.0074
		c/a	1.4169	1.4169
		B (GPa)	146.09	145.95
		B`	4.83	4.81
		E_{min} *(Ryd)*	− 79854.1487	-79854.1486
		M_{Tot} (μ_B)	-	0.00059

(b) $ScTaPd_2Sn_2$

Alloy	***approximation***	***Physical parameters***	***Paramagnetic***	***Ferromagnetic***
$ScTaPd_2Sn_2$ 31_Pmn21	***GGA***	*a (Å)*	4.4029	4.4029
		b	8.8386	8.8385
		c	6.2475	6.2475
		b/a	2.0074	2.0074
		c/a	1.4188	1.4188
		B (GPa)	135.0660	134.9908
		B`	4.8254	4.8345
		Emin (Ryd)	-155307.887786	-155307.887760
		M_{Tot} (μB)	-	-0.00054
	LDA	*a (Å)*	4.3655	4.3652
		b	8.7636	8.7630
		c	6.1945	6.1941
		b/a	2.0074	2.0074
		c/a	1.4188	1.4188
		B (GPa)	145.0508	145.2783
		B`	4.9720	5.0226
		E_{min} *(Ryd)*	-155247.512131	-155247.512098
		M_{Tot} (μ_B)	-	-0.00034

(c) *$ScTaPt_2Sn_2$*

Alloy	***approximation***	***Physical parameters***	***Paramagnetic***	***Ferromagnetic***
$ScTaPt_2Sn_2$ 31_Pmn21	***GGA***	*a (Å)*	4.4245	4.4295
		b	8.8617	8.8717
		c	6.2658	6.2729
		b/a	2.0028	2.0028
		c/a	1.4161	1.4161
		B (GPa)	152.8098	152.7055
		B`	5.0062	4.9982
		E_{min} *(Ryd)*	-262483.766381	-262483.766362
		M_{Tot} (μ_B)	-	-0.00033
	LDA	*a (Å)*	4.3975	4.3930
		b	8.8076	8.7986
		c	6.2276	6.2212
		b/a	2.0028	2.0028
		c/a	1.4161	1.4161
		B (GPa)	162.7297	159.0370
		B`	5.0974	4.2615
		E_{min} *(Ryd)*	-262400.542383	-262400.119412
		M_{Tot} (μ_B)	-	0.00139

Table III.5: Interatomic distance of the DHH alloys $ScX'Y_2Sn_2$ (X'=Nb, Ta; Y=Ni, Pd, Pt) using GGA and LDA approximations.

Alloys	***Interatomic distance***	***GGA***	***LDA***
$ScTaPd_2Sn_2$	d_{Sc-Pd1}	2.72001 (x3)	2.69844 (x3)
	d_{Sc-Pd2}	2.84417 (x1)	2.83635 (x1)
	d_{Sc-Sn1}	3.12966 (x3)	3.10531 (x3)
	d_{Sc-Sn2}	3.09396 (x3)	3.06744 (x3)
	d_{Ta-Pd1}	2.58594 (x1)	2.55564 (x1)
	d_{Ta-Pd2}	2.67836 (x3)	2.65271 (x3)
	d_{Ta-Sn1}	3.13954 (x3)	3.10793 (x3)
	d_{Ta-Sn2}	3.11014 (x3)	3.08592 (x3)
	d_{Sn-Pd1}	2.69 (x3); 2.77 (x1)	2.67 (x3); 2.76 (x1)
	d_{Sn-Pd2}	2.70 (x3); 2.64 (x1)	2.68 (x3); 2.61 (x1)
$ScTaSn_2Pt_2$	d_{Sc-Pt1}	2.883 (x1)	2.863 (x1)
	d_{Sc-Pt2}	2.742 (x3)	2.723 (x3)
	d_{Sc-Sn1}	3.099 (x3)	3.077 (x3)
	d_{Sc-Sn2}	3.120 (x3)	3.099 (x3)
	d_{Ta-Pt1}	2.68 (x3)	2.66 (x3)
	d_{Ta-Pt2}	2.576 (x1)	2.55 (x1)
	d_{Ta-Sn1}	3.157 (x3)	3.135 (x3)
	d_{Ta-Sn2}	3.163 (x3)	3.139 (x3)
	d_{Sn-Pt1}	2.72 (x3); 2.66 (x1)	2.70 (x3); 2.64 (x1)
	d_{Sn-Pt2}	2.70 (x3); 2.69 (x1)	2.68 (x1); 2.77 (x1)
$ScNbNi_2Sn_2$	d_{Sc-Ni1}	2.646 (x3)	2.586 (x3)
	d_{Sc-Ni2}	2.758 (x1)	2.697 (x1)
	d_{Sc-Sn1}	3.049 (x3)	2.98 (x3)

	$d_{Sc\text{-}Sn2}$	3.0231 (x3)	2.95 (x3)
	$d_{Nb\text{-}Ni1}$	2.5005 (x1)	2.44 (x1)
	$d_{Nb\text{-}Ni2}$	2.6125 (x3)	2.55 (x3)
	$d_{Nb\text{-}Sn1}$	3.05024 (x3)	2.983(x3)
	$d_{Nb\text{-}Sn2}$	3.0259 (x3)	2.96 (x3)
	$d_{Sn\text{-}Ni1}$	2.63(x3); 2.57(x1)	2.56(x3); 2.64(x1)
	$d_{Sn\text{-}Ni2}$	2.62(x3); 2.70(x1)	2.57(x3); 2.51(x1)

III.4. Electronic properties

The electronic properties of the double half Heusler alloys $ScX'Y_2Sn_2$ (X'=Nb, Ta; Y=Ni, Pd, Pt) were examined in this section. Energy bands in solid-state physics represent the possible energies of an electron as a function of the wave vector k. The electronic properties include band structures, densities of states, and gap energies E_g, all of which are determined by the dispersion equation $E(k)$, which is a critical property in semiconductors.

III.4. 1. Band structure

The band structure of the DHH alloys $ScX'Y_2Sn_2$ (X'=Nb, Ta; Y=Ni, Pd, Pt) was obtained using several approximations such as GGA, LDA, mBJ-GGA, mBJ-LDA and EV-GGA for the equilibrium lattice parameter found in the previous section along the high symmetry points in the first Brillouin zone of the simple orthorhombic structure $(\Gamma - X - S - Y - \Gamma - Z - U - R - T - Z - T - Y - S - R - U - X)$.

The Fermi energy level E_F is represented by a dotted horizontal line. The first Brillouin zone of the orthorhombic structure is shown in Figure III.10. The band structures obtained for every alloy using the GGA, mBJ-GGA, LDA, mBJ-LDA, and EV-GGA approximations have similar appearances behavior, as shown in Figure.III.11.a, Figure.III.11.b and Figure.III.11.c. However, they differ in terms of the energy band gap value, as indicated Table III.6.

Based on the provided Figure.III.18.a, Figure.III.19.b and Figure.III.20.c. it is evident that the double half Heusler alloys $ScX'Y_2Sn_2$ (X'=Nb, Ta; Y=Ni, Pd, Pt) have a bandgap where the minimum of the conduction band (CBM) is at X point, and the maximum of the valence band (VBM) are at another point Y of the first Brillouin Zone, Consequently, the DHH alloys possess an indirect band gap along the direction Y_v-X_c with optimal value of 0.47 eV, 0.549 eV and 0.851 eV for $ScNbNi_2Sn_2$, $ScTaSn_2Pd_2$ and $ScTaPt_2Sn_2$, respectively by EV-GGA approximation which proves that our DHH alloys exhibit semiconductor behavior.

The bandgap values in Table III.6.are provided using various approximations. Unfortunately, no experimental or theoretical results exist to compare our findings.

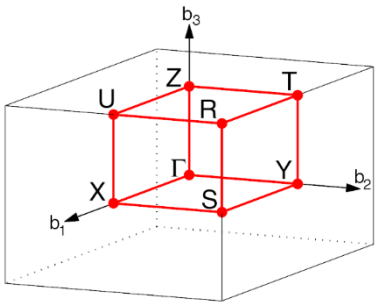

ORC path: Γ-X-S-Y-Γ-Z-U-R-T-Z|Y-T|U-X|S-R

Figure.III.10: First Brillouin zone of simple orthorhombic lattice.

III.4. 2. Densities of states (DOS)

The concept of density of states (DOS) is probably the most crucial in comprehending the physical properties of materials due to the straightforward manner in which intricate electronic structures can be described. The DOS clearly reveals key features that indicate the electrical and optical properties of materials. Thus, to conduct a deeper examination of the electronic structure of the DHH alloys $ScX'Y_2Sn_2$ (X'=Nb, Ta; Y=Ni, Pd, Pt), we provide the total and partial densities of states for these alloys using different approximations (see Figure.III.12.a,b, c, d, e and f).

As shown in the Figure.III.21.a,b, c, d, e and f the density of states for the three DHH alloys $ScX'Y_2Sn_2$ (X'=Nb, Ta; Y=Ni, Pd, Pt) exhibits a considerable degree of similarity, however the distance in the proximity to the Fermi level, which signifies the energy band gap, varies from one approximation to another. Therefore, we will focus our investigation primarily on the $ScNbNi_2Sn_2$ alloy as an illustrative example. As seen in Figure.III.12.a it seems clear that the main contribution occupied by the Ni-d in the energy range of -5.4 eV to 0 eV (E_F) also a few contributions of Nb-d states at the level of the valence band, the other side of the band structure which is the conduction band shows a slight contribution to the Ni -d whereas the Sc/Nb-d appear in strong contribution from the of the energy gap limit (0.47eV) to -6.02 eV. In addition, Sn contributions are negligible in both VB and CB.

It can be noted that the contribution of d orbital of both atoms Ta and Sc is high at the level of conduction band using EV-GGA for $ScTaPd_2Sn_2$ and mBJ-GGA/mBJ-LDA for $ScTaPt_2Sn_2$ whereas it is considerable strong in the rest of all approximation as illustrated in Figure.III.12.c, d, e, f.

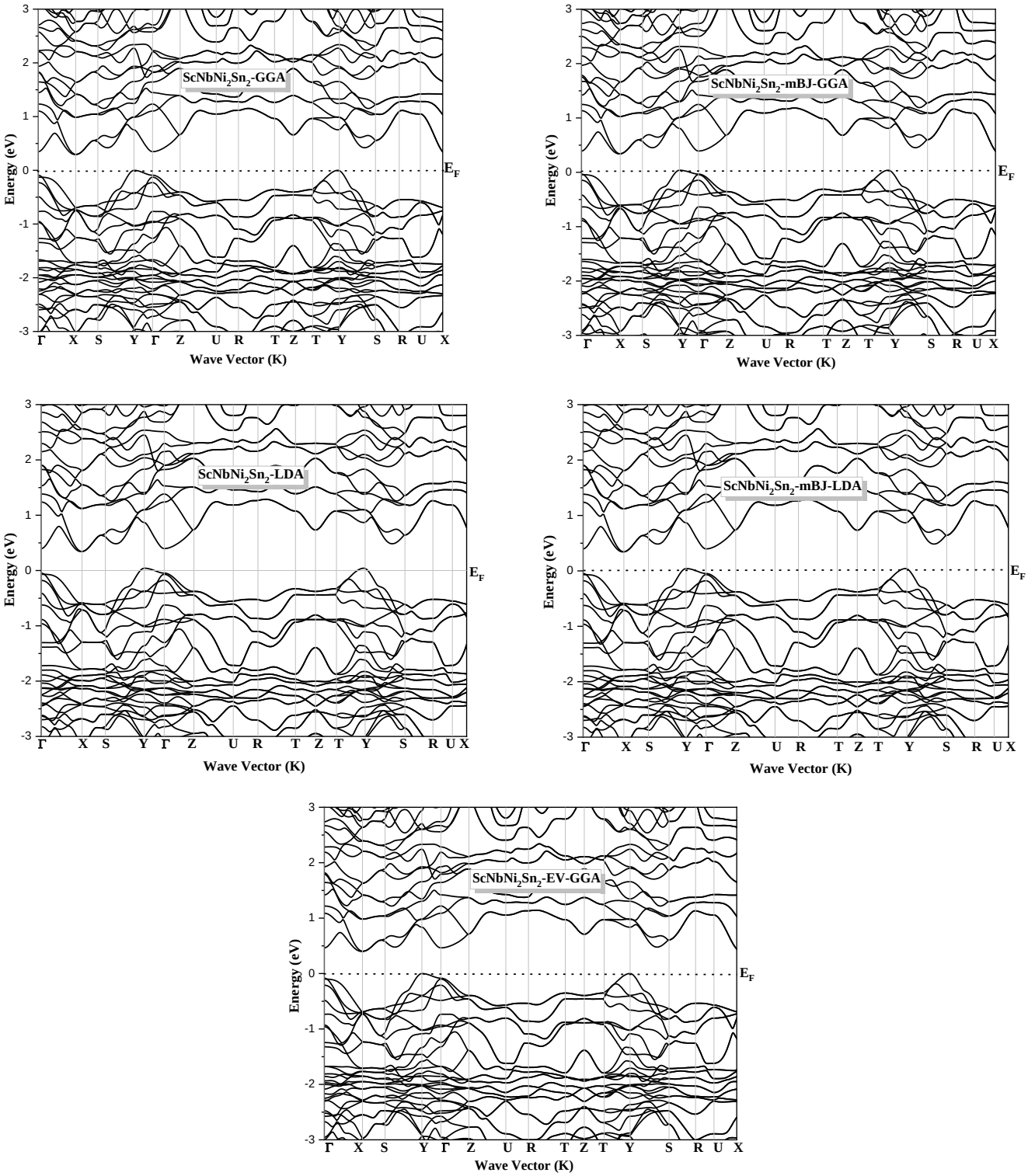

Figure.III.11.a : The band structure along the symmetry lines of the BZ of DHH $ScNbNi_2Sn_2$ using GGA, mBJ-GGA, LDA, mBJ-LDA and EV-GGA approximations.

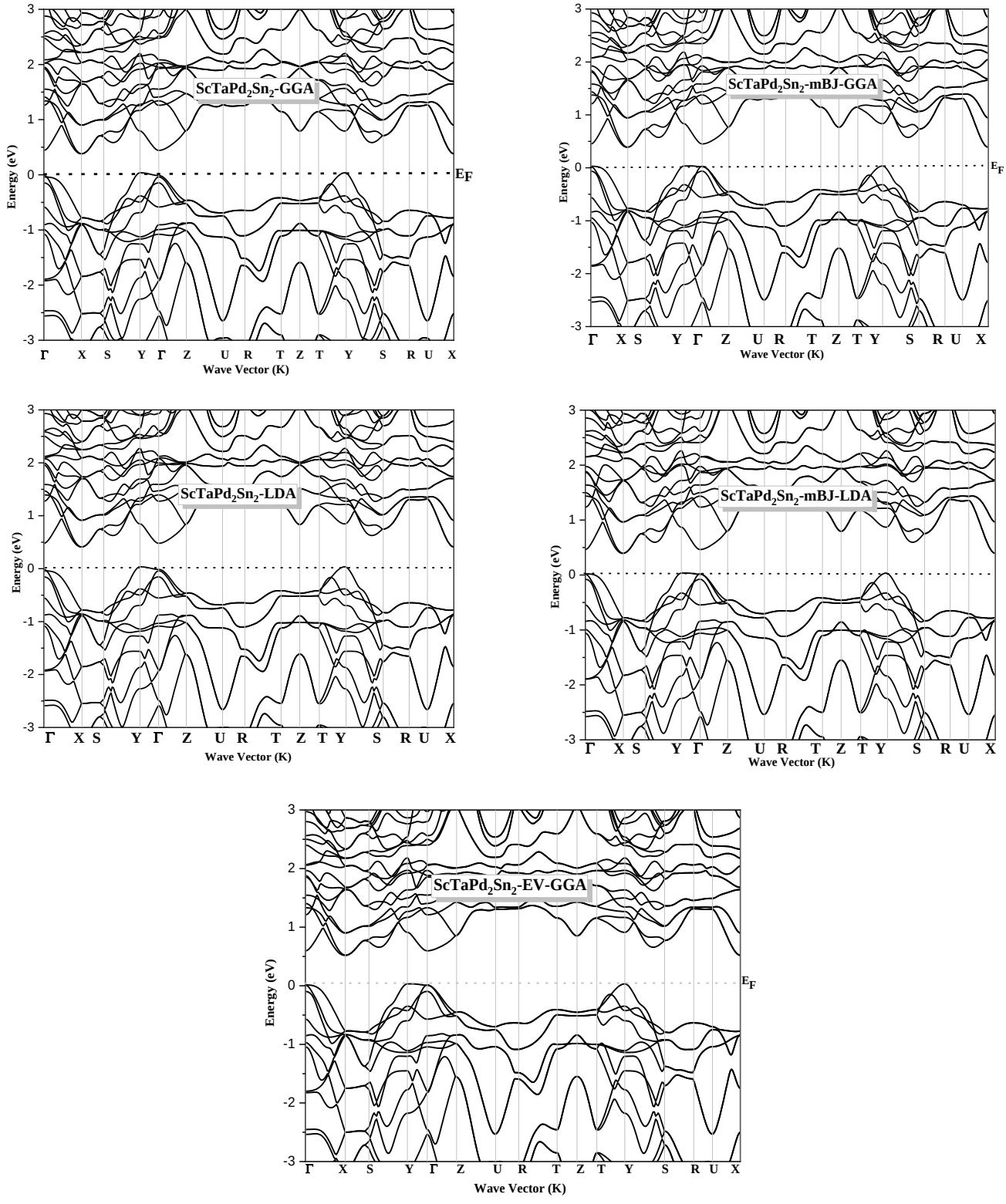

Figure.III.11.b: The band structure along the symmetry lines of the BZ of DHH $ScTaPd_2Sn_2$ using GGA, mBJ-GGA, LDA, mBJ-LDA and EV-GGA approximations.

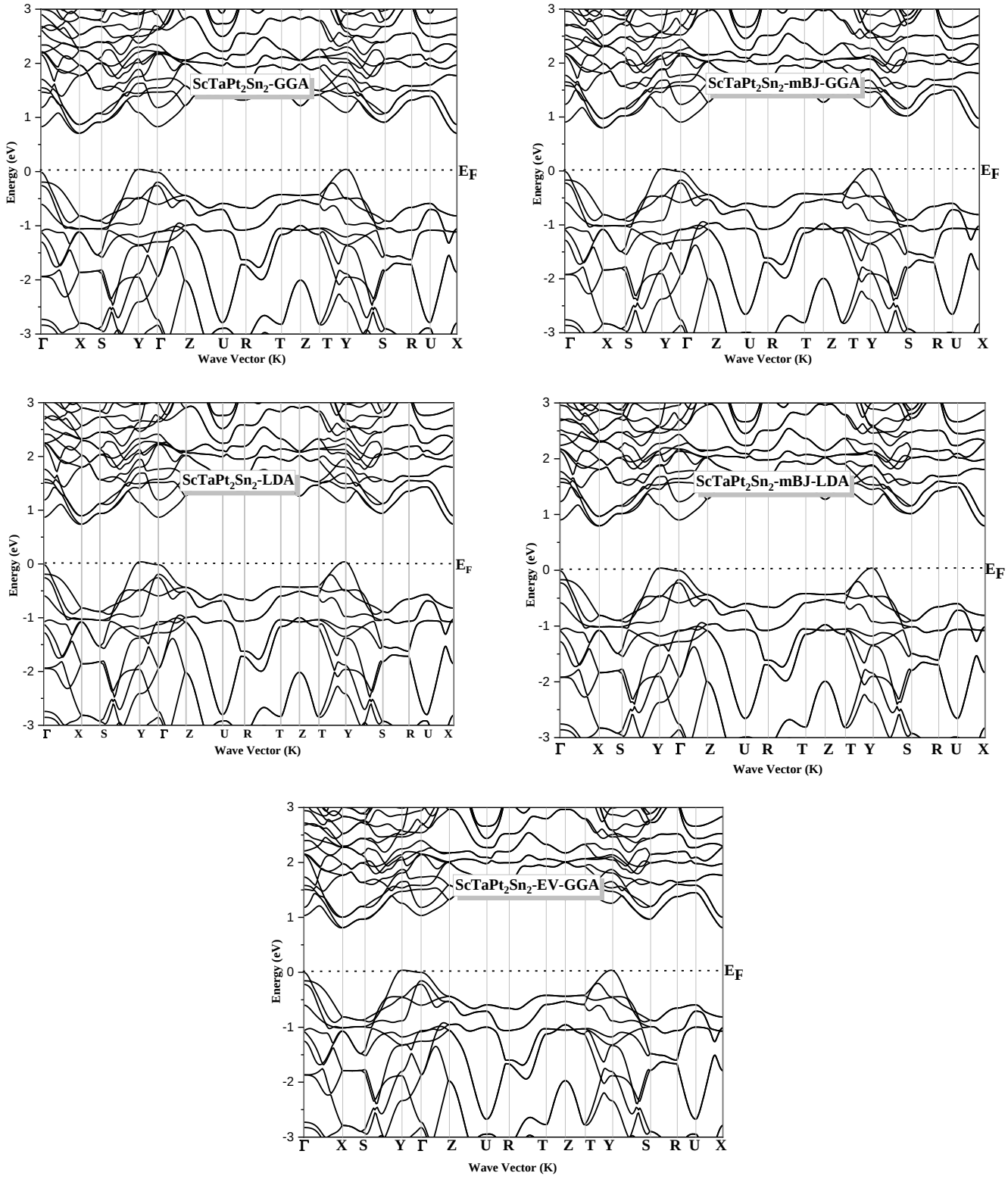

Figure.III.11.c: The band structure along the symmetry lines of the BZ of DHH $ScTaPt_2Sn_2$ using GGA, mBJ-GGA, LDA, mBJ-LDA and EV-GGA approximations

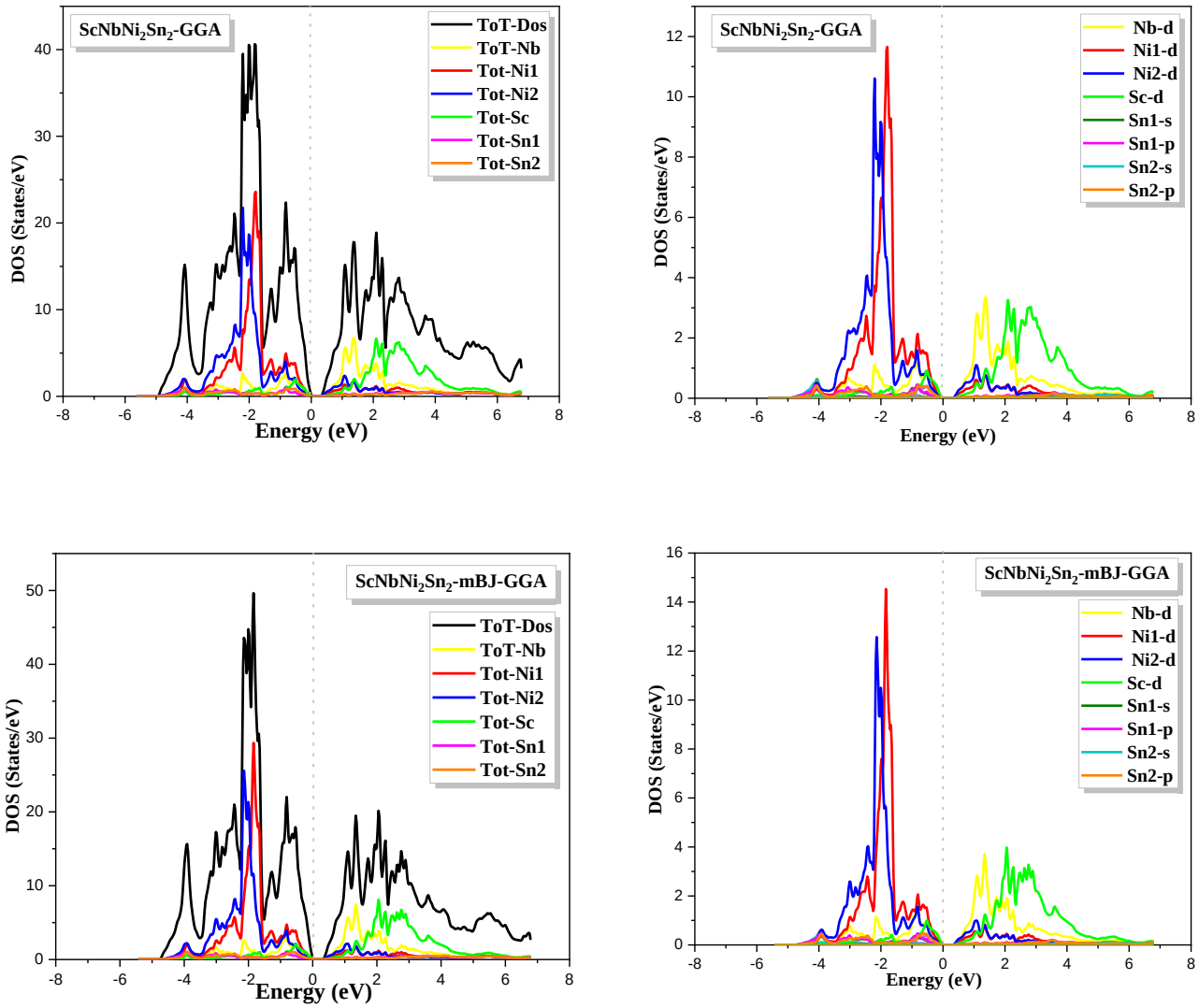

Figure.III.12.a: Total and partial density of state for DHH alloy $ScNbNi_2Sn_2$ using GGA and mBJ-GGA approximations.

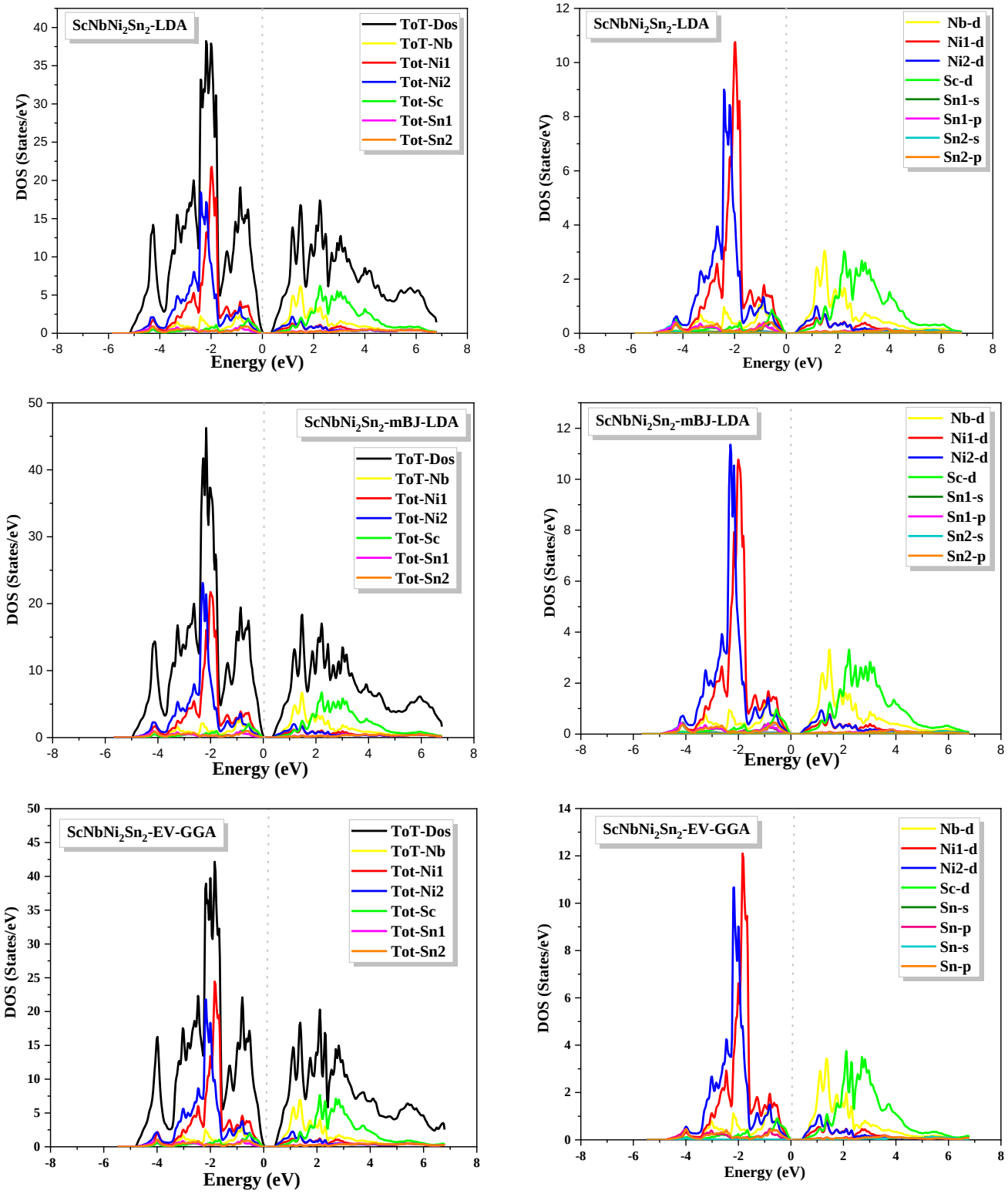

Figure.III.12.b: Total and partial density of state for DHH alloy $ScNbNi_2Sn_2$ using LDA, mBJ-LDA and EV-GGA approximations.

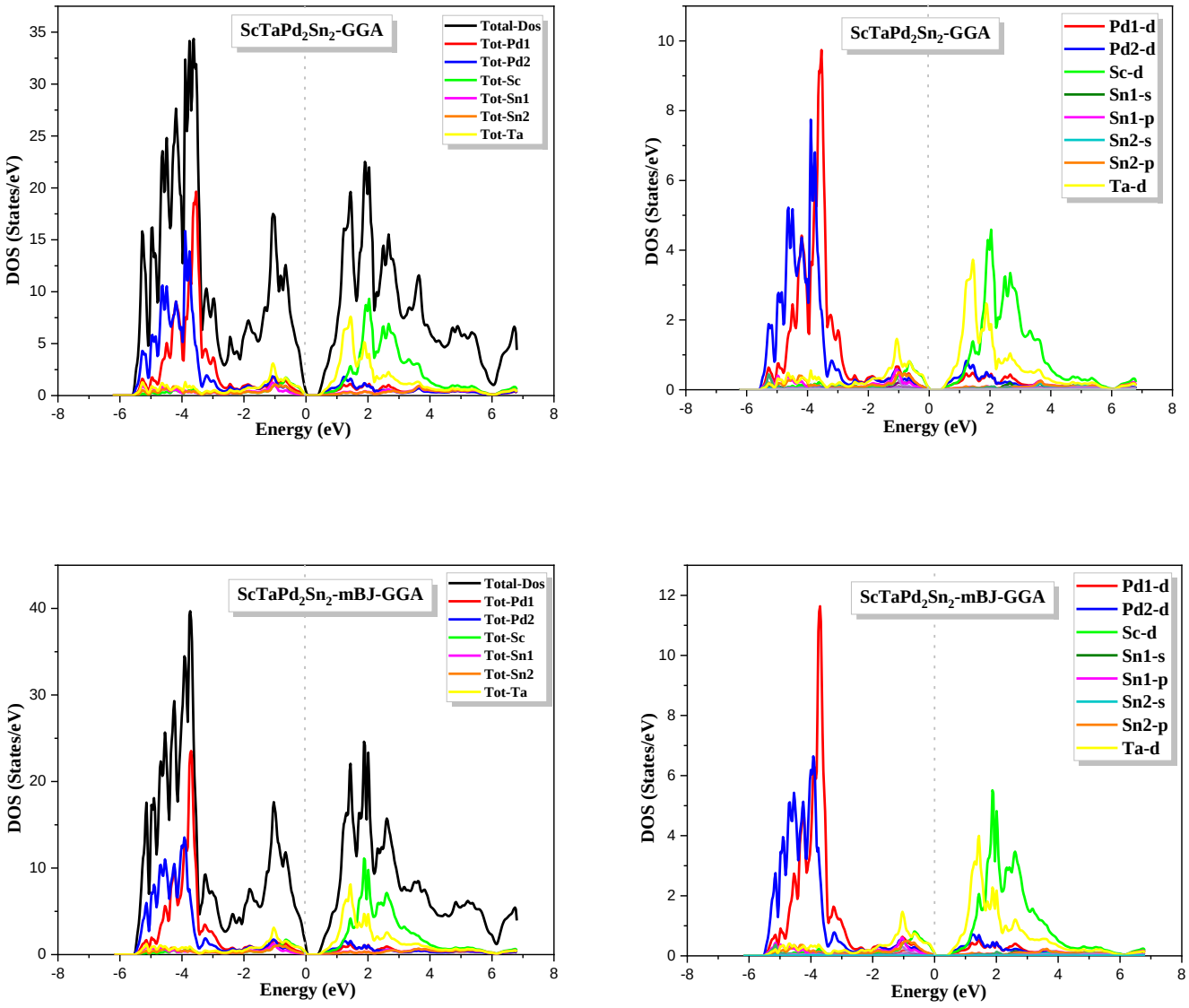

Figure.III.12.c: Total and partial density of state for DHH alloy $ScTaPd_2Sn_2$ using GGA and mBJ-GGA approximations.

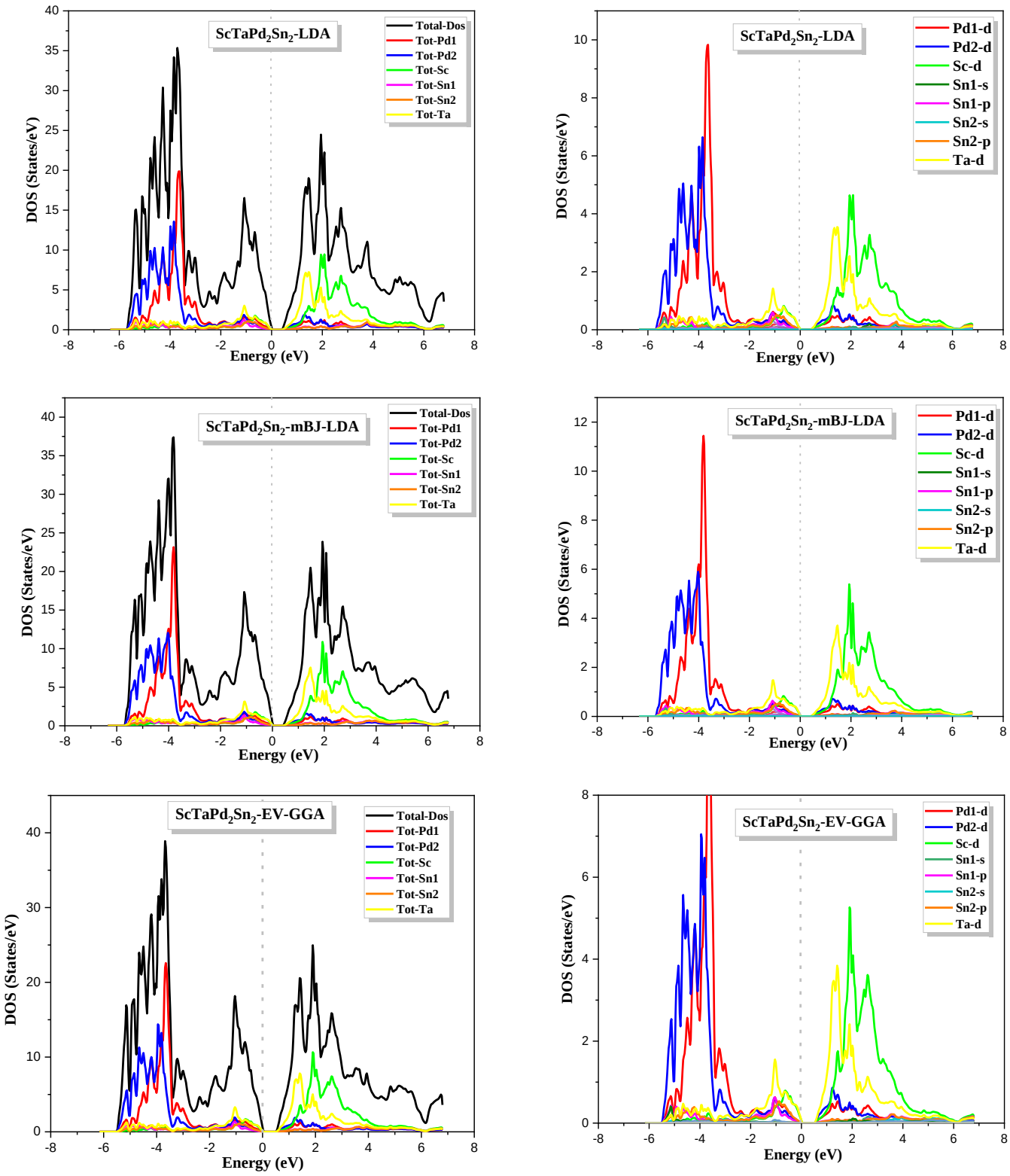

Figure.III.12.d: Total and partial density of state for DHH alloy $ScTaPd_2Sn_2$ using LDA, mBJ-LDA and EV-GGA approximations.

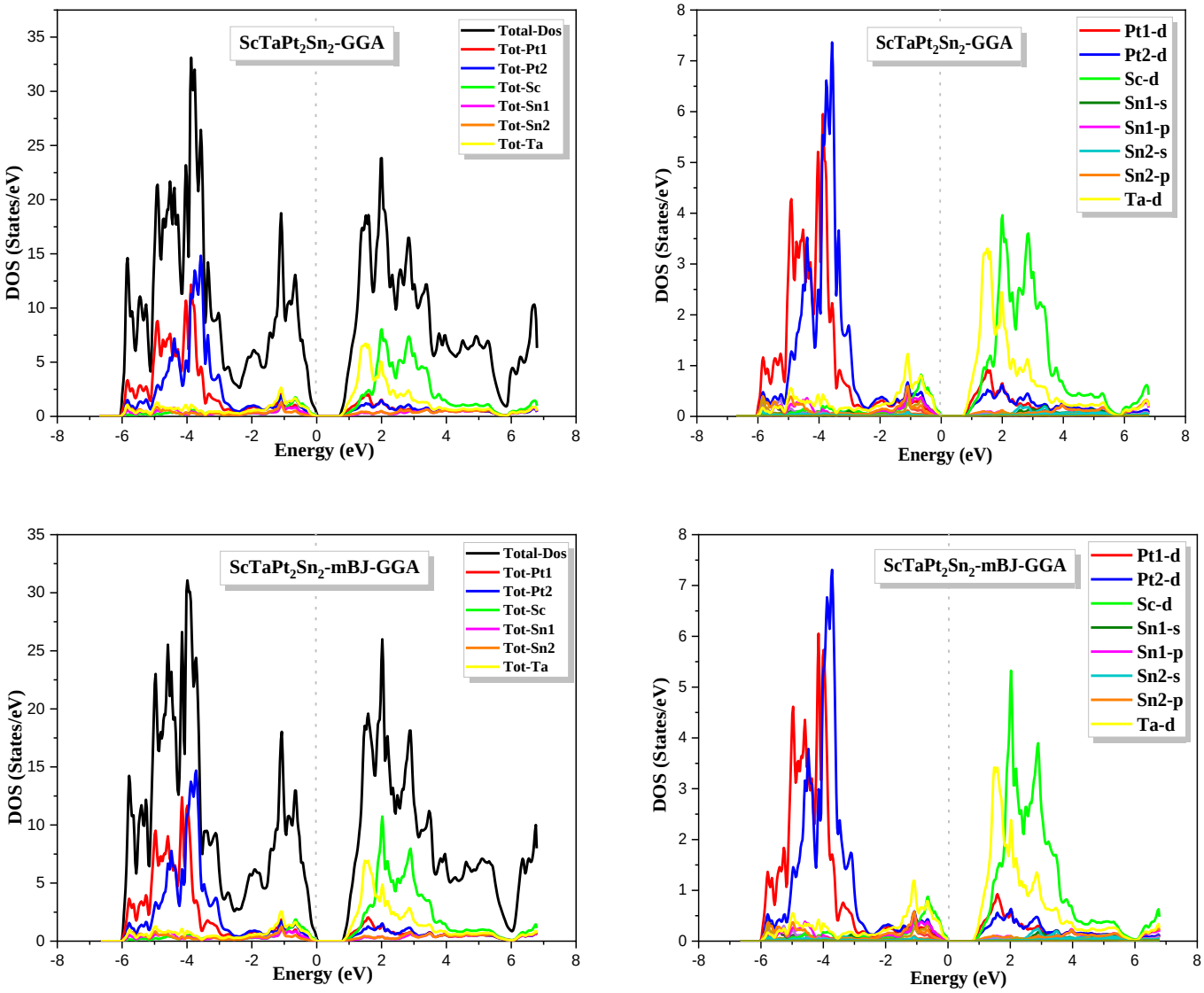

Figure.III.12.e: Total and partial density of state for DHH alloy $ScTaPt_2Sn_2$ using GGA and mBJ-GGA approximations.

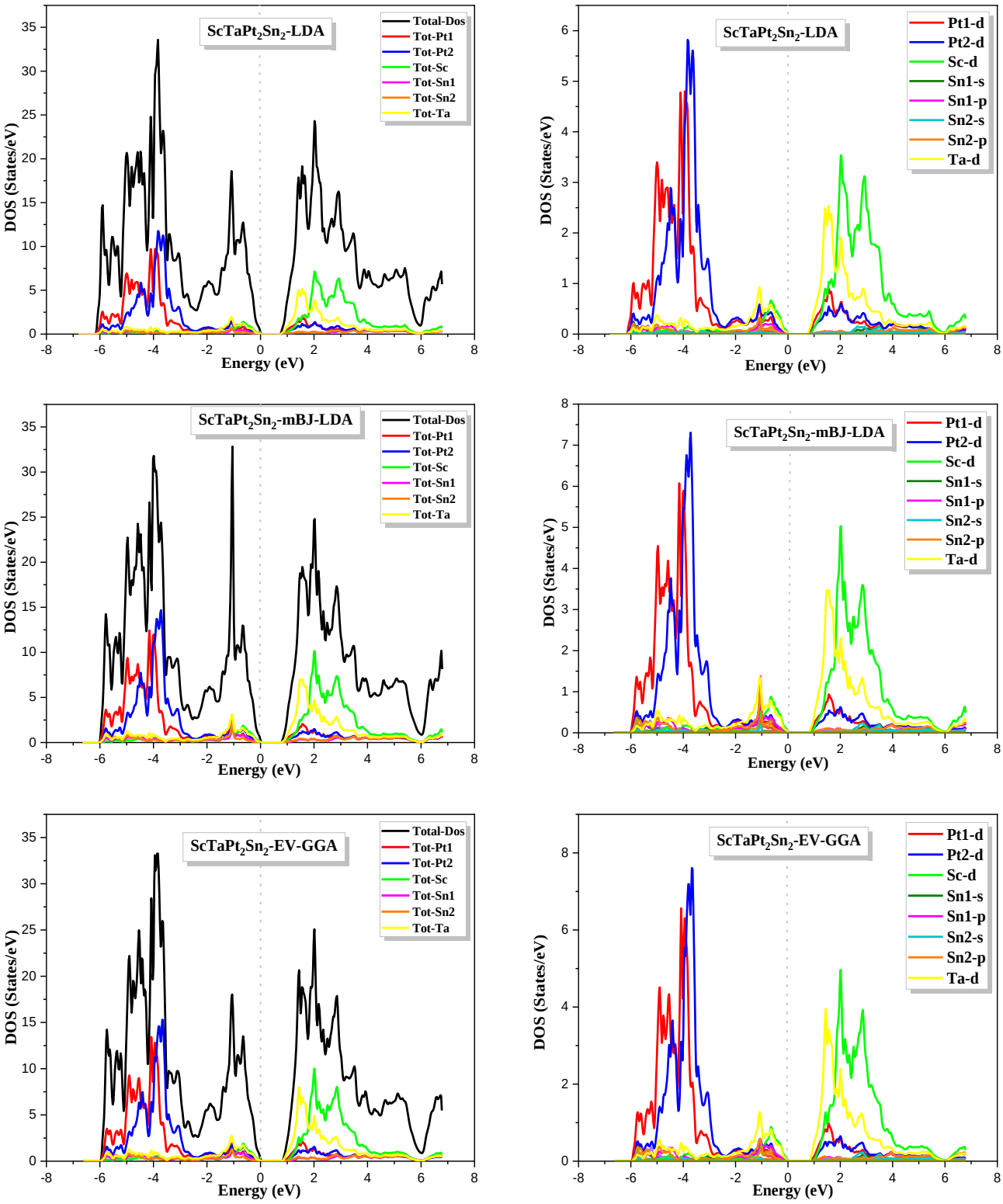

Figure.III.12.f: Total and partial density of state for DHH alloy $ScTaPt_2Sn_2$ using LDA, mBJ-LDA and EV-GGA approximations.

Table III.6: The energy band gap E_g of the DHH alloys $ScX'Y_2Sn_2$ (X'=Nb, Ta; Y=Ni, Pd, Pt) with GGA, LDA, EV-GGA, mBJ-LDA and mBJ-LDA.

Compounds	***Eg(eV)***				
	GGA	***LDA***	***EV-GGA***	***mBJ-GGA***	***mBJ-LDA***
$ScNbNi_2Sn_2$	0.373	0.382	0.470	0.379	0.388
$ScTaPd_2Sn_2$	0.416	0.447	0.549	0.425	0.453
$ScTaPt_2Sn_2$	0.740	0.775	0.851	0.828	0.884

III.5. Optical properties

First-principles calculations of optical constants and dielectric response started including excitonic effects around the year 1998. From investigating simple, wide-gap insulators and semiconductors, researchers have moved on to more complicated materials, clusters, and so forth.

The complex dielectric function explains how the incident wavelength of light affects the optical characteristics of a material and can be defined as:

$$\varepsilon(\omega) = \varepsilon_1(\omega) + i\varepsilon_2(\omega) \tag{III-5}$$

Where $\varepsilon_1(\omega)$ and $\varepsilon_2(\omega)$ represents the real part $\varepsilon_2(\omega) = \mathrm{Re}(\varepsilon(\omega))$ and imaginary part $\varepsilon_2(\omega) = \mathrm{Im}(\varepsilon(\omega))$, respectively. Which were obtained through the calculation of the electronic band structure. the imaginary part of the dielectric function is given by the equation [175,176]:

$$\varepsilon_2(\omega) = \frac{2e^2\pi}{\Omega\varepsilon_0}\sum_{k,V,C}\int_{BZ}\left|\left\langle \Psi_k^C \left| \hat{u}\times r \right| \Psi_k^V \right\rangle^2\right| \delta\left(E_k^C - E_k^V - E\right) \tag{III-6}$$

Where Ω is the unit cell volume, Ψ_k^C and Ψ_k^V are the wave functions of the electron at the k point in the valence and conduction bands, respectively.

On the other side $\varepsilon_1(\omega)$ represents the real part of the dielectric function can be obtained from the imaginary part $\varepsilon_2(\omega)$ using Kramers-Kroning relations [177,178]:

$$\varepsilon_1(\omega) = 1 + \frac{2}{\pi} P \int_0^{\infty} \frac{\omega' \varepsilon_2(\omega')}{\omega^2 - \omega^2} d\omega' \quad \text{(III-7)}$$

P represents the main value of the Cauchy integral.

Having knowledge of both the real and imaginary parts of the dielectric function allow the calculation of important optical properties, such as the refractive index $n(\omega)$, extinction coefficient $k(\omega)$, reflectivity $R(\omega)$, and absorption coefficient $I(\omega)$ [179].

$$n(\omega) = \left[\frac{\varepsilon_1(\omega)}{2} + \frac{\sqrt{\varepsilon_1^2(\omega) + \varepsilon_2^2(\omega)}}{2} \right]^{1/2} \quad \text{(III-8)}$$

The extinction coefficient $k(\omega)$ and the absorption coefficient $I(\omega)$ are given by the following relations:

$$k(\omega) = \left[-\frac{\varepsilon_1(\omega)}{2} + \frac{\sqrt{\varepsilon_1^2(\omega) + \varepsilon_2^2(\omega)}}{2} \right]^{1/2} \quad \text{(III-9)}$$

$$I(\omega) = \frac{\sqrt{2}}{c} \omega \sqrt{-\varepsilon_1(\omega) + \sqrt{\varepsilon_1^2(\omega) + \varepsilon_2^2(\omega)}} \quad \text{(III-10)}$$

The reflectivity spectrum for a crystal surface under normal incidence can be inferred from the given relation:

$$R(\omega) = \left| \frac{\sqrt{\varepsilon(\omega) - 1}}{\sqrt{\varepsilon(\omega) + 1}} \right|^2 \quad \text{(III-11)}$$

To explain the physical consequences of these formulations, for low frequency $\omega = 0$ $(\text{E}=0)$ and based on equation (III-8) we derive the subsequent relation:

$$n(0) = \varepsilon^{1/2}(0) \quad \text{(III-12)}$$

III.5. 1. Direct and indirect Interband transition

The direct transition probability occurs only between electrons and photons when they occupy the same k point in the valence and conduction bands (direct band gap), on the other hand, the indirect transition probability (indirect band gap) between electrons and photons is obtained by taking into account a crystal's vibrations called energy phonon E_{ph} (see Figure.III.13).

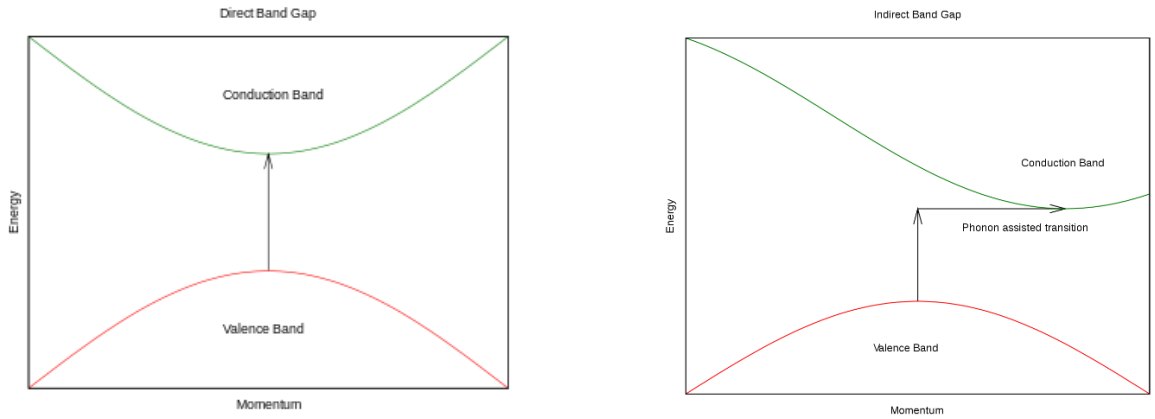

(a) **(b)**

Figure.III.13: (a) Direct and (b) indirect band transition.

III.5. 2. Determination of the dielectric function by the Wien2k code

In order to accurately represent optical characteristics, it is necessary to employ the most precise sampling of the Brillouin zone. Therefore, the electronic structure is computed using the self-consistent field "SCF" method. Subsequently, the corresponding eigenvalues E_i and eigenvectors $|\varphi_{ik}\rangle$ are determined for a significantly large number of *k* points. In this section, we explore the method used in the Wien2k code for computing the dielectric function, which assists us in the following Figure.III.14.

The subroutine "optic" subsequently computes, for each point k and each combination (occupied band / empty band), the constituents of the matrix dipole moment.

The "joint" subroutine is used to calculate the $\varepsilon_2(\omega)$ components on the Brillouin zone.

The subroutine "kram" is utilized to apply the Kramers-Kronig formula for calculating the ε_1 components. At this level, we assign a value to the "scissors operator" based on the difference between the experimentally reported optical gap and the theoretically predicted optical gap. Additionally, a Lorentzian enlargement that reflections the experimental broadening can be incorporated. This facilitates a comparison between the acquired spectra and the EELS (Electron Energy Loss Spectroscopy) data.

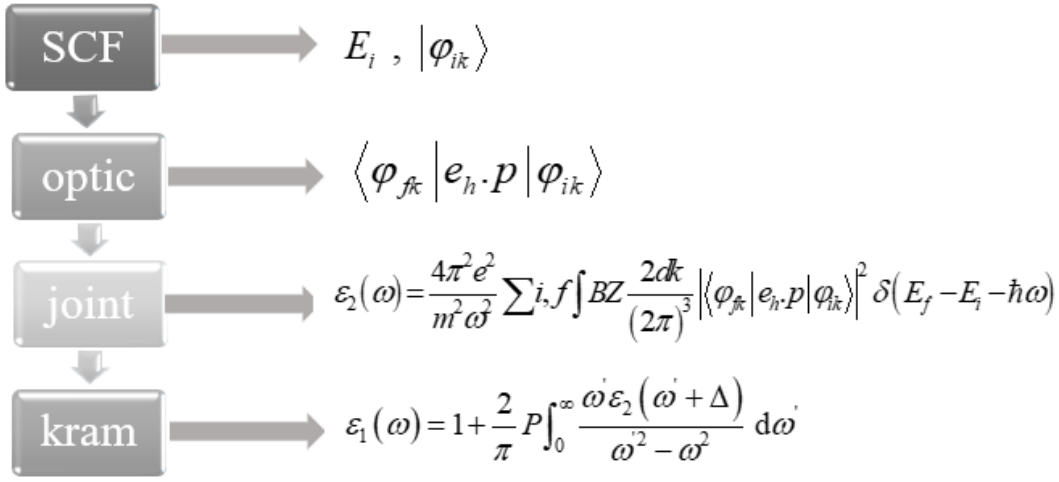

Figure.III.22: Diagram of the different steps of calculating the complex dielectric constant.

To achieve a more accurate optical spectrum of the dielectric function $\varepsilon(\omega)$, a high dense mesh consisting of 10000 k-points distributed over the Brillouin Zone (BZ) is required. The optical characteristics of materials (semiconductors) arise from the interaction between electromagnetic radiation and the material. This interaction gives rise to diffraction, reflection, refraction, and scattering phenomena when light waves pass through the interfaces of two different media. In order to describe the behavior of the DHH alloys $ScX'Y_2Sn_2$ (X'=Nb, Ta; Y=Ni, Pd, Pt), and to give a clear idea of their applications in optoelectronic devices. To fully characterize these optical properties, it is only necessary to determine the imaginary part $\varepsilon_2(\omega)$ of the dielectric function. Calculations were conducted within the energy range of 0 to 40 eV using various approximations (GGA, EV-GGA, and mBJ-GGA). Typically, we analyze our findings using the EV-GGA approximation based on the optimized lattices parameters.

III.5. 3. The imaginary part of the dielectric function

The double half Heusler alloys $ScX'Y_2Sn_2$ (X'=Nb, Ta; Y=Ni, Pd, Pt) crystallize in orthorhombic structure, based on this symmetry, we examined three polarization planes: (100), (010), and (001), which represent the crystallographic direction aligned with the polarization vector. As a result, the dielectric tensor has three components $\varepsilon_{xx}(\omega), \varepsilon_{yy}(\omega)$ and $\varepsilon_{zz}(\omega)$.

Figure.III.15. a, Figure.III.16. a and Figure.III.17. a (b) depicts the variation of the imaginary part of the dielectric function as a function of energy for double half Heusler alloy $ScX'Y_2Sn_2$ (X'=Nb, Ta; Y=Ni, Pd, Pt). The analysis of the imaginary part of the dielectric function $\varepsilon_2(\omega)$ reveals that the spectra of the three investigated alloys are nearly identical. The initial critical points of the dielectric function, which correspond to the fundamental absorption thresholds, roughly 0.4 eV, 0.54 eV and 0.8 eV for $ScNbNi_2Sn_2$, $ScTaPd_2Sn_2$ and $ScTaPt_2Sn_2$, respectively within the EV-GGA approximation which represents the transition between the maximum valence band (Ni-d, and Pd/Pt-d) and the minimum conduction band (Nb/Ta-d, and Sc-d states) in the path of $(Y_V - X_C)$. In addition, there is strong absorption in the energy range 2 - 4.6 eV for the three DHH alloys, the absorption highest peak value is 35.52 for $\varepsilon_{2xx}(\omega)$, 27.28 for $\varepsilon_{2yy}(\omega)$ and 32.70 for $\varepsilon_{2zz}(\omega)$ at 2.89 eV, 3.76 eV, and 2.81 eV, respectively for $ScNbNi_2Sn_2$, while the highest peak value is 34.92 for $\varepsilon_{2xx}(\omega)$, 29.02 for $\varepsilon_{2yy}(\omega)$, and 26.87 for $\varepsilon_{2zz}(\omega)$ located at about 2.84 eV and 3.08 eV respectively for $ScTaPd_2Sn_2$, regarding the third alloy $ScTaPt_2Sn_2$ the highest peak value is 34.16 for $\varepsilon_{2xx}(\omega)$, 27 for $\varepsilon_{2yy}(\omega)$, and 28.7 for $\varepsilon_{2zz}(\omega)$ located at about 3.3 eV and 3.4 eV respectively. which indicates that the DHH alloys $ScX'Y_2Sn_2$ (X'=Nb, Ta; Y=Ni, Pd, Pt) are isotropic, in the other hand these peaks represent the transitions $(Y_V - X_C)$.

The optical absorption of the DHH alloys $ScX'Y_2Sn_2$ (X'=Nb, Ta; Y=Ni, Pd, Pt) for $\varepsilon_{2xx}(\omega)$ is slightly higher with EV-GGA approximation comparing to other GGA and mBJ-GGA approximations.

III.5. 4. Real part of the dielectric function and refractive index

Using Kramers-Kronig transformations [177,178], the real part $\varepsilon_1(\omega)$ of the dielectric function is derived from the imaginary part $\varepsilon_2(\omega)$ as seen in Figure.III.15. a, Figure.III.16. a and Figure.III.17. a (a). The static dielectric constants obtained from the zero-frequency limit have been computed using several approximations and presented in Table III.9.

It should be noted that the optical spectra depicted in this image exhibit similarities, with only slight variations in the location and magnitude of the peaks. Figure.III.15. a, Figure.III.16. a and Figure.III.17. a (a) displays the computed findings for the real part (dispersive) $\varepsilon_1(\omega)$ of the dielectric function of the DHH alloys $ScX'Y_2Sn_2$ (X'=Nb, Ta; Y=Ni, Pd, Pt). The zero crossing of the spectra indicates the non-existence of diffusion (the absence of diffusion) resulting in maximum absorption. The calculated static values for the real part $\varepsilon_1(\omega)$ of dielectric function for our alloys using the EV-GGA approximation along the three crystallographic directions is found to be 17.2252, 15.7646 and 13.687 for $\varepsilon_{1xx}(0)$, 17.2534, 15.6355 and 13.65 for $\varepsilon_{1yy}(0)$ and 17.0558, 15.5857 and 13.62 for $\varepsilon_{1zz}(0)$,the average static value of $\varepsilon_1(0)$ is 17. 1781, 15. 6619 and 13.625 for $ScNbNi_2Sn_2$, $ScTaPd_2Sn_2$ and $ScTaPt_2Sn_2$, respectively. Considering that there is a similarity between our DHH alloys, we will pick $ScNbNi_2Sn_2$ for further investigation (see Figure.III.15. a, Figure.III.16. a and Figure.III.17. a (a)). As we can see in Figure.III.15. a (a) from the zero-frequency limit they start increasing and reach the maximum value of 34.06 for $\varepsilon_{1xx}(\omega)$, 37.46 for $\varepsilon_{1yy}(\omega)$ at 2.108 eV, and 31.63 for $\varepsilon_{1zz}(\omega)$ at 2.13 eV, respectively. After that they start decreasing. furthermore, in addition under the energy ranges shifting from 4.7 to 18.7 eV $ScNbNi_2Sn_2$ behaves similarly to metals due to the negative value of $\varepsilon_1(\omega)$ as a result of the incident photon radiations have been reflected in this region by our alloy.

A slight degree of isotropy is observed in the real part of the dielectric function $\varepsilon_1(\omega)$ for all three alloys in close proximity to the principal peak, as depicted in Figure.III.15. a (a). In addition, $ScNbNi_2Sn_2$ has a higher dielectric constant at high frequencies compared to other DHH alloys $ScTaPd_2Sn_2$ and $ScTaPt_2Sn_2$. Therefore, it is important to note that the small energy gap is

associated with the high value of $\varepsilon_1(0)$ as explained by Penn's model $\varepsilon_1(0) \approx 1+\left(\frac{\hbar\omega_p}{E_g}\right)^2$ [180]

where ω is the plasma frequency and E_g is the energy band gap. Our analysis verifies the Penn model by demonstrating that the band gap of $ScTaPt_2Sn_2$ is greater than that of $ScNbNi_2Sn_2$ and $ScTaPd_2Sn_2$. Thus, a small energy gap yields a large value of $\varepsilon_1(0)$.

By employing the resulting frequency-dependent dielectric function's imaginary and real parts, it is possible to estimate further optical parameters such as the absorption coefficient $I(\omega)$ and reflectivity spectra $R(\omega)$.

The phenomenon of a light beam passing through a translucent medium is explained by the refractive index, denoted as $n(\omega)$. The spectra are shown in Figure.III.15. b, Figure.III.16. b and Figure.III.15. b (b) using different approximations. It is evident that the refractive index $n(\omega)$ often adopts the form of the real part $\varepsilon_1(\omega)$ that it is connected to by $n(0)=\sqrt{\varepsilon_1(0)}$. The estimated static refractive index $n(0)$ is presented in the same table with the static real part $\varepsilon_1(0)$. due to similarity of the curves of the refractive index we select the $ScNbNi_2Sn_2$ alloy as our object of study for investigation using the EV-GGA approximation as usual. The refractive index is shown in Figure.III.15. b (b) from the plot $n(\omega)$ emerges from 4.1503, 4.1537 and 4.1298 for $n_{xx}(0)$, $n_{yy}(0)$, and $n_{zz}(0)$ directions respectively. So, the average value of $n(0)$ is equal to 4.1446 and it is obtained from the real part of the dielectric function to be $n(0)=\sqrt{\varepsilon_1(0)}=\sqrt{17.1781}=4.1446$. It is evident that the refractive index reaches its maximum values of 5.94, 6.21, and 5.73 for n_{xx}, n_{yy}, and n_{zz} directions respectively, at 2.13 eV energy. Then it begins to decline with several minor peaks and continues to decline up to 20 eV and it begins to rise slightly forming very small peaks at the end of the energy range.

The calculated findings also indicate that both the real part $\varepsilon_1(\omega)$ and the refractive index $n(\omega)$ show an insignificant degree of isotropy for the DHH alloys.

The refractive index of the $ScNbNi_2Sn_2$ alloy is greater compared to other DHH alloys, such as $ScTaPd_2Sn_2$ and $ScTaPt_2Sn_2$, when using the mBJ-GGA approximation.

Table III.8: the calculated values of $\varepsilon_1(0)$ and $n(0)$ within GGA, LDA, EV-GGA, mBJ-LDA and mBJ-GGA for DHH alloys $ScX'Y_2Sn_2$ (X' =Nb, Ta; Y=Ni, Pd, Pt).

Alloys	$\varepsilon_1(0)$						$n(0)$					
	ε_{ii}	***GGA***	***LDA***	***EV-GGA***	***mBJ GGA***	***mBJ LDA***	n_{ii}	***GGA***	***LDA***	***EV-GGA***	***mBJ GGA***	***mBJ LDA***
$ScNbNi_2Sn_2$	ε_{1xx}	17.6755	17.3615	17.2252	18.0074	17.5958	n_{xx}	4.2042	4.1667	4.1503	4.2435	4.1947
	ε_{1yy}	17.6611	17.3581	17.2534	17.9752	17.5837	n_{yy}	4.2025	4.1663	4.1537	4.2397	4.1933
	ε_{1zz}	17.4793	17.1902	17.0558	17.8159	17.4184	n_{zz}	4.2025	4.1461	4.1298	4.2209	4.1735
$ScTaPd_2Sn_2$	ε_{1xx}	16.1305	15.6574	15.7646	15.8695	15.4768	n_{xx}	4.0163	3.9569	3.9704	3.9836	3.9340
	ε_{1yy}	15.9754	15.4761	15.6355	15.6844	15.3006	n_{yy}	3.9969	3.9339	3.9542	3.9548	3.9116
	ε_{1zz}	15.9316	15.4339	15.5857	15.6406	15.2414	n_{zz}	3.9914	3.9286	3.9478	3.3954	3.9040
$ScTaPt_2Sn_2$	ε_{1xx}	14.2820	13.8641	13.687	13.179	13.2354	n_{xx}	3.7791	3.7234	3.6434	3.633	3.6386
	ε_{1yy}	14.2345	13.8333	13.652	13.162	13.1903	n_{yy}	3.7728	3.7193	3.6388	3.627	3.6318
	ε_{1zz}	14.1907	13.7784	13.623	13.110	13.1555	n_{zz}	3.7670	3.7119	3.6347	3.620	3.6270

III.5. 5. Extinction coefficient

Figure.III.15. b, Figure.III.16. b and Figure.III.17. b (a) shows the extinction coefficient $k(\omega)$ which describe how strongly a DHH alloys reflect the radiation. The spectra exhibit resemblances with minor variations in particulars. From Figure.III.15. b, (a) the extinction coefficient $k(\omega)$ reflects the maximum absorption in the medium at 2.95 eV for $k_{xx}(\omega)$,4 eV for $k_{yy}(\omega)$, and 4.23 eV for $k_{zz}(\omega)$ with average value 3.43 for $ScNbNi_2Sn_2$. In addition, the curves shown in Figure.III.16. b and Figure.III.17. b (a) reveals the highest values of $k_{xx}(\omega)$, $k_{yy}(\omega)$ and $k_{zz}(\omega)$ and to be 3.58, 3.45 and 3.36 at 3.19 eV ,4.01 eV and 4.04 eV, respectively for $ScTaPd_2Sn_2$.

Similarly, for the alloy $ScTaPt_2Sn_2$, the maximum values are 3.75, 3.37, and 3.19 at energy of 3.6 eV, 4.12 eV, and 4.10 eV. The energy at which the extinction coefficient reaches its maximum value the real part of the dielectric function equals zero.

Regardless of the approximation employed, all the DHH alloys exhibit a larger extinction coefficient $k_{xx}(\omega)$ in the x direction comparing to other alloys.

III.5. 6. Optical conductivity and absorption coefficient

Figure.III.15. c, Figure.III.16. c and Figure.III.17. c (a) illustrates the optical conductivity of the double Heusler alloys $ScX'Y_2Sn_2$ (X' =Nb, Ta; Y=Ni, Pd, Pt).

From Figure.III.15. c (a) we can see that the optical conductivity $\sigma(\omega)$ begins to increase at 1.5 eV and develops to the value of 12.52 at 2.92 eV for $\sigma_{xx}(\omega)$,12.45 at 3.79 eV for $\sigma_{yy}(\omega)$, and 11.18 at 2.84 eV for $\sigma_{zz}(\omega)$ then it gradually decreases until it reaches 28 eV. After that it increases again with the appearance of other medium peaks up to 40 eV for $ScNbNi_2Sn_2$ whereas $ScTaPd_2Sn_2$ exhibits its highest peaks of optical conductivity $\sigma(\omega)$ at 3.088 eV ($14.511x10^3$) for $\sigma_{xx}(\omega)$,3.93 eV for $\sigma_{yy}(\omega)$ (12.759) and $\sigma_{zz}(\omega)$ (11.98). In the other hand the alloy $ScTaPt_2Sn_2$ exhibits the value of $16x10^3$ at 3.523eV for $\sigma_{xx}(\omega)$,13.217 at 4.013 for $\sigma_{yy}(\omega)$ and 12.913 at 3.33 eV for $\sigma_{zz}(\omega)$ respectively. The primary structure extends between the threshold and 28 eV. Additionally, intermediate peaks appear up to 40 eV.

Regardless of the approximation employed, all the DHH alloy $ScTaPt_2Sn_2$ exhibit a larger optical conductivity $\sigma_{xx}(\omega)$ in the x direction comparing to other alloys.

The absorption coefficients $I(\omega)$ of the DHH alloys $ScX'Y_2Sn_2$ (X' =Nb, Ta; Y=Ni, Pd, Pt) are displayed in Figure.III.15. c, Figure.III.16. c and Figure.III.17. c (b). It is observed that the absorption coefficient significantly increases at low energies and reaches its maximum value at higher energies.

From Figure.III.15. c (b) the absorption coefficient $I(\omega)$ for $ScNbNi_2Sn_2$ starts from the energy 1.5 eV, in which the absorption begins to increase until reaching the value of about 200.909×10^4

Cm^{-1} at an energy range of 9.72 eV then it begins to increase again to arrive at an extremely intense about 304 at 34 eV along the *x* axe. By examining Figure.III.16. c (b) and Figure.III.17. c (b) we observe that the absorption starts at 1.52 eV /2 eV and increase gradually with the increasing of the photon energy then reaching a maximum value 204.9×10^4 Cm^{-1} at 7.08 eV /217×10^4 Cm^{-1} at 9.15 eV after that it begins to increase again to arrive at an extremely intense about 322 at 37.81 eV / 297.4 at 38 eV along the *x* axe for $ScTaPd_2Sn_2$ and $ScTaPt_2Sn_2$, respectively.

Whichever of the approximation used, all the DHH alloy $ScTaPt_2Sn_2$ have a higher absorption coefficient $I(\omega)$ when compared to other DHH alloys.

III.5. 7. The reflectivity spectrum and energy loss function (ELF)

The reflectivity spectra calculation findings of the DHH alloys $ScX'Y_2Sn_2$ (X'=Nb, Ta; Y=Ni, Pd, Pt) under study are depicted in Figure.III.15. d, Figure.III.16. d, Figure.III.17. d (a). According to these curves, the reflectivity spectra originate at the zero-frequency corresponds to the static components of the reflectivity $R_{xx}(\omega), R_{yy}(\omega)$ and $R_{zz}(\omega)$, the value of the reflectance is about 37.3% where the greatest value emerges at 58% in the energy range 2.83-8.47 eV for $ScNbNi_2Sn_2$.in the other hand, the $ScTaPd_2Sn_2$ has the value of the reflectance is about 35.5% ,there are several intense peaks in the energy range 2.3-12 eV however the most intense has a reflectivity about 59.9% , while the $ScTaPt_2Sn_2$ alloy has significantly same behavior as $ScTaPd_2Sn_2$ and its reflectivity is about 60% .These alloys have a wide range of applications in the medical and space industries because it has a high reflectivity in the UV region.

Regardless of the approximation employed (GGA, mBJ-GGA, and EV-GGA), the reflectivity of double Heusler alloys remains nearly same. Furthermore, when considering the values at zero frequency (see Table III.10), it is observed that $ScNbNi_2Sn_2$ has the greatest value among all the alloys in all approximations.

The energy loss function (ELF) characterizes the interaction between electrons and matter within solid materials which can be calculated using the dielectric function. It can be described by the expression:

$$L(\omega) = \mathrm{Im}\left(-\frac{1}{\varepsilon(\omega)}\right) \qquad \text{(III-13)}$$

This can also be expressed in the following manner

$$L(\omega)=\left(\frac{\varepsilon_2(\omega)}{\varepsilon_1(\omega)^2+\varepsilon_2(\omega)^2}\right) \quad \text{(III-14)}$$

The variation of the energy loss spectrum function is shown in Figure.III.15. d, Figure.III.16. d and Figure.III.16. d (b) for the DHH alloys $ScX'Y_2Sn_2$ (X'=Nb, Ta; Y=Ni, Pd, Pt). The energy loss spectra exhibit significant values within the energy range of 18.9-35.5 eV for $ScNbNi_2Sn_2$, 17-38 eV for $ScTaPd_2Sn_2$, and 16-38 eV for $ScTaPt_2Sn_2$. The primary peaks are situated at 19.03 eV, 25.2 eV and 25.4 eV for $ScNbNi_2Sn_2$, $ScTaPd_2Sn_2$ and $ScTaPt_2Sn_2$ respectively for all the directions.

The preceding values of the apparent peaks is commonly referred to as the plasma frequency and correlates to the trailing edges in the reflection spectra. The maximum energy peak is described as the plasma resonance energy, which often occurs when the imaginary part $\varepsilon_2(\omega)$ of the dielectric function is below one and the real part $\varepsilon_1(\omega)$ is zero **[**175]. This indicates that there is a transition from metallic behavior ($\varepsilon_1(\omega)$ is negative) to dielectric behavior ($\varepsilon_1(\omega)$ is positive). The analysis of $L(\omega)$ and $R(\omega)$ reveals that the plasma energy $\hbar\omega_p$ is located at approximately 20.5 eV, 25.07 eV and 25.3 eV for $ScNbNi_2Sn_2$, $ScTaPd_2Sn_2$ and $ScTaPt_2Sn_2$, respectively. This indicates that the peaks in the function are associated with a significant decrease in the reflectivity spectra.

The $ScTaPt_2Sn_2$ alloy exhibits a significant energy loss in comparison to the other DHH alloys as estimated by the EV-GGA approximation.

Table III.9: the calculated values of $R(0)$ and $L(0)$ within GGA, LDA, EV-GGA, mBJ-LDA and mBJ-GGA for DHH alloys $ScX'Y_2Sn_2$ (X'= Nb, Ta; Y=Ni, Pd, Pt).

Alloys	*R*(0)						*L*(0)					
	R_{ii}	***GGA***	***LDA***	***EV GGA***	***mBJ GGA***	***mBJ LDA***	L_{ii}	***GGA***	***LDA***	***EV GGA***	***mBJ GGA***	***mBJ LDA***
$ScNbNi_2Sn_2$	R_{xx}	0.379	0.3756	0.3741	0.3826	0.3782	L_{xx}	3.896 x10^{-4}	3.815 x10^{-4}	3.954 x10^{-4}	3.928 x10^{-4}	3.857 x10^{-4}
	R_{yy}	0.3789	0.3756	0.3744	0.3823	0.3780	L_{yy}	3.861 x10^{-4}	3.777 x10^{-4}	3.925 x10^{-4}	3.897 x10^{-4}	3.821 x10^{-4}
	R_{zz}	0.3769	0.3737	0.3722	0.3806	0.3662	L_{zz}	0.39 x10^{-4}	3.819 x10^{-4}	3.962 x10^{-4}	3.937 x10^{-4}	3.865 x10^{-4}
$ScTaPd_2Sn_2$	R_{xx}	0.3615	0.3558	0.3571	0.3584	0.3536	L_{xx}	3.922 x10^{-4}	4.052 x10^{-4}	3.992 x10^{-4}	4.162 x10^{-4}	4.140 x10^{-4}
	R_{yy}	0.3597	0.3536	0.3555	0.3561	0.3514	L_{yy}	3.903 x10^{-4}	4.038 x10^{-4}	3.983 x10^{-4}	4.151 x10^{-4}	4.133 x10^{-4}
	R_{zz}	0.3591	0.3530	0.3549	0.3556	0.3596	L_{zz}	3.931 x10^{-4}	4.067 x10^{-4}	4.001 x10^{-4}	4.186 x10^{-4}	4.162 x10^{-4}
$ScTaPt_2Sn_2$	R_{xx}	0.3381	0.3324	0.3240	0.3227	0.3235	L_{xx}	3.797 x10^{-4}	3.957 x10^{-4}	4.104 x10^{-4}	4.105 x10^{-4}	4.098 x10^{-4}
	R_{yy}	0.3375	0.3320	0.3236	0.3224	0.3228	L_{yy}	3.778 x10^{-4}	3.935 x10^{-4}	4.086 x10^{-4}	4.08 x10^{-4}	4.086 x10^{-4}
	R_{zz}	0.3369	0.3312	0.3231	0.3216	0.3223	L_{zz}	3.797 x10^{-4}	3.959 x10^{-4}	4.105 x10^{-4}	4.109 x10^{-4}	4.105 x10^{-4}

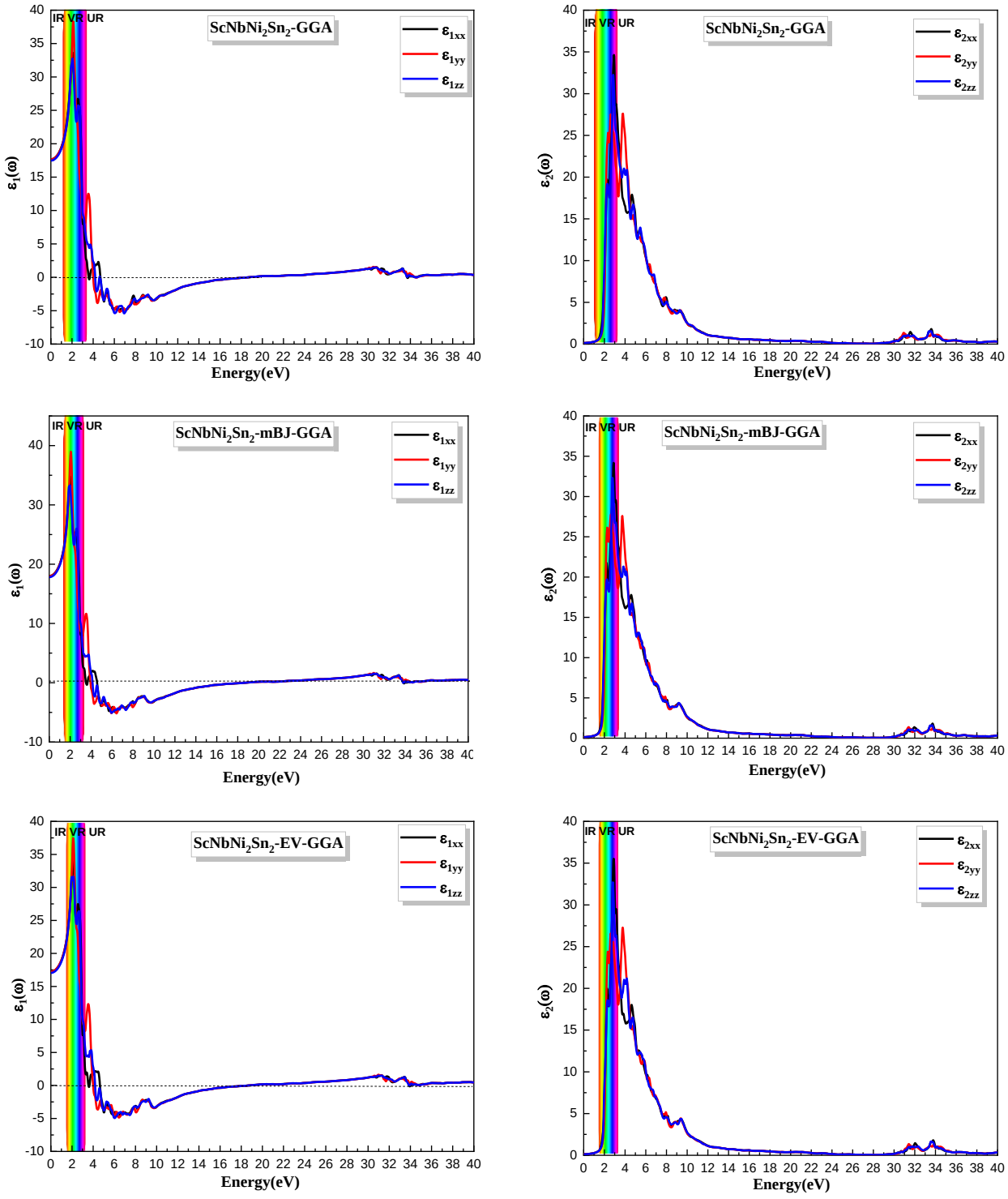

Figure.III.15.a: Variation of **(a)** the real part ε_1, **(b)** the imaginary part of the dielectric function for $ScNbNi_2Sn_2$ alloy within the GGA, mBJ-GGA and EV-GGA approximations.

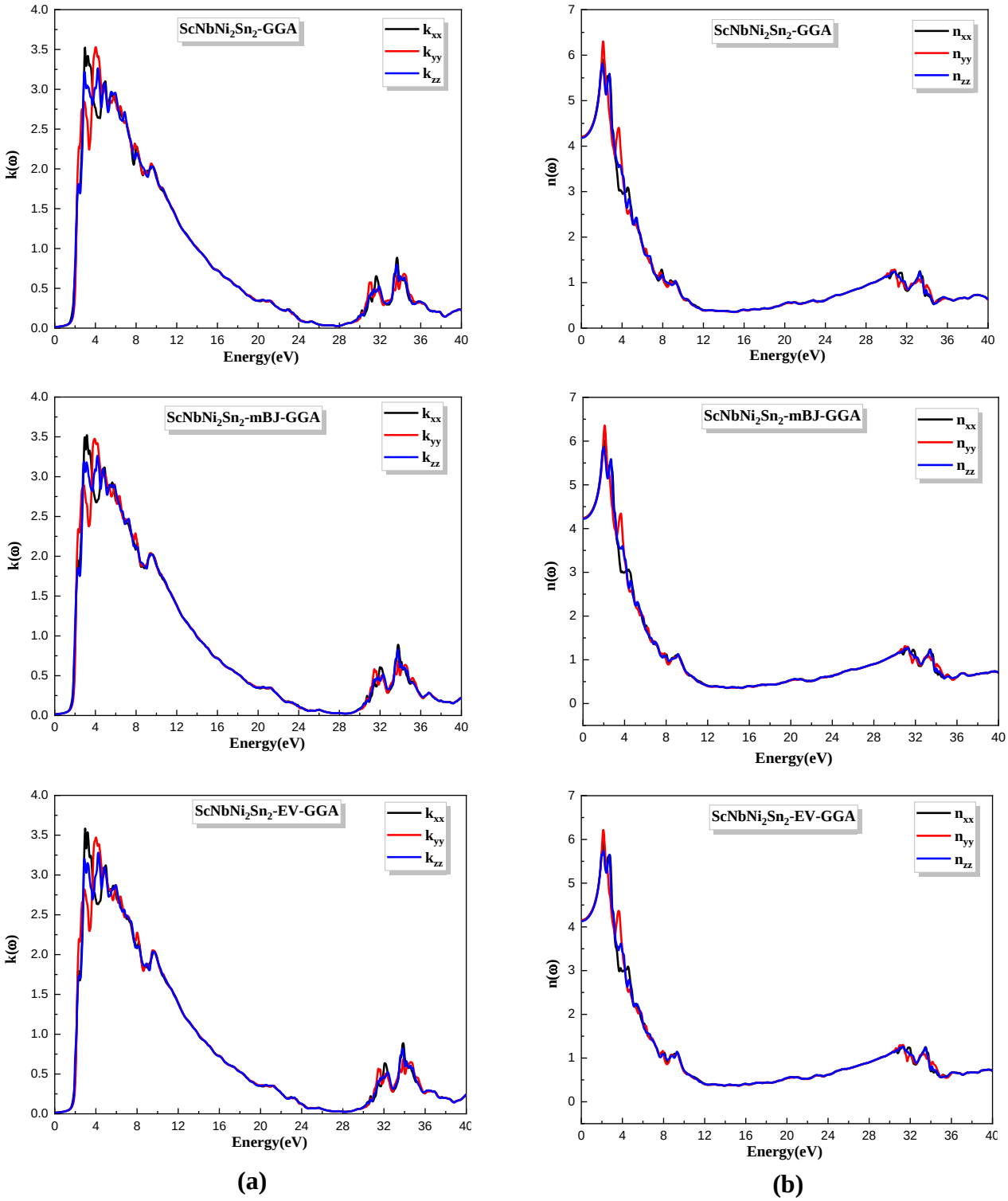

Figure.III.15.b: Optical spectra as a function of photon energy (**a)** the extinction coefficient, **(b)** the refractive index for the $ScNbNi_2Sn_2$ alloy within the GGA, mBJ-GGA and EV-GGA approximations.

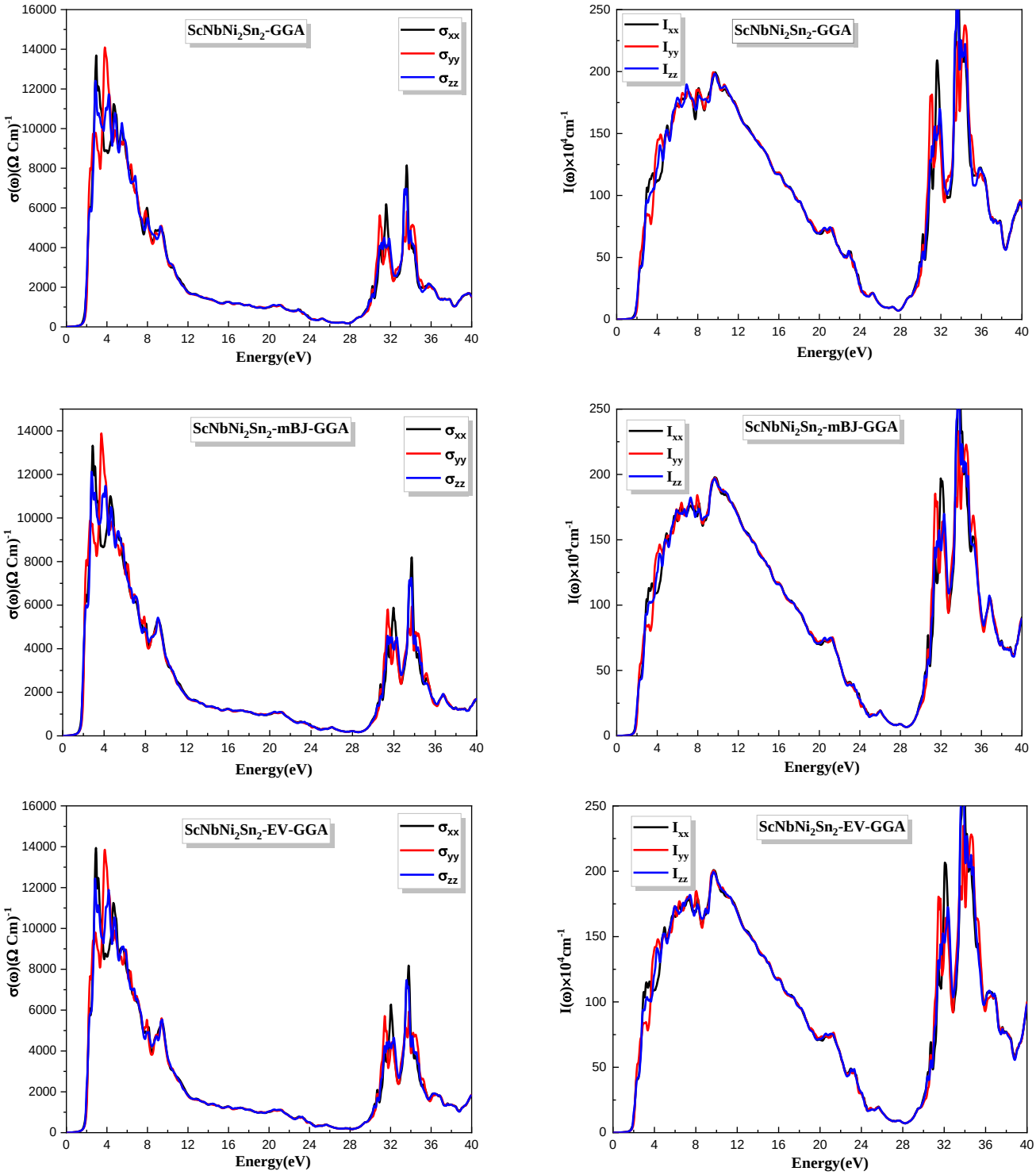

Figure.III.15.c: Variation of **(a)** the optical conductivity, and **(b)** the absorption coefficient for the $ScNbNi_2Sn_2$ alloy within the GGA, mBJ-GGA and EV-GGA approximations.

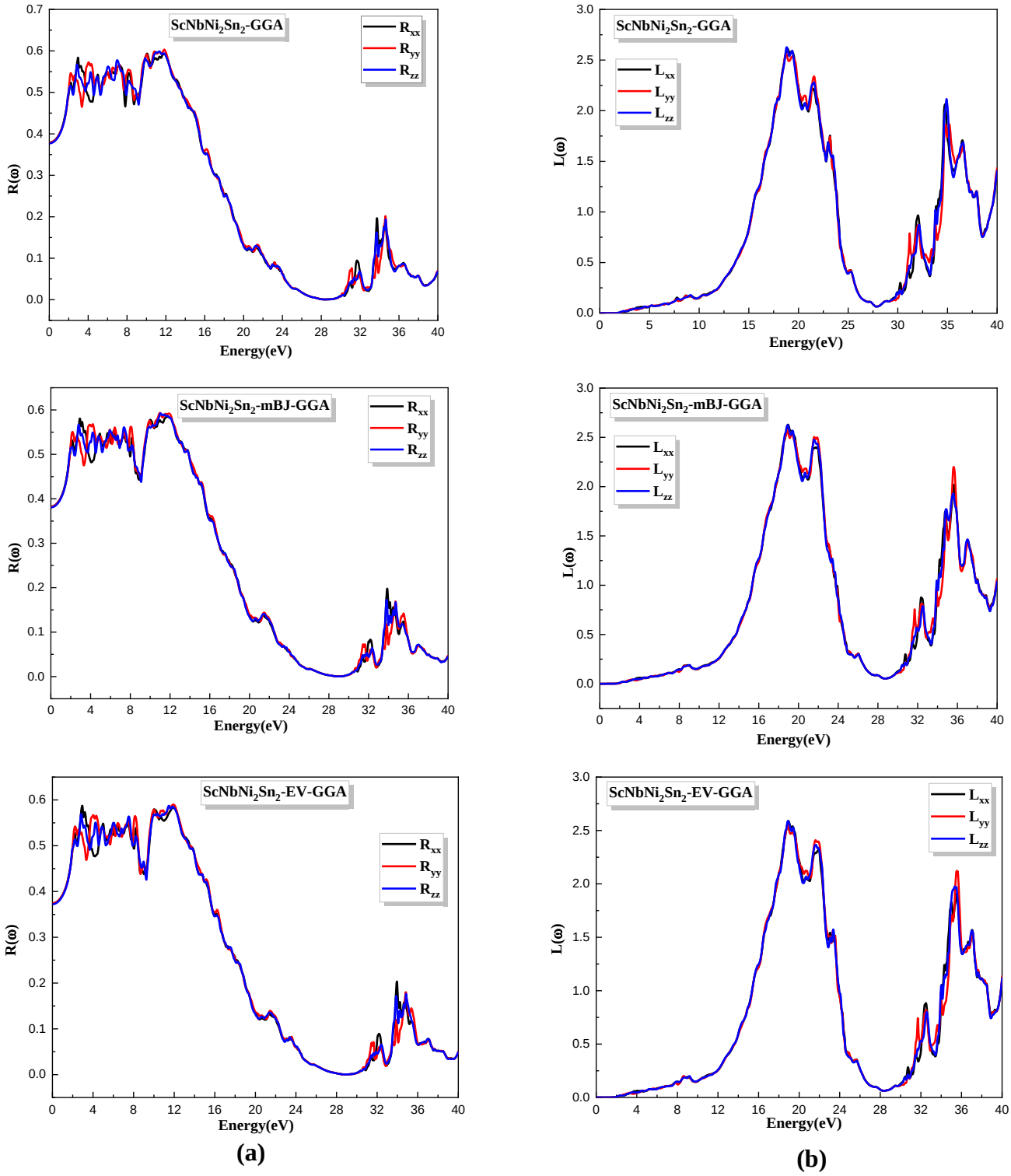

Figure.III.15.d: Optical spectra as a function of photon energy **(a)** reflectivity spectra, and **(b)** the energy loss function for the $ScNbNi_2Sn_2$ alloy within the GGA, mBJ-GGA and EV-GGA approximations.

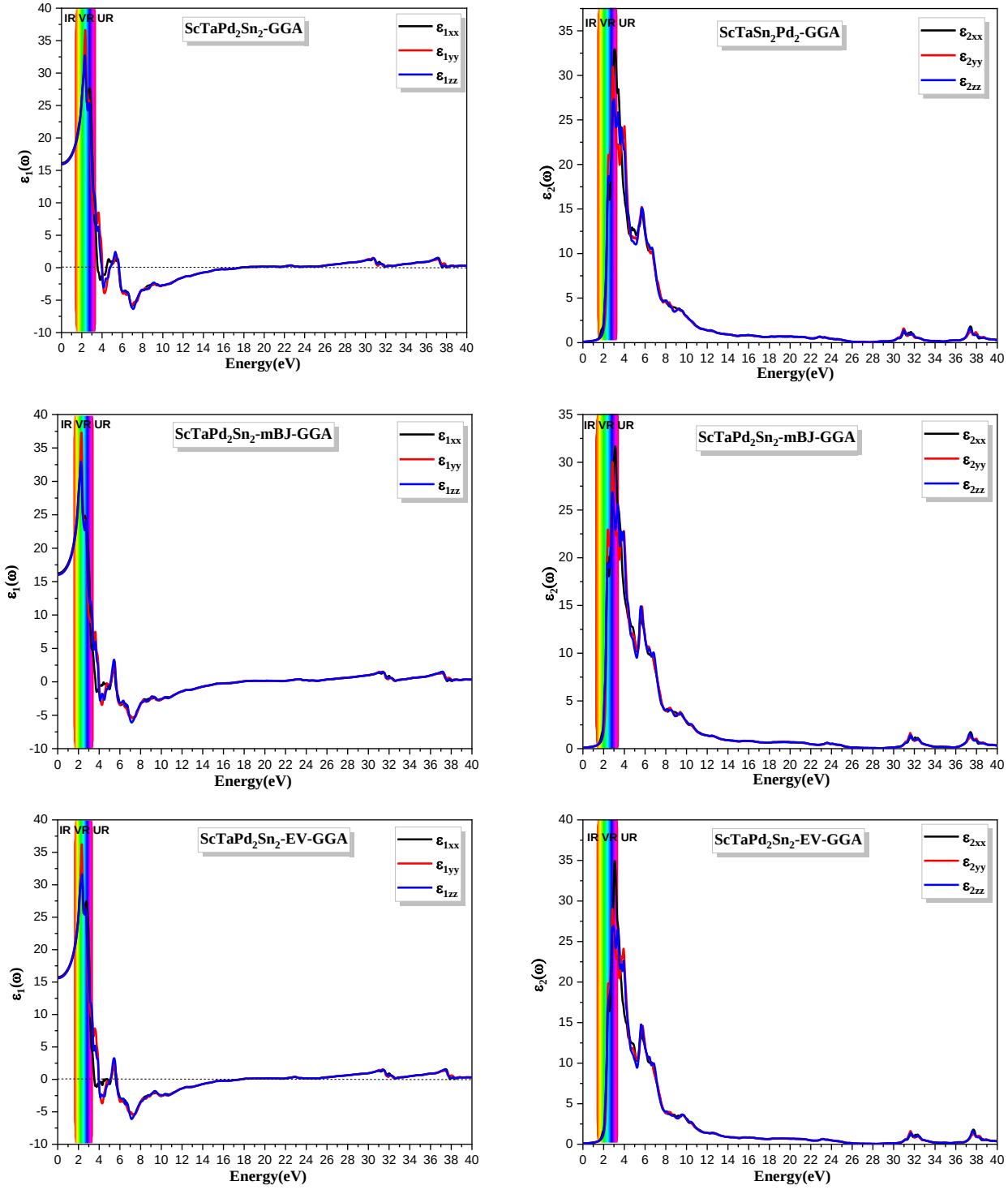

Figure.III.16.a: Variation of **(a)** the real part ε_1, **(b)** the imaginary part of the dielectric function for the $ScTaPd_2Sn_2$ alloy within the GGA, mBJ-GGA and EV-GGA approximations.

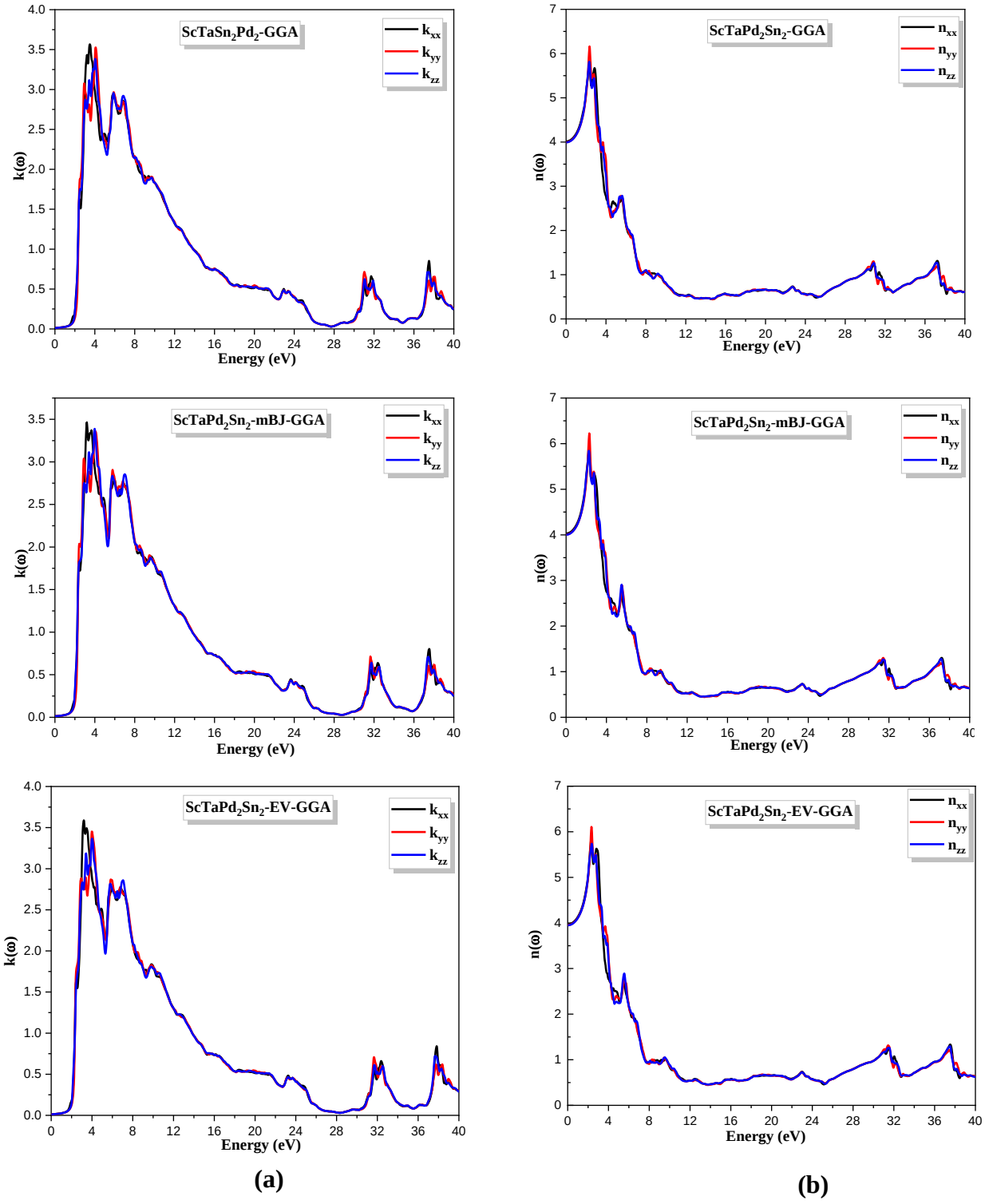

Figure.III.16.b: Optical spectra as a function of photon energy (**a)** the extinction coefficient, **(b)** the refractive index for the $ScTaPd_2Sn_2$ alloy within the GGA, mBJ-GGA and EV-GGA approximations.

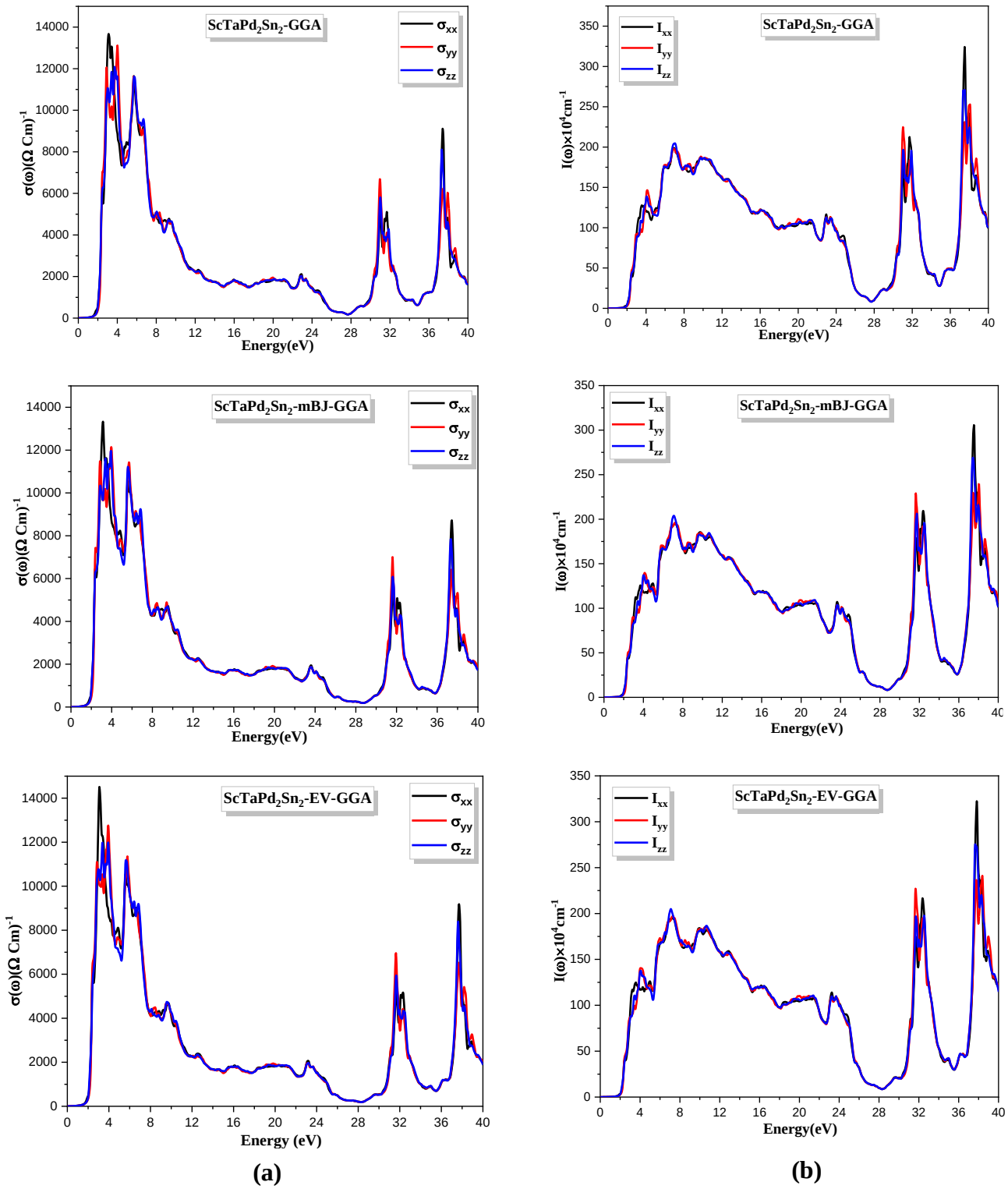

Figure.III.16.c: Variation of **(a)** the optical conductivity, and **(b)** the absorption coefficient for the $ScTaPd_2Sn_2$ alloy within the GGA, mBJ-GGA and EV-GGA approximations.

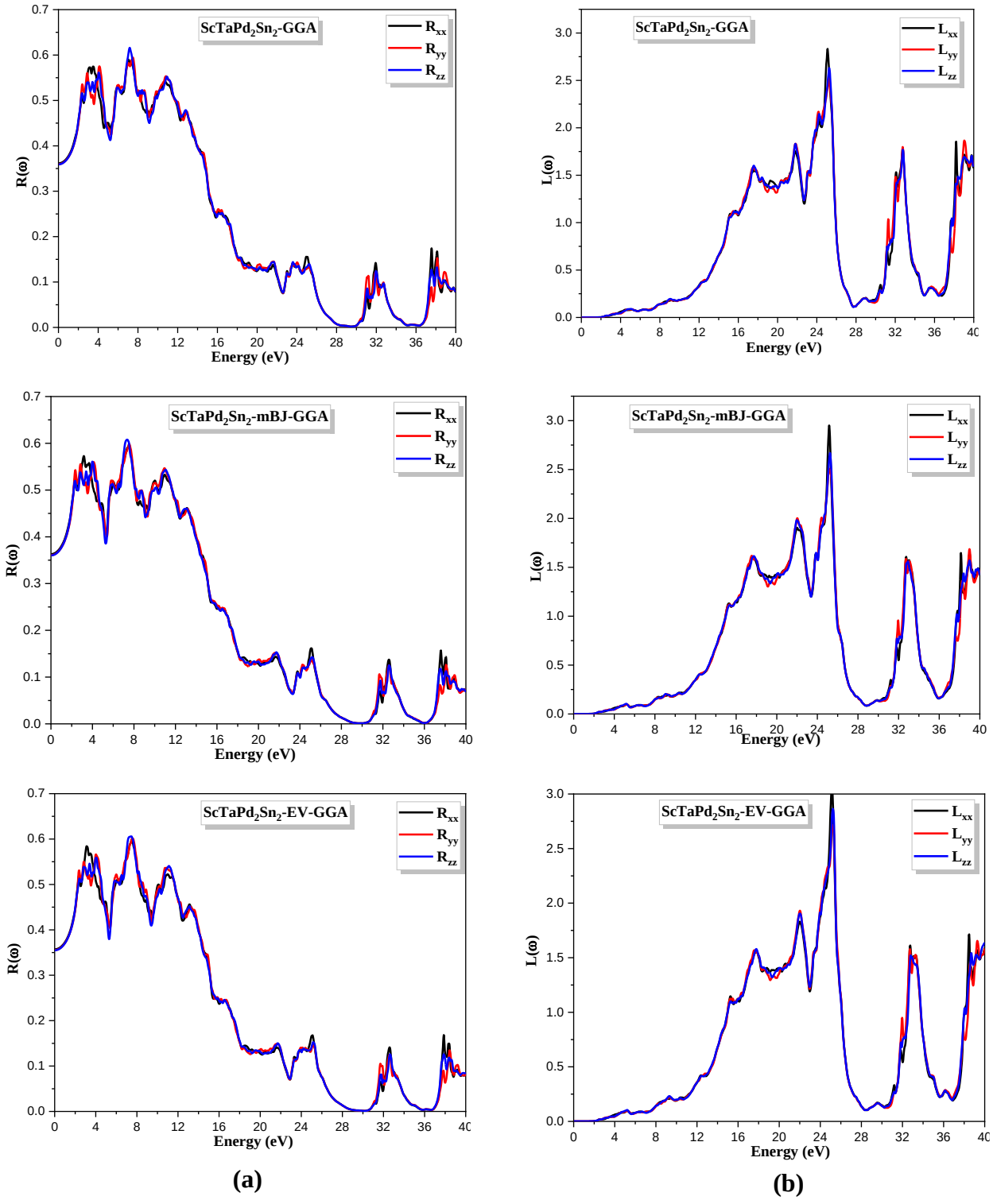

Figure.III.16.d: Optical spectra as a function of photon energy **(a)** reflectivity spectra, and **(b)** the energy loss function for the $ScTaPd_2Sn_2$ alloy within the GGA, mBJ-GGA and EV-GGA approximations.

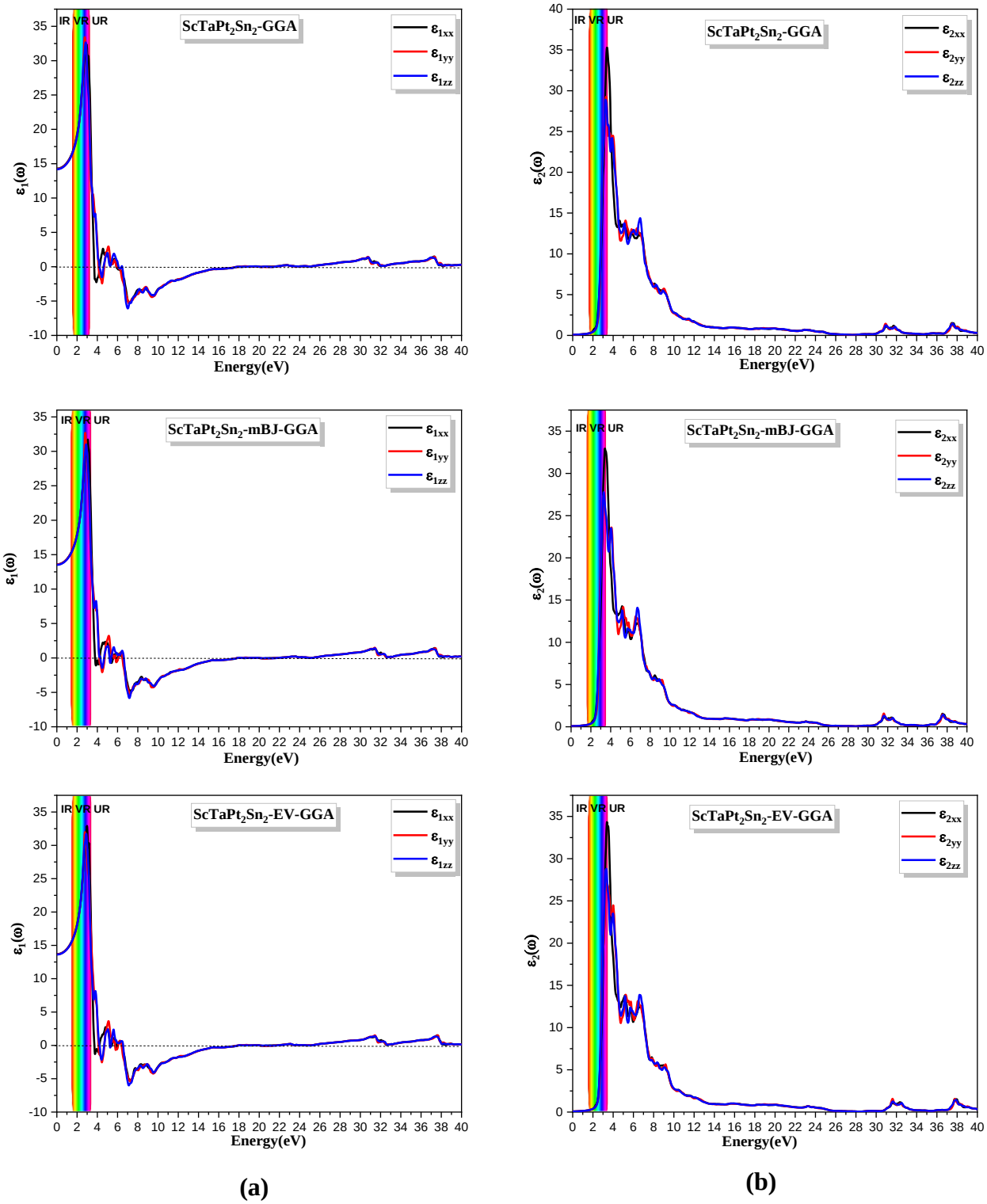

Figure.III.17.a: Variation of **(a)** the real part ε_1, **(b)** the imaginary part of the dielectric function for the $ScTaPt_2Sn_2$ alloy within the GGA, mBJ-GGA and EV-GGA approximations.

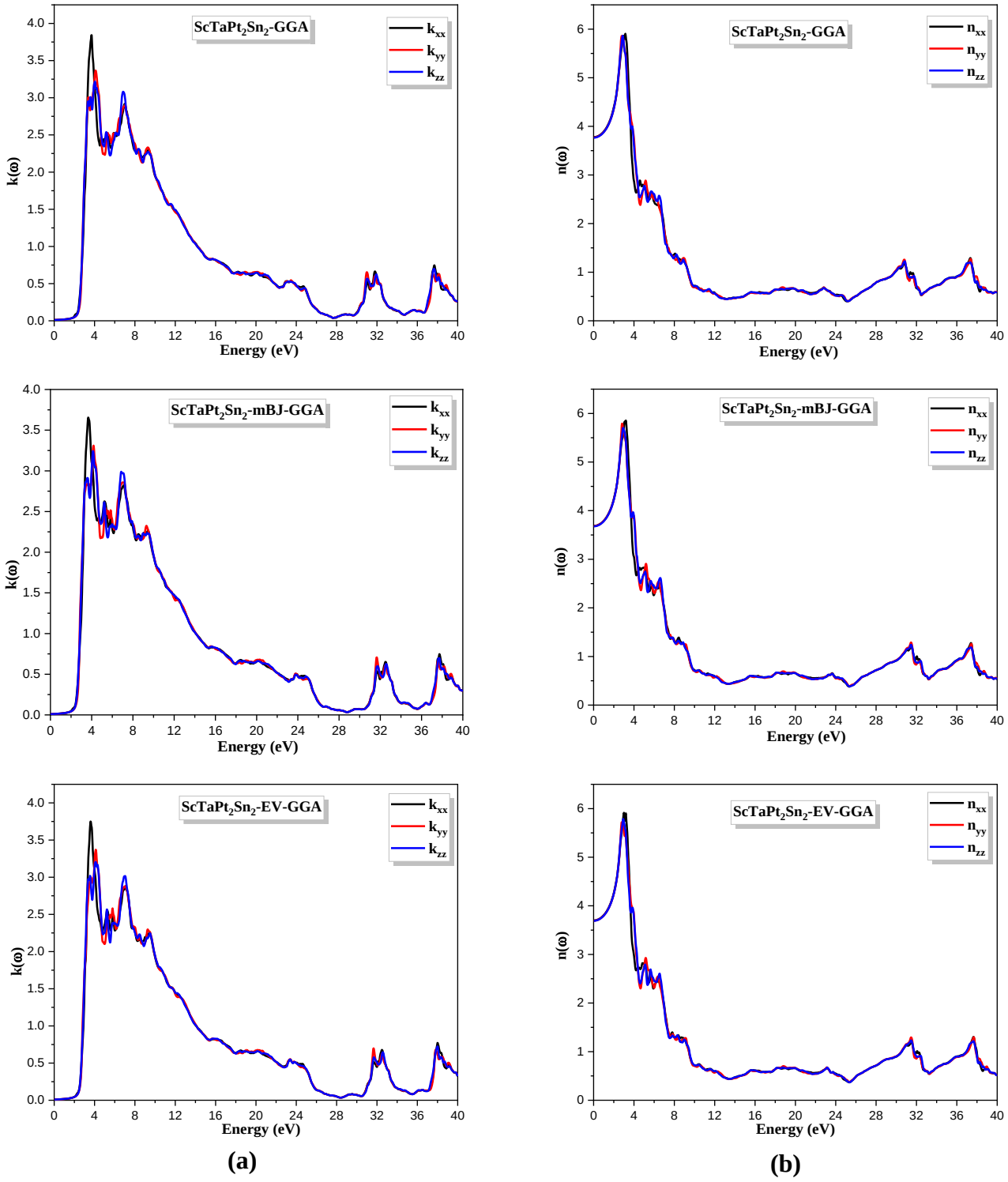

Figure.III.17.b: Optical spectra as a function of photon energy (**a)** the extinction coefficient, **(b)** the refractive index for the $ScTaPt_2Sn_2$ alloy within the GGA, mBJ-GGA and EV-GGA approximation

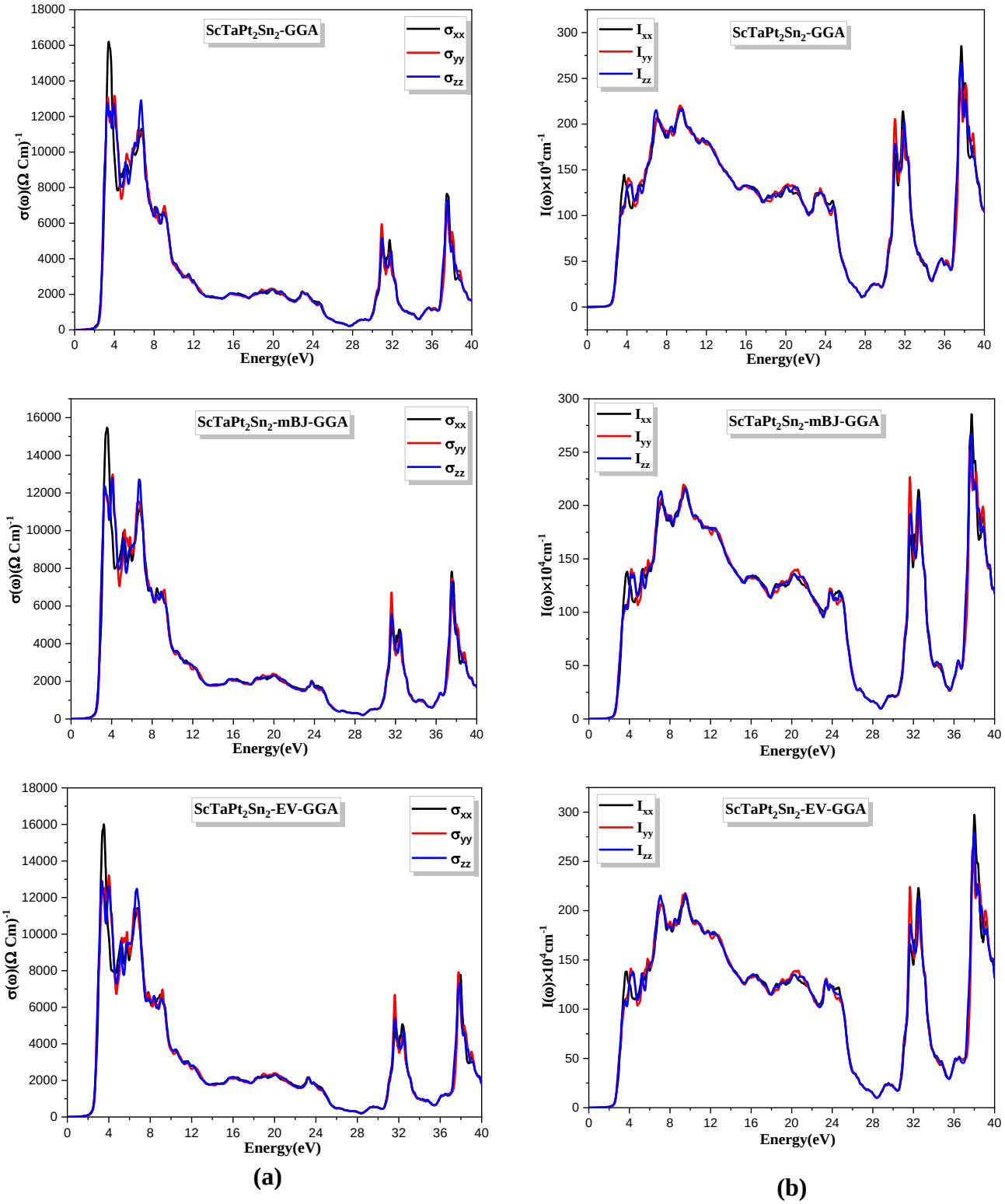

Figure.III.17.c: Variation of **(a)** the optical conductivity, and **(b)** the absorption coefficient for the $ScTaPt_2Sn_2$ alloy within the GGA, mBJ-GGA and EV-GGA approximations.

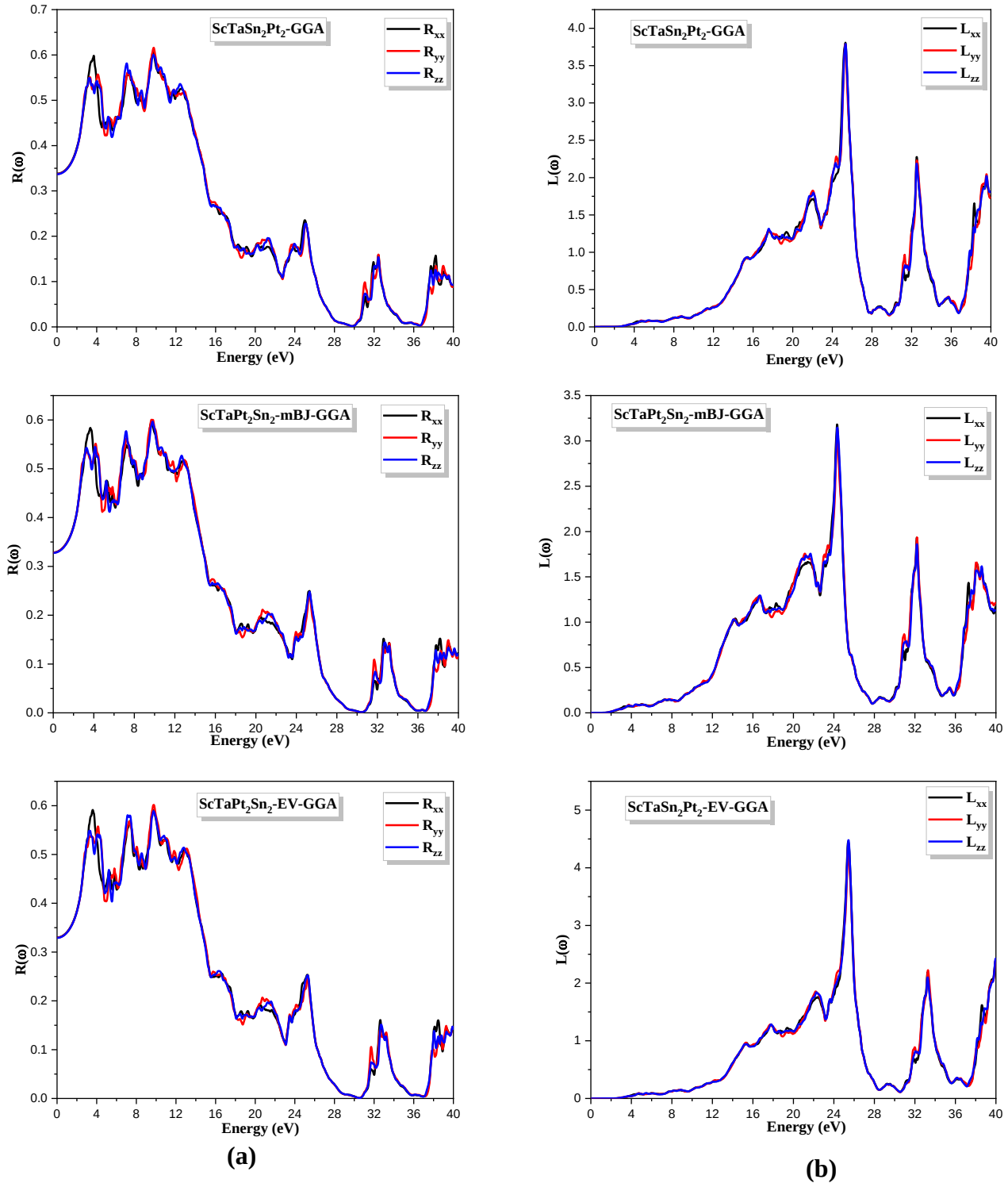

Figure.III.17.d: Optical spectra as a function of photon energy **(a)** reflectivity spectra, and **(b)** the energy loss function for the $ScTaPt_2Sn_2$ alloy within the GGA, mBJ-GGA and EV-GGA approximations.

III.6. Elastic properties

The mechanical response of solids is typically identified by essential stress-strain relationships. Elastic deformation refers to a type of deformation in which the stress is a linear function of the strain. In simple terms, stress and tension adhere to Hooke's law. Apart of the linear domain, stress and strain exhibit non-linear characteristics. The phenomenon of this non-reversible response is referred to as plastic deformation (see figure. III.18). Hooke's law states that the relationship between stress σ_{ij} and strain ε_{kl} is as follows in the elastic region:

$$\sigma_{ij} = \sum_{kl} C_{ijkl}\varepsilon_{kl} \qquad \text{(III-15)}$$

Where i, j, k, and l are indices ranging from 1 to 3. The elastic constants, denoted as C_{ijkl}, constitute a tensor of fourth-order elasticity. Typically, it consists of 3^4 components, resulting in a total of 81. The number of independent elastic constants is reduced to 21 as a result of symmetry C_{ijkl}, C_{ijlk}, C_{jikl}, C_{klij} [181,182]. On certain occasions, employing matrix notation, specifically Voigt notation, can be efficient in order to arrange the twenty-one constants in a symmetric 6 × 6 matrix. By utilizing the Voight notation, equation (III-15) can be expressed as:

$$\sigma_{\alpha} = \sum_{\beta} C_{\alpha\beta}\varepsilon_{\beta} \qquad \text{(III-16)}$$

The new α and β indices range from 1 to 6. Crystal symmetry can further decrease the number of elastic constants, in the case of cubic crystals, three independent parameters are present: C_{11}, C_{12}, C_{44}.

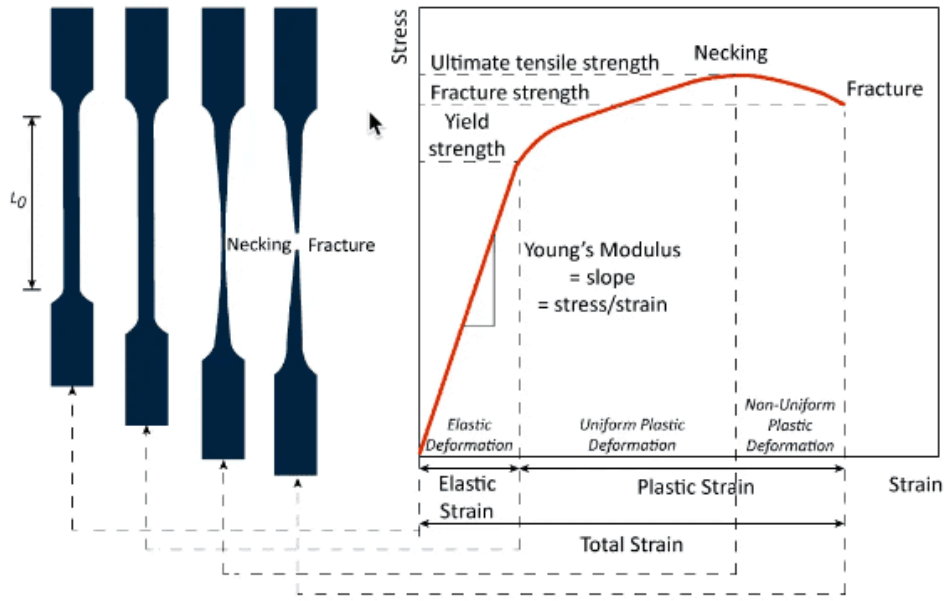

Figure. III.18: Shape changes of a test sample during stress-strain curve stages [183].

III.6. 1. Case of a crystal with orthorhombic symmetry:

In order to comprehend the elastic behavior and get the elastic constants (components of the elasticity tensor C) of a material with orthorhombic symmetry, normal and shear strain must be applied to a unit-cell volume of the solid.

The orthorhombic system exhibits the subsequent regularities $\left(a \neq b \neq c, \alpha = \beta = \gamma = 90^{\circ}\right)$ and the elasticity tensor C consists of 9 independent constants. Figure. III.19 illustrates the response of the unit-cell volume under strain.

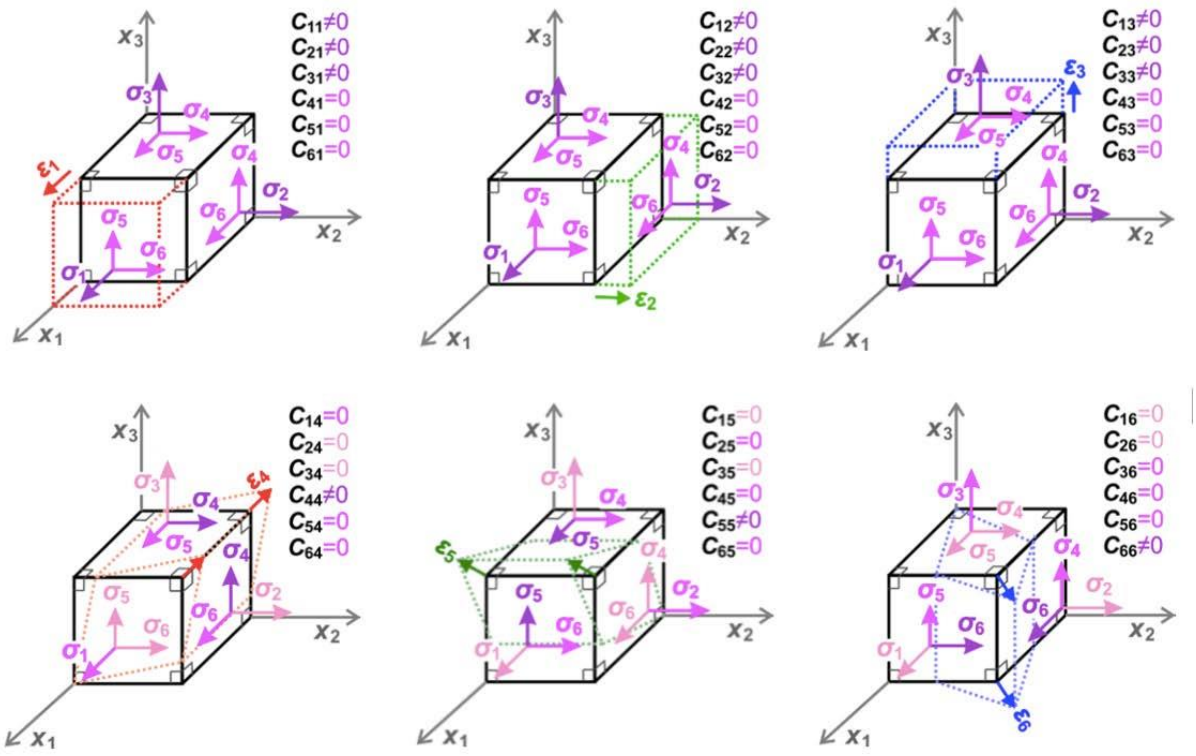

Figure. III.19: The unit cell with orthorhombic symmetry is subjected to shear and normal strain.

It is evident that normal strain does not induce shear stress, resulting in the equality of the following components of the elasticity tensor to zero:

$$C_{41} = C_{51} = C_{61} = C_{42} = C_{52} = C_{62} = C_{43} = C_{53} = C_{63} = 0 \qquad \text{(III-17)}$$

The component C_{ij} of the elasticity tensor relates the stress σ_i and strain ε_j . Furthermore, the shear strain does not induce normal shear stresses, leading to:

$$C_{45} = C_{46} = C_{56} = 0 \qquad \text{(III-18)}$$

An elasticity tensor for the orthorhombic symmetry system includes nine distinct components that are not equal to zero.

The matrix $[C]$ is expressed as [184-186]:

$$C_{ij} = \begin{bmatrix} C_{11} & C_{12} & C_{13} & 0 & 0 & 0 \\ 0 & C_{22} & C_{23} & 0 & 0 & 0 \\ 0 & 0 & C_{33} & 0 & 0 & 0 \\ 0 & 0 & 0 & C_{44} & 0 & 0 \\ 0 & 0 & 0 & 0 & C_{55} & 0 \\ 0 & 0 & 0 & 0 & 0 & C_{66} \end{bmatrix} \quad \text{(III-19)}$$

The elastic compliances matrix $[S]$, which has the same form as $[C]$, is reciprocally related to the matrix $[C]$ by Hooke's relation, and may thus be represented as follows [186]:

$$S_{ij} = \begin{bmatrix} S_{11} & S_{12} & S_{13} & 0 & 0 & 0 \\ 0 & S_{22} & S_{23} & 0 & 0 & 0 \\ 0 & 0 & S_{33} & 0 & 0 & 0 \\ 0 & 0 & 0 & S_{44} & 0 & 0 \\ 0 & 0 & 0 & 0 & S_{55} & 0 \\ 0 & 0 & 0 & 0 & 0 & S_{66} \end{bmatrix} \quad \text{(III-20)}$$

S_{ij} component explicit equations as a function of C_{ij} terms are given by [187]:

$$\begin{aligned} &S_{11} = \left(C_{22}C_{33} - C^2{}_{23}\right)/\Delta \ , S_{22} = \left(C_{11}C_{33} - C^2{}_{13}\right)/\Delta \ , \ S_{33} = \left(C_{11}C_{22} - C^2{}_{12}\right)/\Delta \\ &S_{12} = \left(C_{13}C_{23} - C_{12}C_{23}\right)/\Delta \ , S_{13} = \left(C_{12}C_{23} - C_{13}C_{22}\right)/\Delta \ , S_{23} = \left(C_{12}C_{13} - C_{11}C_{23}\right)/\Delta \end{aligned} \quad \text{(III-21)}$$

Where $Sii = \dfrac{1}{Cii}$ (i=4, 5, 6), Δ is defined as:

$$\Delta = C_{13}\left(C_{12}C_{23} - C_{13}C_{22}\right) + C_{23}\left(C_{12}C_{13} - C_{23}C_{11}\right) + C_{33}\left(C_{11}C_{12} - C_{12}^2\right) \quad \text{(III-22)}$$

The elastic compliances S_{ij} are calculated so that they can be used to compute mechanical parameters such as Young's modulus and Poisson's coefficient.

III.6. 2. Mechanical Properties

Mechanical characteristics refer to the response of a material to external forces and the resulting deformations. These forces can be exerted through several means, such as tension, compression, shear, or torsion. Comprehending these characteristics is essential for choosing appropriate materials for various technical purposes. The elastic modulus is a fundamental mechanical property that quantifies a material's ability to resist elastic deformation when subjected to stress such as bulk modulus B , shear modulus G , Young modulus E and Poisson ratio ν . These will be further described in the parts that follow.

III.6. 2. 1. Mechanical stability criteria of the crystal

The concept of mechanical stability in unstressed crystalline structures was first introduced by Max Born and colleagues in the 1940 [188,189]. Subsequent textbooks typically outline the fundamental criteria for elastic stability in crystal lattices and provide simplified versions of these criteria for certain crystal classes with high symmetry. Specifically, for orthorhombic crystals, the stability criteria are simplified to a straightforward form [190]:

$$\begin{aligned} &C_{11}>0, C_{22}>0, C_{33}>0, C_{44}>0, C_{55}>0, C_{66}>0, \left[C_{11}+C_{22}-2C_{12}\right]>0, \\ &\left[C_{11}+C_{33}-2C_{13}\right]>0, \left[C_{22}+C_{33}-2C_{23}\right]>0, C_{11}+C_{22}+C_{33}+2\left[C_{12}+C_{13}+C_{23}\right]>0, \\ &\frac{1}{3}\left[C_{12}+C_{13}+C_{23}\right]<B<\frac{1}{3}\left[C_{11}+C_{22}+C_{33}\right] \end{aligned} \qquad \text{(III-23)}$$

The equations shown above, which pertain to the orthorhombic crystal system, are widely recognized and denoted to as the 'Born stability criteria'.

The elastic behavior of an orthorhombic structure is determined by nine independent constants, as previously stated, these constants are: $\left(C_{11}, C_{22}, C_{33}, C_{12}, C_{13}, C_{23}, C_{44}, C_{55}, C_{66}\right)$, where C_{11}, C_{22} and C_{33} reflect the resistance to the unidirectional compression respectively along the main directions $[100], [010]$ and $[001]$(i.e. along the main axes a, b and c). However, the remaining ones show shear stress resistances $C_{12}, C_{13}, C_{23}, C_{44}, C_{55}$ and C_{66}. Table.III.10 show that C_{22} value of $ScTaPd_2Sn_2$ and $ScTaPt_2Sn_2$ is larger than C_{11} and C_{33} which indicate the strong resistance to deformation on the b-axis than the c-axis and the a-axis, therefore C_{11} and C_{22} are higher than the $ScNbNi_2Sn_2$ alloy revealing that both compounds $ScTaPd_2Sn_2$ and $ScTaPt_2Sn_2$ has strong

deformation resistance along a-axis and b-axis, also C_{44} has higher value comparing to $ScNbNi_2Sn_2$, as well as we can state that these DHH alloys display elastic anisotropy.

Table III.11: The elastic constants for DHH alloys $ScX'Y_2Sn_2$ (X'=Nb, Ta; Y=Ni, Pd, Pt) computed using GGA approximation.

Elastic Constants	***Alloys***		
	$ScNbNi_2Sn_2$	***$ScTaPd_2Sn_2$***	***$ScTaPt_2Sn_2$***
C_{11}	210.4750	244.5670	275.1153
C_{22}	235.4668	246.9794	277.4895
C_{33}	234.2404	198.7872	226.3281
C_{44}	74.3929	97.0080	108.2926
C_{55}	72.3223	94.0026	104.3802
C_{66}	72.9843	47.3981	54.3908
C_{12}	77.6167	57.8910	66.4894
C_{13}	78.0717	104.2453	115.6720
C_{23}	90.5160	106.8555	120.1886
A_1	1.0311	1.6521	1.6037
A_2	1.0021	1.6203	1.5848
A_3	1.0042	0.5045	0.6772

III.6. 2. 2. Bulk modulus B

The bulk modulus B, commonly known as the modulus of compressive stiffness, is the ratio of the hydrostatic pressure to the fractional change in volume caused by this pressure [191]. Therefore, it indicates the resistance of a material to volume changes when compressed from all directions.

$$B = -V\frac{\partial P}{\partial V} \tag{III-24}$$

Where V represents the volume of the body when pressure P is applied.

As B increases, the material becomes less compressible. The modulus of compressibility quantifies the ability of solids to resist changes in volume, providing an indication of a material's elasticity in response to external hydrodynamic pressure.

III.6. 2. 3. Shear modulus G

The shear modulus of elasticity is a fundamental parameter used to quantify the mechanical characteristics of solid materials. The formula for shear modulus can be formally represented as:

$$G = \frac{\tau}{\gamma} \tag{III-25}$$

G represents the shear modulus.

τ represents the shear stress.

γ represents the measure of shear strain.

III.6. 2. 4. Pugh's index (B/G)

Ductility is a fundamental property. It is a measure of how much material may be deformed before breaking, whereas brittle material fractures or breaks easily without indicating deformation. In the early 1950s, Pugh employed empirical reasoning to establish a correlation between the bulk modulus (B) and the shear modulus B/G [192]. This criterion has since been extensively utilized

to determine whether a material will exhibit brittle or ductile behavior. For a material with a $B/G \rangle 1.75$ ratio, it exhibits ductile behavior. Otherwise, the material is considered brittle.

III.6. 2. 5. Young's modulus E

Young's modulus, commonly referred to as the elastic modulus or modulus of elasticity, is a mechanical characteristic that quantifies the rigidity or flexibility of a substance. The concept is named after the British physicist Thomas Young, who initially introduced it, which is determined by the ratio of stress to strain within the elastic limit, Young's modulus (E) is defined by the equation:

$$E = \frac{\sigma}{\varepsilon} \tag{III-26}$$

E represents Young's modulus $[MPa]$.

σ represents stress exerted on the material $[MPa]$.

ε represents the strain that the material undergoes (% or unitless).

III.6. 2. 6. Poisson's ratio

The ratio is named after Simeon Poisson, a French physicist and mathematician and is symbolized by the Greek letter 'nu'. It is a dimensionless parameter that links lateral strain (perpendicular to applied stress) to axial strain. This ratio is a measure of the change in volume that occurs during elastic deformation [193]. Theoretically, the value is precisely 0.25 for a fully isotropic material, if the value is 0.5, the material is considered to be absolutely incompressible, meaning there will be no change in volume. mechanical quantity Poisson's ratio describes bonding forces. The lower and upper limits for the central force, as determined by Poisson's ratio assessment, are 0.25 and 0.5, respectively [193].

Consequently, the constants B , E , G , and ν are not independent and can each be represented as a function of two of them. Hill compressibility modulus and shear modulus are:

$$G_H = \frac{1}{2}\left(G_V + G_R\right) \text{ and } B_H = \frac{1}{2}\left(B_V + B_R\right) \tag{III-27}$$

Young's modulus E and Poisson's ratio ν [193] are given by:

$$E = \frac{9BG}{(G+3B)} \qquad \nu = \frac{3B-2G}{2(3B+G)} = \frac{1}{2}\left(1-\frac{E}{3B}\right) \qquad \text{(III-28)}$$

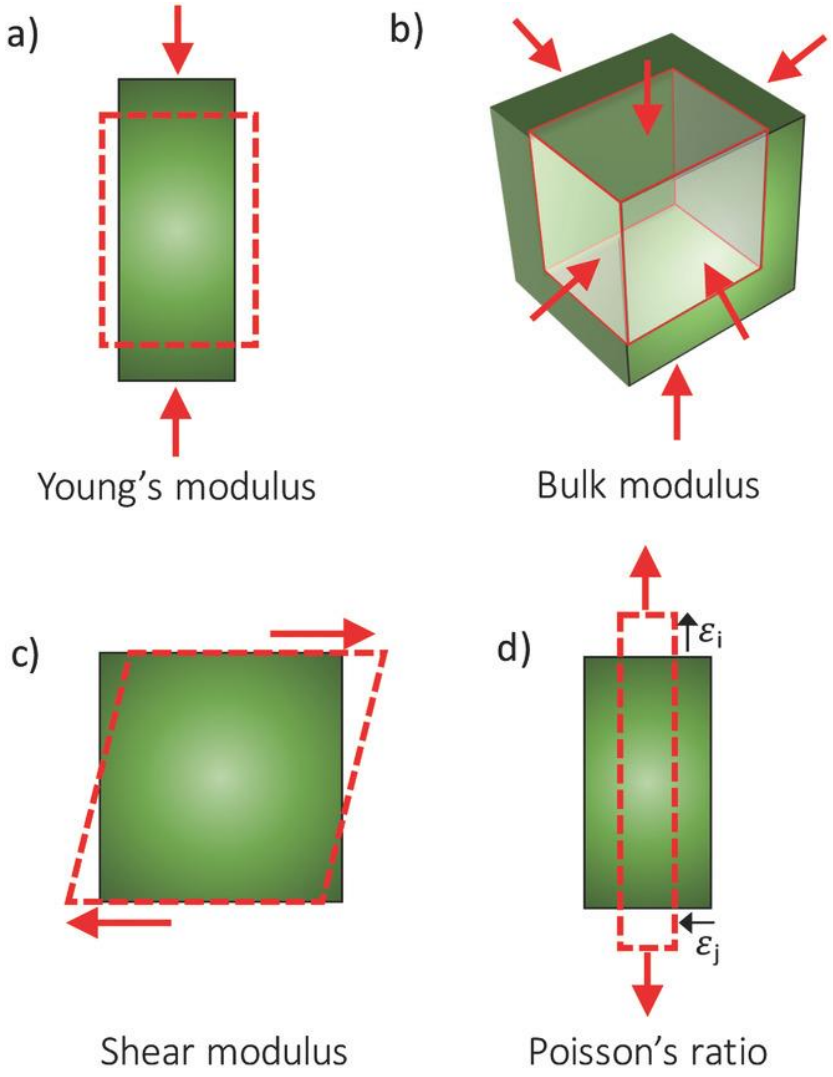

Figure.III.20: Elastic properties in solids include a) Young's modulus E, b) bulk modulus B, c) shear modulus G, and d) Poisson's ratio ν [194].

III.6. 2. 7. Hardness

The material's hardness is a crucial factor in the fields of materials science and material engineering. it refers to the ability of a material to resist localized plastic deformation. The modeling of elastic properties using Density Functional Theory (DFT) can be expressed as [195]:

$$H = \frac{(1-2\nu)E}{6(1+\nu)} \quad \text{(III-30)}$$

Table III.12 presents the values of the bulk modulus (B), Young modulus (E), shear modulus (G) Poisson ratio (ν) and hardness computed using GGA approximation at zero temperature.

Start with the compressibility modulus B so $ScTaPt_2Sn_2$ has high value than the $ScTaPd_2Sn_2$ and $ScNbNi_2Sn_2$ alloys ($B_{H\ ScTaPt2Sn2}$ =153.729 GPa > $B_{H\ ScTaPd2Sn2}$ =136.47 GPa > $B_{H\ ScNbNi2Sn2}$ =129.93 GPa) which indicate that $ScTaPt_2Sn_2$ exhibit elastic stiffness more than the $ScTaPd_2Sn_2$ and $ScNbNi_2Sn_2$ compounds, as well as , The zero-pressure bulk modulus reported in Table III.10 is close to that from the equation of Murnaghan (EOS) for the $ScTaPd_2Sn_2$ and $ScTaPt_2Sn_2$ compounds, with regards to $ScNbNi_2Sn_2$ the value of the bulk modulus from the elastic constants it is slightly far from the (EOS). These alloys have a high shear modulus (71.5 GPa, 80.8 GPa and 72.8 GPa) and are slightly close to one another, our DHH alloys $ScTaSn_2Pd_2$, $ScTaPt_2Sn_2$ and $ScNbNi_2Sn_2$ have strong atomic bonding.

Pugh [192] introduced the bulk to shear modulus (B/G) ratio as an indicator of ductile versus brittle characteristics. If the B/G ratio is more than 1.75, the material is ductile, otherwise, the material is brittle. Both compounds have B/G ratios greater than 1.75, indicating that DHH alloys are ductile. The ratio of tensile stress to tensile strain is defined as the young modulus E which is large for $ScTaPt_2Sn_2$ comparing to the alloys $ScNbNi_2Sn_2$, $ScTaPd_2Sn_2$.

The dimensionless amount the Poisson's ratio is a measure of how well a material resists lateral deformation. For stable alloys, the Poisson's ratio value of a solid is 1 to 0.5 [196]. Table III.10 shows the Poisson's ratio values are in range of 0.263-0.276 for the DHH alloys which confirming that these alloys are stable under shear stress, this suggests that $ScTaPd_2Sn_2$ and $ScTaPt_2Sn_2$ are contracted by 27.6%, and $ScNbNi_2Sn_2$ around 26.3%, respectively. The Poisson ratio is an additional criterion for determining whether a material is brittle or ductile. Specifically, if ν is below 0.26, the material is brittle, otherwise, it is ductile. in the case of our DHH alloys, this value

verifies that these alloys are ductile. Furthermore, the value of ν is about 0.26 which falls within the range of 0.25 to 0.5 this suggests that the bonding in these alloys have an ionic character and the inter-atomic forces are centrally located.

The $ScTaPt_2Sn_2$ DHH exhibits the maximum hardness of 12.08 GPa among other DHH alloys, such as $ScTaPd_2Sn_2$ and $ScNbNi_2Sn_2$, as indicated in Table III.10. Furthermore, the hardness values of our DHH alloys are all equal to or greater than 10 GPa, thereby classifying them as hard materials.

III.6. 3. Elastic anisotropy

Anisotropic behavior is an essential feature that defines the different arrangement of atoms in various orientations. Anisotropic behavior has significant implications for both crystal physics and engineering research. In other word, the degree of anisotropy in the bonding between atoms in various planes is quantified by the shear anisotropic factors. for the shear anisotropy factor for the {100} shear planes between the <011> and <010> directions is [197].

$$A_1 = 4C_{44} / \left(C_{11} + C_{33} - 2C_{13}\right) \quad \text{(III-31)}$$

For the shear anisotropy factor for the {010} shear planes between the <101> and <001> directions [197].

$$A_2 = 2C_{66} / \left(C_{11} - C_{12}\right) \quad \text{(III-32)}$$

Finally, for the shear anisotropy factor for the {001} shear planes between the <110> and <010> directions is [197].

$$A_3 = 4C_{66} / \left(C_{11} - 2C_{12} + C_{22}\right) \quad \text{(III-33)}$$

As well, for isotropic crystals, the factors A_1, A_2 and A_3 must be one. We might confirm that the crystal has elastic anisotropy if any of the three factors is lower or larger than one the crystal represents the degree of the anisotropy.

From Table III.9, it seems that the shear anisotropy for $ScTaPd_2Sn_2$ and $ScTaPt_2Sn_2$ is larger in (100) and (010) shear planes, further the $ScNbNi_2Sn_2$ alloy has shear anisotropy 1 for all three factors which confirm that this alloy has a good isotropy comparing to $ScTaPd_2Sn_2$ and $ScTaPt_2Sn_2$.

The percentage anisotropy for the bulk modulus A_B and shear modulus A_G is given by [198]:

$$\begin{cases} A_B = \left(B_V - B_R\right)/\left(B_V + B_R\right)\times 100 \\ A_G = \left(G_V - G_R\right)/\left(G_V + G_R\right)\times 100 \end{cases} \quad \text{(III-34)}$$

The universal anisotropy index (A^U) is given by [199]:

$$A^U = 5\frac{G_V}{G_R} + \frac{B_V}{B_R} - 6 \quad \text{(III-35)}$$

The values of A_B, A_G, and A^U must be zero for an isotropic material. The degree of anisotropy is represented by a deviation larger than zero. From Table III.11the percentage of bulk modulus A_B% for $ScTaPd_2Sn_2$, $ScTaPt_2Sn_2$ and $ScNbNi_2Sn_2$ is zero because the Voigt and Reuss approaches anticipate the same values for the bulk modulus, indicating that these compounds are slightly isotropic in compressibility. Likewise, the value of the shear modulus percentage is zero for $ScNbNi_2Sn_2$ while $ScTaPd_2Sn_2$ and $ScTaPt_2Sn_2$ have 5.85% 5.3% shear modulus respectively. Thus, are characterized by significant anisotropy in shear modulus and isotropy in bulk modulus.

The study mentioned above is insufficient to adequately characterize the elastic properties of a crystal. Surface structures that show the linear compressibility and the reciprocal of Young's modulus with directions are useful in fact.

The orthorhombic system's linear compressibility is [200]:

$$\beta = n_1^2\left(S_{11} + S_{12} + S_{13}\right) + n_2^2\left(S_{12} + S_{22} + S_{23}\right) + n_3^2\left(S_{13} + S_{23} + S_{33}\right) \quad \text{(III-36)}$$

S_{ij} are the elastic constants of deformability, and n_1, n_2, n_3 : are the directional cosines (in spherical coordinates) following *x, y* and *z*, respectively.

The orthorhombic system defines the reciprocal of Young's modulus E in the direction of the unit vector n_i as [200]:

$$E = \frac{1}{n_1^4 S_{11} + 2n_1^2 n_2^2 S_{12} + 2n_1^2 n_3^2 S_{13} + n_2^4 S_{22} + 2n_2^2 n_3^2 S_{23} + n_3^4 S_{33} + n_2^2 n_3^2 S_{44} + n_1^2 n_3^2 S_{55} + n_1^2 n_2^2 S_{66}} \quad \text{(III-37)}$$

The linear compressibility of $ScNbNi_2Sn_2$, $ScTaPd_2Sn_2$, and $ScTaPt_2Sn_2$ is determined using the theoretical elastic constants depicted in Figure.III.21. (a), (b), and (c). The equations III-36 establish a three-dimensional surface, where the distance from the origin of coordinates to the surface

corresponds to the linear compressibility in a certain direction. The cubic system exhibits isotropic linear compressibility, resulting in a spherical form. The spherical form of Figure.III.21 (a), (b) and (c) illustrates the isotropic nature of linear compressibility of our three alloys $ScNbNi_2Sn_2$ $ScTaPd_2Sn_2$, and $ScTaPt_2Sn_2$. To obtain a more detailed and full understanding of the anisotropic features, it is necessary to examine the orientation-dependent linear compressibility in different planes, as seen in Figure.III.21 (d), (e) and (f) the elastic anisotropy in the (XY) plane is slightly higher than in the (XZ) plane for both $ScNbNi_2Sn_2$ and $ScTaPd_2Sn_2$ alloys. Additionally, the (YZ) plane has the highest elastic anisotropy in both alloys. However, in the $ScTaPt_2Sn_2$ alloy, the (XZ) plane has a larger elastic anisotropy than both the (XY) and (YZ) planes. Figure.III.22 (a), (b) and (c) depicts the predicted orientation-dependent Young's modulus for $ScNbNi_2Sn_2$, $ScTaPd_2Sn_2$, and $ScTaPt_2Sn_2$ alloys by employing the elastic compliance constants. A three-dimensional closed surface is defined by Equation (III-37) when the distance between the surface and the origin of coordinates is equal to Young's modulus in the specified direction. Evidently, the surfaces representing Young's modulus for both alloys $ScTaPd_2Sn_2$, and $ScTaPt_2Sn_2$ exhibited non-spherical shapes Consequently, these two alloys have a significant degree of anisotropy because of the different bonding characteristics between adjacent atomic planes. In other hand $ScNbNi_2Sn_2$ alloy has the spherical form that indicates the young modulus has the isotropic nature.

From Figure.III.22 (d), (e), and (f), the elastic anisotropy in the (X=Y), (XY) and (XZ) planes are almost identical whereas the (YZ) plane is slightly anisotropic for $ScNbNi_2Sn_2$, thus, this alloy is roughly isotropic. Regarding the alloys $ScTaPd_2Sn_2$ and $ScTaPt_2Sn_2$ they display a large elastic anisotropy in the (XY) plane while (X=Y), (XZ) and (YZ) planes are almost identical.

Table III.11: Modules of elasticity B_V, B_R, B_H, G_V, G_R, G_H, E_V, E_R, E_H, H, for DHH alloys $ScX'Y_2Sn_2$ (X'=Nb, Ta; Y=Ni, Pd, Pt) using GGA approximation.

Elasticity Modules	***Alloys***		
	$ScNbNi_2Sn_2$	***$ScTaPd_2Sn_2$***	***$ScTaPt_2Sn_2$***
B_V	130.287	136.479	153.736
B_R	129.586	136.472	153.722
B_H	129.936	136.475	153.729
G_V	72.870	75.77	85.184
G_R	72.783	67.391	76.602
G_H	72.826	71.58	80.893
E_V	184.257	191.813	215.710
E_R	183.916	173.598	197.071
E_H	184.086	182.783	206.464
σ_V	0.264	0.265	0.266
σ_R	0.263	0.287	0.286
σ_H	0.263	0.276	0.276
B_H/G_H	1.7841	1.906	1.9003
H	11.51	10.69	12.08
A_B%	0.269	$2.56x10^{-3}$	$4.55x10^{-3}$
A_G%	0.0597	5.852	5.3045
A^u	0.0113	0.621	0.5602

III.6.4. Debye temperature and elastic wave propagation velocities

The Debye temperature, as described in Debye theory, represents the maximum temperature that may be attained in a crystal due to the highest normal mode of vibration. The Debye temperature can be determined using the calculation of elastic constants, as opposed to relying on

measurements of specific heat at low temperatures. It is an additional fundamental physical term that serves to define phenomena in solid-state physics, including lattice vibration, elastic constants, specific heat, and melting point. Debye temperature magnitude is an important factor for determining the thermal conductivity of solid materials, greater values of the Debye temperature correspond to higher thermal conductivity.

The Debye temperature θ_D can be determined from the average sound velocity v_m as follows:

$$\theta_D = \frac{h}{k_B}\left(\frac{3n}{4\pi}\left(\frac{N_a\,\rho}{M}\right)\right)^{\frac{1}{3}} v_m \qquad \text{(III-38)}$$

Where *h* denotes Planck's constant, k_B Boltzmann's constant, N_a Avogadro's number, ρ molecule density, *M* denotes molecular weight, and *n* is the number of atoms in the molecule. In polycrystalline materials, the average velocity v_m is approximated by [201]:

$$v_m = \left(\frac{1}{3}\left(\frac{2}{v_t^3} + \frac{1}{v_l^3}\right)\right)^{-\frac{1}{3}} \qquad \text{(III-39)}$$

v_l and v_t are the propagation velocities of longitudinal and transverse elastic waves respectively. They are obtained using the stiffness modulus B, the shear modulus Get and the crystal density g from the Navier equation [202]:

$$v_l = \left(\frac{3B + 4G}{3\rho}\right)^{\frac{1}{2}} \qquad \text{(III-40)}$$

$$v_t = \left(\frac{G}{\rho}\right)^{\frac{1}{2}} \qquad \text{(III-41)}$$

The values of V_l, V_t, V_m and θ_D are presented in Table III.13 calculated at zero pressure for DHH $ScXX'Y_2Sn_2$ (X'=Nb, Ta; Y=Ni, Pd, Pt) using *GGA*. The alloy $ScNbNi_2Sn_2$ has the highest Debye temperature, whereas $ScTaPt_2Sn_2$ has the lowest. Therefore, the Debye temperature follows this order $\theta_{ScNbNi_2Sn_2} \rangle \theta_{ScTaPd_2Sn_2} \rangle \theta_{ScTaPt_2Sn_2}$. Consequently, the thermal conductivity of $ScNbNi_2Sn_2$ is higher than that of the other alloys.

Based on the data in the Table III.11, it can be observed that elastic compression waves, also known as longitudinal waves, propagate at a higher speed compared to elastic shear waves, also known as transverse waves by roughly $V_l \approx 2V_t$.

Table III.11: Longitudinal, transversal and average sound velocity (V_l V_t, V_m in m/s), Debye temperature (θ_D in K) for ScX'Y_2Sn_2 (X'=Nb, Ta; Y=Ni, Pd, Pt) using GGA approximation.

Alloys	***V_t (m/s)***	***V_l (m/s)***	***V_m (m/s)***	***Θ_D(K)***
$ScNbNi_2Sn_2$	3159.43	5578.47	3513.34	394.156
$ScTaPd_2Sn_2$	2783.84	5010.86	3100.51	338.605
$ScTaPt_2Sn_2$	2652.3	4769.52	2953.78	321.105

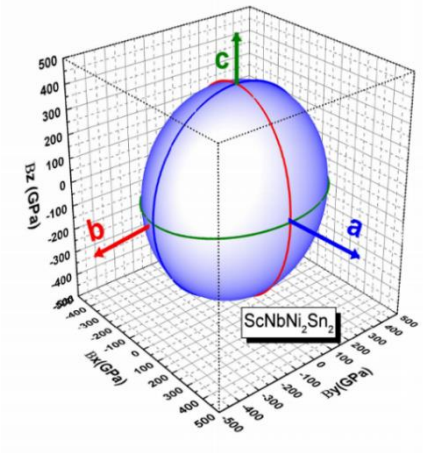

(a)

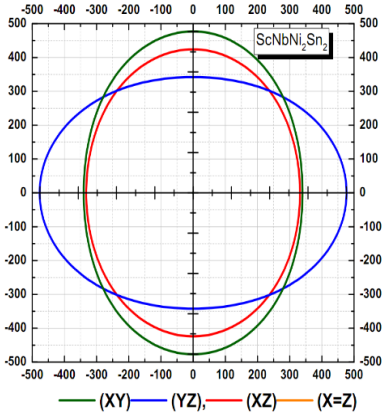

(d)

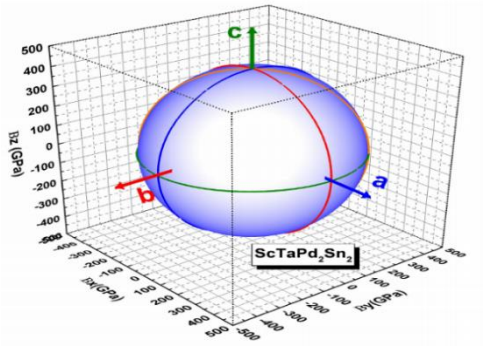

(b)

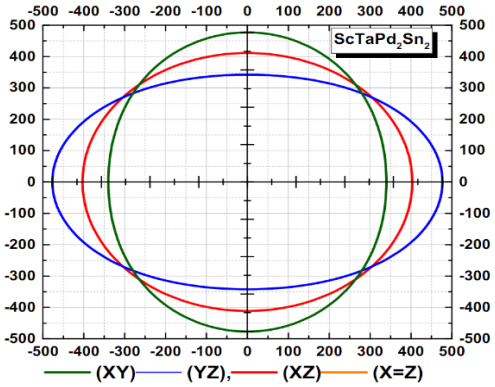

(e)

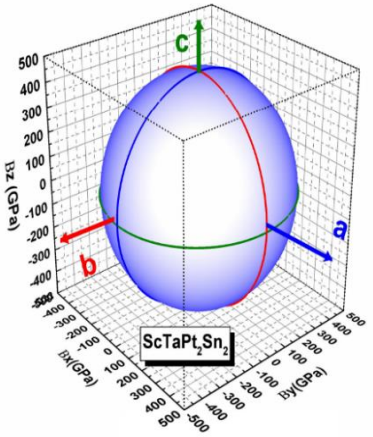

(c)

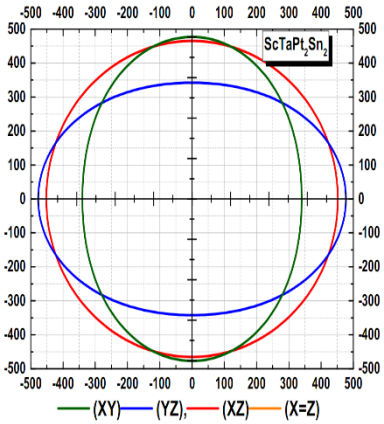

(f)

Figure.III.21: (a), (b) and (c) represent the orientation dependent linear compressibility of $ScNbNi_2Sn_2$, $ScTaPd_2Sn_2$ and $ScTaPt_2Sn_2$ respectively. (d) (e) and (f) represent linear compressibility projections in different planes for $ScNbNi_2Sn_2$, $ScTaPd_2Sn_2$ and $ScTaPt_2Sn_2$ respectively.

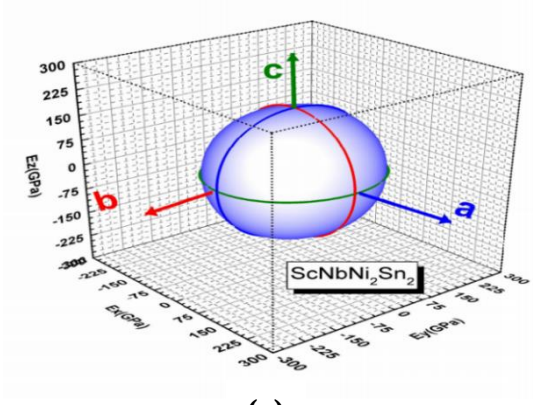

(a)

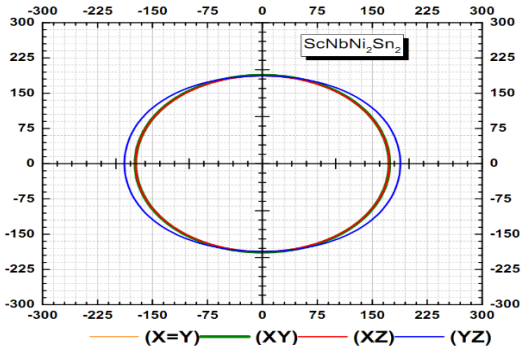

(d)

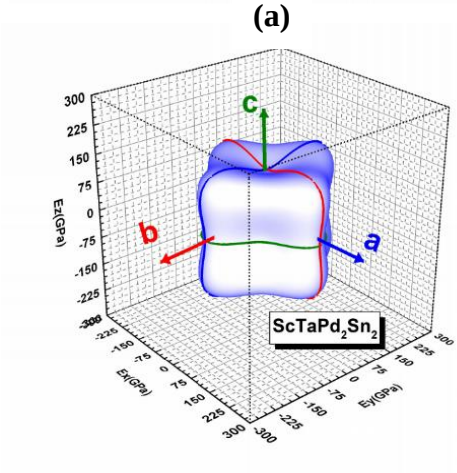

(b)

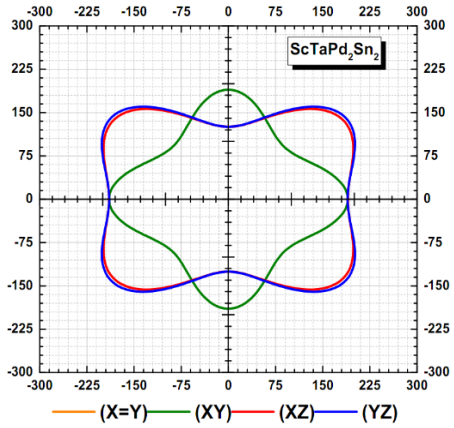

(e)

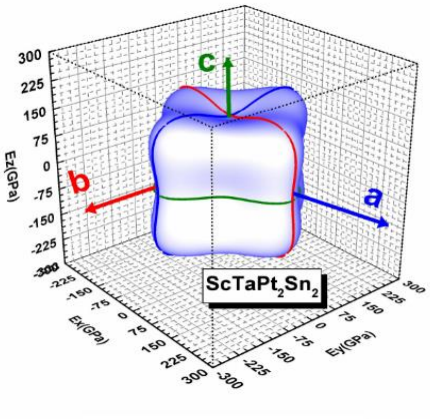

(c)

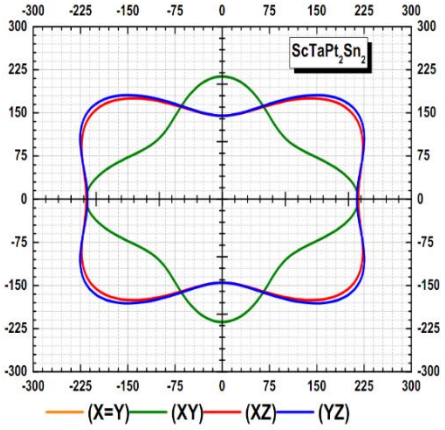

(f)

Figure.III.22: (a), (b) and (c) represent the 3D surface of the Young's modulus for (a) $ScNbNi_2Sn_2$, $ScTaPd_2Sn_2$ and $ScTaPt_2Sn_2$, (d) (e) and (f) their cross sections in different planes $ScNbNi_2Sn_2$, $ScTaPd_2Sn_2$ and $ScTaPt_2Sn_2$ respectively.

III.7. Thermoelectric properties

III.7. 1. Lattice thermal conductivity (LTC)

Lattice thermal conductivity is a crucial and essential physical parameter Which should be explore alongside the other factors that affect the alloy's thermoelectric performance. The lattice contribution k_L to k is a reasonably independent TE parameter that correlates inversely with ZT. Thus, in recent investigations, a reduction in the thermal conductivity of the lattice was performed. The slacks equation is a standard approximation for calculating lattice thermal conductivity [203, 204].

$$k_L = A.\frac{\bar{M}\theta^3\delta}{\gamma^2 T n^{2/3}} \quad \text{(III-42)}$$

Where A is a constant and $\bar{M}$ is the average mass, δ^3 is the average volume occupied by one atom, n is the number of atoms in the primitive unit cell, and the Grüneisen parameter γ is a dimensionless quantity describing the relationship between a variation in the frequency of a mode of vibration of a crystal structure and variation in volume. This parameter is frequently employed to describe the thermodynamic properties of solids under conditions of elevated pressures and temperatures and θ is the Debye temperature.

$$A = \left(2.43*10^{-8}\right) \Big/ \left(1-\left(0.514/\gamma\right)+\left(0.228/\gamma^2\right)\right) \quad \text{(III-43)}$$

According to the equation (III-42), a reduction in both the Debye temperature (θ) and atomic mass (M), accompanied by an elevation in the Grüneisen parameter (γ), and the number of atoms per unit cell (n). The following are the prerequisites for a material to achieve a low thermal conductivity (k_L).

The Debye temperature has been determined using the quasiharmonic Debye model, which was implemented in the original Gibbs code [205-208]. In the quasiharmonic approximation, the Gibbs free energy $G(\vec{x}; p, T)$ is the controlling function for the geometry and phase stability of a solid under constant temperature and pressure conditions. It can be mathematically stated as:

$$G(\vec{x};p,T) = E(\vec{x}) + pV(\vec{x}) + A_{vib}(\vec{x};T) \quad \text{(III-44)}$$

Where $E(\vec{x})$ is the total energy of the crystal, p and V are, respectively, the pressure and volume and $A_{vib}(\vec{x};T)$ is the Helmholtz vibrational free energy:

$$A_{vib}(\vec{x};T) = \int_0^{\infty} \left[\frac{\hbar\omega}{2} + K_B T \ln\left(1 - e^{-\frac{\hbar\omega t}{K_B T}}\right) \right] g(\vec{x};\omega)\, d\omega \quad \text{(III-45)}$$

Where $g(\vec{x};\omega)$ is the phonon density of states and K_B is the Boltzmann constant. Applying Debye's concept of the phonon density of states to express the vibrational contribution, the Helmholtz vibrational free energy can be expressed as a function of the Debye temperature θ :

$$A_{vib}(\theta;T) = nK_B T \left[\frac{9}{8}\frac{\theta}{T} + 3\ln\left(1 - e^{-\frac{\theta}{T}}\right) - D\left(\frac{\theta}{T}\right) \right] \quad \text{(III-46)}$$

Where $D\left(\frac{\theta}{T}\right)$ is the Debye integral, and is defined as:

$$D\left(\frac{\theta}{T}\right) = 3\left(\frac{T}{\theta}\right)^3 \int_0^{T/\theta} \frac{x^3}{e^x - 1} dx \quad \text{(III-47)}$$

The Debye temperature is determined by considering an isotropic solid as:

$$\theta = \frac{\hbar}{K_B}\left[6\pi^2 V^{1/2} n\right]^{1/3} f(\sigma)\sqrt{\frac{B_s}{M}} \quad \text{(III-48)}$$

Where is M the molecular mass, B_s the adiabatic compressibility modulus, σ the Poisson's ratio and f(σ) is given by the following formula:

$$f(\sigma) = \left\{ 3\left[2\left(\frac{2}{3}\frac{1+\sigma}{1-2\sigma}\right)^{3/2} + \left(\frac{1}{3}\frac{1+\sigma}{1-\sigma}\right)^{3/2} \right]^{-1} \right\}^{1/3} \quad \text{(III-49)}$$

The Grüneisen parameter can be expressed in terms of, by:

$$\gamma = -\frac{\partial \ln \theta(V)}{\partial \ln V} \quad \text{(III-50)}$$

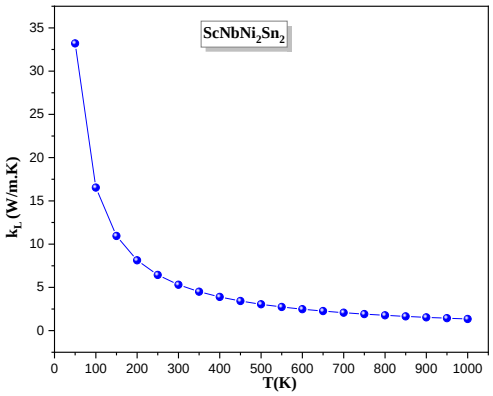

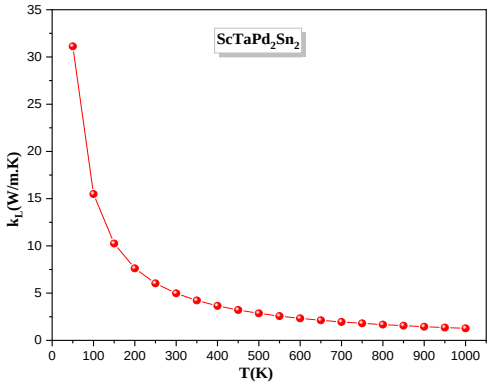

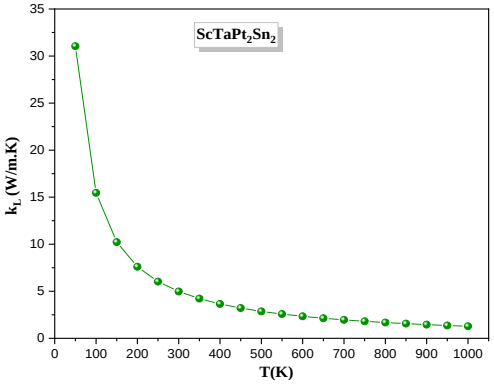

Figure.III.23.a: The lattice thermal conductivity k_L as a function of the temperature for the DHH alloys ScX'Y_2Sn_2 (X'=Nb, Ta; Y=Ni, Pd, Pt).

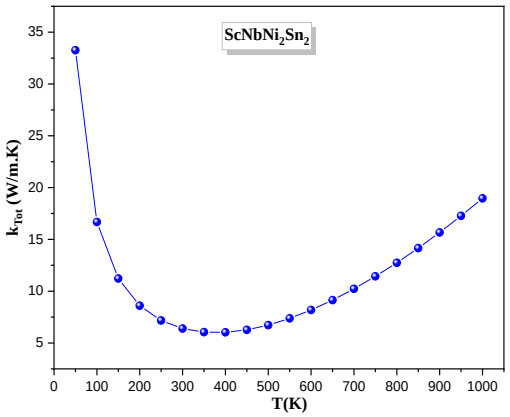

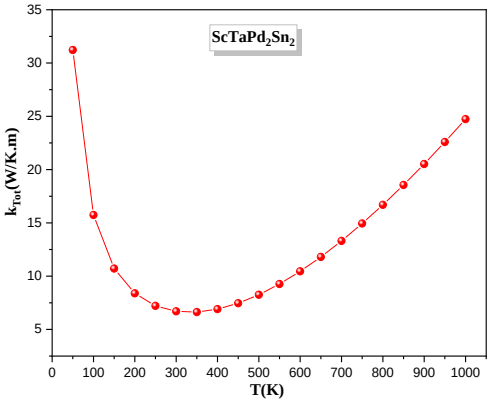

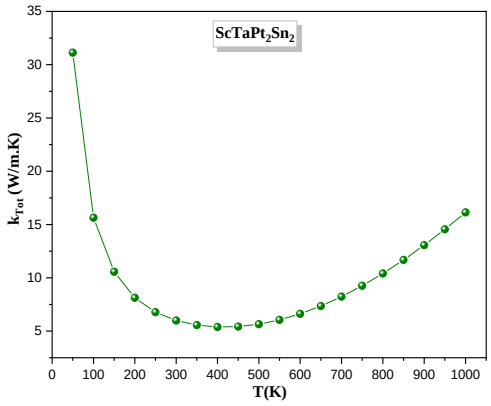

Figure.III.23.b: The total thermal conductivity k_{Tot} as a function of the temperature for DHH alloys ScX'Y_2Sn_2 (X'=Nb, Ta; Y=Ni, Pd, Pt).

The half-Heusler alloys exhibit a comparatively high lattice thermal conductivity compared to most other top-performing thermoelectric materials. This is mostly due to their simple crystal structure and strong chemical bonding [209]. It was recently confirmed that double half Heusler alloys have intrinsically lower lattice thermal conductivity k_L compared to conventional ternary half Heusler alloys due to the disorder scattering and complexity of a primitive cell. $Ti_2FeNiSb_2$ has a 50% lower k_L than TiCoSb due to its lower group velocity and higher scattering rate, indicating that quaternary HH alloys with complicated crystal structures tend to have lower k_L [85].

As depicted in Figure.III.23.a, the values of k_L decrease significantly as temperature rises due to an increase in phonon vibrations for all DHH alloys. These alloys $ScNbNi_2Sn_2$, $ScTaPd_2Sn_2$, and $ScTaPt_2Sn_2$ have attained the lowest k_L values of 1.34 W/m.K, 1.27 W/m.K, and 1.28 W/m.K, respectively, at a temperature of 1000K .In addition, the values of lattice thermal conductivity are remarkably similar at 1000K and ambient temperature (Refer to Table.III.12 for further information). Therefore, our alloys are considered to be promising candidates for thermoelectric applications on account of their low lattice thermal conductivities. This is achieved by attaining a maximum value of figure of merit ZT.

According to Figure.III.23.c, the overall thermal conductivity k_{Tot} consistently decreases as the temperature rises, until it reaches around 400 K at which point the following values are observed. 6.02 W/ (m.K), 6.9 W/ (m.K), and 5.38 W/ (m.K) for $ScNbNi_2Sn_2$, $ScTaPd_2Sn_2$, and $ScTaPt_2Sn_2$ respectively. Subsequently, the conductivity resumes its ascent at high temperatures for all the DHH alloys $ScX'Y_2Sn_2$ (X'=Nb, Ta; Y=Ni, Pd, Pt).

Table III.12: Debye temperature, average Grüneisen parameter and the lattice thermal conductivity calculated at room temperature of the DHH alloys $ScX'Y_2Sn_2$ (X'=Nb, Ta; Y=Ni, Pd, Pt).

Alloys	$\theta(K)$	γ	$k_L(W/m.K)$
$ScNbNi_2Sn_2$	382	2.1	5.3
ScNiSn [210]	-	-	11.7
$ScTaPd_2Sn_2$	350	2.24	4.97
$ScTaPt_2Sn_2$	333	2.33	4.98

III.7. 2. Transport properties

The Seebeck coefficient (S), electronic thermal conductivity (k_e), electrical conductivity (σ), and figure of merit (ZT) of double half Heusler alloys were analyzed as a function of temperature up to 1000 K. This analysis was conducted using the BoltzTrap code, which is based on the Boltzmann transport theory within the constant relaxation time approximation. These parameters can be expressed as [211–214]:

$$\sigma = e^2 \sum_{\vec{k}} \left(-\frac{\partial f_0}{\partial E} \right) \tau_{\vec{k}} \vec{v}_{\vec{k}} \vec{v}_{\vec{k}} \tag{III-51}$$

Where σ is the electrical conductivity, f_0 is a *Fermi* distribution function, τ_k and v_k signify the relaxation time and the group velocity associated with $\vec{k}$ state, respectively. The Seebeck coefficient is given by:

$$S = \sum_{\vec{k}} \left(-\frac{\partial f_0}{\partial E} \right) \vec{v}_{\vec{k}} \vec{v}_{\vec{k}} \left(\varepsilon_k - \mu \right) \Big/ eT \sum_{\vec{k}} \left(-\frac{\partial f_0}{\partial \varepsilon} \right) \vec{v}_{\vec{k}} \vec{v}_{\vec{k}} \tag{III-52}$$

Where ε_k is the band energy, μ is the chemical potential. The electronic contribution to thermal conductivity can be defined as:

$$k_e/\tau = K_B^2 T \sum_{\vec{k}} \left(-\frac{\partial f_0}{\partial E} \right) \vec{v}_{\vec{k}} \vec{v}_{\vec{k}} \left(\frac{\varepsilon_k - \mu}{K_B T} \right)^2 - T \frac{\sigma}{\tau} S^2 \tag{III-53}$$

The primary transport coefficients of the DHH alloys ScX'Y_2Sn_2 (X'=Nb, Ta; Y=Ni, Pd, Pt) including the electrical (σ/τ) and thermal conductivities (k_e/τ), Seebeck coefficient (S) and figure of merit (ZT) are displayed as a function of temperature in Figure.III.23.c-f within the temperature range of 50-1000K, utilizing the EV-GGA approximation.

The electronic thermal conductivities (k_e/τ) depicted in Figure.III.23.c as a function of temperature for the DHH alloys ScX'Y_2Sn_2 (X'=Nb, Ta; Y=Ni, Pd, Pt). It is obvious that the three alloys change linearly with temperature increment particularly after T=600K. This occurs due to the thermal excitation of electrons as the temperature rises, resulting in increased heat conduction.

Regarding the electrical conductivity (σ/τ) curves shown in Figure.III.23.d for the DHH alloys $ScX'Y_2Sn_2$ (X'=Nb, Ta; Y=Ni, Pd, Pt) we can see that they vary linearly with temperature as predicted by the band structure study. This verifies the semiconducting nature of these alloys.

$ScNbNi_2Sn_2$, $ScTaPd_2Sn_2$ and $ScTaPt_2Sn_2$ were found to have a electrical conductivity (σ/τ) of $2.38x10^{18}$ $(\Omega ms)^{-1}$, $3.91x10^{18}$ $(\Omega ms)^{-1}$, and $2.79x10^{18}$ $(\Omega ms)^{-1}$ at a temperature of T=300 K respectively.

The Seebeck coefficient (S) is a measurement of the voltage produced across a material when a temperature gradient is applied, and it is defined as: $S=\Delta V/\Delta T$, thus Figure.III.23.e shows the Seebeck coefficient for the DHH alloys $ScX'Y_2Sn_2$ (X'=Nb, Ta; Y=Ni, Pd, Pt) as a function of temperature hence, at room temperature (T=300K) $S_{ScNbNi2Sn2}$=173.29 μV/K $S_{ScTaPd2Sn2}$ =173.8 μV/K, $S_{ScTaPt2Sn2}$=138.7μV/K and they reached a maximum values of S_{max}=226.81 μV/K at 650 K , S_{max}=211.26 μV/K at 750 K and S_{max}=246.35 μV/K at 950 K that for $ScNbNi_2Sn_2$, $ScTaPd_2Sn_2$ and $ScTaPt_2Sn_2$ respectively. So, all DHH alloys exhibit a positive Seebeck value across the temperature range, indicating that holes or positive charge carriers are the dominating charge carriers, confirming that our materials are p-type.

Since the materials under consideration are semiconductors, it is evident that the figure of merit (ZT) increases as the temperature rises. Figure.III.23.f demonstrates that ZT rises with increasing temperature, displaying a similar trend to electrical and thermal conductivity ((σ/τ) and (k_e/τ)), the maximum value of ZT at 900 K is 0.639 for $ScNbNi_2Sn_2$, and 0.664 and 0.816, $ScTaPd_2Sn_2$ and $ScTaPt_2Sn_2$ at 1000 K respectively within EV-GGA. Similarly, we compute the Seebeck coefficient (S), electrical conductivity (σ/τ) and electronic thermal conductivity (k_e/τ) along the x,y and z axes using EV-GGA approximation, considering that Tensors $(\sigma_{xx} \neq \sigma_{yy} \neq \sigma_{zz})$, $(S_{xx} \neq S_{yy} \neq S_{zz})$, $(k_{e_{xx}} \neq k_{e_{yy}} \neq k_{e_{zz}})$ are diagonal Figure.III.24.a, Figure.III.24.b and Figure.III.24.c present the calculated anisotropic transport properties of DHH alloys. According to Table III.14 all the DHH alloys have a Seebeck coefficient S_{yy} higher than that found in S_{xx} and S_{zz} at T=300K means that the transport along the *yy*-axis is dominant.

Conversely both electrical and electronic thermal conductivity where the xx direction is the most dominating on

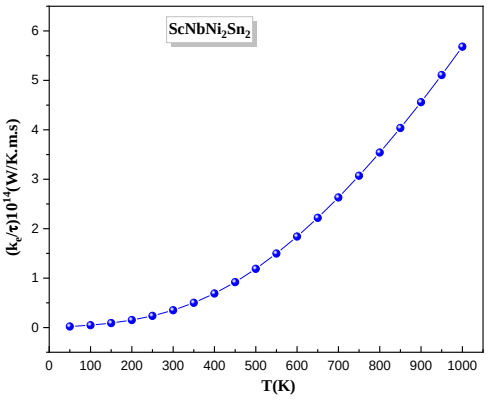

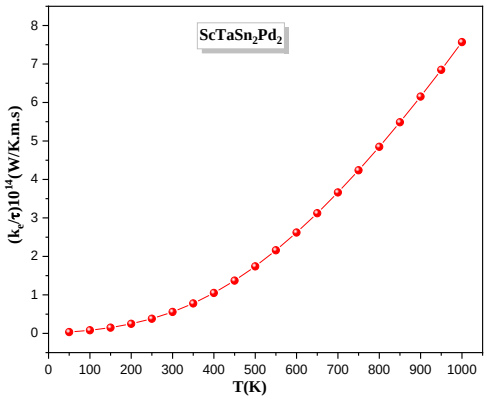

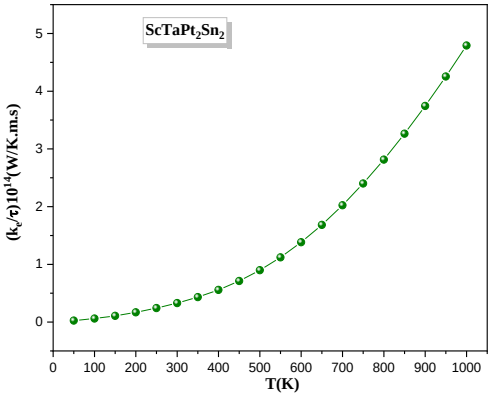

Figure.III.23.c: The electronic thermal conductivity per relaxation time (κ_e / τ) as a function of the temperature for DHH alloys $ScX'Y_2Sn_2$ (X'=Nb, Ta; Y=Ni, Pd, Pt).

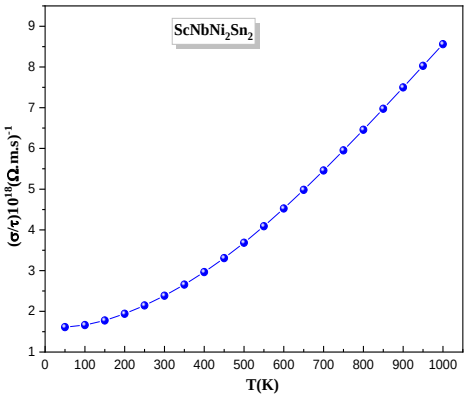

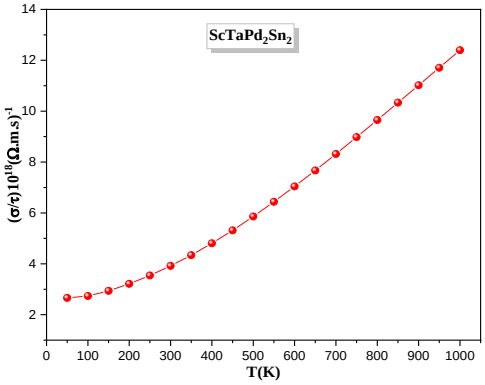

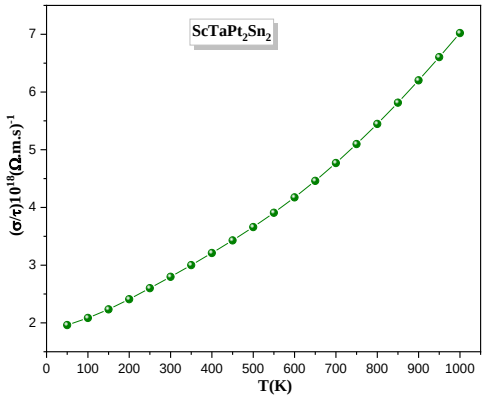

Figure.III.23.d: the electrical conductivity per relaxation time (σ/τ) as a function of the temperature for DHH alloys $ScX'Y_2Sn_2$ (X'=Nb, Ta; Y=Ni, Pd, Pt).

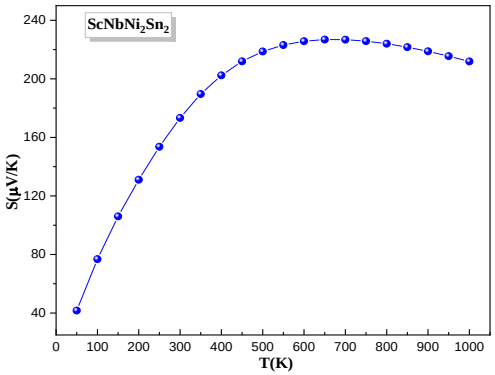

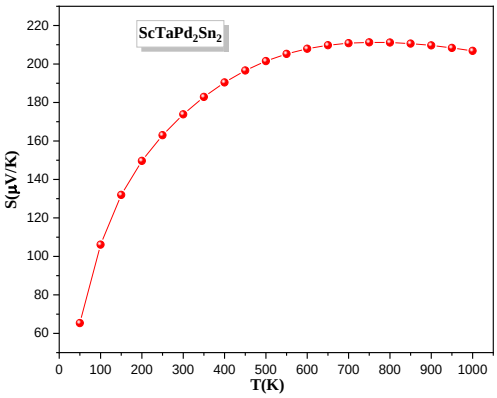

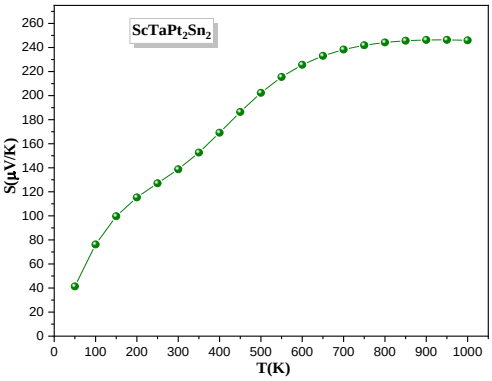

Figure.III.23.e: Seebeck coefficient as a function of temperature for DHH alloys $ScX'Y_2Sn_2$ (X'=Nb, Ta; Y=Ni, Pd, Pt).

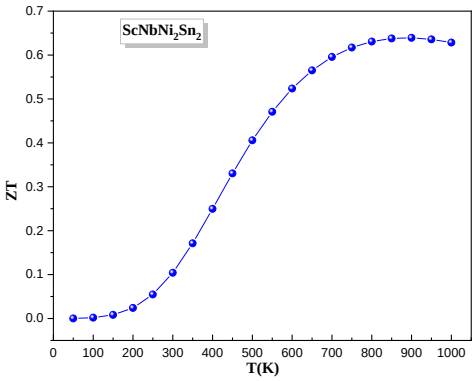

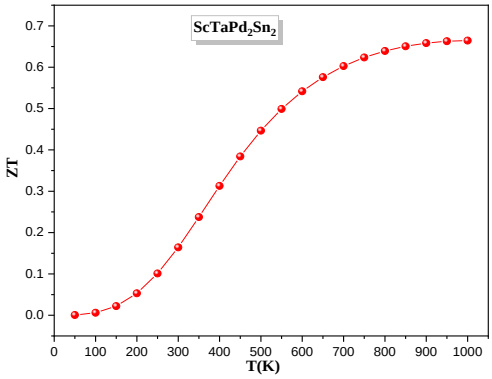

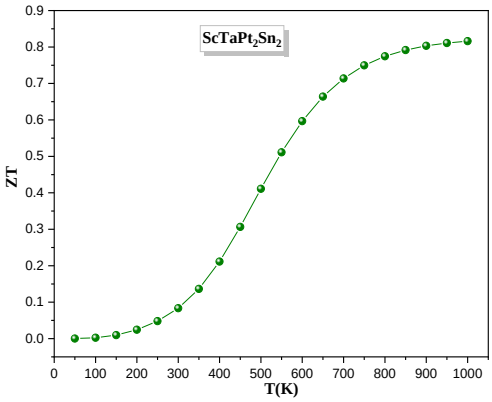

Figure.III.23.f: Figure of merit as a function of the temperature for DHH alloys $ScX'Y_2Sn_2$ (X'=Nb, Ta; Y=Ni, Pd, Pt).

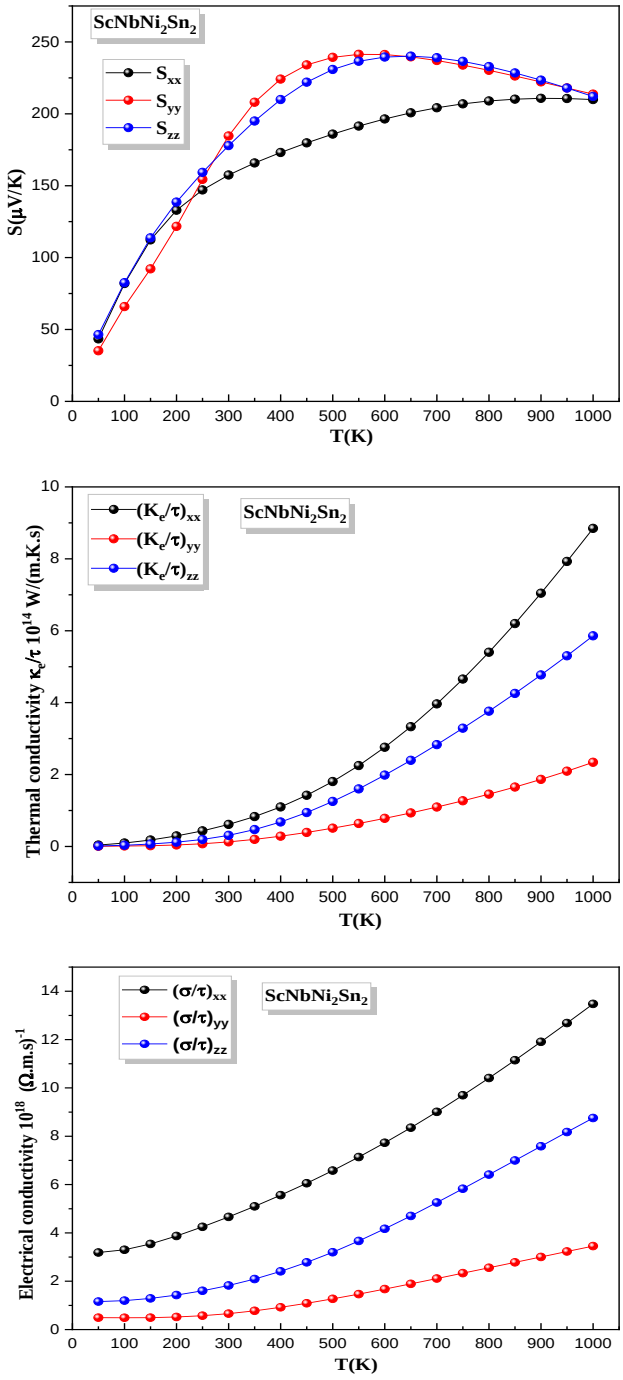

Figure.III.24.a: Calculated anisotropic transport properties of $ScNbNi_2Sn_2$ alloy **(a)** Seebeck coefficient tensor **(b)** electronic thermal conductivity tensor and **(c)** ratio of electrical conductivity tensor components.

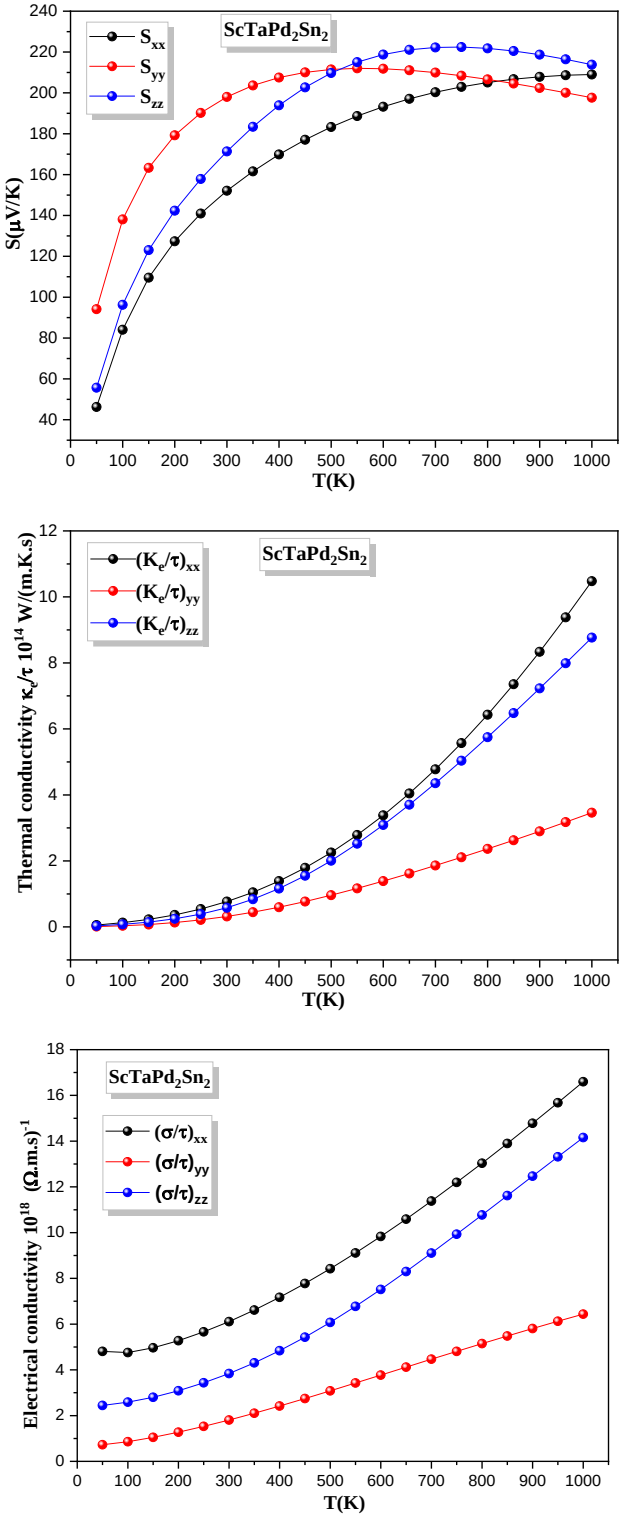

Figure.III.24.b: Calculated anisotropic transport properties of $ScTaPd_2Sn_2$ alloy **(a)** Seebeck coefficient tensor **(b)** electronic thermal conductivity tensor and **c)** ratio of electrical conductivity tensor components.

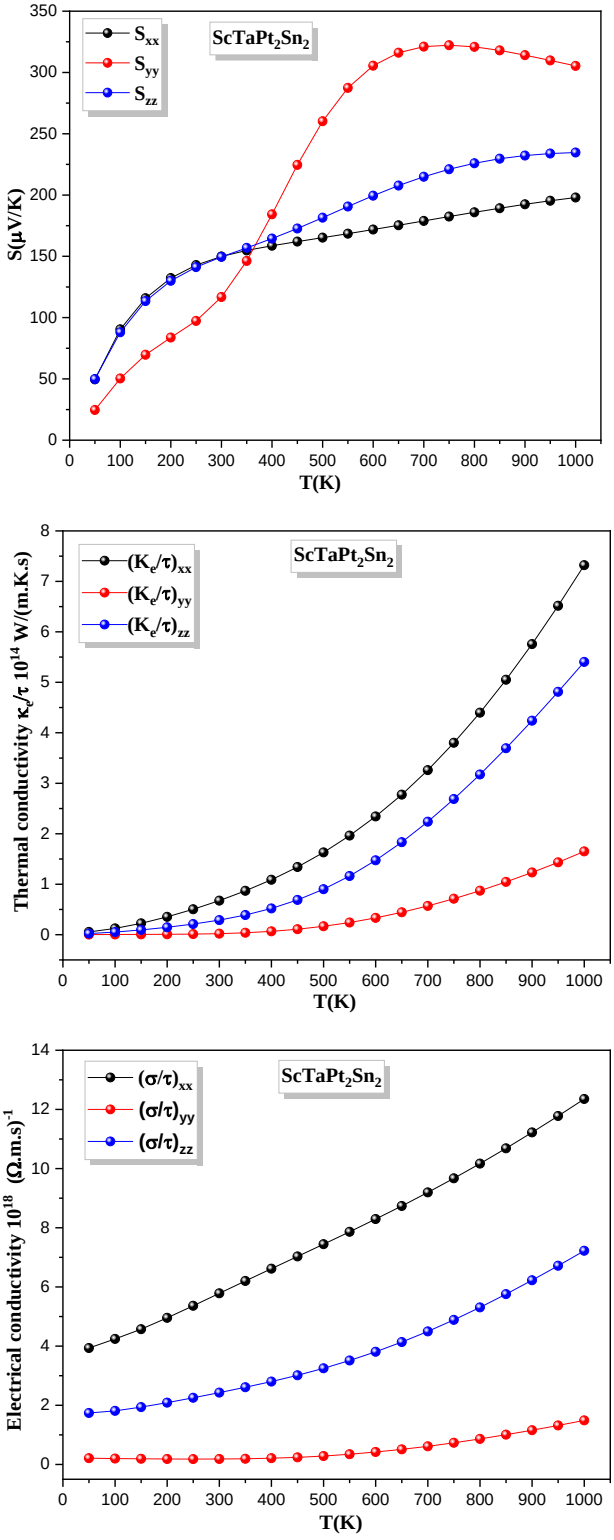

Figure.III.24.c: Calculated anisotropic transport properties of $ScTaPt_2Sn_2$ alloy **(a)** Seebeck coefficient tensor **(b)** electronic thermal conductivity tensor and **c)** ratio of electrical conductivity tensor components.

Table III.13: The calculated of electrical conductivity tensor, the Seebeck coefficient tensor, and the electronic thermal conductivity of the DHH alloys $ScX'Y_2Sn_2$ (X'=Nb, Ta; Y=Ni, Pd, Pt) at 300 K and 1000 K using EV-GGA approximation.

Alloys	***T(K)***	$\sigma/\tau*10^{18}$ $(W.m.s)^{-1}$			***S (μV/K)***			$ke/\tau*10^{14}$ ***(W/m.K)***		
		$(\sigma/\tau)_{xx}$	$(\sigma/\tau)_{yy}$	$(\sigma/\tau)zz$	S_{xx}	S_{yy}	S_{zz}	$(ke/\tau)_{xx}$	$(ke/\tau)_{yy}$	$(ke/\tau)_{zz}$
$ScNbNi_2Sn_2$	***1000***	13.47	3.45	8.75	209.90	213.70	212.03	8.84	2.34	5.85
	300	4.66	0.65	1.82	157.43	184.56	177.89	0.61	0.12	0.3
$ScTaPd_2Sn_2$	***1000***	16.59	6.43	14.15	208.99	197.63	213.83	10.47	3.46	8.76
	300	6.11	1.80	3.83	152.08	198.03	171.36	0.76	0.31	0.58
$ScTaPt_2Sn_2$	***1000***	12.35	1.48	7.22	197.97	305.35	234.65	7.32	1.64	5.4
	300	5.78	0.18	2.42	116.78	149.55	149.55	0.67	0.02	0.28

III.7. 3. Strategies for improving the Seebeck coefficient

Figure.III.25 displays a variation in the Seebeck coefficient within the temperature range of 300-600 K, 300-800K and 300-900K for $ScNbNi_2Sn_2$, $ScTaPd_2Sn_2$ and $ScTaPt_2Sn_2$, respectively. The value of Seebeck coefficient S at T=600 K is 225.704 μV/K, which corresponds to a carrier concentration of n=2. $85x10^{20}$ Cm^{-3} for $ScNbNi_2Sn_2$, while the alloys $ScTaPd_2Sn_2$ and $ScTaPt_2Sn_2$ have the values of S= 211.15 μV/K at T=800K and S=246.26 μV/Kat T=900K which correspond to a carrier concentration of n=4. $92x10^{20}$ Cm^{-3} at and n=3. $34x10^{20}$ Cm^{-3} respectively. In order to enhance the thermoelectric properties of double half Heusler alloys, we conducted a study on the effects of carrier concentration on the Seebeck coefficient at a temperature of 600K, 800 K and 900K for $ScNbNi_2Sn_2$, $ScTaPd_2Sn_2$ and $ScTaPt_2Sn_2$, respectively. Based on the data provided in Figure.III.25. it is evident that the maximum values of Seebeck coefficient are 356.99 μV/K, 343.82 μV/K and 461.18 μV/K, these values occur when the concentration of charge carriers is reduced to a point where $n=3.04x10^{19}$ Cm^{-3}, $n=0.55$ $x10^{19}$ Cm^{-3} and $n=1.31$ $x10^{19}$ Cm^{-3} for $ScNbNi_2Sn_2$, $ScTaPd_2Sn_2$ and $ScTaPt_2Sn_2$, respectively.

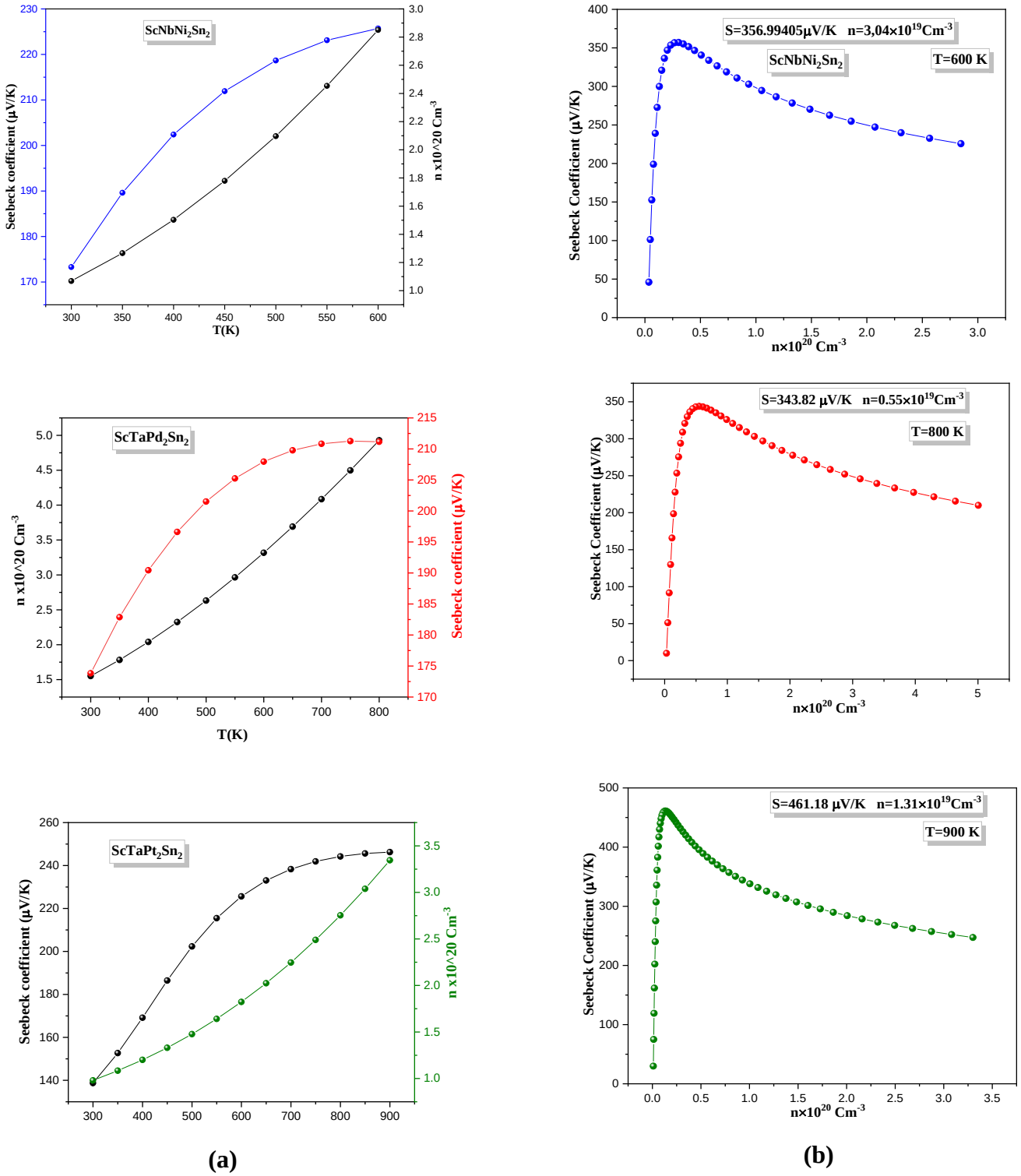

(a) **(b)**

Figure.III.25: The Seebeck coefficient of the DHH alloys $ScX'Y_2Sn_2$ (X'=Nb, Ta; Y=Ni, Pd, Pt) as a function of (a) temperature range 300K-600K, 300K-800K and 300K-900K and carrier concentration, (b) carrier concentration.

III.7. 4. Strategies for improving the figure of merit ZT

Based on Figure.III.23. a, the lattice thermal conductivity values for all the DHH alloys $ScX'Y_2Sn_2$ (X'=Nb, Ta; Y=Ni, Pd, Pt) are low as a result of the described disorder. As the temperature rises, the values of k_L decrease and are almost equal to zero $(k_L \sim 0)$ at extremely high temperatures. In this situation, we can determine an estimated value of ZT without the need to calculate the average value of τ :

$$ZT \sim T \frac{S^2 \left(\sigma/\tau\right)}{\left(k_e/\tau\right)} = T \frac{S^2 \sigma}{k_e} \qquad \text{(III-54)}$$

The rigid band approximation (RBA) assumes that the band structure of a system remains unchanged whether the temperature or doping is altered [215]. We investigated the relation between the figure of merit ZT and the carrier concentration at a temperature of T=300 K, T= 900 K and T= 1000 K for double half Heusler, respectively (see Table III.14). Figure.III.26 indicates that the maximum ZT value is 0.74, which is achieved by the n-doped material (n-type semiconductor) with an optimal carrier concentration of $-3.1x10^{20}Cm^{-3}$ whereas for a p-type semiconductor, the highest ZT value is around 0.71 with carrier concentration $n=4.79\ x10^{20}\ Cm^{-3}$ for the $ScNbNi_2Sn_2$ alloy.

Similarly, the $ScTaPd_2Sn_2$ has a maximum ZT value 0.74, which is achieved by the n-doped material (n-type semiconductor) with an optimal carrier concentration of $-2x10^{20}\ Cm^{-3}$ whereas for a p-type semiconductor, the highest ZT value is around 0.76 with carrier concentration $n=2.66\ x10^{20}\ Cm^{-3}$ for the $ScTaPd_2Sn_2$ alloy. Regrading to $ScTaPt_2Sn_2$ alloy which has the best enhancing figure of merit ZT value comparing the other alloys for the reason that the maximum ZT value is 0.85, which is achieved by the n-doped material (n-type semiconductor) with an optimal carrier concentration of $-3.5x10^{19}\ Cm^{-3}$ whereas for a p-type semiconductor, the highest ZT value is around 1.024 with carrier concentration $n=6.16\ x10^{19}\ Cm^{-3}$ for the $ScTaPt_2Sn_2$ alloy.

Hence, the double half Heusler alloy discussed in our study is considered the most suitable material for thermoelectric applications, primarily due to its high figure of merit, a crucial parameter in the field of thermoelectricity.

Table III.14: Calculated ZT and corresponding transport coefficient at the optimal chemical potential for the DHH alloys $ScX'Y_2Sn_2$ (X'=Nb, Ta; Y=Ni, Pd, Pt) at various temperatures.

Alloys	*μ (eV)*	*T(K)*	*n(Cm^{-3})*	*K_e (W/m.K)*	*σ (10^5/Ω.m)*	*S(μV/K)*	*ZT*
$ScNbNi_2Sn_2$	0.64923	1000	7.37×10^{20}	17.61	8.56	211.8	0.628
		900	6.02×10^{20}	14.13	2.3247	218.78	0.639
		300	1.06×10^{20}	1.08	0.7385	173.29	0.1
	0.65023	900	4.79×10^{20}	12.96	1.9726	227.87	0.7109
	0.68073	900	-3.64×10^{20}	14.98	2.3757	-228.33	0.6747
		300	-4.23×10^{19}	1.1	0.3751	-281.6	0.13
$ScTaPd_2Sn_2$	0.68326	1000	6.82×10^{20}	23.46	3.8428	206.81	0.664
		900	5.84×10^{20}	19.07	3.4159	209.7	0.658
		300	1.55×10^{20}	1.72	1.2148	173.8	0.16
	0.68866	900	2.66×10^{20}	13.67	1.6281	267.08	0.761
	0.68806	900	2.91×10^{20}	14.23	1.7694	260.7	0.69
$ScTaPt_2Sn_2$	0.74039	1000	4.02×10^{20}	14.854	2.1765	245.99	0.816
		900	3.35×10^{20}	11.6	1.922	246.26	0.803
		300	9.8×10^{19}	1.01	8.67745	138.72	0.083
	0.74709	1000	1.67×10^{20}	9.56	0.94888	313.73	0.861
	0.75149	900	6.16×10^{19}	4.81	0.3871	376.36	1.024

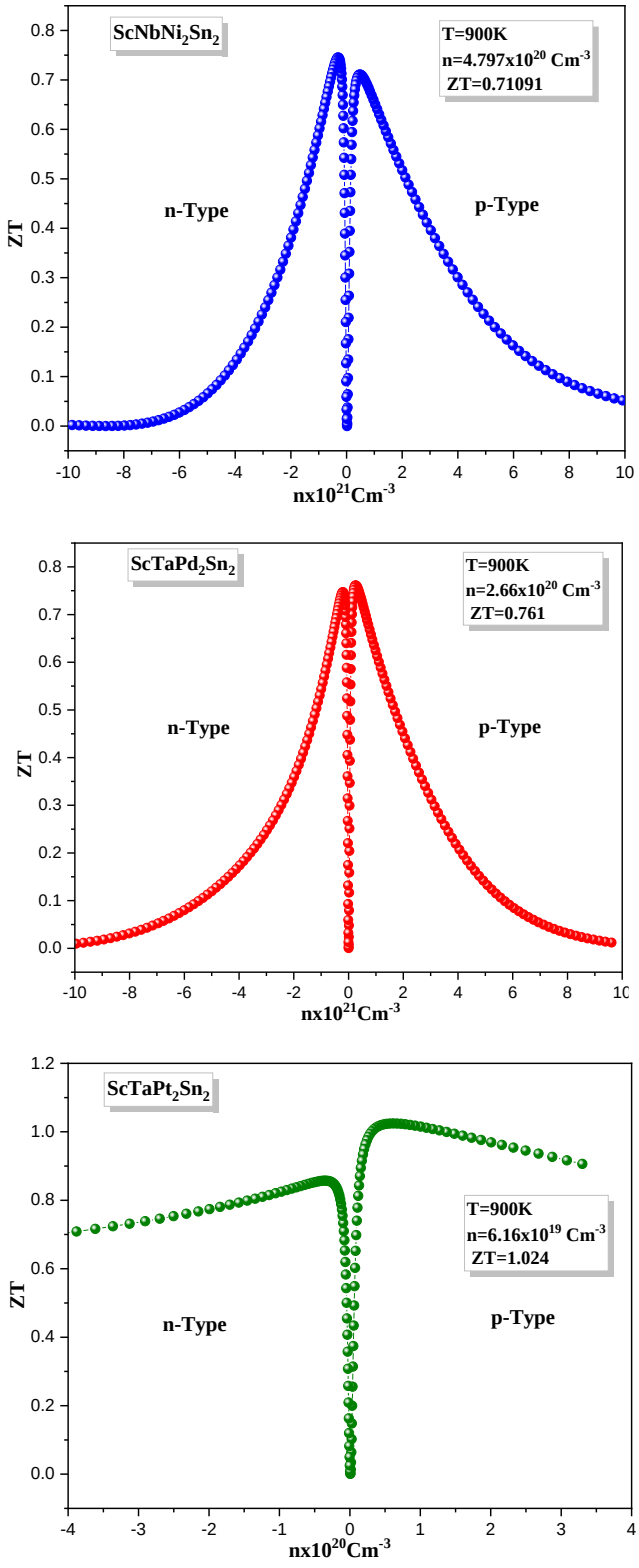

Figure.III.26: The figure of merit ZT of the DHH alloys $ScX'Y_2Sn_2$ (X'=Nb, Ta; Y=Ni, Pd, Pt) as a function of charge carrier concentration at fixed temperature T=900K.

References

References

[1] R. E. Smalley, MRS Bull.,30, 412–417, (2005).

[2] "Energy Flow Charts" | Flowcharts. Accessed: Oct. 25, 2023. [Online]. Available: https://flowcharts.llnl.gov/commodities/energy

[3] T.M. Tritt, Annu. Rev. Mater. Res. 41, 433 (2011).

[4] B.C. Sales, Science 295, 1248 (2002).

[5] J. Yang, T. Caillat, MRS Bull. 31, 224 (2006).

[6] Seebeck, T.J. ,koenigl magnetishe polarization dermatalle and erze durk temeratur differenz, 265, (1822).

[7] “SEEBECK EFFECT- Blog -Tekon Electronics.” Accessed: Oct. 25, 2023. [Online]. Available: https://www.tekonelectronics.com/en/news/tekon-blog/seebeck-effect/

[8] Peltier,J .C., Chim, A, Nouvelles Experiences sur la Caloricite des Courans Electriques,LVI , 371, (1834).

[9] L. Yang, Z. G. Chen, and J. Zou, "High-performance thermoelectric materials for solar energy application," in Emerging Materials for Energy Conversion and Storage, Elsevier, pp.3–38, (2018).

[10] Thomson,W.,in proceeding Royal society, 910,(1851).

[11] R. Freer and A. V. Powell, "Realizing the potential of thermoelectric technology: A Roadmap," Journal of Materials Chemistry C, vol. 8, no. 2. Royal Society of Chemistry, pp. 441–463, (2020).

[12] E. Altenkirch, Phys., Zeitschrift12, 920–924, (1911).

[13] C. Gayner and K. K. Kar, "Recent advances in thermoelectric materials," Progress in Materials Science, vol. 83. Elsevier Ltd, pp. 330–382, Oct. 01, (2016).

[14] G. J. Synder and E. S. Toberer. Nat Mater., 7, 105-114, (2008).

[15] J. P. Heremans, V. Jovovic, E. S. Toberer, A. Saramat, K. Kurosaki, A. Charoenphakdee, S. Yamanaka and G. J. Snyder, Science., 321, 554–557, (2008).

[16] H. Muta, T. Kanemitsu, K. Kurosaki and S. Yamanaka, J. Alloys Compd.469, 50–55, (2009).

[17] A. Ioffe, Semiconductor Thermoelements and Thermoelectric Cooling (Infosearch, London, (1957).

[18] A. Ioffe, Sci. Am. 199, 31 (1958).

[19] Goldsmid H., Douglas R W, British Journal of applied physics, ,5(11),386,(1954).

[20] M. A. Zoui, S. Bentouba, J. G. Stocholm, et M. Bourouis, « A review on thermoelectric generators: Progress and applications », Energies, vol. 13, no 14. MDPI AG, (1 juillet 2020).

[21] Romanjek, K.; Vˇešín, S.; Aixala, L.; Baffie, T.; Bernard-Granger, G.; Dufourcq, J. High-Performance Silicon–Germanium-Based Thermoelectric Modules for Gas Exhaust Energy Scavenging. J. Electron. Mater 44, 2192–2202, (2015).

[22] Vining, C.B. The Thermoelectric Limit ZT 1: Fact or Artifact. In Proceedings of the XIth International Conference on Thermoelectrics; University of Texas: Melville, NY, USA; Arlington, TX, USA, pp. 223–231, (1992).

[23] Crane, D.T.; Bell, L. Progress Towards Maximizing the Performance of a Thermoelectric Power Generator; Institute of Electrical and Electronics Engineers (IEEE): Piscataway, NJ, USA, pp. 11–16,(2006).

[24] W. Xie, J. He, H.J. Kang, X. Tang, S. Zhu, M. Laver, S. Wang, J.R. Copley, C.M. Brown, Q. Zhang. Nano letters 10 3283-3289, (2010).

[25] B. Poudel, Q. Hao, Y. Ma, Y. Lan, A. Minnich, B. Yu, X. Yan, D. Wang, A. Muto, D. Vashaee, X. Chen, J. Liu, M.S. Dresselhaus, G. Chen, Z. Ren. Science 320634-638, (2008).

[26] LaLonde, A.D.; Pei, Y.; Wang, H.; Snyder, G.J. Lead telluride alloy thermoelectrics. Mater, 14, 526–532, (2011).

[27] G. Slack. CRC Handbook of Thermoelectrics,(1995).

[28] Wan, C.; Wang, Y.; Wang, N.; Koumoto, K. Low-Thermal-Conductivity (MS)1+x(TiS2)2 (M = Pb, Bi, Sn) Misfit Layer Compounds for Bulk Thermoelectric Materials. Materials, 3, 2606–2617, (2010).

[29] Iversen, B.B.; Palmqvist, A.; Cox, D.E.; Nolas, G.S.; Stucky, G.D.; Blake, N.P.; Metiu, H. Why are Clathrates Good Candidates for Thermoelectric Materials? J. Solid State Chem, 149, 455–458, (2000).

[30] Xun Shi, Jiong Yang, James R. Salvador, Miaofang Chi, Jung Y. Cho, Hsin Wang, Shengqiang Bai, Jihui Yang, Wenqing Zhang, and Lidong Chen. Multiple-Filled Skutterudites: High Thermoelectric Figure of Merit through Separately Optimizing Electrical and Thermal Transports. J. Am. Chem. Soc, 133, 20, 7837–7846, (2011).

[31] A. Saramat; G. Svensson; A. E. C. Palmqvist., Large thermoelectric figure of merit at high temperature in Czochralski-grown clathrate Ba8Ga16Ge30, J. Appl. Phys. 99, 023708, (2006).

[32] Klaus Habicht. Skutterudites, (2018).

[33] Gascoin, F.; Ottensmann, S.; Stark, D.; Haile, S.M.; Snyder, G.J. Zintl Phases as Thermoelectric Materials: Tuned Transport Properties of the Compounds CaxYb1-xZn2Sb2. Adv. Funct. Mater, 15, 1860–1864, (2005).

[34] Shuai, J.; Mao, J.; Song, S.; Zhang, Q.; Chen, G.; Ren, Z. Recent progress and future challenges on thermoelectric Zintl materials. Mater. Today Phys, 1, 74–95, (2017).

[35] Jifeng Sun and David J Singh. Thermoelectric properties of AMg2X2, AZn2Sb2 (A

= Ca, Sr, Ba; X = Sb, Bi), and Ba2ZnX2 (X = Sb, Bi) Zintl compounds. Journal of Materials Chemistry A, 5(18):8499–8509, (2017).

[36] Wang, Y.F.; Lee, K.H.; Ohta, H.; Koumoto, K. Fabrication and thermoelectric properties of heavily rare-earth metal-doped SrO(SrTiO3)n (n=1, 2) ceramics. Ceram. Int, 34, 849–852, (2008).

[37] Wang M, Baek P, Akbarinejad A, Barkerab D, Travas-Sejdic J. Conjugated polymers

and composites for stretchable organic electronics. J Mater Chem C2019;7(19):5534–52

[38] Yu, J.; Xia, K.; Zhao, X.B.; Zhu, T. High performance p-type half-Heusler thermoelectric materials. J. Phys. D, 51, 113001, (2018).

[39] C. Uher, J. Yang, S. Hu, D. T. Morelli, and G. P. Meisner,Transport properties of pure and doped MNiSn (M=Zr, Hf) ,Phys. Rev. B 59, 8615 – Published (1 April 1999).

[40] S.J. Poon; T.M. Tritt; Y. Xi; S. Bhattacharya; V. Ponnambalam; A.L. Pope; R.T. Littleton; V.M. Browning, Bandgap features and thermoelectric properties of Ti-based half-Heusler alloys.Eighteenth International Conference on Thermoelectrics. Proceedings ,Baltimore, MD, USA,pp.45-51, (1999).

[41] A. V. Powell and P. Vaqueiro, in Thermoelectric Materials and Devices, ed. I. Nandhakumar, N. M. White, S. Beeby, Royal Society of Chemistry, Cambridge, ch. 2, pp. 27–59, (2017).

[42] S. He ´bert, R. Daou, Y. Bre ´ard, D. Pelloquin, E. Guilmeau, F. Gascoin, O. Lebedev and A. Maignan, Searching for new thermoelectric materials: some examples among oxides, sulfides and selenides, J. Phys.: Condens. Matter, 28, 013001, (2016).

[43] M. Rull-Bravo, A. Moure, J. F. Fernandez and M. MartinGonzalez, Skutterudites as thermoelectric materials: revisited, RSC Adv., 5, 41653–41667, (2015).

[44] E. S. Toberer, A. F. May and G. J. Snyder, Zintl chemistry for designing high efficiency thermoelectric materials, Chem. Mater, 22, 624–634, (2010).

[45] H. Kleinke, New bulk materials for thermoelectric power generation: clathrates and complex antimonides, Chem. Mater , 22, 604–611,(2010).

[46] J. W. G. Bos and R. A. Downie, Half-heusler thermoelectrics: a complex class of materials, J. Phys.: Condens. Matter, 26, 433201,(2014).

[47] A. Nozariasbmarz, A. Agarwal, Z. A. Coutant, M. J. Hall, J. Liu, R. Liu, A. Malhotra, P. Norouzzadeh, M. C. O¨ztu¨rk, V. P. Ramesh, Y. Sargolzaeiaval, F. Suarez and D. Vashaee,

Thermoelectric silicides: a review, Jpn. J. Appl. Phys, 56, 05DA04, (2017).

[48] F. Heusler, W. Starck, and E. Haupt. Verh. d. DPG, 5:220 223, (1903).

[49] F. Heusler. Verh. d. DPG, 5:219, (1903).

[50] A.J. Bradley, J.W. Rodgers, The crystal structure of the Heusler alloys. P. Roy. Soc. Lond. A. Mat 144, 340–359, (1934).

[51] Heusler O. Kristallstruktur und Ferromagnetismus der Mangan- Aluminium Kupferlegierungen. Adv.Phys.411:155–201,(1934).

[52] Castelliz L.Eine ferromagnetische Phase im System Nickel-Mangan-Antimon. Monatsh. Chem.82:1059–1085, (1951).

[53] Castelliz L. Über eine Mischkristallreihe zwischen zwei terärenVertreterndes C1-Typs. Monatsh.Chem.83:1314–1317, (1952).

[54] R.A. de Groot, F.M. Mueller, P.G. Van Engen, K.H.J. Buschow, New class of materials: half-metallic ferromagnets. Phys. Rev. Lett. 50, 2024–2027 , (1983).

[55] H. Zabel, « Progress in spintronics », Superlattices and Microstructures, vol. 46, no 4. p. 541 553, (octobre 2009).

[56] K. Bartholomé, B. Balke, D. Zuckermann, M. Köhne, M. Müller, K. Tarantik, Jan König, J.

Electron. Mater. 43, 1775 , (2014).

[57] J.P.A. Makongo, D.K. Misra, X. Zhou, A. Pant, M.R. Shabetai, X. Su, C. Uher, K.L. Stokes, and Pierre F.P. Poudeu, J. Am. Chem. Soc. 133, 18843, (2011).

[58] C. Yu, T. Zhu, K. Xiao, J. Shen, X. Zhao, Funct. Mater. Lett. 03, 227, (2010).

[59] J.E. Garay, Annu. Rev. Mater. Res. 40, 445, (2010).

[60] H.P.J.Wijin: Alloys and compounds of 3d elements with main group elements 5 . 1 3d elements and Cu , Ag or Au.SpringerLink , (1991).

[61] Singh, M., Saini, H.S., Thakur, J., Reshak, A.H., Kashyap, M.K.: Electronic structure ,

magnetism and robust half-metallicity of new quaternary Heusler alloy FeCrMnSb. J.

Alloys Compd. 580, 201–204 , (2013).

[62] R. Farshchi, M. Ramsteiner, Spin injection from Heusler alloys into semiconductors: A

materials perspective. J Appl Phys 113, 191101, (2013).

[63] Kübler, J., William, A.R., Sommers, C.B.: Formation and coupling of magnetic moments in Heusler alloys. Phys. Rev. B. 28, 1745–1755, (1983).

[64] Oxley, D.P., Tebble, R.S., Williams, K.C.: Heusler alloys. J. Appl. Phys. 34, 1362–1364, (1963).

[65] « Heusler alloys - Solid State Chemistry @Aalto - Aalto University Wiki ». [En ligne]. Disponible à: https://wiki.aalto.fi/display/SSC/Heusler+alloys, Consulté le: (30 novembre 2023).

[66] K. Hayashi, H. Li, M. Eguchi, Y. Nagashima, and Y. Miyazaki, 'Magnetic Full-Heusler Compounds for Thermoelectric Applications', Magnetic Materials and Magnetic Levitation. IntechOpen, (Mar. 24, 2021).

[67] H. C. Kandpal, C. Felser and R. Seshadri, J. Phys. D. Appl. Phys, 39, 776–118785,(2006).

[68] J. Tobola, J. Pierre, S. Kaprzyk, R. V. Skolozdra, and M. A. Kouacou. J. Phys.: Condens. Matter, 10:1013 – 1032, (1998).

[69] J. Tobola and J. Pierre. J. All. Comp., 296:243 – 252, (2000).

[70] R .A. de Groot, F. M. M¨uller, P. G. van Engen, and K. H. J. Buschow. Phys. Rev. Lett., 50:2024, (1983).

[71] J. R. Sootsman, D. Y. Chung, and M. G. Kanatzidis. Angew. Chem., 48(46):8616–8639, (2009).

[72] S. Ouardi, G. H. Fecher, B. Balke, M. Schwall, X. Kozina, G. Stryganyuk, C. Felser, E. Ikenaga, Y. Yamashita, S. Ueda, and K. Kobayashi. Appl. Phys. Lett., 97:252113, (2010).

[73] Feng W, Xiao D, Zhang Y Yao Y Physical Review B - Condensed Matter and Materials Physics 82(23), (2010).

[74] T. Ghellab, H. Baaziz, Z. Charifi, et H. Latelli, « Enhancement of thermoelectric performances in n-type RbCrZ (Z = S, Se, Te) half-metallic ferromagnetic alloys via charge carrier concentration or chemical potential », Physica B Condens Matter, vol. 653, p. 414678, (mars 2023).

[75] Köhler, J., Deng, S., Lee, C., and Whangbo, M.-H.On the Origin of a Band

Gap in Compounds of Diamond-like Structures. Inorg. Chem. 46, 1957–1959 , (2007).

[76] Zeier, W. G., Schmitt, J., Hautier, G., Aydemir, U., Gibbs, Z. M., Felser, C., et al. Engineering Half-Heusler Thermoelectric Materials Using Zintl Chemistry. Nat. Rev. Mater. 1, 16032, (2016).

[77] Anand, S., Xia, K., I. Hegde, V., Aydemir, U., Kocevski, V., Zhu, T., et al. A Valence Balanced Rule for Discovery of 18-electron Half-Heuslers with Defects. Energy Environ. Sci. 11, 1480–1488, (2018).

[78] R. J. Quinn et J. W. G. Bos, « Advances in half-Heusler alloys for thermoelectric power generation », Materials Advances, vol. 2, no 19. Royal Society of Chemistry, p. 6246 6266 (7 octobre 2021).

[79] Aravindan, V., Rajarajan, A.K., Mahendran, M.: First-Principles Study of Structural,

Electronic, Magnetic and Elastic Properties of the Mn2XSb (X = Co, Fe) Inverse Heusler

Alloys. J. Electron. Mater. 50, 1786–1793 , (2021).

[80] Luo, H., Xin, Y., Liu, B., Meng, F., Liu, H., Liu, E., Wu, G.: Competition of L21 and XA

structural ordering in Heusler alloys X2CuAl (X = Sc, Ti, V, Cr, Mn, Fe, Co, Ni). J. Alloys Compd. 665, 180–185, (2016).

[81] Xu, G.Z., Liu, E.K., Du, Y., Li, G.J., Liu, G.D., Wang, W.H., Wu, G.H.: A new spin

gapless semiconductors family: Quaternary Heusler compounds. Epl. 102, (2013).

[82] V. Alijani, Winterlik J, Fecher G H, S. S. Naghavi and C. Felser, Phys. Rev. B 83184428, (2011).

[83] S. Ghosh et S. Ghosh, « Half-Metallicity in Quaternary Heusler Alloys with 3d and 4d Elements: Observations and Insights from DFT Calculations », Phys Status Solidi B Basic Res, vol. 256, no 8, (août 2019).

[84] K. Asokan et S. Paranthaman, « Heusler alloys: A Computational Perspective », Eur. Chem. Bull. 2023, 12(Issue 8), 4778-4814.

[85] S. Anand, M. Wood, Y. Xia, C. Wolverton and G. J. Snyder, Joule, 3(5) 1226-1238, (2019).

[86] Anand, S., Xia, K., Hegde, V.I., Aydemir, U., Kocevski, V., Zhu, T., Wolverton, C., and Snyder, G.J. A valence balanced rule for discovery of 18-electron half-Heuslers with defects. Energy Environ. Sci. 11, 1480, (2018).

[87] Heusler F, Starck W, Haupt E. Verh DPG 5:220e3, (1903).

[88] Heusler F. Verh DPG 5:219, (1903)..

[89] Casper F, Felser C. Z Allgem Anorg Chem 634:2418-22,(2008).

[90] Žutić, I.; Fabian, J.; Das Sarma, S. Spintronics: Fundamentals and applications. Rev. Mod. Phys. 2004, 76, 323] Hirohata, A.; Takanashi, K. Perspectives of Heusler compounds. J. Phys. D Appl. Phys, 47, 193001, (2014).

[91] R. A. de Groot and F. M. Mueller, "New Class of Materials: Half-Metallic Ferromagnets," Phys. Rev. Lett., vol. 50, no. 25, pp. 2024–2027, (Jun. 1983).

[92] I. Galanakis, « Slater–Pauling Behavior in Half-Metallic Heusler Compounds », Nanomaterials, vol. 13, no 13. Multidisciplinary Digital Publishing Institute (MDPI), (1 juillet 2023).

[93] Kübler J. Theory of itinerant electron magnetism. Oxford: Clarendon Press, (2000).

[94] Wurmehl S, Fecher GH, Kandpal HC, Ksenofontov V, Felser C, Lin H-J, et al.

Phys Rev B; 72:184434,(2005).

[95] Galanakis, I.; Dederichs, P.H.; Papanikolaou, N. Origin and Properties of the Gap in the Half-Ferromagnetic Heusler Alloys. Phys. Rev. B, 66, 134428, (2002).

[96] Thuy Hoang, T.; Rhim, S.H.; Hong, S.C. Robust half-metallicities of alkali-metal-based half-Heusler compounds. Phys. Rev. Mater, 6, 055001,(2022).

[97] Damewood, L.; Busemeyer, B.; Shaughnessy, M.; Fong, C.Y.; Yang, L.H.; Felser, C. Stabilizing and increasing the magnetic moment of half-metals: The role of Li in half-Heusler LiMnZ (Z = N, P, Si). Phys. Rev. B, 91, 064409, (2015).

[98] Skaftouros, S.; Özdo˘gan, K.; ¸Sa¸sıo˘glu, E.; Galanakis, I. Generalized Slater-Pauling rule for the inverse Heusler compounds. Phys. Rev. B, 87, 024420, (2013).

[99] Özdoˇgan, K.; ¸Sa¸sıoˇglu, E.; Galanakis, I. Slater-Pauling behavior in LiMgPdSn-type multifunctional quaternary Heusler materials: Half-metallicity, spin-gapless and magnetic semiconductors. J. Appl. Phys. 113, 193903, (2013).

[100] Nepal, S.; Dhakal, R.; Galanakis, I.; Winter, W.M.; Adhikari, R.P.; Kaphle, G.C. Ab-initio study of stable 3d, 4d and 5d transition metal based Quaternary Heusler compounds. Phys. Rev. Mater, 6, 114407, (2022).

[101] X. L. Wang, "Proposal for a New Class of Materials: Spin Gapless Semiconductors", Phys. Rev. Lett. 100, 156404, (2008).

[102] S. Ouardi, G. H. Fecher, C. Felser, and J. K¨ubler, "Realization of Spin Gapless Semiconductors: The Heusler Compound Mn2CoAl", Phys. Rev. Lett. 110, 100401, (2013).

[103] J. W. G. Bos, « Theoretical prediction of strain tuneable quaternary spintronic Heusler compounds », IUCrJ, vol. 4. International Union of Crystallography, p. 712 713, (2017).

[104] T Graf, T., Felser, C., Parkin, S.S.P.: Simple rules for the understanding of Heusler compounds. Prog. Solid State Chem. 39, 1–50, (2011).

[105] Aksoy, S., Krenke, T., Acet, M., Wassermann, E.F., Moya, X., Mañosa, L., Planes, A.: Tailoring magnetic and magnetocaloric properties of martensitic transitions in ferromagnetic Heusler alloys. Appl. Phys. Lett. 91, 2005–2008, (2007).

[106] Yoo, J.W., Chen, C.Y., Jang, H.W., Bark, C.W., Prigodin, V.N., Eom, C.B., Epstein, A.J.: Spin injection/detection using an organic-based magnetic semiconductor. Nat. Mater. 9, 638–642 , (2010).

[107] Grünberg P, Schreiber R, Pang Y, Brodsky MB, Sowers H. Phys Rev Lett1986;57:2442.

[108] Guo, L., Gu, X., Zhu, X., Sun, X.: Recent Advances in Molecular Spintronics: Multifunctional Spintronic Devices. 1805355, 1–8, (2019).

[109] Jung, M., Korea, S.: Chapter 12 spintronics. 405–423: Book series on complex metallic alloys, (2010).

[110] Page, A., Poudeu, P.F.P., Uher, C.: A first-principles approach to half-Heusler thermoelectrics: Accelerated prediction and understanding of material properties. J. Mater.

2, 104–113, (2016).

[111] Chadov, S., Qi, X., Kübler, J., Fecher, G.H., Felser, C., Zhang, S.C.: Tunable

multifunctional topological insulators in ternary Heusler compounds. Nat. Mater. 9, 541–

545, (2010).

[112] Lin, S.Y., Chen, M., Yang, X.B., Zhao, Y.J., Wu, S.C., Felser, C., Yan, B.: Theoretical search for half-Heusler topological insulators. Phys. Rev. B - Condens. Matter Mater. Phys. 91, 1–6, (2015).

[113] D. S. Sholl and J. A. Steckel, DENSITY FUNCTIONAL THEORY A Practical Introduction.

[114] C.Kittel, introduction à la physique de l'état solide, (1996).

[115] M. Born, J. R. Oppenheimer, Ann. Phys. 87, 457, (1927).

[116] D.R. Hartree. Proc.Camb. Philos. Soc. 24 ,89, (1928).

[117] V. Fock, Z. Phys .62 ,795, (1930).

[118] C. J. Cramer, Essentials of Computational Chemistry: Theories and Models, England: WILEY, (2004).

[119] W. Kohn, «Electronic Structure of Matter, Wave functions and Density Functionals» Nobel Lectures, (1999).

[120] S. Matar, « Approches Monoélectroniques, Institut de Chimie de la Matière Condensée de Bordeaux, » CNRS 33608 PESSAC Cedex Preprint, (2004).

[121] W. Pauli Jr., Z. Physik, , 31, 765, (1925).

[122] J.C. Slater, Phys. Rev., 34, 1293, (1929).

[123] Vladimir Fock, Zeitschrift für Physik 61, 126, (1930).

[124] E Fermi. Un metodo statistice per la determinazione di alcune proprieta dell'atomo. Rend. Accad. Nazl. Lincei, 6:602–607, (1927).

[125] L. H. Thomas, Proc. Cambridge Phil. Roy. Soc. 23, 542, (1927).

[126] P.A.M. Dirac, Proc. Camb. Phil. Soc., 26, 376, (1930).

[127] P. Hohenberg and W. Kohn, Phys. Rev. 136, B864, (1964).

[128] W. Kohn, L. J. Sham, Phys. Rev. A 140 ,1133, (1965).

[129] von Maedeh Zahedifar, « Role of electron-phonon scattering in the relaxation of hot carriers at surfaces ».

[130] E. Fermi, Rend. Accad. Naz. Lincei 6, 602, (1927).

[131] D. M. Ceperley, B.J. Alder, phys. Rev. Lett. 45, 566, (1980).

[132] J. P. Perdew, K. Burke, M. Ernzerhof, Phys. Rev. Lett. 77, 3865, (1996).

[133] E. P. Wigner, Trans. R. Faraday Soc, 34 , 678, (1938).

[134] S. H. Vosko, L. Wilk and M. Nussair, Can.J. Phys. 58 , 1200, (1980).

[135] J.P.Perdew, A. Zunger, Phys. Rev. B 23; 5048; (1981).

[136] . M. Ceperley, B. J. Alder, Phys Rev. Lett. 45, 566, (1980).

[137] U. von Barth and L. Hedin, J. Phys. C: Solid State Phys. 5, 1629, (1972).

[138] A. D. Becke, Phys. Rev. A 38, 3098, (1988).

[139] J. P. Perdew, J. A. Chevary, S. H. Vosko, K. A. Jackson, M. R. Pederson, and C. Fiolhais, Phys. Rev. B 46, 6671, (1992).

[140] A. D. Becke and E. R. Johson, J. chem. Phys. 124 , 221101, (2006).

[141] F. Tran and P.Blaha, Phys Rev.lett 102 , 226401, (2009).

[142] Axel D Becke and Marc R Roussel, Physical Review A 39 (8), 3761, (1989).

[143] P. Blaha, K. Schwarz, G. Madsen, D. Kvasnicka, J. Luitz, Wien2k, Techn. Universitat, Vienna, Austria, (2001).

[144] E. Engel, S. H. Vosko, Phys. Rev. B47,20, (1993).

[145] F. Bloch, Z. Phys., 52555, (1928).

[146] J.C. Slater, « Quantum Theory of Molecules and Solids », V2, Ch. (1965) 8.

[147] C. Herring, Phys. Rev. 57, 1169, (1940).

[148] J.C. Slater, Phys. Rev. 51, 846, (1937).

[149] O.K. Andersen, Phys. Rev. B 12, 3060, (1975).

[150] N. Troullier and J. L. Martins, Phys. Rev. B 43, 1993, (1991).

[151] G. Kresse, J. Hafner and R. J. Needs, J. Phys. Condens. Matter 4, 7451, (1992).

[152] O. H. Nielsen and R. M. Martin, Phys. Rev. Lett 50, 697, (1983).

[153] W. C. Topp and J. J. Hopfield, Phys. Rev. B 7, 1295, (1974).

[154] M. B. Kanoun, Thèse de doctorat, université de Tlemcen, (2004).

[155] D.D. Koelling and G.O. Arbman, J. Phys. F 5 2041, (1975).

[156] S. Cottenier, ISBN 807215 90, (2002).

[157] D. J. Singh, Phys. Rev. B 44, 7451, (1991).

[158] S. Goedecker and K. Maschke, Phys. Rev. B 42, 8858, (1990).

[159] D. J. Singh and H. Krakauer, Phys. Rev. B 43, 1441, (1991).

[160] D. J. Singh, K Schwarz and P. Blaha, Phys. Rev. B 46, 5849, (1992).

[161] E. Sjostedt, L. Nordstrom and D. J. Singh, Solid State Commun. 15 114, (2000).

[162] P. Blaha, K. Schwarz, G. Madsen, D. Kvasnicka, J. Luitz, Wien2k, Techn. Universitat, Vienna, Austria, (2001).

[163] « Overview of CyGutz with WIEN2k and model interfaces — CyGutz_user_guide 2.0.0 documentation ». Consulté le: 25 octobre 2023. [En ligne]. Disponible à: https://cygutz.readthedocs.io/en/latest/overview.

[164] Andrés Cantarero and F Xavier Àlvarez, Nanoscale Thermoelectrics, 1, (2014).

[165] A. Crépieux, Introduction à la physique de la matiére condensée : propriétes

électroniques, Dunod 140, (2019).

[166] Prabhu Lal Bhatnagar, Eugene P Gross, and Max Krook, Physical review 94 (3), 511 , (1954).

[167] TJ Scheidemantel, C Ambrosch-Draxl, Timo Thonhauser, JV Badding, and Jorge O Sofo, Physical Review B 68 (12), 125210, (2003).

[168] T Thonhauser, TJ Scheidemantel, JO Sofo, JV Badding, and GD Mahan, Physical Review B 68 (8), 085201, (2003).

[169] G. K. Madsen and D. J. Singh, Comput. Phys. Commun. 175, 67, (2006).

[170] David Parker and David J Singh, Physical Review B 82 (3), 035204, (2010).

[171] C.Fesler, G.H. Fecher, B. Balke, Angew. Chem. Int. Ed. 46, 668-699, (2007).

[172] M. Jamal, M. Bilal, I. Ahmad, et S. Jalali-Asadabadi, « IRelast package », J Alloys Compd, vol. 735, p. 569 579, (2018).

[173] I. Mili, H. Latelli, Z. Charifi, H. Baaziz, et T. Ghellab, Comput Mater Sci, vol. 213, (2022).

[174] F.D. Murnaghan, *Proc. Natl. Acad. Sci.* 30 244, (1944).

[175] Saniz R, Ye L-H, Shishidou T and Freeman A J Structural, electronic, and optical properties of NiAl3: first-principles calculations Phys. Rev. B 74 014209, (2006).

[176] Liu Q-J, Liu Z-T, Feng L-P and Tian H First-principles study of structural, elastic, electronic and optical properties of rutile GeO2 and α-quartz GeO2 Solid State Sci. 12 1748–55, (2010).

[177] Kramers H A Some remarks on the theory of absorption and refraction of x-rays Nature 117 774–5, (1926).

[178] Kronig R D L On the theory of dispersion of x-rays J. Opt. Soc. Am. 12 547–57, (1926).

[179] F. Wooten, Optical Properties of Solids, Academic Press, New York, London, (1972).

[180] D. R. Penn, *Phys. Rev.B* 128 2093, (1962).

[181] G. Grimvall. Thermophysical Properties of Materials. North-Holland, Amsterdam, (cit. on pp. 9, 29), (1999).

[182] J. F. Nye. Physical Properties of Crystals. North-Holland: North-Holland, Amsterdam, (cit. on p. 9), (1964).

[183] https://www.admet.com/effect-specimen-geometry-tensile-testing-results

[184] N. Labgaa, Thèse de Doctorat en physique du solide, Université Ferhat Abbas-Sétif, (2011).

[186] S. Adachi, John Wiley & Sons, New York, (1992).

[185] S. Adachi, John Wiley & Sons, New York, (2005).

[186] M. Grundmann, Springer-Verlag Berlin Heidelberg, (2006).

[187] T. Shen *et al.*, « First-principles calculations of structural and mechanical properties of YFeO 3 ».

[188] M. Born, Math. Proc. Camb. Phil. Soc. 36, 160, (1940).

[189] M. Born and K. Huang, Dynamics Theory of Crystal Lattices (Oxford University Press, (1954).

[190] Voigt W., Lehrbuch der Kristallphysik, Verlag und Druck, Von BG Teubner, Leipzig und Berlin, (1928).

[191] J. R. Buschert, F. C. Peiris, N. Samarth, H. Luo, and J. K. Furdyna. Phys. Rev. B 49

4619, (1994).

[192] S. F. Pugh, Philos. Mag. 45, 823, (1954).

[193] P. Ravindran, L. Fast, P. A. Korzhavyi, B. Johansson, J. Wills, O. Eriksson, J. Appl. Phys. 84, 4891, (1998).

[194] N. C. Burtch, J. Heinen, T. D. Bennett, D. Dubbeldam, et M. D. Allendorf, *Advanced Materials*, vol. 30, n° 37. Wiley-VCH Verlag, (13 septembre 2018).

[195] M Naher and Naqib *Sci Rep* 11 1, (2021).

[196] L. Bao, D. Qu, Z. Kong, Y. Duan, Solid State Sci., 98, 106027, (2019).

[197] P. Ravindran, L. Fast, P.A. Korzhavyl, B. Johansson, J. Wills, O. Eriksson, J. Appl.Phys. 84 4891, (1998).

[198] D.H. Chung, W.R. Buessem, Proceedings, Plenum Press, (1968).

[199] S. Ranganathan, M. Ostoja-Starzewski, Phys. Rev. Lett. 101 055504–055507, (2008).

[200] J.F. Nye, *Oxford University Press, Great Britain*, (1957).

[201] Anderson O L , ‘ A simplifi ed method for calculating the Debye temperature from elastic constants ’, J Phys Chem Solids , 24 909 – 917, (1963).

[202] Schreiber E , Anderson O L , Soga N , Elastic Constants and their Measurements , McGraw-Hill , New York , (1973).

[203] G. A. Slack, *J. Phys. Chem. Solids* 34, 321, (1973).

[204] S. L. Shinde and J. Goela, *Condens. Matter Phys. XVIII* 271, 133, (2006).

[205] M. A. Blanco, E. Francisco and V. Lua~na, *Comput. Phys. Commun.* 158, 57. Source code distributed by the CPC program library: http://cpc.cs.qub.ac.uk/ , (2004)

[206] C. Toher *et al.*, *Phys. Rev. B* 90, 174107, (2014).

[207] M. Blanco *et al., J. Mol. Struct. Theochem.* 368, 245, (1996).

[208] J.-P. Poirier, *Introduction to the Physics of the Earth's Interior* (Cambridge University Press, 2000).

[209] Q. Wang *et al.*, « Enhanced Thermoelectric Properties in p-Type Double Half-Heusler Ti2−yHfyFeNiSb2−xSnx Compounds », *Physica Status Solidi (A) Applications and Materials Science*, vol. 217, n° 11, juin, (2020).

[210] Rabin D, Fuks D,Gelbstein Y , *Phys. Chem. Chem. Phys.*, 25, 520-528, (2023).

[211] J.-C. Zheng, *Front. Phys. China* 3, 269 (2008).

[212] B. R. Nag, *Electron Transport in Compound Semiconductors* (Springer, New York, 1980), pp.171{229}.

[213] T. J. Scheidemantel *et al.*, *Phys. Rev. B* 68, 125210 (2003).

[214] T. Thonhauser *et al.*, *Phys. Rev. B* 68, 085201 (2003).

[215] AI Liechtenstein, Vladimir I Anisimov, and Jan Zaanen, Physical Review B **52** (8), R5467 (1995).

General Conclusion

General Conclusion

The present dissertation offers a comprehensive examination of a new class of the quaternary double-half Heusler alloys that have multifunctional applications such as thermoelectric and optoelectronics.

We conducted an investigation on the structural, electrical, optical, elastic, and thermoelectric properties of the double half-Heusler alloys $ScX'Y_2Sn_2$ (X'=Nb, Ta; Y=Ni, Pd, Pt). The calculations are carried out using the ab-initio method of augmented plane waves within the density functional theory (DFT) framework. To calculate the total energy, LDA and GGA manipulate correlation and exchange potentials, respectively. Furthermore, we utilized several approximations for the computation of electronic and optical properties including the GGA, mBJ-GGA, LDA, mBJ-LDA, and Engel-Vosko (EV-GGA) approximations. In contrast, we exclusively used the GGA approximation to compute the elastic properties. Boltzmann transport equations were also utilized to calculate the thermoelectric properties of the new DHH alloys.

We have employed ab initio total energy calculations to investigate the stability structure, electronic properties, optical properties, elastic properties and thermoelectric properties for the DHH alloys $ScX'Y_2Sn_2$ (X'=Nb, Ta; Y=Ni, Pd, Pt). In brief, the main findings can be outlined as follows:

The obtained results indicate that our DHH alloys crystallize in a simple orthorhombic space group of 31_Pmn21.the optimization of these calculation with non-magnetic state for our alloys reveals that the GGA approximation is the most adequate approximation to describe the structural properties.

For the analysis of the electronic properties, we employed various approximations. Specifically, we selected the EV-GGA approximation, which yielded the most accurate bandgap measurement. Our findings indicate that the band structures of the double half Heusler alloys $ScNbNi_2Sn_2$, $ScTaPd_2Sn_2$, and $ScTaPt_2Sn_2$ are all semiconductors. The respective indirect bandgaps for these

alloys are 0.47 eV, 0.549 eV, and 0.851 eV. The main contributions to the total density of states arise from the d states located in close proximity of the Fermi level.

The dielectric function of DHH alloys at the main peak exhibits significant isotropy in both the real and imaginary parts. Additionally, absorption coefficient α(x), reflectivity spectrum R(ω), and refractive index n(ω) are computed and analyzed for radiation with energies up to 40 (eV). these alloys have a high reflectivity in the UV region.

The independent elastic constants, including the compressibility modulus B and shear modulus G, were determined at zero pressure. Furthermore, the Voigt-Reuss-Hill approximation was employed to estimate the elastic parameters (Young's modulus E, Poisson's ratio) for $ScX'Y_2Sn_2$ (X'=Nb, Ta; Y=Ni, Pd, Pt). From these calculations we conclude that our DHH alloys are mechanically stable and the measured value of B/G validates the ductile nature of these alloys.

We have computed the thermoelectric properties of the DHH alloys using the BoltzTrap code incorporated in the Wien2k program. Our findings shows that these alloys are of the p-type as evidenced by their positive Seebeck coefficient Additionally, they exhibit a significantly high Seebeck coefficient and exceptional electrical conductivity at room temperature.

At a temperature of 900 K, we have predicted extremely enhanced p-type figure of merit $ZT = 0.71$, $ZT = 0.76$ and $ZT = 1.02$ values for the DHH alloys $ScNbNi_2Sn_2$, $ScTaPd_2Sn_2$, and $ScTaPt_2Sn_2$, respectively. Based on our calculations, we found that quaternary half-Heusler materials have great potential as new thermoelectric materials. They are worth further efforts in synthesis due to their reduced thermal conductivity and improved electronic transport capabilities